Aftalion, Marc (2023) Simulating the gravimetric detection of submarines, calculating high-accuracy terrain corrections using LIDAR elevation data and performing a microgravity survey in the Campsie Fells. PhD thesis.

https://theses.gla.ac.uk/83702/

Simulating the Gravimetric Detection of Submarines, Calculating High-Accuracy Terrain Corrections using LIDAR Elevation Data and Performing a Microgravity Survey in the Campsie Fells

Marc Aftalion

Submitted in fulfilment of the requirements for the
Degree of Doctor of Philosophy

School of Physics and Astronomy
College of Science and Engineering
University of Glasgow

May 2023

Abstract

The work in this thesis relates to the field of gravimetry, the measurement of gravitational fields and their variations, which is carried out using highly-sensitive accelerometers known as gravimeters. By using gravimeters to measure the changes in gravitational field strength from place to place, it is possible to detect differences in the concentration of mass around the gravimeter and this has historically been used to monitor geophysical activity (such as variations in groundwater, volcanic activity or glacial mass), for geological exploration (such as searching for mineral or hydrocarbon resources) and many other applications.

This work covers a range of topics in gravimetry, starting with the use of computer programs to simulate the gravitational fields that would be generated when a submarine travelled past a stationary gravimeter, or array of gravimeters, situated underwater. This is done with the aim of estimating the efficacy of a new gravimeter known as the 'Wee-g' under development at the University of Glasgow at the time of writing and also has applications to the gravitational detection of submarines more generally. The gravitational field of a 100 m-long submarine is simulated, using a simplified one-dimensional density profile approximating the real density variations along the length of a large submarine. The simulated gravity field is then compared to the sensitivity of a prototype Wee-g gravimeter of $5\,\mu\text{Gal}/\sqrt{\text{Hz}}$ to give an initial estimate of the maximum detection range of such a signal by the Wee-g, which is found to be approximately 20 m. Then, synthetic noisy signals are made by combining the simulated gravity signals with real Wee-g sensor noise data and digital signal processing methods are used to try and recover the corrupted signal from the noise in a way that maximises the detection range. Matched filtering is applied which uses foreknowledge of the signal being searched for to significantly increase the signal to noise ratio (SNR) in the noisy data by an order of magnitude, which increases the Wee-g's detection range of the modelled submarine to ~ 30 m.

In addition, computer programs are made that determine a quantity known as the terrain correction at a given gravity survey point using digitised elevation data describing the surrounding topography. Terrain correction is the effect that the presence of surrounding hills and valleys has on the gravitational field strength at a location and, if it is not accounted for, substantial variations in gravity (and hence, potentially useful information) can be partially or completely obscured. Methods already exist to calculate the terrain correction but these are either slow and laborious, inaccurate (in comparison to contemporary gravimeter performance) or both, while the program presented in this work makes use of modern computing speed and high-accuracy elevation maps to improve on these. The terrain correction program presented here analyses terrain out to a distance of 166.735 km from the survey point, using 1 m-resolution LiDAR elevation data to describe the nearest 2 km^2, and can calculate terrain correction values in approximately 9 s when run on a computer with 8 GB of RAM. Terrain at all distances from the survey point is modelled using many flat-topped rectangular prisms and the gravitational field strength due to each prism is calculated using an already existing analytic solution. An in-depth analysis of the terrain correction computation of the innermost 2 km is carried out to compare the accuracy of the method used with simple analytic solutions. This analysis concludes that terrain corrections can be calculated with an uncertainty of 2 μGal or less when using 1 m^2-resolution elevation data, provided the terrain immediately around the survey point has an incline of less than 10°.

Finally, two gravity surveys carried out in January of 2020 by the author with a Scintrex CG-5 commercial gravimeter are described: one in the Campsie Fells — a range of hills roughly 10 km north of Glasgow — and the second in the cloisters of the Gilbert-Scott building on the University of Glasgow campus. The Campsies survey is compared with a gravimeter survey of the same region carried out in 1969 and discrepancies of up to a few mGal are observed, understood to be due to terrain correction inaccuracies in the older survey. Results from the survey in the cloisters are compared to the gravitational field due to underfloor air ducts described by plans of the building but little correlation is found. This is suspected to be the result of either inaccuracies in the building plans or the impact of environmental noise on the measurements.

Contents

List of Tables

List of Figures

Acknowledgements

I would first like to express my gratitude to my supervisor Prof. Giles Hammond, who has patiently provided me with valuable advice and guidance during the course of my work and without whom it would likely remain unfinished. I would also like to thank all of my friends and my family, who have all brought joy to my life and continue to make the future worth pursuing.

Declaration

I, the author, certify that the thesis presented here is solely my own work except in the places I have clearly indicated. The work was carried out in the Institute of Gravitational Research, part of the School of Physics and Astronomy at the University of Glasgow between October 2016 and July 2022, under the supervision of Prof. Giles D. Hammond. This PhD program was part-funded by an industrial sponsor: QinetiQ, a UK-based defence company which did so in the interest of supporting the work on Submarine gravity modelling in chapter 2. I declare that this thesis does not include work forming part of a thesis presented successfully for another degree. I declare that this thesis has been produced in accordance with the University of Glasgow's Code of Good Practice in Research.

Chapter 1

Introduction

1.1 Gravity

Gravity has been a subject of human inquiry since antiquity, beginning with Aristotle (384 to 322 BCE) who postulated that heavy objects like earth and water were imbued with the quality of ‘gravity’ which causes their downward motion, towards the centre of the world, which he saw as their natural place [1]. Aristotle also theorised that the rate at which heavy objects fall due to gravity was proportional to their weight. This was experimentally disproven in the 16th century, most rigorously by Galileo Galilei (1564 to 1642) who concluded that all objects fall at the same rate, regardless of their mass, provided that air resistance is negligible.

In 1687, Issac Newton published his *Philosophiæ Naturalis Principia Mathematica* (*Mathematical Principles of Natural Philosophy*) [2] in which he described gravity as a force acting between all massive objects, with a strength inversely proportional to the square of the distance between them. The magnitude of this gravitational force can be calculated using Newton’s Universal Law of Gravitation, shown in equation eq. (1.1).

$$\mathbf{F} = GM_1M_2\frac{\mathbf{r}}{|\mathbf{r}|^3}\ , \tag{1.1}$$

where $\mathbf{F}$ is the gravitational force vector in N, G is the gravitational constant ($G = 6.67 \times 10^{-11}\,\mathrm{m^3\,kg^{-1}\,s^{-2}}$), M_1 and M_2 are the individual masses of the two objects in kg and $\mathbf{r}$ is the distance vector between the objects in metres [2]. From this equation, the concept of a gravitational field can be derived as the acceleration a 1 kg test mass would experience when placed a certain distance from a massive object. This acceleration is known as the gravitational field strength and can be calculated using equation (1.2),

$$\mathbf{g} = GM\frac{\mathbf{r}}{|\mathbf{r}|^3}\ , \tag{1.2}$$

where, M is the mass of the object in question.

Equation 1.2 can be generalised to find the gravitational field due to any volume, V, with a non-uniform density distribution, $\rho(\mathbf{r})$, using the following expression,

$$\mathbf{g} = G \int_A \frac{\mathbf{r}-\mathbf{r}_0}{|\mathbf{r}-\mathbf{r}_0|^3}\,\rho(\mathbf{r})\,dV \ , \tag{1.3}$$

where dV is an infinitesimal volume element within the volume, A, and $\mathbf{r}$ is the vector to this element from the computation point (where g is to be calculated) and $\mathbf{r}_0$ is the vector from the origin to the computation point.

In 1915, Albert Einstein (1879 to 1955) published his theory of general relativity [3,4] which revolutionised the understanding of gravity as arising due to the curvature of spacetime, rather than an instantaneous, force acting between distant objects (as John Wheeler put it, "space acts on matter, telling it how to move. In turn, matter reacts back on space telling it how to curve." [5]). General relativity explains phenomena Newtonian gravity cannot, such as the anomalous perihelion precession of the planet Mercury, gravitational time dilation, gravitational lensing and gravitational waves, among others. However, the practical differences between Einstein's theory of gravity and that of Newton are only significant in situations of extreme mass and/or velocity which are extremely uncommon in most terrestrial circumstances, in which Newton's theory remains a highly accurate approximation.

On the surface of a planet like the Earth, gravity is most clearly observable as a downwards force felt by all objects with non-zero mass as a result of the gravitational attraction of the planet's own mass. The resulting magnitude of gravitational field strength, g, on the Earth's surface is, on average $g \approx 9.8\,\mathrm{m\,s^{-2}}$ but the exact value differs slightly from place-to-place. Variations in local g arise due to changes in latitude or elevation above (or below) mean sea level, the shape of surrounding topography, and because of variations in the thickness and density of the Earth's crust. That surface gravitational field strength is affected by density variations in the Earth's crust has been of particular interest in many fields of study because this provides the opportunity to use measurements of these gravity variations to help detect and characterise underground density changes.

1.2 Gravimetry and its applications

Gravimetry is the practice of using specialised accelerometers known as gravimeters to measure the strength of gravitational fields, g, and to identify changes in g between different locations or over time, which are known as gravitational anomalies. Traditionally, gravitational anomalies have been described using units of 'Gal' (named after Galileo Galilei) instead of the SI unit of acceleration, $\mathrm{m\,s^{-2}}$, and these share the relation, $1\,\mathrm{Gal} = 0.01\,\mathrm{m\,s^{-2}}$. Units of Gal will be used frequently in this work and some conversions between Gal, mGal and μGal and $\mathrm{m\,s^{-2}}$ are listed

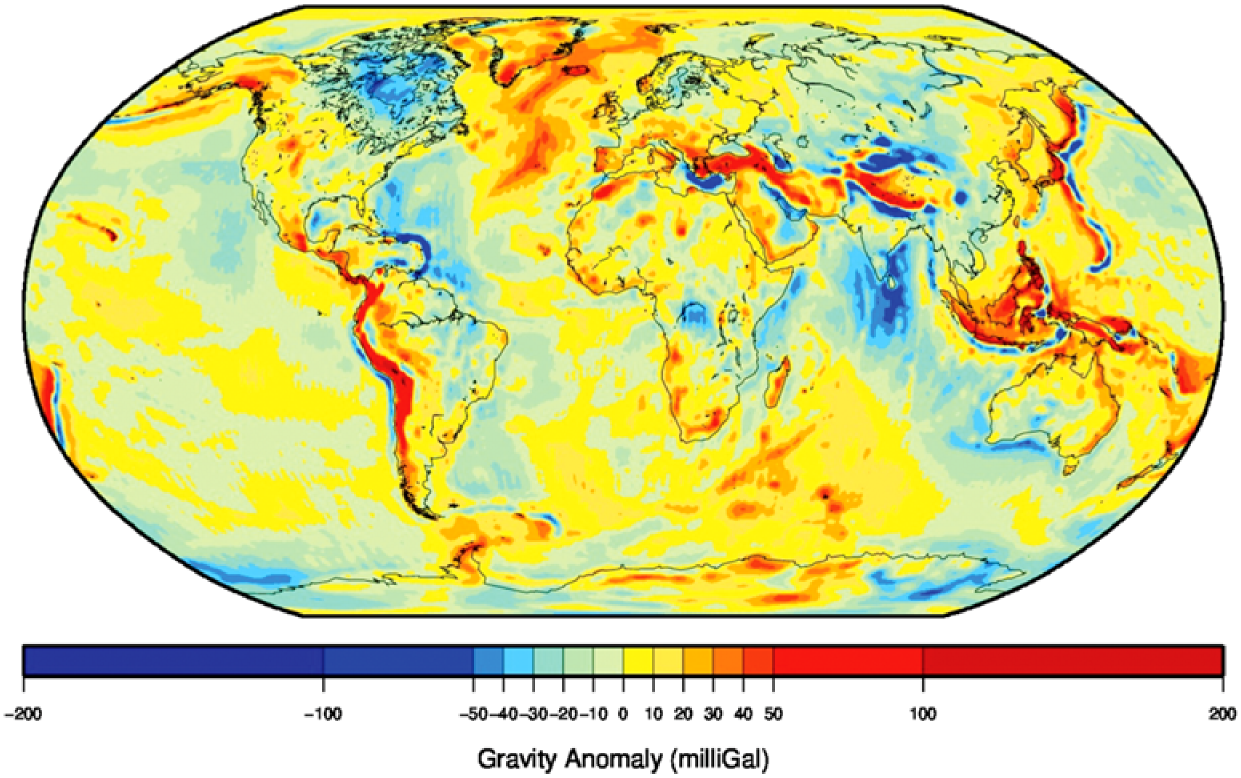

Figure 1.1: Map of global gravity anomaly as measured by the GRACE (Gravity Recovery And Climate Experiment) satellite. Image provided by University of Texas Center for Space Research and NASA (2016) [6].

in table 1.1 for reference.

	SI units ($\mathrm{m\,s^{-2}}$)
1 Gal	1×10^{-2}
1 mGal	1×10^{-5}
1 μGal	1×10^{-8}

Table 1.1: Table of conversions between Gal and $\mathrm{m\,s^{-2}}$

Gravity anomalies on the surface of the Earth are typically several orders of magnitude smaller than the total gravitational field strength of, on average, $g \approx 9.81\,\mathrm{m\,s^{-2}}$ (981 Gal). This can be seen in fig. 1.1 which shows a global map of gravity anomalies as measured by the GRACE (Gravity Recovery And Climate Experiment) satellite that operated between 2002 and 2017. The largest gravity anomalies on a global scale are of the order of hundreds of mGal ($\sim 1 \times 10^{-3}\,\mathrm{m\,s^{-2}}$) while on a smaller, regional scale less than a few hundred kilometres, they are usually a few tens of mGal ($\sim 1 \times 10^{-4}\,\mathrm{m\,s^{-2}}$) or less. At an even smaller scale of a few kilometres or less, gravitational anomalies are most commonly tens to hundreds of μGal in size.

Because of the properties of gravity, gravimetry can be used to collect useful information about mass distributions and density variations on and below the Earth's surface, which has made it a useful tool in geophysics and the Earth sciences more broadly. The following will give an overview of some of the applications of gravimetry.

1.2.1 Resource exploration

Gravimetry is most commonly used in the detection and characterisation of underground deposits of mineral or hydrocarbon resources alongside other prospecting methods such as seismic and electromagnetic techniques [7, 8]. Broadly speaking, this is done by studying the surface gravitational anomalies caused by underground density variations, specifically for those caused by density contrasts between a mineral deposit or geological feature of interest and the rock surrounding it. In the past, gravimetry has been used in this way to help estimate the depth of ore deposits detected through other means [9] and to help identify the size and contents of such deposits by analysing the associated gravity anomaly in detail [8]. For the case of particularly large and/or dense deposits such as metal sulphide orebodies (important sources of non-ferric metal ores with densities ranging from $3750\,\mathrm{kg\,m^{-3}}$ to $7700\,\mathrm{kg\,m^{-3}}$ [8, 10]), the surface gravity anomaly can be as large as a few mGal [11] and gravimetry can be used as a primary detection method [12, 13].

Gravimetric methods are also used to locate certain geological features that are known to coincide with deposits of useful resources or to constrain an area of exploration by other means within likely regions. This method of indirect search is common when searching for oil and gas reserves, which are often found near large formations of salt (salt domes) that can trap hydrocarbons in their vicinity when they form [14, 15]. In addition, borehole gravimetry is a method of determining the average density of a chosen layer of subterranean rock by measuring the change in gravity at different depths down a vertical (or almost-vertical) borehole (see fig. 1.2) [16]. Through repeated borehole gravity measurements, it is possible to observe changes in the density of rock strata over time which has been an important method of searching for and monitoring the depletion of hydrocarbon reservoirs [16, 17].

Gravimeter surveys for resource exploration are often required to be carried out over large areas, tens or even hundreds of kilometres in size, to search entire regions and this can be costly and time-consuming to do using land-based surveying methods. Instead, airborne gravimetry is a popular method of large-area gravity surveying, in which gravimeters carried by helicopters or light aircraft are flown over the region of interest to survey it faster and at reduced cost, especially in hard-to-access areas [18–20]. The main difficulty of airborne gravimetry is that flying platforms like helicopters and light aircraft are a strong source of vibrations which can severely impact the accuracy of on-board gravimeters and are generally only accurate to within a few hundreds of µGal at best [19, 20].

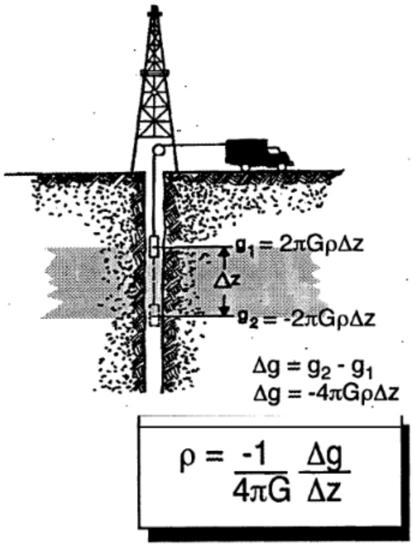

Figure 1.2: Diagram depicting how borehole gravimetry is able to measure the average density, ρ, of a certain layer of rock by observing the change in gravity, Δg, that results from a given change in depth down the borehole, Δz, which marks the distance from the top of the layer to its base. Image from Ander *et. al.* (1997) [16].

1.2.2 Hydrology and glaciology

Hydrology is the study of how water is distributed and moves around the surface, underground and atmosphere of the Earth, phenomena which have a critical impact on global climates and ecosystems [21]. Gravimetry has been an important tool in hydrology to detect temporal and spatial changes in the amount of water stored at and below the Earth's surface and to validate established hydrological models of these systems [21–23]. Most gravity data used for hydrology has been collected by the Gravity Recovery and Climate Experiment (GRACE) and the GRACE Follow-On (GRACE-FO) satellite gravimetry missions (the former of which operated from 2002 to 2017 and the latter from 2018 to the present) that aim to map the Earth's gravity field with a horizontal resolution of roughly 400-500 km^2 [22, 24, 25].

GRACE gravity data has been used to monitor changes in continental groundwater storage and has been used to observe changes in the upper surface of the water table in a region (below which, porous material is saturated with water) to within an accuracy of a few centimetres [26]. Such observations have been used to observe seasonal changes in water storage [27,28] as well as the multi-year depletion of groundwater reserves associated with droughts [29–32]. Similarly, long-term reductions in the total mass of glaciers and ice caps due to rising global average temperatures have also been detected by the GRACE experiment and the observed mass change has been used to improve estimates of the effect this has on sea levels [33–35]. During the operation of the first GRACE experiment, between 2002 and 2016, a global reduction in glacial mass of approximately 3000 Gt was observed, a reduction of 199 ± 32 Gt per year, which would result in an increase in global sea level of about 8 mm [35]. The magnitude of the gravitational

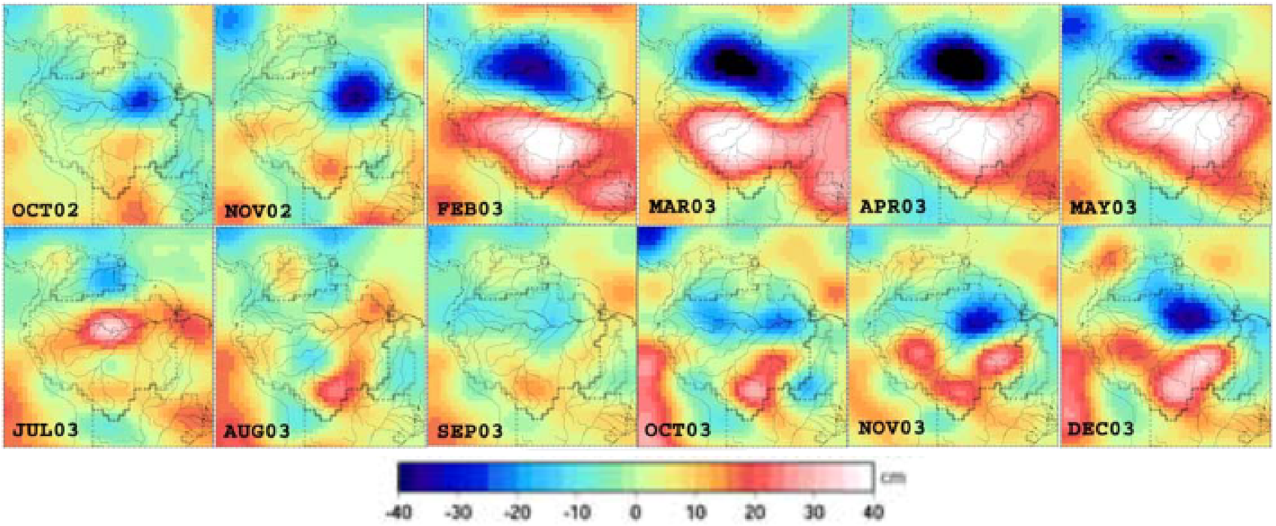

Figure 1.3: Water table surface height variations in Africa over the course of more than a year derived from GRACE satellite gravimetry measurements (from Han *et.al.* (2005) [26]).

anomalies associated with the aforementioned hydrological and glaciological effects is generally $\sim 1\,\mu\text{Gal}$ ($\sim 1 \times 10^{-8}\,\text{m}\,\text{s}^{-2}$) [24].

1.2.3 Volcanology and tectonics

Gravimetry is commonly used in the field of Volcanology to help investigate the underground structure and plumbing of active volcanoes and to observe transient gravity anomalies caused by volcanic activity. The geological structure of volcanoes can manifest significant density contrasts due to volumes of higher-density magma and volcanic rock close to lower-density, uncompacted rock or ash which result in positive and negative gravity anomalies at the surface. In extreme cases, these anomalies can have magnitudes of up to $30\,\text{mGal}$ or $-60\,\text{mGal}$, relative to the surrounding region, while other cases may exhibit little or no overall gravity anomaly [36]. Measurement of these anomalies can be used to survey deep and near-surface magmatic structures to better understand the mechanisms and characteristics of volcanoes [36–38].

Underground movements of magma are commonly accompanied by changes in surface gravity resulting from subterranean displacements of mass and monitoring these gravity changes can be a useful source of information about ongoing volcanic activity. The magnitude of these gravity changes depends on how much mass is displaced and its depth below the surface but such signals are generally quite small, of the order of 10s of μGal or less [39]. The monitoring of these gravity changes is particularly useful when performed in concert with other monitoring techniques such as observing seismic activity, ground deformations and gas emissions near a volcano, which can be used together to help forecast when volcanic eruptions are likely to occur [40–42].

Because surface gravity changes are directly linked to mass movements, volcano gravimetry can help determine the cause of other observed phenomena; for example, identifying whether a particular surface deformation is caused by the growth of a gas pocket or a similarly-sized magma intrusion, since the latter will result in a much larger gravity anomaly. Gravimetry is a particularly important tool for cases where magmatic intrusion is not accompanied by either seismic signals or ground deformation, in which case it becomes the primary method of detecting such phenomena [43].

Gravimetry has also found applications as a method of observing and studying tectonic effects like earthquakes and other large-scale dynamic changes in the structure of the Earth's crust. For example, large earthquakes have been observed to cause lasting changes in regional gravity (usually of a few µGal) because of vertical displacements of the crust and changes in the densities of the crust and mantle [44–46]. Studying these anomalies has helped better understand the causes and effects of individual earthquakes — for example, by clarifying the fault line and any resulting mass redistributions — and earthquake processes more generally [47–49].

1.2.4 Archaeology and void detection

Small-scale gravimetry surveys can be used to detect subterranean voids because of the density contrast between such open spaces and the surrounding rock. This has applications in the fields of archaeology, as a non-intrusive method of searching for suspected buried structures [50–52]; in defence applications, to search for tunnels or larger underground installations [53]; and in engineering, to investigate bedrock quality and search for possible sources of sinkholes [54,55]. The use of gravimetry for such purposes is generally quite rare due to high instrument costs and difficulty of these surveys which are commonly searching for small signals (commonly only a few µGal) and frequently must be performed in noisy urban environments that limit detector performance.

1.3 Corrections for Gravimetry

In order to use gravimetry to detect underground density variations, it is necessary to isolate gravitational anomalies caused by the features of interest (such as density variations) from those caused by other factors (such as a change in latitude, elevation or in the surrounding topography). This is done using a process known as gravitational correction (or gravitational reduction) in which the size of the effects caused by other factors are calculated as accurately as possible then removed from the data, leaving only the effects of interest. Calculating the size of most of these effects can be done using relatively simple equations that are reproduced below along with more information about the effects themselves.

1.3.1 Latitude correction

The Earth is not a perfect sphere but is, in fact, an oblate spheroid, meaning that the poles are slightly closer to the Earth's centre than the equator. In addition, the centrifugal acceleration due to the rotation of the Earth gets weaker as one moves closer to the poles as the distance to the planet's rotational axis decreases. Both of these effects cause the sea level gravitational field strength to gradually increase from 9.78 m/s at the equator to 9.83 m/s at the poles. An expression for the sea level gravitational field strength, g_θ, in $\mathrm{m\,s^{-2}}$ at a latitude of θ rad is given by [12],

$$g_\theta(\theta) = g_\mathrm{e}(1 + 5.297\,041\,4 \times 10^{-3}\sin^2\theta + 2.327\,18 \times 10^{-5}\sin^4\theta \\ + 1.262 \times 10^{-7}\sin^6\theta + 7 \times 10^{-10}\sin^8\theta)\ , \tag{1.4}$$

where g_e is an accurate measure of the vertical gravitational field strength at the equator. In this work the value used is $g_\mathrm{e} = 9.780\,326\,771\,5\,\mathrm{m\,s^{-1}}$ (from Moritz [56]) with which eq. (1.4) can calculate g_θ values with an uncertainty of $\pm 1 \times 10^{-9}\,\mathrm{m\,s^{-1}}$ ($\pm 0.1\,\mu$Gal). From this, the difference in g_θ between two points at latitudes θ_1 and θ_2 due to the latitude difference alone can be found with,

$$\Delta g_\lambda = g_\theta(\theta_2) - g_\theta(\theta_1)\ , \tag{1.5}$$

which is known as the latitude effect or latitude correction. At all latitudes, the variation in g_θ per kilometre travelled towards the nearest pole is of the order of $\sim 100\,\mathrm{mGal\,km^{-1}}$ and is as large as $\sim 800\,$mGal per kilometre travelled north or south at a latitude of ±45° [12].

1.3.2 Elevation corrections

Local gravitational field strength is affected by the elevation above sea level, h, of a location in three separate ways, known as the free-air correction, Bouguer correction and curvature correction, all of which are solely dependent on h.

Free-air correction

The free-air effect describes the reduction in gravitational field strength that occurs when moving to higher elevations due to the increasing distance from the centre of the Earth, leading to a decrease in g. The rate at which vertical gravitational field decreases (*i.e.* the vertical gravity gradient) is also dependent on R but for positions on the surface of the Earth, where elevation changes are approximately 0.1 % of the total radius, this change can be assumed to be linear. For a change in elevation of Δh metres on the Earth's surface, the free-air effect can be calculated with an uncertainty of $< 1 \times 10^{-9}\,\mathrm{m\,s^{-2}}$ [57] using,

$$\begin{aligned}\Delta g_{\mathrm{fa}} &= -\frac{2GM_E\Delta h}{{R_E}^2}, \\ &= -3.086 \times 10^{-6}\,\Delta h,\end{aligned} \tag{1.6}$$

where Δg_{fa} is the free-air effect in $\mathrm{m\,s^{-2}}$, G is the gravitational constant, and M_E and R_E are the mass and mean radius of the Earth in kg and m, respectively [12]. For locations at an elevation Δh metres from sea level, the free-air correction is applied by subtracting Δg_{fa} from measured gravity.

Bouguer correction

A greater than zero elevation at a point on the surface of the Earth implies the presence of additional material below the location in the form of a hill of some kind, the mass of which will act to increase g at the location, acting in opposition to the free-air effect. The Bouguer effect is a simple, first approximation of this gravitational effect that makes the assumption that all material between a location and sea level forms a completely flat slab of infinite horizontal extent and a uniform density, ρ_{B}, with a thickness equal to the point's elevation, Δh. Such an object is known as a Bouguer slab or Bouguer plate and its vertical gravitational field, Δg_{B}, can be calculated analytically with an uncertainty of $< 1 \times 10^{-9}\,\mathrm{m\,s^{-2}}$ [57] using the simple expression,

$$\begin{aligned}\Delta g_{\mathrm{B}} &= 2\pi G\rho_{\mathrm{B}}\Delta h, \\ &= 4.192 \times 10^{-10}\,\rho_{\mathrm{B}}\Delta h,\end{aligned} \tag{1.7}$$

where Δg_{B} is in $\mathrm{m\,s^{-2}}$, ρ_{B} is an estimated average density of terrain in the region in $\mathrm{kg\,m^{-3}}$ and Δh is the the thickness of the Bouguer slab (*i.e.* the elevation of the survey point relative to sea level) in m.

The Bouguer correction (also known as the Bullard A correction [58, 59]) is usually applied to gravity data by subtracting Δg_{B} from local measured g. More careful consideration is needed for locations that are below-ground (mine shafts, boreholes, etc.) or underwater, where Δg_{B} becomes negative and ρ_{B} must be the average density of the surrounding rock or water, as appropriate.

Curvature correction

The Bouguer slab is only a very simple approximation of terrain on the Earth's surface and a more accurate model is necessary to calculate high-accuracy gravity corrections. The curvature correction (also known as the Bullard B correction [58, 59]) makes an adjustment to the Bouguer correction that replaces the flat, infinitely-extending Bouguer slab with a curved, truncated spherical cap that more realistically represents the surrounding terrain, as shown in fig. 1.4a. This change in how mass is distributed leads to a change in g at the survey point; firstly, because the infinite slab is replaced with a finite object and secondly, because parts of the cap (the black areas in fig. 1.4a) are moved downwards relative to the slab due to its curvature. These two effects act in opposite directions, the former acting to decrease g and the latter acting to increase it, in comparison to an infinite Bouguer slab. The combined effect of these changes gives the curvature correction, g_{c}, the magnitude of which depends on the survey point's elevation above sea level, h, and the surface radius used for the truncated spherical cap.

By convention (following from Bullard in 1936 [59]), a cap surface radius of 166.735 km is generally used when calculating curvature corrections because this minimises the variations in g_{c} over an elevation range of 0 m to 4000 m, which applies to most of the Earth's surface. This is demonstrated in fig. 1.4b which plots variation in g_{c} over this elevation range for the case of several different cap radii. Ultimately, the choice of a 166.735 km cap radius is somewhat arbitrary but the standardisation of the curvature correction in this way helps maintain consistency between different gravity surveys. Using this standard cap radius, a good approximation for the curvature correction, Δg_{c}, in $\mathrm{m\,s^{-2}}$ is calculated by the power series,

$$\Delta g_{\mathrm{c}} = Ah - Bh^2 + Ch^3 + Dh^4\,, \tag{1.8}$$

where h is the elevation above sea level in metres and $A = 1.464\,139 \times 10^{-3}\,\mathrm{s^{-2}}$, $B = 3.533\,047 \times 10^{-7}\,\mathrm{m^{-1}s^{-2}}$, $C = 1.002\,709 \times 10^{-13}\,\mathrm{m^{-2}s^{-2}}$ and $D = 3.002\,407 \times 10^{-18}\,\mathrm{m^{-3}s^{-2}}$ [58]. When near sea-level, the curvature correction results in a $14\,\mathrm{\mu Gal\,m^{-1}}$ change in gravity when the elevation of the survey point is increased [60].

As mentioned in section 1.3.1, the Earth is an oblate spheroid which means it's curvature varies slightly with latitude and, therefore, the curvature correction also has some latitude-dependency. The impact of this latitude-dependence is more significant at higher elevations but at the latitudes and elevations used in this work, eq. (1.8) has an accuracy better than 0.01 μGal so is a suitable and time-saving approximation. At extremes of latitude (near poles or equator) and when there are large differences in elevation between survey points, it may be necessary for high-accuracy surveys to use the exact solution for Δg_{c} such as that given by LaFehr [60].

1.3.3 Terrain correction

The gravitational terrain correction, Δg_{tc}, (also called the Bullard C correction [58,59]) accounts for the gravitational effects arising from the topography around a survey point and is widely considered the most complicated and tedious to calculate of the corrections discussed [61–63]. Any topographic variations (*i.e.* departures from completely flat surroundings) around a location will act to reduce g and the more rugged the surroundings are, the larger this effect is. For example, Yen [62] calculated terrain corrections to be only a few mGal in size in relatively flat

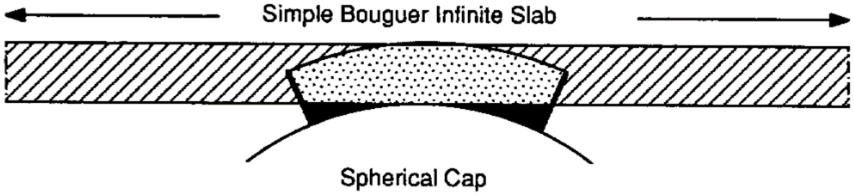

(a)

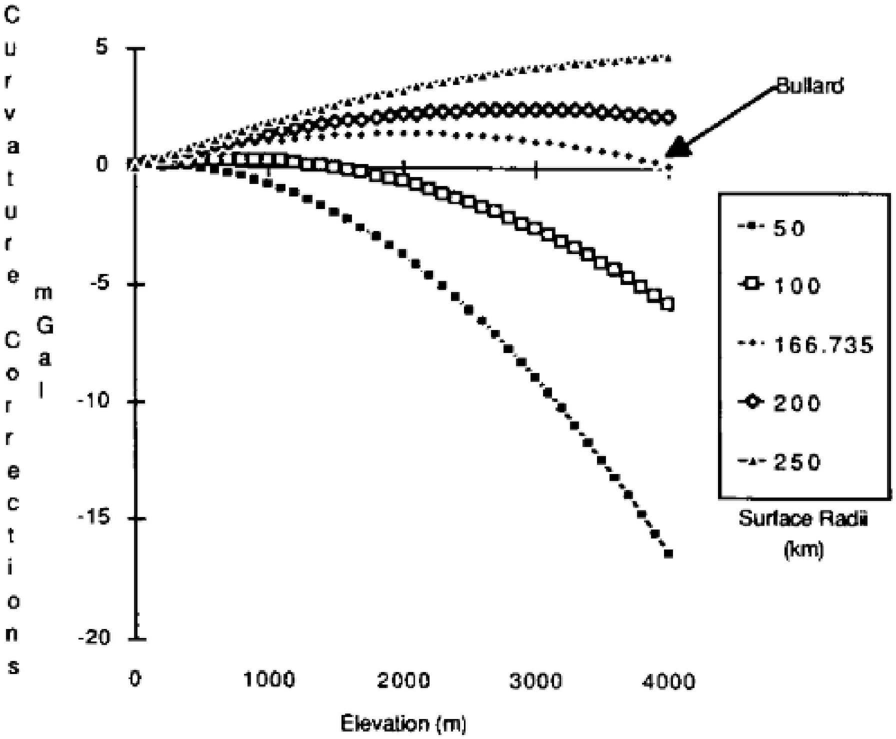

(b)

Figure 1.4: (a): Representation of the Bouguer infinite slab and the truncated spherical cap approximations used in the Bullard A and Bullard B corrections, respectively, to model the gravitational effect of the ground between a survey point and mean sea level. (b): Graph showing how the magnitude of the curvature correction varies with elevation (*i.e.* thickness of the cap) for the case of several different cap surface radii. Both diagrams from LaFehr (1991) [60].

regions of Taiwan but greater than 90 mGal in very mountainous areas.

The size of the terrain effect is difficult to calculate exactly and is generally estimated by dividing terrain features into discrete regions, simplifying the real topography of these and using analytic solutions to find g due to these representations. Terrain correction calculation is the main topic of chapter 3 of this work and a detailed description of it and how it can be calculated are found in section 3.1.

1.3.4 Time-varying corrections

As well as the gravitational corrections that relate to the location and surroundings of a gravity survey point, it is also important to correct for time-varying changes in g at a location that can otherwise obscure signals of interest. One of the most significant time-varying effects is the Earth tides; the periodic elastic deformation of the Earth's crust caused by the gravitational tidal forces of the Sun and Moon. This causes periodic, latitude-dependent changes in elevation (of approximately 0.2 m - 0.3 m at most [64] which result in significant variations in g of up to 0.3 mGal over the course of hours and days [58]. The tide signals consist of two main frequency components arising from the motion of the Sun-Earth-Moon system, one with a period of approximately 24 hours (known as Diurnal i.e. daily) due to the gravitational influence of the sun and one with a roughly 12-hour period (known as semidiurnal — half-daily) due to the Moon. The exact gravitational effect of the Earth tides can be accurately modelled using equations [57] or suitable software implementations of these (e.g. the free software *Tsoft* [66]) and can then be subtracted from data to correct for it. Established methods of calculating the Earth tides can do so with an uncertainty of less than 0.1 µGal [57]. Figure 1.5 shows an example of measured gravity variation over the course of 19 days alongside the theoretical effect of Earth tides on g over the same period. The total period of oscillations can be seen to vary as the diurnal and semidiurnal frequency components of the tides move in and out of phase with one another (because their periods are, in fact, slightly more than 24 hours and 12 hours, respectively).

Ocean tides can also cause time-varying changes in g due to the shifting mass of water on the earth's surface and the slight deformations of the crust that result due to the loading of the water mass on the sea floor (an effect known as 'ocean loading'). The magnitude of these gravitational effects depends on the elevation and proximity to the coastline of the survey point in question and can be as large as 20 µGal at particularly susceptible locations [12,67]. Ocean loading effects on gravity are generally slightly out of phase with the Earth tides due to the perturbation of tidal currents by bathymetry (seafloor topography), which can delay the movement of water to and from coastlines [68]. The magnitude of gravitational ocean loading effects can be calculated mathematically with an uncertainty of < 0.1 µGal [69].

For high-accuracy gravity surveys, other time-varying effects may need to be considered as well, such as g changes caused by variations in atmospheric pressure and groundwater levels. In the case of the former, a change in local atmospheric pressure indicates a change in the mass of

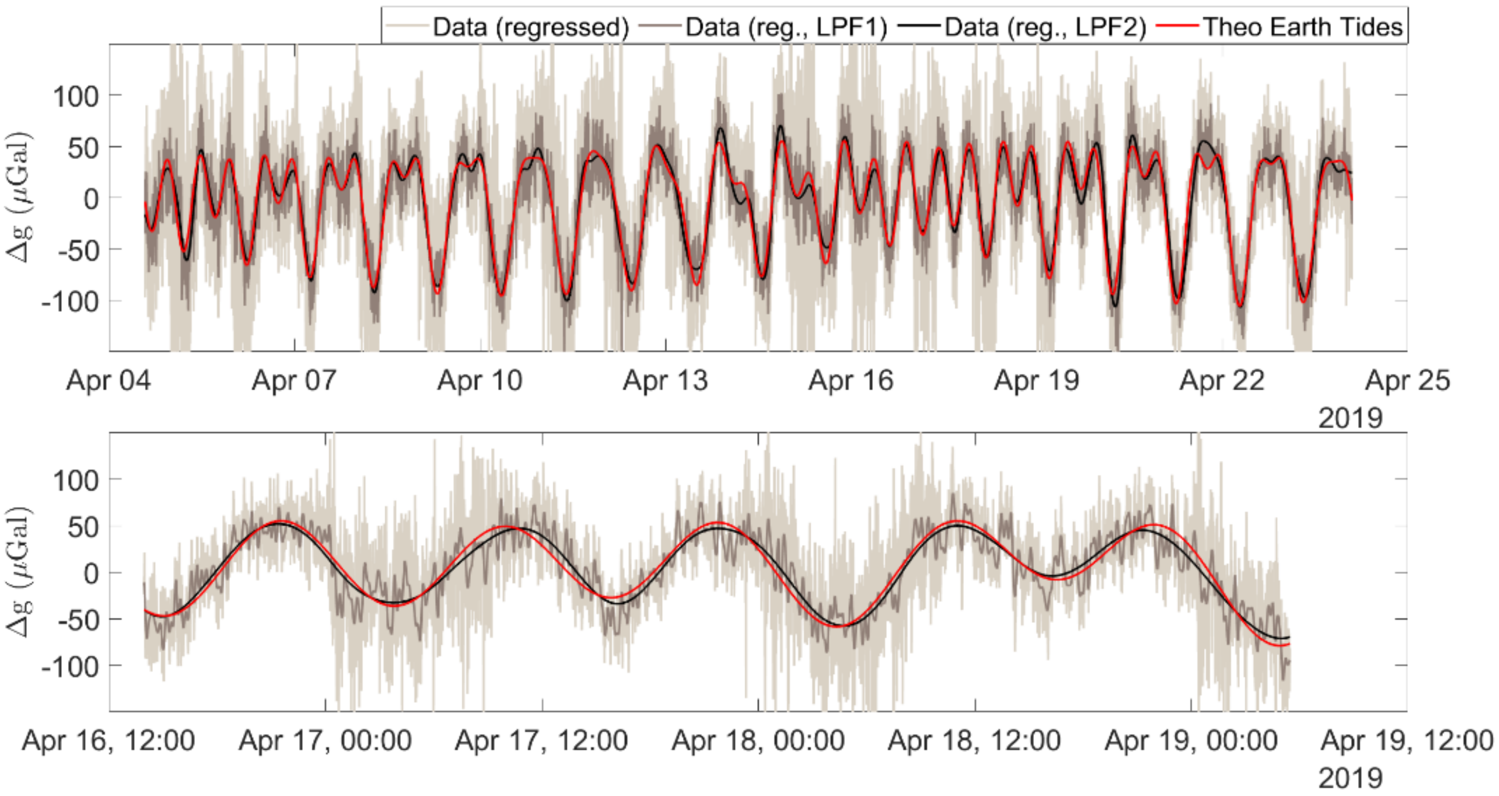

Figure 1.5: Graph showing theoretically calculated Earth tides (red line) alongside gravity measurements by a ‘Wee-g’ MEMS gravimeter (described in more detail in section 1.4.2) performed at the University of Glasgow in April 2019. The light grey line shows raw acceleration data from the sensor after regression to remove long-term drifts, the dark grey line (LPF1) is the same data with a 1 mHz-bandwidth low pass filter applied and the black line (LPF2) shows the result of applying a 20 μHz-bandwidth low pass filter to the dark grey line. The lower plot shows a zoomed-in extract of the upper plot between April 16 and April 19 [65].

the air column above a gravity survey point, which affects the vertical gravitational field strength at that point. An approximate relationship between a change in atmospheric pressure, ΔP, and the resulting gravitational effect, Δg_{P} is given by [70],

$$\Delta g_{\mathrm{P}} = -3.56\,\mu\mathrm{Gal/kPa}\,. \tag{1.9}$$

If local pressure is measured with an accuracy of $\sim 10\,\mathrm{kPa}$ or better, this expression can calculate Δg_{P} with a maximum error of roughly $0.1\,\mu\mathrm{Gal}$. Because atmospheric pressure changes are usually only a kPa or less over the course of a day, the resulting Δg_{P} is normally less than $1\,\mu\mathrm{Gal}$ during field surveys and rarely considered. However, the passage of high pressure weather formations like thunderstorms can cause more significant changes of pressure and gravitational effects of more than $10\,\mu\mathrm{Gal}$ in a few hours [70].

Similarly, a change in groundwater level (i.e. the level below which most porous rocks and underground cavities are fully saturated with water — also called the water table) indicates a change in mass below a location that will affect local gravitational field strength. The exact gravity change accompanying a certain groundwater level change, Δw, will depend on the porosity of the geology in the region and so is difficult to calculate precisely. Instead, an upper estimate of the gravitational effect, Δg_{w}, caused by a groundwater level change, Δw, can be calculated analytically by assuming the ground is completely porous and using a Bouguer slab approximation, as shown in eq. (1.7), with a slab density of $\rho = 1000\,\mathrm{kg\,m^{-3}}$ and letting $\Delta h = \Delta w$ which gives [12],

$$\Delta g_{\mathrm{w}} = 4.192 \times 10^{-10} \Delta w\,\mathrm{m\,s^{-2}}\,, \tag{1.10}$$

$$\Delta g_{\mathrm{w}} = 41.92\,\mu\mathrm{Gal/m}\,. \tag{1.11}$$

The uncertainty in the calculation of this effect is difficult to determine but is mostly dependant on how accurately groundwater level can be measured and how well the surrounding geology and its porosity is known [12].

Most surveys also correct for instrumental drift — the erroneous gradual change in measured g arising due to internal factors in the survey instruments themselves — and this will be described in more detail in section 1.4.

1.3.5 Bouguer anomaly

After applying all the corrections listed so far (latitude, free-air, Bouguer, curvature, terrain and time-varying corrections), the remaining gravity variations are referred to as the 'Bouguer anomaly' or 'complete Bouguer anomaly' which, in theory, shows gravitational changes due to underground density variations. If the terrain and curvature corrections are left out during the correction process then the result is referred to as the 'simple Bouguer anomaly' and if only latitude and free-air corrections are applied the result is called the 'free-air anomaly' [71]. For convenience, a comparison of the non-time-varying gravitational corrections discussed is presented in section 1.3.5.

Table 1.2: Table comparing the various gravitational corrections; their dependencies, magnitudes and uncertainties. The uncertainty values given assume that there is no uncertainty in latitude and elevation of gravitational survey points.

Gravitational correction	Dependency	Effect magnitude	Uncertainty
Latitude, Δg_λ	Latitude variation	$\sim 0.1\,\mathrm{mGal\,km^{-1}}$ to $\sim 0.8\,\mathrm{mGal\,km^{-1}}$ [*]	$< 0.1\,\mu\mathrm{Gal}$
Free-air, Δg_{fa}	Elevation	$-0.3086\,\mathrm{mGal\,m^{-1}}$	$< 0.1\,\mu\mathrm{Gal}$
Bouguer, Δg_{B}	Elevation	$0.112\,\mathrm{mGal\,m^{-1}}$ [†]	$< 0.1\,\mu\mathrm{Gal}$
Curvature, Δg_{c}	Elevation	$\sim 14\,\mu\mathrm{Gal\,m^{-1}}$ [‡]	$< 0.01\,\mu\mathrm{Gal}$
Terrain, Δg_{tc}	Topography	$\sim 1\,\mathrm{mGal}$ to $\sim 10\,\mathrm{mGal}$ [§]	Method-dependent [‖]
Earth tides	Latitude, Longitude, Time (period: $\sim$ hours to months)	$\sim 100\,\mu\mathrm{Gal}$ to $300\,\mu\mathrm{Gal}$	$< 0.1\,\mu\mathrm{Gal}$
Ocean loading	Latitude, Longitude, Proximity to ocean Time (period: $\sim$ hours to months),	Up to $\sim 20\,\mu\mathrm{Gal}$	$< 0.1\,\mu\mathrm{Gal}$
Atmospheric pressure, Δg_{P}	Weather, Time (period: $\sim$ hours)	$-3.56\,\mu\mathrm{Gal\,kPa^{-1}}$	$\sim 0.1\,\mu\mathrm{Gal}$
Groundwater level, Δg_{w}	Precipitation, Time (period: days to seasons)	$41.192\,\mu\mathrm{Gal\,m^{-1}}$	Varies [#]

[*] Depending on the latitude at which the survey is being performed.

[†] Assuming a ground density of $2670\,\mathrm{kg\,m^{-3}}$.

[‡] When near sea level.

[§] When in moderately hilly surroundings.

[‖] Different methods of terrain correction and their associated uncertainties are discussed in detail in section 3.1.

[#] Depends on how accurately the groundwater level and porosity of the surrounding geology are known.

1.4 Gravimeters

Gravimeters are devices used to measure the strength of the gravitational field at a given location and are, in essence very sensitive accelerometers that can measure tiny variations in g on the surface of a planet like the Earth. In contrast with other high-accuracy accelerometers like seismometers, gravimeters must also demonstrate a long-term stability and repeatability when taking measurements in order to reliably characterise changes in gravity; either between multiple locations or at one point over time.

Gravimeters can be grouped into two categories determined by their capabilities — Absolute gravimeters and Relative gravimeters — which will now be described in more detail:

Absolute gravimeters: Absolute gravimeters are devices that directly measure the acceleration due to gravity, g, at a particular location. They do this either by measuring the oscillation period of a pendulum of known length (which is dependent on g) or through careful measurement of the acceleration of a freely-falling mass in a vacuum using laser interferometry. The pendulum method was the first method to be developed and deployed in early gravimeters but free-fall gravimeters have since demonstrated a greater accuracy and most contemporary absolute gravimeters are free-fall devices. These instruments work by, essentially, using a freely falling mass as one of the end mirrors of a vertical interferometer arm and interfering this light with that from a perpendicular, fixed-length reference arm to precisely measure the mirror's position, from which its free-fall acceleration can be determined [72, 73].

More recently, another type of absolute gravimeter has been developed called an atom gravimeter, which works on the same principle as a traditional free-fall gravimeter but measures the acceleration of a cloud of freely-falling atoms cooled to cryogenic temperatures [74]. Atom gravimeters utilise atom interferometry, wherein a cloud of atoms is directed, split into two and recombined using laser pulses (analogous to beam-splitters and mirrors in optical interferometers) and, due to the wave characteristics of matter, a path difference in the trajectories of the split and recombined atoms causes a detectable phase shift. Using an appropriate experimental layout, this path difference can be made to depend on the strength of the inertial forces that affect the moving atoms in the system and so can be used to measure these forces, including the gravitational field strength, g [75, 76].

Modern absolute gravimeters are very accurate but tend to be large, heavy and expensive devices. For example, the Micro-g Lacoste FG5-X absolute gravimeter, pictured in fig. 1.6a, weighs 150 kg and costs approximately $US500,000 while commonly demonstrating a measurement accuracy of roughly 2 μGal [73]. Their large size and weight means that these devices aren't practically useful for conducting regional gravitational surveys and they are usually used to establish gravitational 'base stations' instead, where exact g is well-known.

Relative gravimeters: Relative gravimeters are devices that measure relative changes in gravitational acceleration, g, over time and between locations but are unable to determine the total magnitude of g as absolute gravimeters can. Contemporary relative gravimeters work using some variation of a vertical spring balance system where a test mass is suspended by a zero-length spring; a spring that is pre-tensioned during manufacture so that it's un-stretched length is theoretically zero [77]. If this suspension is constructed in the correct way, the downwards force of gravity on the mass can be balanced almost exactly by the restoring force of the spring system over its entire range of motion (one notable variation is a superconducting gravimeter,

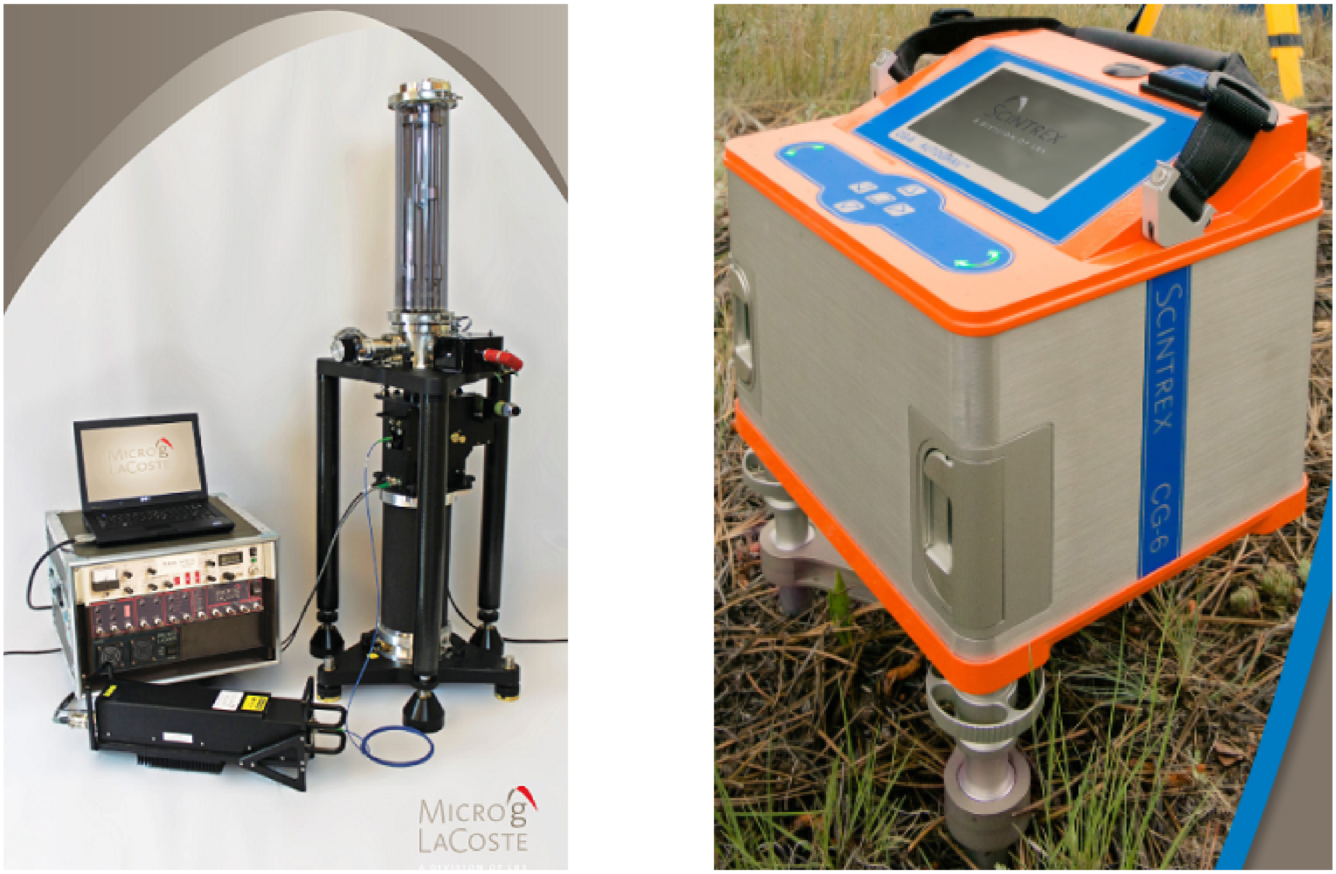

(a) (b)

Figure 1.6: (a): Photo of a Micro-g LaCoste FG5-X absolute gravimeter [80]. (b): Photo of a Scintrex CG-6 relative gravimeter [79].

where a superconducting test mass is suspended by magnetic levitation [78]). A change in g will alter the vertical position of the test mass until a new equilibrium is reached and careful monitoring of the test mass position allows the size of the gravity change, Δg, to be measured. After their manufacture, relative gravimeters must be calibrated to identify how exactly the movement of the test mass relates to a change in local g. This is most commonly done by transporting the device between two locations where the magnitude of g is already known to a high degree of accuracy, such as gravitational base stations previously established using absolute gravimeters.

Modern relative gravimeters tend to be less expensive and heavy than absolute gravimeters but are still complicated and costly instruments. For example, a Scintrex CG-6 quartz spring relative gravimeter costs approximately $US100,000, weighs 5.2 kg, has a 0.1 μGal reading resolution and exhibits tares of less than 5 μGal when repositioned under normal operating conditions [79]. Relative gravimeters are generally much more portable than absolute devices and are used more frequently when carrying out gravity surveys of extended regions, sometimes using measurements at absolute gravimeter base stations to convert their relative Δg measurements into variations in overall g.

1.4.1 Noise in gravimeters

The performance of both absolute and relative gravimeters is affected by various factors which are unrelated to the gravitational field strength that show up in gravimeter data as unwanted sources of noise. The most significant of these factors are the tilt of the instrument, variations in external temperature and vibrations coupled into the system, all of which can obscure or distort gravitational signals and usually determine the accuracy limits of a gravimeter.

Device tilt is significant because gravimeters are only sensitive in a single direction since they work by measuring the height of a falling test mass or the linear displacement of a test mass on a spring (or equivalent system). Therefore, if the gravimeter's sensitive axis is misaligned with the gravitational field, g, by an angle, θ, then it will instead measure g_θ, where

$$g_\theta = g\cos\theta\,, \tag{1.12}$$

which will lead to an underestimate of the true g. This means that gravimeters must be carefully levelled before use to accurately measure g and most commercial devices are equipped with tilt-sensors and an adjustable base to facilitate this. Also, if θ is measured during device operation it is possible to use equation eq. (1.12) to estimate the true g from the observed g_θ but any uncertainty when measuring θ will lead to uncertainty in the calculated g.

Temperature changes can also affect the physical function of gravimeters and have a particularly significant impact in spring-based relative gravimeters since the spring constant (*i.e.* the stiffness) of the spring used in these systems usually has some temperature dependence. A change in spring constant will cause a change in the equilibrium position of the test mass that the instrument will be unable to distinguish from a real change in g and so contribute to error in the data. To reduce the impact of temperature changes, gravimeters are generally insulated or internally temperature-controlled to minimise the temperature variations of the device's internal components. The effect of temperature can also be removed from gravity data to some extent through consideration of the temperature-dependent behaviour of the spring material used and close monitoring of temperature changes, estimating the size of the effect and subtracting it from data.

Gravimeters are also very sensitive to external vibrations which can interfere with the precise position measurements of falling or suspended test masses used in both absolute and relative devices. Relevant sources of vibrational noise include anthropogenic effects like the device being bumped or ground vibration due to nearby infrastructure as well as vibrations from wind or seismic effects like earthquakes or even waves crashing on distant shoreline. These vibrational noise sources tend to have a much higher frequency than gravitational signals of interest, which change much slower over time or almost not at all, so the effect of vibrational noise can be reduced by averaging gravimeter data over a period of time. To counter vibrational noise, some high-accuracy gravimeters use sophisticated active isolation systems to insulate them from the effects of ground motion and let them measure free-falling masses (and thereby, g) even more accurately. This adds to the complexity, size and cost of the device and so such vibration isolation systems are usually only found on absolute gravimeters at gravitational base stations and not used for field surveys.

The sensitivity of different gravimeters is usually compared by considering the amplitude spectral density (ASD) of individual device measurements, which describes how a device's acceleration sensitivity varies with the frequency of acceleration it is subjected to. The ASD of a measurement is found by taking the square-root of the power spectral density (PSD) of the same measurement and is commonly used to describe the performance of accelerometers and various electrical components such as op-amps [*]. Since power spectral density is presented with units of power per frequency (commonly $\mathrm{W}/\sqrt{\mathrm{Hz}}$), the units of amplitude spectral density are the square root of this, namely amplitude per square-root of frequency (amplitude$/\sqrt{\mathrm{Hz}}$). In the case of gravimeters, the ASD of measurements is usually expressed in units of $\mathrm{Gal}/\sqrt{\mathrm{Hz}}$ and the ASD at a frequency of 1 Hz is often used when making comparison between device sensitivities.

1.4.2 The 'Wee-g' MEMS gravimeter

Much of the work in this thesis is focused around a new type of relative gravimeter under development at the University of Glasgow, at the time of writing, that aims to be substantially smaller and cheaper than its contemporaries while still exhibiting good performance. This device, called the 'Wee-g', is based on a miniaturised mass-on-a-spring system small enough to be classified as a MEMS (Micro Electro-Mechanical Systems) device and its performance as a gravimeter was first demonstrated by a measurement of the Earth tides over five days (see section 1.3.4) in 2016 [81].

MEMS are miniaturized mechanical or electro-mechanical devices with features that range from $\sim 1\,\mu\mathrm{m}$ to several millimetres in size. They are most commonly made out of semiconductors, particularly silicon, for which microfabrication techniques have been well-developed by the integrated circuit industry. MEMS devices have found many applications and can be used to make many types of sensor, such as accelerometers, microphones and pressure sensors, capable of matching or exceeding the capabilities of their macro-scale counterparts. In addition, MEMS are often cheaper to make due to the well-developed microfabrication processes used in their production that allow the batch-production of many devices at once to reduce unit cost. This has resulted in the proliferation of small, low-cost MEMS sensors that are commonly used in smartphones, cars and other consumer electronics [82].

The Wee-g MEMS gravimeter measures relative changes in local gravitational field strength, g, by monitoring the displacement of a tiny, 0.02 mg, test mass suspended by four spring cantilevers as pictured in fig. 1.7. The position of the test mass is measured in one direction only

---

[*] An ASD plot effectively presents the same information as a PSD plot but the vertical scale of the former is linear, which can be preferable when variations in spectral density are relatively small.

(indicated by the red arrow in fig. 1.7b) so, like other spring gravimeters, the device must be carefully levelled with its sensitive axis oriented vertically to avoid tilt-induced errors. Also, the stiffness of the four silicon spring cantilevers is temperature dependent so the entire Wee-g device (pictured partially-assembled in fig. 1.7a) is placed in a thermally insulated and temperature-controlled enclosure to reduce temperature-induced errors.

In 2019, the Wee-g was used to measure gravity for 19-days and produced the measurement of Earth tides shown in fig. 1.5, demonstrating its long-term stability [65]. The amplitude spectral density of this measurement is plotted in fig. 1.8 and clearly shows the presence of signals with frequencies that correspond to the diurnal and semidiurnal periods of the Earth tides, highlighted by the left-most grey area. The main series in fig. 1.8 is comprised of data collected using a fast sampling rate of 20 Hz (the orange line) and data collected with a slower sampling rate of 0.18 Hz (the blue line), the latter of which was used for most of the measurement to reduce the digital storage space required. The fast-sampling dataset in fig. 1.8 also shows the presence of signals corresponding to microseismic vibrations — seismic signals originating from the effect of ocean waves on the coast and seafloor [83, 84] — and due to the resonant frequency of the Wee-g mass-on-spring system, itself. The unlabelled peak at approximately 25 mHz does not have a real geophysical source but was caused by the temperature control electronics used at the time [65]. Also, the blue and yellow lines can be seen to decrease in amplitude at higher frequencies but this is simply a result of low-pass filtering the data.

The yellow line in fig. 1.8 plots the ASD of the true electronic noise floor of the sensor and is used to estimate the sensitivity of the Wee-g itself in the higher-frequency region, which is otherwise dominated by seismic noise. Ideally, a seismometer would have been used in tandem with the Wee-g during the measurement so that higher-frequency seismic effects could be measured and subtracted from the gravimeter data but no seismometer was available. Instead the electronic noise floor serves as an estimate of the device's best performance. The noise floor is measured by altering the device operation in such a way that its output is decoupled from any gravitational field changes or inertial movements, giving a measure of the noise originating within the device itself.

Analysis of the data in fig. 1.8 by Prasad [65] concludes that during this measurement, the Wee-g achieved a peak sensitivity of $\sim 18\,\mu\text{Gal}/\sqrt{\text{Hz}}$ when using a 20 Hz sampling rate. More recent iterations of the Wee-g have demonstrated improved noise performance over that shown in fig. 1.8. Figure 1.9 shows the ASD of a 10-minute sensor noise measurement (comparable to the yellow line in fig. 1.8) taken in May 2023 by a newer Wee-g device, showing a sensitivity of $\sim 5\,\mu\text{Gal}/\sqrt{\text{Hz}}$ at a frequency of 1 Hz which is comparable to commercially available relative gravimeters.

As well as demonstrating comparable noise performance to contemporary commercial gravimeters, the Wee-g promises at least an order of magnitude reduction in the size, weight and cost of a relative gravimeter [85], thanks to its nature as a MEMS-based sensor. Such a device would

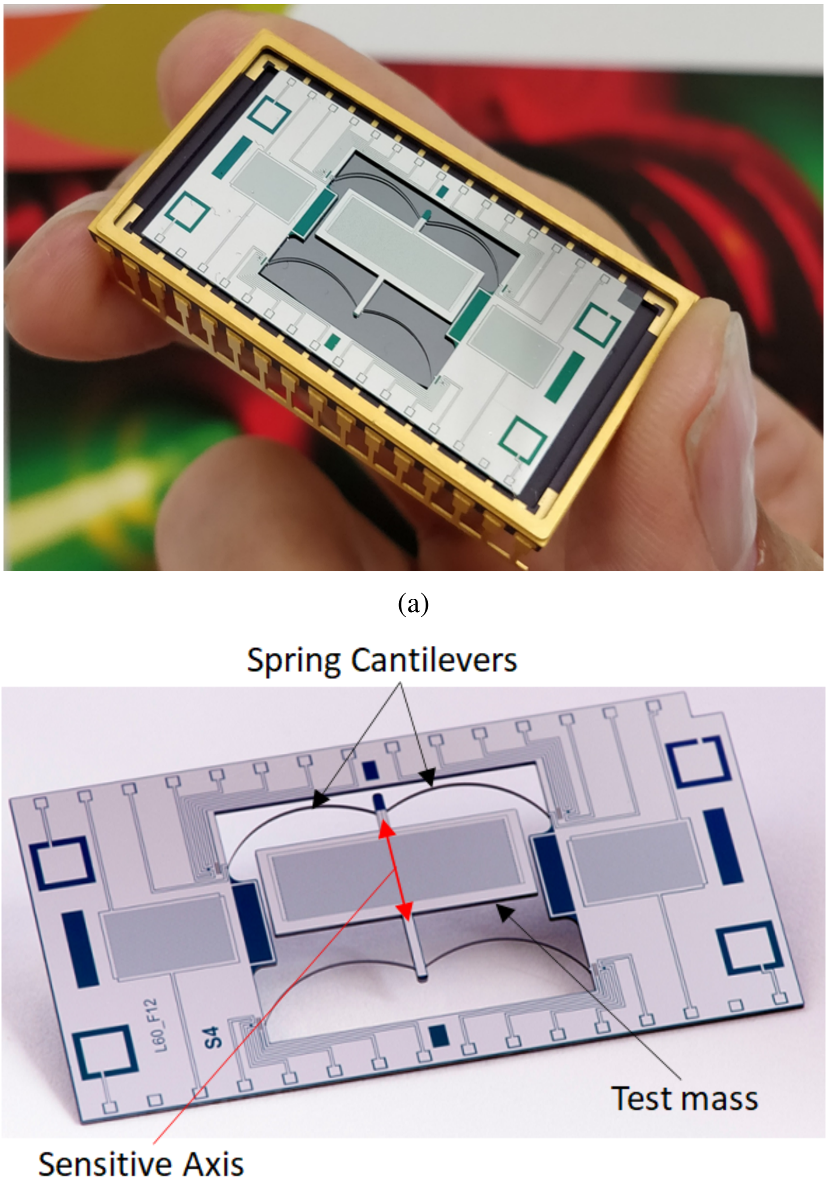
(a)

(b)

Figure 1.7: (a): Photograph of a Wee-g MEMS gravimeter. The device is shown mounted in an open package which is placed inside a thermally controlled enclosure inside another external casing when assembled for use. (b): Labelled close-up of the moving parts of a Wee-g MEMS gravimeter.

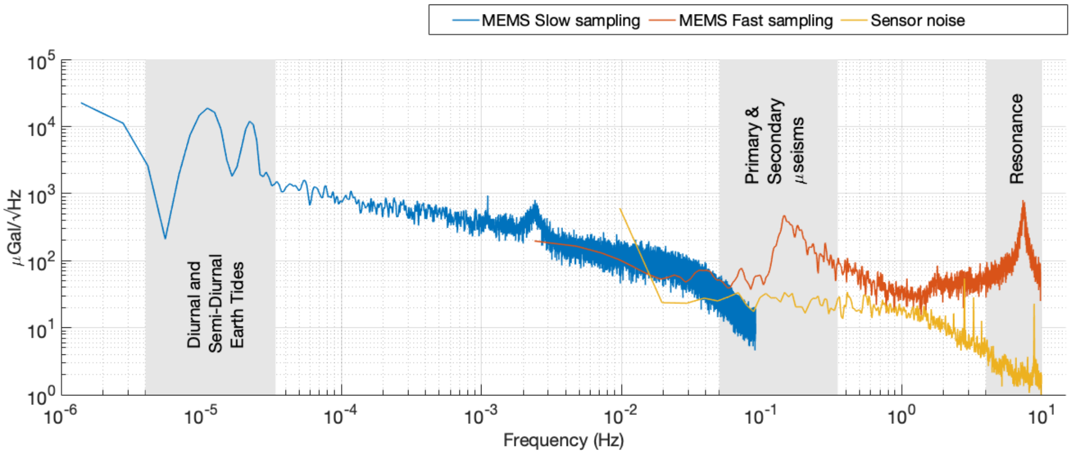

Figure 1.8: Amplitude spectral density plot for drift-corrected data from a 19-day measurement of gravity by a MEMS gravimeter for data collected using sampling rates of 0.18 Hz (blue line) and 20 Hz (orange & yellow lines). Due to a plotting error, data is only shown to a lower frequency limit of Notable signals are visible in the data with frequencies corresponding to the Earth tides, microseismic vibrations and at the resonant frequency of the detector. The unlabelled peak at ∼ 25 mGal. was caused by the device temperature control electronics. The yellow line shows a measurement of sensor noise, obtained by decoupling the device's output from gravitational and inertial disturbances, giving a measure of the devices internal noise floor.

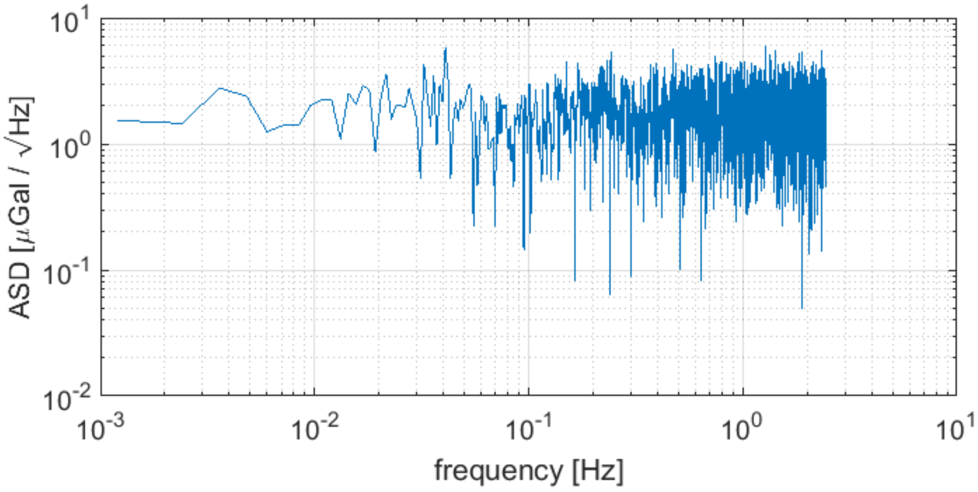

Figure 1.9: ASD of a 10 min-long Wee-g sensor noise measurement performed in 2023 using a sampling frequency of 5 Hz. The sensor output was decoupled from gravitational and inertial signals during the measurement to characterise the internal noise of the device, arising from its electronics.

have a significant impact on the field of gravimetry, making it more affordable to projects with limited budgets and allowing new strategies of sensor deployment that are unfeasible with larger and more expensive gravimeters. For example, the Wee-g's small size and weight could allow it to be drone-mounted and used to conduct aerial gravity surveys of extended regions at reduced cost when compared to the traditional approach of using large, expensive gravimeters carried by light aircraft [18, 19]. Also, the Wee-g's low cost would substantially reduce the financial risk associated with deploying a gravimeter in remote locations for extended periods of time to take long-term measurements and support the simultaneous deployment of multiple devices in arrays. A gravimeter array using Wee-g sensors is currently being planned as part of the 'NEWTON-g' project which aims to establish a long-term gravity imaging network on Mt Etna, an active volcano in Sicily, to better understand correlations between gravitational changes and volcanic eruptions [86].

As mentioned previously, much of the work in this thesis is focused around the Wee-g, with chapter 2 investigating the potential use of Wee-g arrays to detect submarines and chapter 4 detailing a gravity survey conducted using a contemporary gravimeter, performed to set a benchmark to test future Wee-g sensors against.

Chapter 2

Modelling the detection of submarines by gravimeters and gravimeter arrays

This chapter describes the work done to simulate the gravitational field of submarines and the detection of these signals by arrays of gravimeters. The case that is modelled involves short-range detection (under 50 metres) of a passing submarine by an array of multiple gravimeters, as this exploits the potential advantages of the Wee-g MEMS gravimeter under development at the University of Glasgow at the time of writing, spring 2023 (as discussed in section 1.4.2). This PhD thesis was part-funded by the UK defence technology company QinetiQ in order to support the work carried out in this chapter.

First, some background is given on contemporary underwater sensing techniques and their advantages and disadvantages are discussed; particularly active and passive sonar, as these are two of the most commonly used methods of submarine detection. Then, the gravitational method of detecting submarines is described and compared to sonar methods. The advantages of the Wee-g MEMS gravimeter and the use of gravitational detector arrays will then be described as this sets out the motivation for the following modelling work. The gravitational model that has been made will be described in detail, showing how a submarine was represented and how its gravitational field was calculated. Then, simulations of gravity at a single gravimeter and an array of gravimeters due to a submarine passing will be presented.

2.1 Underwater sensing

Underwater sensing can be defined as the detection and/or location of underwater objects and has many different applications [87]. These include detecting fish and coral for marine ecology or commercial fishing purposes [88, 89], mapping the topography of the sea floor or lake beds (bathymetry) [90–94] and also in defence applications for the location submarines or other vessels [95–97]. Underwater sensing is a very different challenge in comparison to sensing in air or vacuum, primarily because electro-magnetic radiation (i.e. light) of all wavelengths is heavily attenuated underwater due to absorption and scattering as it propagates. Even in pure water at the least-attenuated wavelengths (in the violet and ultraviolet range at $\lambda = 380\,\mathrm{nm}$ to $490\,\mathrm{nm}$ [98, 99]), light has an attenuation length of approximately $250\,\mathrm{m}^{-1}$ [100], meaning that after travelling 250 m in this medium, such light will have its intensity reduced by a factor of $1/e$ to approximately 37 % of its original intensity. This effect is even more pronounced in seawater, predominantly because of increased light scattering by small particles and organisms suspended in the medium [101, 102]. In deep ocean water, at a depth of $\sim 200\,\mathrm{m}$, the ambient intensity of visible light falls to 1 % of that at the ocean surface and in more turbid (i.e. hazy) coastal waters, this 1 % light intensity is reached at depths of only tens of metres (the region between the surface and the 1 % light intensity depth is known as the euphotic — meaning 'well-lit' in Greek — zone) [103, 104]. Light is also heavily attenuated by liquid water in the radio, microwave, infrared, ultraviolet and higher-frequency parts of the EM spectrum [105].

The strong attenuation of light by water means that it cannot be used effectively to detect objects or transmit information over long distances underwater as it can in air or vacuum. This means that sensing and location techniques like optics, radar and GPS location (using visual light, radio waves and microwaves, respectively) are far less useful in a marine environment. While underwater environments are much less suitable for light detection methods than air or vacuum, acoustic signals can travel further and faster in water than in air and, as a result, the most commonly used method of underwater detection is sonar [96, 106, 107].

2.1.1 Sonar

Sonar detection methods use acoustic waves to find and/or locate objects and can be split into two different approaches known as active sonar [108, 109] and passive sonar [110]. Active sonar works by first emitting acoustic waves and then listening for the reflection of the emitted signal by underwater objects or the sea floor. By timing the interval between a signal being emitted and its reflection being detected, and using sophisticated signal processing, it is possible to determine the location, distance and even relative speed of a detected object. This method has been used to detect submarines at a range of over 14 km in favourable conditions [109]. Passive sonar, on the other hand, works without emitting any acoustic signals and instead only listens for sounds made by objects of interest (e.g. marine animals, surface ships, submarines) and filtering them out from background noise. Its detection range varies greatly depending on how much noise is emitted by the object in question.

As mentioned, there are many different applications for underwater sensing, however, it is most commonly used for defence applications on military submarines or surface ships as a way of detecting other submerged or surface vessels and in these contexts, sonar methods have several disadvantages. One drawback of active sonar is that when a sonar signal is emitted it is easy for the passive sonar of another submarine or a surface vessel to detect it which means that it shouldn't be used by a submarine trying to stay undetected [111]. Also, the emitted acoustic waves can be so intense that they damage the nearby environment and organisms in the water. The main drawbacks of passive sonar are that it can be rendered less effective through the design of quieter propulsion systems and is incapable of detecting anything that isn't emitting noise, such as a stationary ship, submarine or the sea floor. Both sonar methods are also adversely affected by bad weather or proximity to waves breaking on a shoreline because these can increase the acoustic background noise.

2.1.2 Gravitational sensing

Gravimetry offers a unique benefit compared to sonar sensing methods in that it is impossible for any object (or more accurately, any variation in density) to hide the change in gravitational field caused by its mass. This means that any object heavy enough (or with sufficiently large internal density variations) that is within the sensitive range of a gravitational sensor will be detected. Also, like passive sonar, gravitational sensing does not require the emission of any acoustic signals so a gravimeter can operate without giving its position away. Unlike passive sonar, however, gravitational sensing can also be used to detect objects emitting little or no sound like stationary or quiet vessels or the sea floor.

There are also drawbacks to gravitational sensing, the most obvious of which is that, due to the inherent weakness of the gravitational field, the gravitational signal from even the largest of ships and submarines will be very small and difficult to detect. In theory, these fields could be reduced further by adjusting the internal layout of vessels to try and reduce large changes in density (relative to the vessel's surroundings) over short distances. This would reduce the size of the gravitational anomaly caused by the vessel but such design changes could only be done to a limited extent while maintaining operational capability.

Also, as described in section 1.4, gravimeters are very sensitive to sources of noise like device tilt, vibration and temperature variation so it is very challenging to make sensitive devices and operate them in potentially noisy environments. These drawbacks mean that even with highly sensitive devices, the detection range of underwater gravitational sensors will likely be limited in comparison to sonar detection methods. The gravitational detection scenarios modelled in this work are those in which a gravimeter or array of gravimeters are deployed on the sea floor, attempting to detect a submarine as it passes nearby.

2.2 Modelling the gravitational field of a submarine

The aim of this work is to estimate the detection range of a Wee-g MEMS gravimeter when used underwater to detect submarines. By modelling the gravitational field around a hypothetical submarine and comparing this to the sensitivity of the Wee-g gravimeter, an estimate of the device's maximum range can be found. Because the gravitational signal of a submarine is likely to be very small and hard to detect, this estimate will help decide whether the Wee-g is suitable for these applications and whether further work is worth pursuing. Also, modelling background noise in the measurement will help indicate what averaging time and data extraction techniques would be necessary to detect the submarine signal in a real environment. This section will describe how the gravitational detection of a submarine was simulated and the approximations and estimates made in this process.

2.2.1 Making a density model of a submarine

The first problem when trying to simulate the gravitational field caused by a submarine is in how to describe the shape and density distribution to a sufficient degree of accuracy. The design and internal layout of submarines is determined by their function: they need to be capable of submerging, moving underwater and resurfacing while carrying various sensors, means of propulsion and weapons systems as well as housing a crew for long periods of time. This results in submarines having a complicated, non-uniform density that is difficult to describe mathematically, making calculating a submarines exact gravitational field a daunting prospect. As well as this, detailed descriptions of the internal layout of submarines aren't publicly available for security reasons so this work will instead make simple assumptions about the density variations within a submarine and will not be finding exact detection ranges.

To make a model of a submarine, it was decided to use a suitably sized cylinder with a length-varying density chosen to approximate the size, shape and internal density variations of a large submarine. The dimensions chosen for the cylinder were a length of 100 m and a diameter of 10 m, as shown in fig. 2.1a. For the length-varying density, a one-dimensional density profile was provided by the author's supervisor, Prof. Giles D Hammond, that is presented in fig. 2.1b. This profile describes the cylinder's density as varying in a roughly sinusoidal fashion along its length, consisting of regions more dense than the surrounding water at the midpoint and near either end and areas less-dense than water elsewhere. There are also two spikes in density added close to and equidistant from the midpoint to represent particularly heavy equipment, such as a nuclear reactor. The specific density values used have been chosen such that the overall density of the cylinder is very similar to that of the surrounding water to make it neutrally buoyant and capable of maintaining a fixed depth when submerged underwater. While this density profile is unlikely to match that of a real submarine, it has been confirmed as a reasonable estimate by Dr. Gillian Marshall of *QinetiQ*, a UK-based defence company and part-sponsor of this work.

All models presented in this work assume the submarine is travelling in a straight line at a fixed depth and that it's density does not change. It is also assumed that the submarine modelled is travelling through an isotropic and uniform-density environment of seawater with a density of $\rho_w = 1030\,\mathrm{kg\,m^{-3}}$ (ρ_w is chosen as the approximate density of seawater at $10\,^{\circ}\mathrm{C}$ with a salinity of 35 ppt (parts per thousand) [112]; slightly more dense than pure water due to dissolved salts).

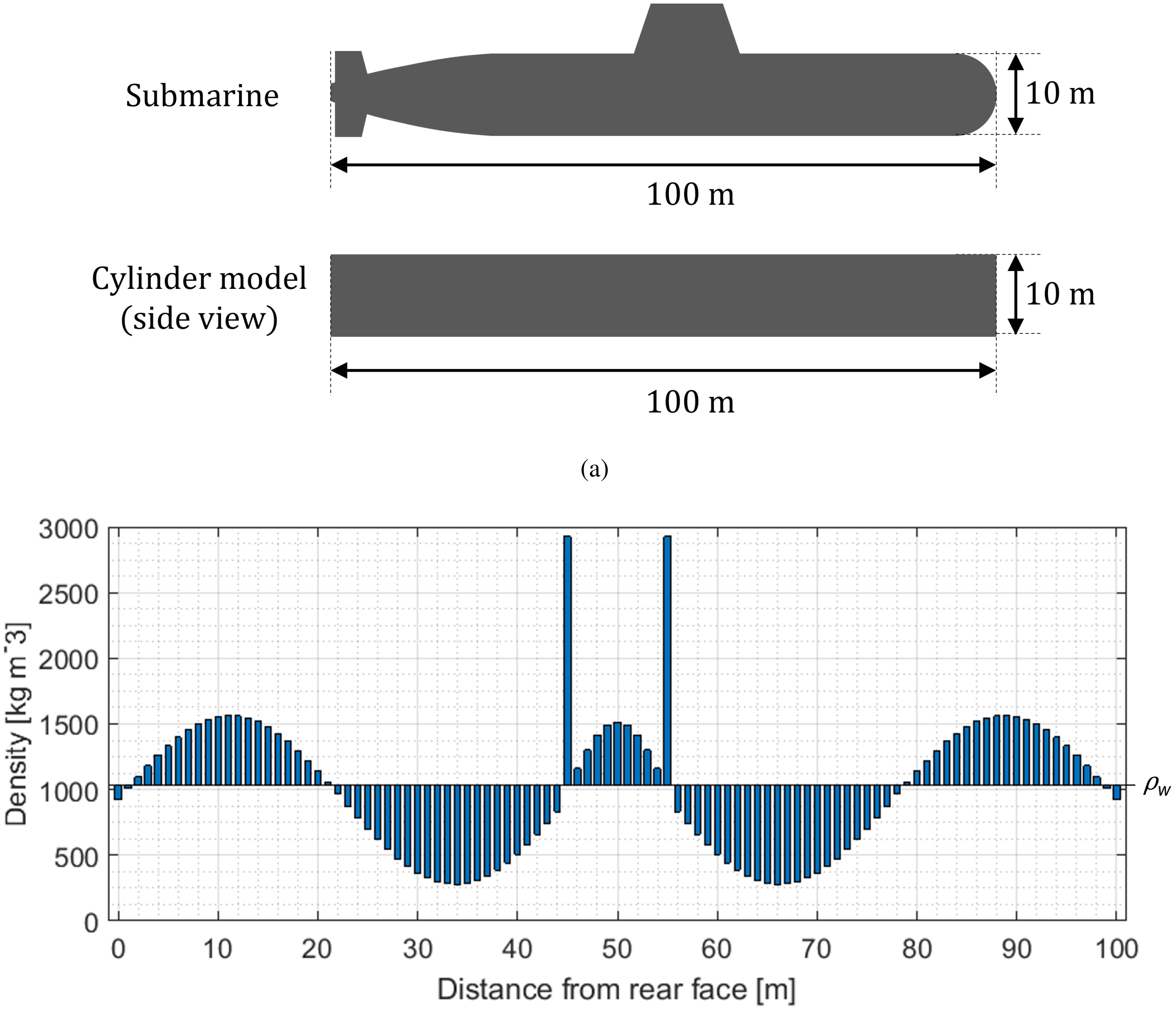

(a)

(b)

Figure 2.1: (a) Schematic of a submarine and the cylindrical object used to represent it when calculating its gravitational field. (b) A length-varying density profile similar to the one describing the cylinder used to represent a submarine. The real density profile used is not shown here on request of QinetiQ. The dashed line marks, ρ_w the density of water.

In reality, the density of seawater varies spatially and temporally with changes in temperature and salinity [112, 113] but consideration of these effects is beyond the scope of this work.

The total mass of the specified cylinder with this density profile applied is $8\,089\,600\,\mathrm{kg\,m^{-3}}$ and its volume is approximately $7854\,\mathrm{m^3}$. The cylinder has an overall density of about $1029.6\,\mathrm{kg\,m^{-3}}$, making it effectively neutrally buoyant in its surroundings.

2.2.2 Calculating the gravitational field

Now that a model of a submarine has been made, the gravitational field around it needs be calculated to compare with the known sensitivity of the Wee-g MEMS gravimeter. As mentioned in section 1.1 the gravitational field vector **g** around any density distribution $\rho(\mathbf{r})$ can be found with eq. (1.3),

$$\mathbf{g} = G \int\limits_A \frac{\mathbf{r}-\mathbf{r}_0}{|\mathbf{r}-\mathbf{r}_0|^3}\,\rho(\mathbf{r})\,dV \;, \tag{1.3}$$

where G is the gravitational constant, $\rho(\mathbf{r})$ describes the density distribution, V is the volume of the cylinder and $\mathbf{r}$ is the vector from a volume element, $\mathrm{d}V$, to the point at which $\mathbf{g}$ is being found.

The integration in eq. (1.3) is difficult to solve for the submarine density model because of it's cylindrical shape and length-varying density. Instead of trying to find an exact analytic solution, this work uses a Finite Element Analysis (FEA) technique to find approximate values of **g** and its components.

Finite Element Analysis

Finite Element Analysis (FEA) is a numerical method that splits a complex problem into many smaller, simpler elements, solves them individually, and then combines the element solutions to find an approximate answer to the overall problem. FEA methods are commonly used in engineering and physics for the numerical modelling of systems described by differential equations or other analytic solutions that become very difficult to solve for all but the most simple of situations. This technique takes advantage of a computer's high processing speed to run relatively simple calculations many times, replacing complicated mathematics with a multitude of simpler, small-scale assumptions. FEA analyses can easily become very computationally demanding because they tend to require a very large number of very small elements to form suitably accurate representations. Increasing the number of elements used will cause the FEA solution to converge on the true answer but at some point a compromise must be made between the number of elements — and therefore, the time the analysis takes — and the desired accuracy.

Numerical methods have been used in the past to calculate gravitational fields for gravity inversion as part of gravimetry [114, 115] and in astronomy to compute the gravitational field of asteroids [116]. Here, an FEA method is used to solve eq. (1.3) for the case of the cylindrical,

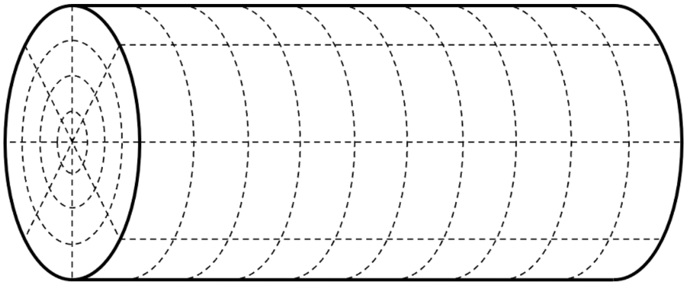

Figure 2.2: Demonstration of how a cylinder is divided into cylindrical polar volume elements as part of the finite element analysis performed to numerically calculate its gravitational field.

submarine-like object described in section 2.2.1. To do this, the cylinder is first imagined to be divided into N cylindrical polar volume elements in the way shown in fig. 2.2, with each element given a density determined by the length-varying density profile of the object. Then, the gravitational field due to each element is calculated separately using a simplified method that will be described below. Finally, the overall **g** due to the entire cylinder is found by summing the contributions of all the elements. In this way, eq. (1.3) is changed from the complicated integral over an object with a varying density into the straightforward summation shown by eq. (2.1),

$$\mathbf{g} = \sum_{i}^{N} \mathbf{g}_i \ , \tag{2.1}$$

where $\mathbf{g}_i$ is the gravitational field strength at the computation point due to the ith mass element of the cylinder. Then, the x, y, z-components of $\mathbf{g}_i$ are given by,

$$g_{\mathrm{x}i} = \sum_{i}^{N} \mathbf{g}_i \cos\theta_i \sin\phi_i \ , \tag{2.2}$$

$$g_{\mathrm{y}i} = \sum_{i}^{N} \mathbf{g}_i \sin\theta_i \sin\phi_i \ , \tag{2.3}$$

$$g_{\mathrm{z}i} = \sum_{i}^{N} \mathbf{g}_i \cos\phi_i \ , \tag{2.4}$$

where θ_i is the angle between the vector $\mathbf{g}_i$ and the x-axis in the x-y plane and ϕ_i is the angle between $\mathbf{g}_i$ and the z-axis.

For each element, $\mathbf{g}_i$ is found by assuming all of the element's mass is located at it's centre of mass and then using Newton's law of universal gravitation 1.2 to find the gravitational field of this point mass. For non-spherically symmetric objects, this is an inaccurate assumption and will only find an approximation of the true $\mathbf{g}_i$ due to the element. The accuracy of this assumption increases when elements are either smaller or farther away from the computation point because this will make them appear more point-like. Since the distantness of elements is dictated by the situation being considered, the FEA's accuracy is controlled by the number of elements used,

N, because when more elements are used, each one is smaller. Therefore, a sufficient number of elements, N, must be used for the FEA to calculate an accurate value of $\mathbf{g}$ due to the entire cylinder, and the exact amount necessary will depend on the proximity of the cylinder to the computation point. How an appropriate N is chosen will be covered later in section 2.2.3.

To find g_i using a point mass approximation, it is necessary to know where the element's centre of mass is in relation to the computation point to find appropriate values for $\mathbf{r}$ in eq. (1.3) and θ_i and ϕ_i in eqs. (2.2) to (2.4). This is simple for symmetric objects with a uniform density for which the centre of mass is always at the geometric centre but more complicated for cylindrical polar elements like the one pictured in fig. 2.3a due to their asymmetry. In this case, the element's centre of mass is not at it's centre but is instead closer to the shorter of its two curved faces by an amount dependent on the element's size and position. This can be seen in fig. 2.3b which shows how the element's centre of mass is not half-way along its thickness but is instead closer to the coordinate origin.

The radial distance from the z-axis to an element's centre of mass r_{com} can be calculated mathematically using the following method. For any object, the vector from the origin to its centre of mass, $\mathbf{R}_{\text{com}}$ can be found with eq. (2.5),

$$\mathbf{R}_{\text{com}} = \frac{1}{M}\int \mathbf{r}\, dM \, , \tag{2.5}$$

where M is the total mass of the object and $\mathbf{r}$ is the vector to an infinitesimal mass element, dM, within it. In a Cartesian coordinate system, $\mathbf{R}_{\text{com}}$ consists of (x, y, z) components shown in eq. (2.6) and in a cylindrical polar system the components change to those shown in equation eq. (2.7).

$$\mathbf{R}_{\text{com}} = \frac{1}{M}\left(\int x\, dM\,\hat{\mathbf{i}} + \int y\, dM\,\hat{\mathbf{j}} + \int z\, dM\,\hat{\mathbf{k}}\right) \, , \tag{2.6}$$

$$\mathbf{R}_{\text{com}} = \frac{1}{M}\left(\int r\cos\theta\, dM\,\hat{\mathbf{i}} + \int r\sin\theta\, dM\,\hat{\mathbf{j}} + \int z\, dM\,\hat{\mathbf{k}}\right) \, . \tag{2.7}$$

For the case of the cylindrical polar volume elements used here, eq. (2.7) can be simplified thanks to the uniform density and partial symmetry of individual elements. Due to symmetry, the centre of mass of an element will always be halfway along its length in the $\hat{\mathbf{k}}$ direction and halfway along its angular extent in the θ direction, with only the radial position, r_{com}, unknown. By considering the arrangement shown in fig. 2.3b where the element is bisected into two equal halves by the x-axis, it is clear that r_{com} is equal to the component of eq. (2.6) in the $\hat{\mathbf{i}}$ direction and can therefore be expressed as,

$$r_{\text{com}} = \frac{1}{M}\int r\cos\theta\, dM \, . \tag{2.8}$$

This expression will apply for cylindrical polar elements in all locations, including those not bisected by the x-axis because of how such elements are defined in a cylindrical polar coordinate

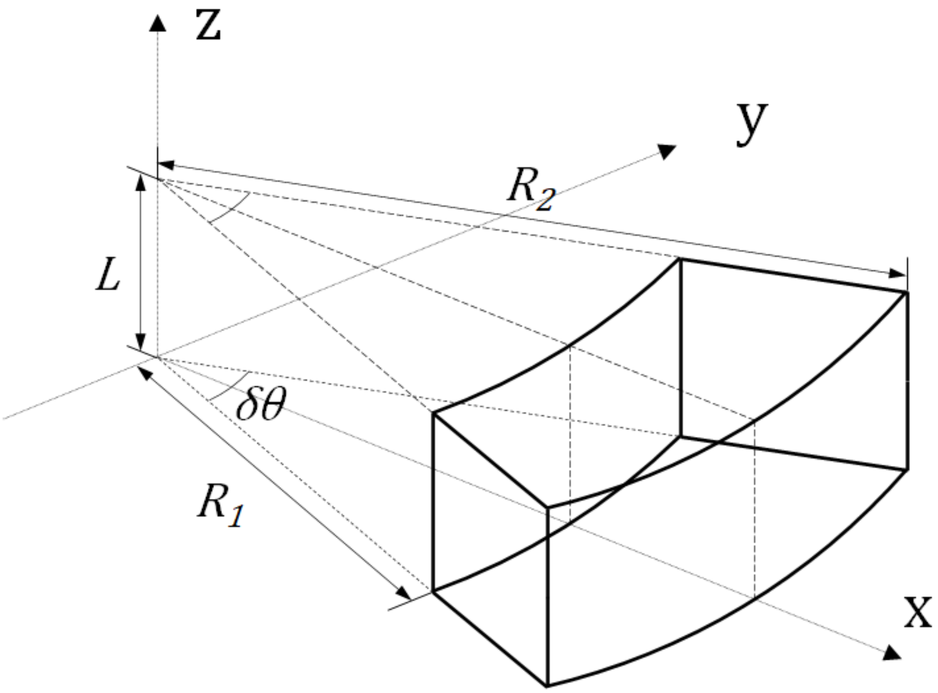

(a) A cylindrical polar volume element of thickness L, angular size $\delta\theta$ and inner and outer radii R_1 and R_2, respectively.

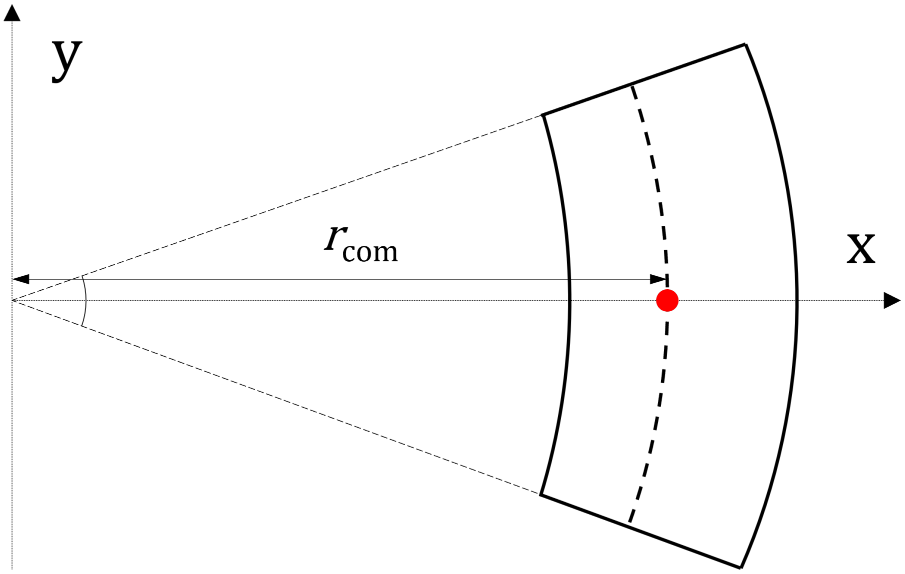

(b) Top-down view of a cylindrical polar volume element. The centre of mass is labelled with a dot and its radial distance from the centre is r_{com}.

Figure 2.3: Isometric and plan diagrams of cylindrical polar volume elements like those used in the Finite Element Analysis method to find gravity due to a cylindrical object.

system. In the FEA model, individual elements have a uniform density, ρ, and so the cylindrical polar mass element dM can be expressed as

$$dM = \rho \, dV \ . \tag{2.9}$$

Using the appropriate volume element for cylindrical polar coordinates, $dV = r\,dr\,d\theta\,dz$, and the substitution shown in eq. (2.9), eq. (2.8) becomes eq. (2.10), below, which can then be evaluated by using the element boundaries as limits of integration,

$$r_{\text{com}} = \frac{\rho}{M} \int_{0}^{L} \int_{-\frac{\delta\theta}{2}}^{\frac{\delta\theta}{2}} \int_{R_1}^{R_2} r^2 \cos\theta \; dr\,d\theta\,dz \ , \tag{2.10}$$

where L, $\delta\theta$, R_1 and R_2 are the thickness, angular size and inner and outer radii of the element, as shown in fig. 2.3a. Evaluating this integral results in the following:

$$\begin{aligned} r_{\text{com}} &= \frac{\left({R_2}^3 - {R_1}^3\right)\rho}{3M} \int_{0}^{L} \int_{-\frac{\delta\theta}{2}}^{\frac{\delta\theta}{2}} \cos\theta \; d\theta\,dz \ , \\ &= \frac{2\left({R_2}^3 - {R_1}^3\right)\rho}{3M} \sin\left(\frac{\delta\theta}{2}\right) \int_{0}^{L} dz \ , \\ r_{\text{com}} &= \frac{2\left({R_2}^3 - {R_1}^3\right)\rho L}{3M} \sin\left(\frac{\delta\theta}{2}\right) \ . \end{aligned} \tag{2.11}$$

The mass of the element, M, in eq. (2.11) can also be expressed only in terms of the element's dimensions and density by calculating the element's volume. This is done by integrating the volume element, dV, over the element dimensions.

$$\begin{aligned} V &= \int_{0}^{L} \int_{-\frac{\delta\theta}{2}}^{\frac{\delta\theta}{2}} \int_{R_1}^{R_2} r\,dr\,d\theta\,dz \ , \\ &= \frac{\left({R_2}^2 - {R_1}^2\right)}{2} \int_{0}^{L} \int_{-\frac{\delta\theta}{2}}^{\frac{\delta\theta}{2}} d\theta\,dz \ , \\ V &= \frac{\left({R_2}^2 - {R_1}^2\right)\delta\theta L}{2} \ . \end{aligned} \tag{2.12}$$

Substituting eq. (2.12) into eq. (2.11) using $M = \rho V$ then gives eq. (2.13) for r_{com} in terms of the element's dimensions,

$$r_{\text{com}} = \frac{4({R_2}^3 - {R_1}^3)}{3({R_2}^2 - {R_1}^2)\delta\theta} \sin\left(\frac{\delta\theta}{2}\right) \,. \tag{2.13}$$

Once r_{com} is found for an element, it is then relatively easy to find the location of this element's centre of mass relative to the computation point when calculating g_i (this is described in more detail in the next section). Then, when g_i for all elements has been calculated, the total gravitational field due to the entire cylinder, g, can be calculated using eq. (2.1). Since a large number of elements is required for the FEA to be accurate, it is sensible to use a computer to save time when calculating g_i values and the total g. To do this, MATLAB scripts and functions have been written to carry out the FEA method described above to estimate g due to the submarine-like cylinder detailed in section 2.2.1.

2.2.3 A MATLAB model of the gravitational field of a submarine

As mentioned in the last section, Finite Element Analysis (FEA) methods split problems into a large number of smaller domains and apply simplified solutions to each separately, relying on high computing speed to perform the many calculations reasonably quickly. For this work, the FEA described has been implemented in a series of MATLAB scripts and functions that approximate the gravitational field strength at a point as the cylindrical submarine-like density described in section 2.2.1 moves past. These programs are structured so that there is one main program run by the user which accepts all relevant input parameters and refers to other MATLAB scripts as functions in the course of calculating the desired output. Two main programs were made to calculate gravitational field strength and its components at a single position or at a square array of multiple positions as a submarine density model is moved past in a straight line. Both of these programs refer to the same two function scripts that allow the program to describe the starting position of the cylindrical submarine model and to find g at the computation point or points during its travel. Full copies of these MATLAB scripts are presented in appendix A and a more detailed summary of them will now be given.

'single_detector_g_field.m' and 'multiple_detector_g_field.m' — the main programs: As mentioned, these are the only programs actually run by the user and simulate the gravitational field at either a single location ('single_detector_g_field.m') or at a square grid of multiple locations ('multiple_detector_g_field.m') as a cylindrical submarine density model travels past in a straight line. For inputs, these programs require the dimensions of the cylindrical density (length and radius), its starting position and orientation, the length-varying density profile describing the cylinder (in the form of a vector of density values) and the density of the background medium. Also needed are the number of radial, angular and length elements to split the cylinder into for the FEA analysis (how these are chosen for this work is covered later in this section), details of the cylinder's trajectory (in the form of the total distance moved and the distance interval to use when calculating g) and, for 'multiple_detector_g_field.m', the number of sensors in the detector array and their spacing.

After all necessary inputs are provided, these programs call the first function script, 'cylinder_elements.m', which generates a cylinder of the specified dimensions and orientation at the given starting location, divides this cylinder into the specified number of cylindrical polar elements and calculates the centre-of-mass coordinates, volume and density of each element. Following this, the second function script, 'cylinder_g.m' is called which calculates the total gravitational field, g, and its x-, y-, z-components at the computation point (or points, in the case of a sensor array) at regular intervals during the cylinder's motion and stores the results as vectors, which can then be plotted or outputted to a file. At this point, the 'multiple_detector_g_field.m' program differs from 'single_detector_g_field.m' by repeatedly applying 'cylinder_g.m' using suitable displacements to the cylinder elements' starting positions which allows calculation of the gravitational field at the various locations in the sensor array. This results in multiple vectors showing g variation at each sensor in the array which are then stored as elements of a cell array for plotting or outputting.

'cylinder_elements.m' — the first function: This function starts by describing a vertical cylinder of the specified dimensions, centred at the origin and divided into cylindrical polar volume elements using the number of radial, angular and length elements. The number of elements that the cylinder is to be divided into is specified in the input of the main programs by the variables N_r, N_θ and N_l which describe the number of elements to use in the radial, angular and length-wise directions. The volume, V of each element is calculated using eq. (2.12) and the radial position of each element's centre of mass, r_{com}, is found with eq. (2.13). These quantities (and other values describing the element features) are stored in arrays of size $N_r \times N_\theta \times N_l$ in such a way that a quantity's index in the array corresponds to it's position in the cylinder such that the N_r-dimension counts elements from the central axis of the cylinder outwards, the N_θ-dimension counts clockwise around the z-axis (starting from the positive x-axis) and the N_l-dimension counts elements along the cylinder length from its lowest face.

Following this, the Cartesian coordinates of each element's centre of mass are determined (and stored as arrays of x-coordinates, y-coordinates and z-coordinates) from the calculated r_{com} values and the partial symmetry of each element, which (due to each element's uniform density) means the centre of mass is always located halfway along it's angular and length-wise extents (see fig. 2.3). A vector describing the density, ρ, of each length segment of the cylinder is read from an external file (in this work, a '.xls' file type is used) and then re-sized into an $N_r \times N_\theta \times N_l$-sized array to describe the density of all elements in each length segment (since a one-dimensional density profile is used here, all elements in a given length segment have the same density). Finally, the element coordinates are all rotated about the origin using rotation matrices to give the desired cylinder orientation and then translated from the origin to the specified starting point of the cylinder's motion. The results of this program are arrays describing the centre-of-mass coordinates, volumes and densities of all elements describing the specified cylinder at the starting position of its trajectory.

'cylinder_g.m' — the second function: This function moves the cylinder elements described along the desired trajectory in increments and calculates g and it's x, y, z-components at the origin at each step of the motion using eq. (1.3) to calculate the gravity field due to each element and eqs. (2.1) to (2.4) to find the total g and its components. The mass of each element is found from its volume and density values and with this, the contribution to g at the origin of each element can be found at each step and the element's coordinates. The components of g (g_x, g_y and g_z) are found by converting the Cartesian coordinates of elements to a spherical polar coordinate system (r,θ,ϕ) and then using eqs. (2.2) to (2.4). Both the step size and total number of steps used in the trajectory must be provided at the start and, once gravity values have been calculated for a step, all element coordinates are incremented by one step size in the direction of motion and the process repeats.

Choosing the appropriate number of elements

As mentioned in section 2.2.2, the FEA method is only accurate when the number of elements used during the analysis, N, is large enough to make the point-mass assumption used to calculate g_i (the gravitational field due to individual elements) reasonable. In addition, the point-mass approximation becomes less accurate when elements are close to the computation point and, therefore, more elements are needed when the cylindrical density in question is nearby. To get an idea of how many elements are required, the FEA model was used to find the gravitational field of a cylinder multiple times while increasing the number of elements used. This was repeated at different distances from the cylinder to see exactly how proximity and the number of elements used affects the calculated g.

The cylinder used for this test had the same dimensions as the submarine-like density profile described in section 2.2.1 (R = 5m, L = 100m) but was given a uniform density of $\rho = 3000\,\mathrm{kg\,m^{-3}}$, chosen arbitrarily, and had its central axis aligned with the z-axis. For simplicity, the number of elements the cylinder was divided into was decided by a single variable, N_α, that dictated how many radial, angular and length elements were to be used ($N_\alpha = N_r = N_\theta = N_l$). Examples of how the cylinder was divided for different values of N_α are shown in fig. 2.4.

It is clear from fig. 2.4 that using an equal number of radial, angular and length elements is not the most efficient way to divide the cylinder because this approach exaggerates the number of radial elements used which will make the program take longer to run. The surplus of radial elements has no benefit because the accuracy of the FEA will instead be limited by the number of angular and length elements used, and length elements will generally be underused

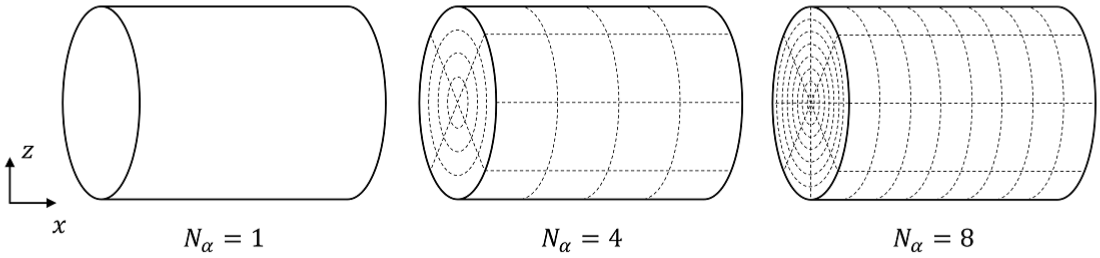

Figure 2.4: Examples of how cylinders were split into elements when trying to find an appropriate number of elements to use. Here N_α is a constant equal to the chosen number of radial, angular and length elements.

in comparison (as visible in fig. 2.4) which will negatively accuracy. A more efficient method of dividing the cylinder is not investigated in this work because the less efficient programs still only take a matter of seconds to run on contemporary computers.

Figure 2.5 shows the results of running the FEA using increasing values of N_α when trying to calculate the x-component of the gravitational field g_x when the cylinder's central axis is a distance, x, from the origin. The calculated g_x varies greatly at low values of N_α before quickly converging to a consistent value when N_α gets larger and the FEA gets more accurate. As expected, fewer elements are needed to make g_x converge when the cylinder is farther away because a point-mass approximation is a better representation of more distant objects. Even for the closest case considered where $x = 20\,\mathrm{m}$, variations in g_x when $N_\alpha = 10$ are less than 1µGal, lower than the observed noise performance of the Wee-g MEMS gravimeter at time of writing.

An N_α of 30 is used for all further calculations comparing the FEA to the analytic solution to ensure any inaccuracies aren't due to an insufficient number of elements being used.

2.2.4 Testing the accuracy of the model

Now that FEA model of gravity around a cylinder has been presented, it is important to check whether its results are accurate in order to have confidence in the predictions it makes. To do this, the model's performance has been compared to that of an analytic solution made by Na *et al.* [117] for finding the gravitational attraction due to a vertically-oriented, uniform density cylinder as pictured in fig. 2.6.

Analytic solution

The analytic solution finds the radial and angular components of gravitational field strength, g_r and g_θ, shown in fig. 2.6 using eqs. (2.14) and (2.15) and from these the Cartesian components,

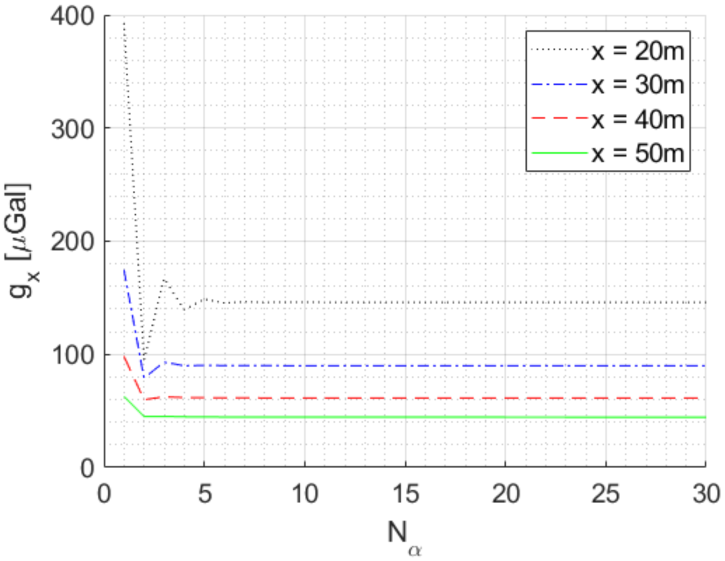

Figure 2.5: Graph showing how the number of elements affects performance of the FEA when at different distances from the cylinder in question. g_x is the x-component of gravity due to a uniform-density vertical cylinder and N_α is the number of angular, radial and length elements used ($N_\alpha = N_r, N_\theta, N_l$).

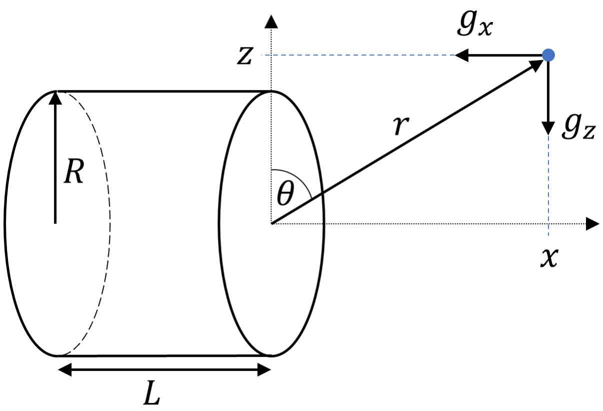

Figure 2.6: Diagram of the uniform density cylinder considered when comparing the FEA model with an analytic solution. The point at which gravitational field strength is calculated is shown by the blue dot.

g_{x} and g_{z}, can also be found with eqs. (2.16) and (2.17):

$$g_{\mathrm{r}} = GM\left[\frac{1}{r^2} - \frac{L}{r^3}P_1(\cos\theta) + \left(L^2 - \frac{3}{4}R^2\right)\frac{1}{r^4}P_2(\cos\theta)\right.$$
$$\left. + \left(\frac{3R^2L}{2} - L^3\right)\frac{1}{r^5}P_3(\cos\theta) + \ldots\right] , \tag{2.14}$$

$$g_{\theta} = GM\left[-\frac{L}{2r^3}\frac{dP_1(\cos\theta)}{d\theta} - \left(\frac{L^2}{3} - \frac{R^2}{4}\right)\frac{1}{r^4}\frac{dP_2(\cos\theta)}{d\theta}\right.$$
$$\left. - \left(\frac{3R^2L}{8} - \frac{L^3}{4}\right)\frac{1}{r^5}\frac{dP_3(\cos\theta)}{d\theta} + \ldots\right] , \tag{2.15}$$

$$g_{\mathrm{x}} = g_{\mathrm{r}}\cos\theta + g_{\theta}\sin\theta , \tag{2.16}$$

$$g_{\mathrm{z}} = g_{\mathrm{r}}\sin\theta - g_{\theta}\cos\theta , \tag{2.17}$$

where r, and θ are the polar coordinates from the centre of the cylinder's top face to the computation point (see fig. 2.6); R, L and M are the radius, length and mass of the cylinder; G is the gravitational constant ($G = 6.67 \times 10^{-11}\,\mathrm{m}^3\,\mathrm{kg}^{-1}\,\mathrm{s}^{-2}$) and $P_n(\cos\theta)$ is the nth order Legendre polynomial in $\cos\theta$. For reference, the first three Legendre polynomials and their differentials as used in eqs. (2.14) and (2.15) are [118]:

$$P_1(\cos\theta) = \cos\theta , \qquad \frac{dP_1(\cos\theta)}{d\theta} = -\sin\theta , \tag{2.18}$$

$$P_2(\cos\theta) = \frac{1}{2}\left(3\cos^2\theta - 1\right) , \qquad \frac{dP_2(\cos\theta)}{d\theta} = -3\sin\theta\cos\theta , \tag{2.19}$$

$$P_3(\cos\theta) = \frac{1}{3}\left(5\cos^3\theta - 3\cos\theta\right) , \qquad \frac{dP_3(\cos\theta)}{\cos\theta} = -\frac{15}{2}\sin\theta\cos^2\theta + \frac{3}{2}\sin\theta . \tag{2.20}$$

This analytic solution is not valid for calculating g at positions that are too close to the cylinder's axis. Specifically, if z is the perpendicular distance between the cylinder's axis and the computation point, the accuracy of the calculated g_{x} and g_{z} values decreases as x approaches the limit of $x = L$ or $x = R$ and are invalid when $x < L$ or $x < R$. This is kept in mind when comparing the performance of the FEA model and the analytic solution and some disagreement is expected when approaching the limits mentioned. It should also be noted that the analytic solution as used here is not entirely accurate because only the first three terms of the Legendre polynomial are considered. However, this is still a good approximation when not close to the $x < L$ or $x < R$ limits [117].

Comparing the FEA and analytic solutions

The FEA model and analytic solution were used to calculate g_{x} and g_{z} at a point as the cylinder pictured in fig. 2.6 moved past in a vertical straight line trajectory, parallel to the x-axis.

It was decided arbitrarily to use cylinder dimensions of $R = 5\,\mathrm{m}$, $L = 20\,\mathrm{m}$, and a density $\rho = 3000\,\mathrm{kg\,m^{-3}}$. The cylinder's geometric centre was moved from $x = -200\,\mathrm{m}$ to $x = 200\,\mathrm{m}$ and g_x and g_z were calculated in 1 metre intervals along the trajectory. This was repeated for several parallel trajectories at different z positions, ranging from 20 m to 150 m, to find where the cylinder was far away enough from the $x < L, R$ limit that inaccuracies in the analytic solution would be negligible.

Figure 2.7 shows some examples of g_x and g_z found by both models as the cylinder moved past along three different z trajectories. The general shape of the FEA and analytic solutions show close agreement but there is some difference between them in places, most easily visible at the peaks in g_x and g_z. The disagreement between the models is more clearly shown by fig. 2.8 which plots the percentage difference between the maximum g_z calculated by the FEA and analytic solutions for all x positions used. The percentage difference, Δ, was calculated by first finding the difference between the FEA and analytic g_z values and then determining what percentage of the FEA value this difference amounted to.

As the x-position of the moving cylinder increases, the percentage difference between g_x values found by the FEA and analytic models decreases and seems to be tending to zero. This suggests that the FEA is finding accurate results because the analytic solution is known to increase in accuracy as x gets farther from the limit $x < L, R$ and this is where the most agreement is shown. This is not a direct confirmation that the FEA model is accurate in the region where $x < L, R$ but suggests that the FEA has been correctly implemented here and that, as long as enough elements are used, should be accurate in near-field regions too.

2.3 Simulating submarine detection by Wee-g MEMS gravimeters

As mentioned at the start of this chapter, the aim of this area of work is to investigate how effective the Wee-g MEMS gravimeter would be when used for the gravitational detection of submarines. With the FEA program and submarine density model described in section 2.2, it is now possible to approximate the gravity field around a submarine and to use this to estimate the maximum detection range of these fields by the Wee-g. In addition, arrays of multiple Wee-g detectors can be simulated to look at the benefits of using sensor arrays to detect submarines, something the Wee-g is well suited to because of its low cost. This section will present and discuss the results of using the FEA program to simulate single Wee-g detectors and detector arrays when attempting to detect the gravitational field of a submarine-like density.

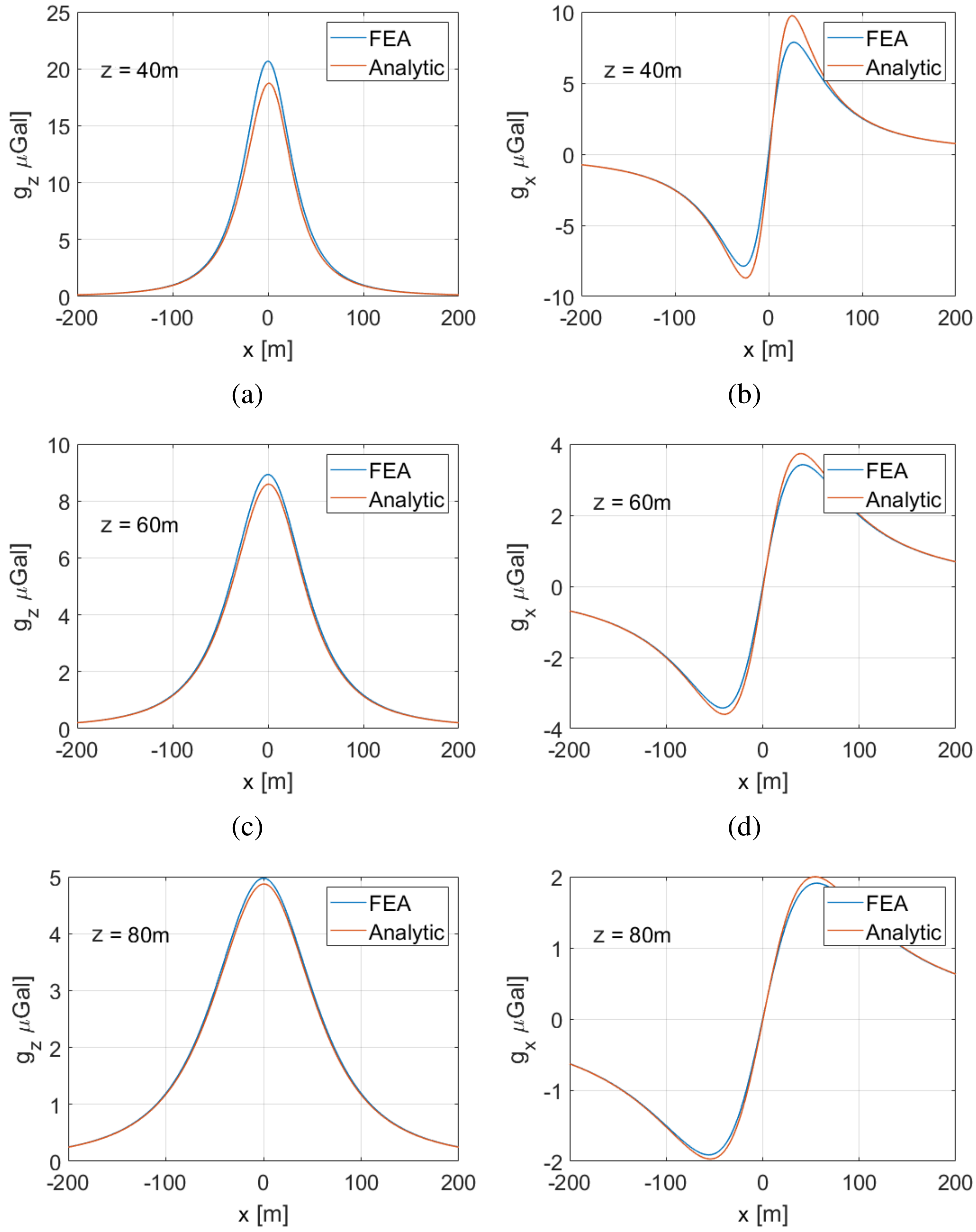

(a) (b)

(c) (d)

(e) (f)

Figure 2.7: Comparisons between the FEA method and analytic solution when calculating g at the origin as a vertical cylinder with uniform density moves past, travelling in the z-direction. The cylinder modelled is described in section 2.2.4.

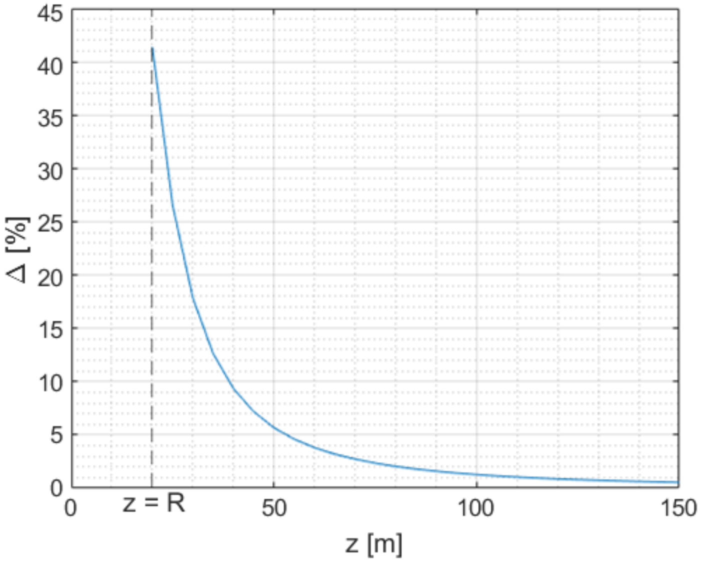

Figure 2.8: Percentage difference, Δ between the FEA and analytic solutions when finding the maximum g_z at a point when a uniform-density cylinder, like the one in fig. 2.6, moves past in a straight line in the x-direction with it's central axis z metres above the point. Specifically, Δ shows the difference between the g_z values found by the two solutions as a percentage of that found by the FEA solution.

2.3.1 Single detector

The first situations considered are those shown in fig. 2.9a, in which a cylindrical density travels in a straight line past a single detector located at the origin. The cylindrical density used is described in section 2.2.1: 100m long with a radius of 5m and the submarine-like length-varying density profile shown in fig. 2.1. During the simulation, this cylinder moves in a straight line in the x-z plane from $x = -200\,\mathrm{m}$ to $x = 200\,\mathrm{m}$ with a constant speed of $5\,\mathrm{m\,s^{-1}}$ ($\approx$ 10 knots, a realistic value for a submerged submarine [119]) at a fixed z-distance from the detector. This motion takes 80 s, during which the gravitational field magnitude $|g|$ and its x-z components, g_x and g_z, are calculated at the detector in 0.4 s intervals.

To estimate the detection range of the Wee-g, this simulation was repeated several times using cylinder trajectories with different z-positions relative to the detector. The gravitational fields resulting from these simulations can then be compared with the known sensitivity of the Wee-g to infer a detection range of the device. Figures 2.9b to 2.9d plot the results of some of these simulations performed for a number of different z values.

Figures 2.9b and 2.9c show that despite having the same overall density as water, the cylindrical density still causes a change in gravitational field strength when it moves past the detector. This is because of the length-varying density of the cylinder: when one part is significantly closer to the detector than the rest, that part's density will have a dominant effect on determining gravitational field strength. This explains why, for example, g_z in fig. 2.9c becomes negative around 25 s because at this point, the large less-dense parts of the cylinder are closer than the

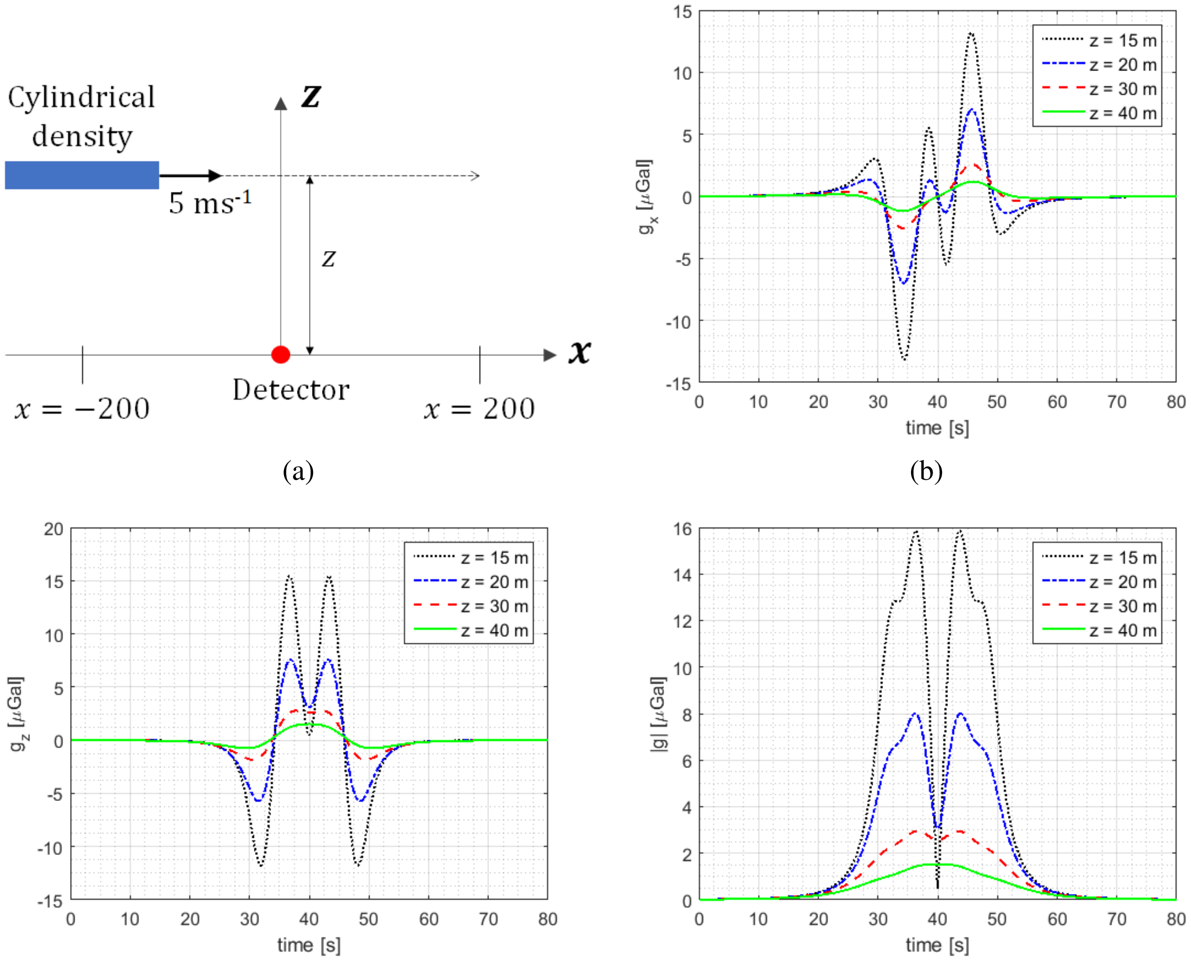

(a) (b)

(c) (d)

Figure 2.9: (a): Diagram of the situation being modelled. (b), (c) and (d): Plots showing how g_x, g_z, and $|g|$ at the detector vary with time during the cylindrical density's motion.

(much heavier) middle area of the cylinder and so have a dominant effect on total g_z. This effect becomes more pronounced when z is smaller and the cylinder is closer to the detector because, in such cases, there is a more disparate distance from the detector to the nearest part than to the rest of the cylinder. This also explains why a distinct, double-peak shape can be seen in figs. 2.9c and 2.9d when z is below 30 m because of the individual interactions of the two density peaks either side of the cylinder's centre, visible in fig. 2.1. The close-range g_x profile in fig. 2.9b looks yet more complicated since the overall g_x shifts between being positive and negative (i.e. pointing left and right) multiple times in quick succession as the cylinder passes. However, this behaviour is easily explained by considering the particular shape of the density profile; first g_x is positive (to the right) as the first large lower density region closes on the detector, it then shifts negative (to the left) as the first density peak approaches, then switches positive (to the right) again as the first peak passes, and then reaches zero as the two peaks become equidistant from the detector. This same behaviour is then observed in reverse as the cylinder continues travelling past the mid-point of its journey, because of the symmetry of the density profile.

Perhaps counter-intuitively, the gravitational field at the 40 s point in figs. 2.9c and 2.9d, at the midpoint of its journey, is seen to actually reduce at smaller z values. This is because in this position, both of the central density peaks and large low density areas either side of them become equally distant from the detector, thanks to the density profile's symmetry, and the low density areas (being large enough to make the entire cylinder neutrally buoyant) begin to substantially cancel out the effect of the peaks.

As discussed, a submerged neutrally-buoyant object will only have a gravitational field distinct from the surrounding water because of its internal density variations. If these density variations are too small, or if the object is too far away for them to be spatially resolved, a gravimeter would not be able to distinguish it from the surrounding water. This is visible in fig. 2.9 where larger values of z lead to reduced variations in gravitational field at the detector position. Because a gravimeter would detect a submarine by the density variations within it, it could be possible to identify the type of submarine from these variations if it is close enough, as well as simply detecting its presence. Investigating this further would require various different submarine density models to be made as well as improving their accuracy, and is beyond the scope of this work.

Detection range

As mentioned in the section 1.4.2, the most recent version of the Wee-g has demonstrated a noise-limited sensitivity of $\sim 5\,\mu\text{Gal}/\sqrt{\text{Hz}}$ at a frequency of 1 Hz (see fig. 1.9, meaning it can detect gravitational changes as small as 5 μGal when using an averaging time of 1 s. By comparing this to the predicted maximum gravity signal caused when the submarine like density moves past a point at different distances, it is possible to make an estimate of the maximum range at which the Wee-g would be able to detect the gravitational field of real submarines.

Currently, the Wee-g is a one-dimensional detector, meaning it is only sensitive to gravitational fields in a single direction: along the vertical axis of the test mass shown in fig. 1.7b. Here, the maximum detection range will be found by assuming that the detector's sensitive axis is aligned with the z direction as shown in fig. 2.9a so that it measures g_{z}. Figure 2.9c shows that when the submarine model moves past the detector at 20 m, the simulated g_{z} peaks twice at approximately 7 μGal and is more than 5 μGal for a few seconds in total, which suggests that the Wee-g's maximum detection range of this object would be just over 20 m. However, it is important to consider that the simulation is a simplification of the real-world scenario it aims to model and this will cause the predicted detection range to differ from the true value.

For example, the cylindrical density model used to represent a submarine is only a rough approximation of a real submarine, in terms of its shape and internal density and this could affect the accuracy of the simulation significantly. Real submarines are not entirely cylindrical in shape for hydrodynamic reasons and their internal density is very complicated as discussed in section 2.2.1. Also, it is assumed that the Wee-g would be able to achieve the same sensitivity of $5\,\mu\mathrm{Gal}/\sqrt{\mathrm{Hz}}$ when used in an underwater environment as it has demonstrated in land-based field tests [85]. In reality, using the Wee-g underwater (presumably inside a waterproof enclosure) could expose the device to additional sources of environmental noise which could worsen it's noise performance and reduce the detection range. These additional noise sources could be due to an increase in vibrational noise from ocean currents and differences in the acoustic properties of water compared to air; as well as changes in local gravitational field caused by varying water density (as temperature/salinity changes), and the effect of waves on the ocean surface.

This is a very short detection range, substantially less than the length of the submarine itself, but such a detector could still be useful in shallow waters such as those near ports or coastlines.

2.3.2 Gravimeter arrays

According to the simulations detailed in this chapter, a single gravimeter is only likely to detect submarines at short ranges. However, the area of sensor coverage could be increased by using multiple gravimeters simultaneously, spread apart from each other in lines or arrays. Detector arrays are commonly used in other fields — such as sonar detection, radar detection, seismology and astronomy [120–125] — to better determine the direction that a signal originates from and to improve noise performance (and hence, detection range) by correlating measurements from multiple detectors.

Using gravimeters in arrays could offer similar benefits as for other sensors but deploying many gravimeters at once is an expensive prospect because of the high-cost of contemporary devices. The Wee-g MEMS gravimeter would be particularly well-suited to use in arrays since its significantly lower cost per-unit would make gravimeter arrays more affordable, while still offering good performance. In this section, basic models of submarine detection by gravimeter arrays are presented to explore the advantages of this mode of operation. This work only considers simple arrays, either a one-dimensional line of equally-spaced detectors or a regular 2D square grid of detectors, with the centre of the array at the coordinate origin which are modelled using the array program described in section 2.2.3.

1D arrays

The 1D arrays modelled here consist of 4 gravimeters arranged in a straight line in intervals of 5 m positioned around the origin, as shown in figs. 2.10a and 2.10c. Each sensor in the arrays is assumed to be sensitive in one direction only, and to have its sensitive axis pointing in the z-direction. In both cases, the submarine density moves at $5\,\mathrm{m\,s^{-1}}$ along a path parallel to the x-axis and in the same plane as the array but displaced by 20 m in the z-direction. Plots of g_z at each detector as the submarine moves past are shown in fig. 2.10b for the parallel array and fig. 2.10d for the perpendicular array, relative to the cylinder's path of motion.

For the case shown in fig. 2.10a, where the submarine's path is parallel to the detector array, all sensors in the array measure the same gravity profile but in delayed intervals, due to the detectors being spread out along the path of travel. If the submarine's position and motion were unknown, the measurements shown in fig. 2.10b could be used to deduce that the submarine travels parallel to the array, since this is the only way all detectors would measure the same changes in g_z with the observed delay. Also, the submarine's direction of travel could be found by observing which detectors in the array measure changes in g_z first, since this shows which side of the array that the submarine approaches first. In addition, an estimate of the vessel's speed could be made from the time delay between g_z readings in different detectors and their relative position in the array. One limitation of the array in fig. 2.10a is that it would not be able to identify which side of the x-axis the submarine is travelling on, as the path shown, where $z = 20\,\mathrm{m}$, will result in the same g_z measurements as a path for which $z = -20\,\mathrm{m}$.

The other case modelled here is that shown in fig. 2.10c where a submarine travels along the same path as before but past an array aligned along the z-axis, perpendicular to the direction of travel. As shown in fig. 2.10d, this causes detectors in the array to measure different gravity profiles, due to their different proximities to the submarine's path, but without the delay between peak g_z measurements seen in the parallel case. Detectors farther from the submarine's path are seen to measure smaller and slower changes in g_z as it moves past which can be used to identify which side of the array the submarine is travelling on and the lack of delay between detectors indicates a perpendicular path. However, because there is no time delay between detector readings, this array cannot determine the direction that the submarine is travelling in.

In reality, it is likely that a passing submarine won't be moving exactly parallel or perpendicular to a linear detector array as modelled here. In these in-between cases, the detected g_z by the detectors in an array is expected to appear as a combination of the results modelled in figs. 2.10b and 2.10d, showing a time delay between measurements as well as differences in the strength of g_z changes at each detector. Extracting information about the submarine's location or direction

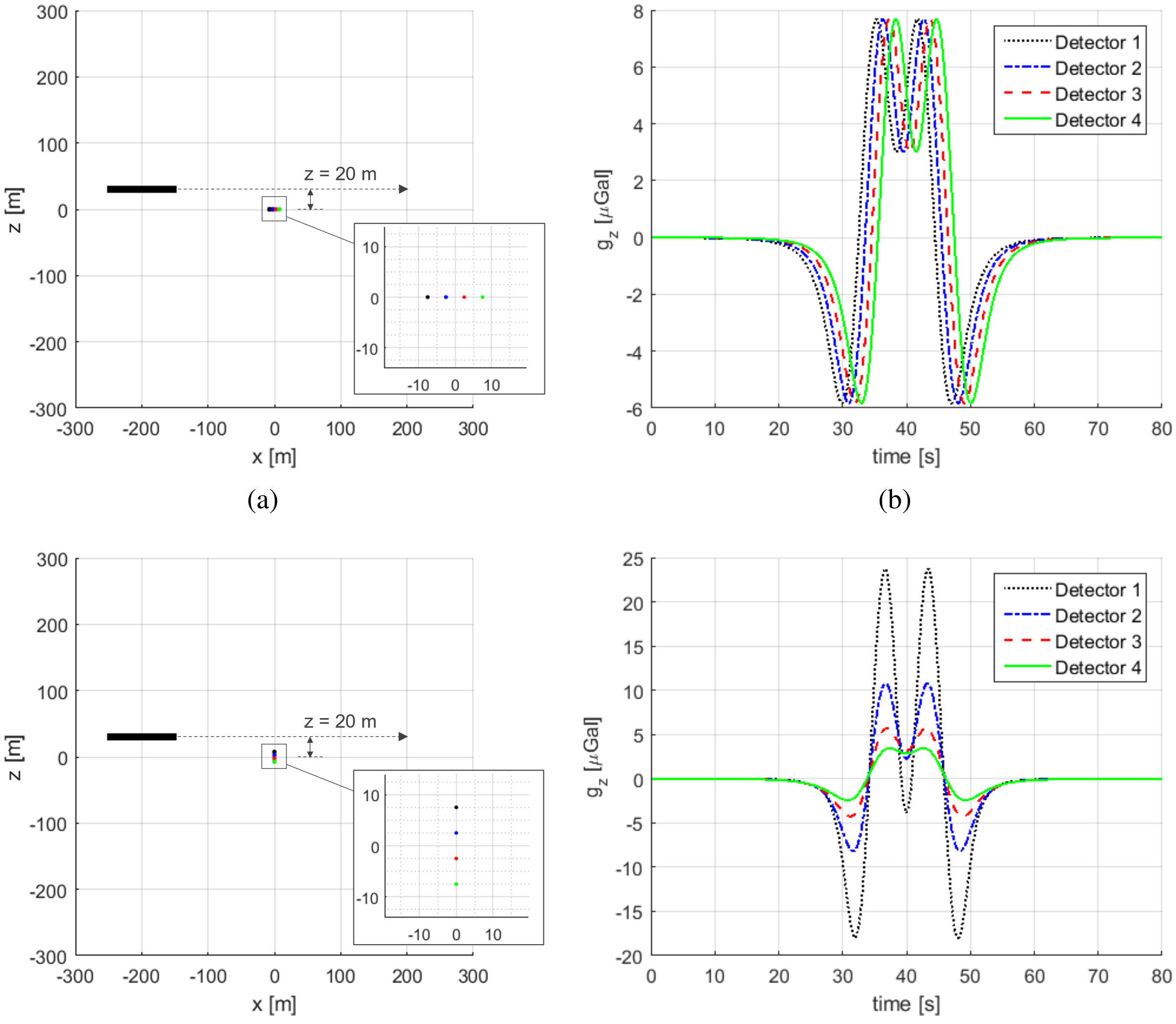

(a) (b)

(c) (d)

Figure 2.10: Modelling of 1D detector arrays. (a) and (c) show top-down diagrams of a submarine's motion past 1D gravimeter arrays aligned either parallel or perpendicular to the submarine's direction of travel. (b) and (d) plot the g_z at each detector in the arrays during the motion shown in (a) and (c), respectively. Detectors 1 to 4 list detectors from left to right in (a) and top to bottom in (c). In both situations, the arrays are centred on the origin and the submarine travels in the same plane, along the line $z = 20\,\text{m}$.

of travel relative to the array will be more complicated in these cases and developing techniques to do so is beyond the scope of this work. Similar problems of array signal processing have been addressed in other fields of study to extract information from array signals [120] and some techniques developed for these purposes could be useful in gravitational arrays as well. However, some of these methods may not work for gravimeter arrays due to the particular properties of the gravitational force, like its high speed of propagation (the speed of light, $c \approx 3 \times 10^8\,\mathrm{m\,s^{-1}}$) and the inability to block incoming gravitational signals from a specific direction. Models like those presented in this chapter will be useful when developing signal processing systems trying to extract useful information (such as the direction to the source, its speed and direction of travel) from gravimeter array data.

2D arrays

Simulations shown in fig. 2.10 show that, in some cases, 1D gravimeter arrays have limitations in their ability to determine the location and direction of travel of a passing submarine. One way to improve upon these arrays would be to extend them in a second dimension and this section presents a basic simulation of submarine detection by such 2D gravimeter arrays.

Figure 2.11 shows the results of modelling g_z at the square 10x10 array of gravimeters visible in fig. 2.11a as the submarine density described in section 2.2.1 travels over the array. The submarine in the simulation moves at a speed of $5\,\mathrm{m\,s^{-1}}$ in a straight line, parallel to the x-axis for which $z = 20\,\mathrm{m}$ and the grid spacing of the array is $8\,\mathrm{m}$. Due to the number of detectors in the array, it is inconvenient to plot g_z as a function of time for all detectors simultaneously so, instead, surface plots of g_z at the detectors in the array have been made for three points during the submarine's motion (at 25 s, 32 s and 45 s), shown in fig. 2.11b. The cylinder position at these times is shown in the schematic in fig. 2.11a in which the position of detectors in the array is indicated by green dots. The surface plots themselves only show the $80\mathrm{m} \times 80\mathrm{m}$ area occupied by the array and each vertex on the surface corresponds to a detector position.

From the surface plots in fig. 2.11, a similar gravity profile to earlier simulations can be seen but these plots offer a more complete visualisation of the shape of the gravitational field around the submarine density modelled here. As with the 1D array simulations, models like this one would be useful when designing the layout of future gravimeter arrays and developing signal processing techniques for them. In future such models could also be useful when designing submarines to try and reduce the gravitational field that they generate as much as possible by changing how internal mass is distributed.

2.3.3 Matched Filtering to extend detection range

Since the gravitational signals simulated in this chapter are small (only a few μGal), the detection range of submarines using a gravimetric method is likely to be limited and any signal processing

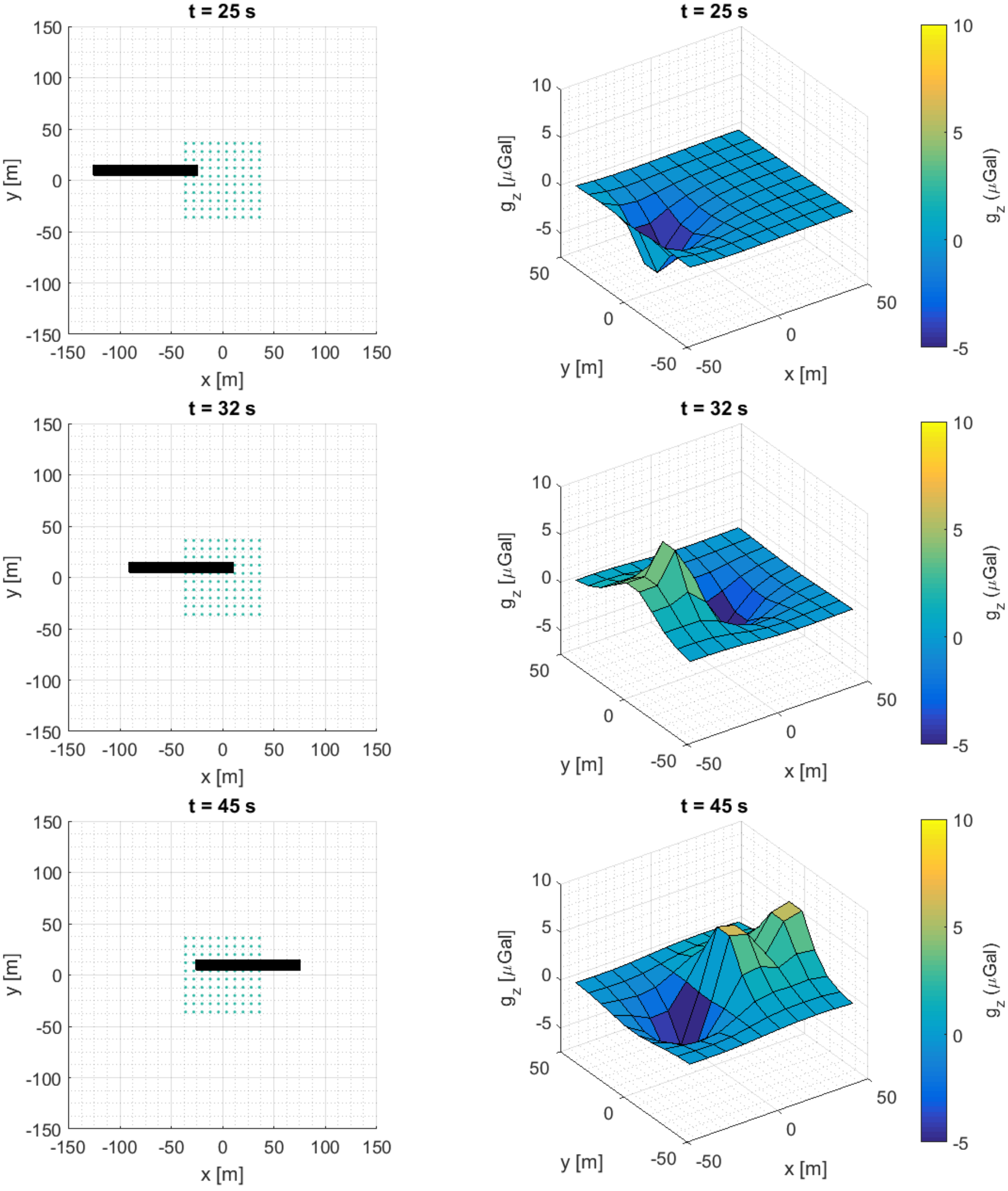

(a)

(b)

Figure 2.11: Modelling of a 2D detector array. (a) top-down schematics of the submarine motion, 20 m above the array in the z-direction, at the indicated times. (b) corresponding surface plots of g_z at the detector array.

methods that could improve the performance of a detection system would be very useful. Here, the use of signal processing methods is investigated with the aim of reducing the impact of noise when searching for submarine gravity signals in an attempt to increase the detection range of the Wee-g. To do this, noisy submarine gravity signals are generated by combining simulated submarine signals (made using the method described in section 2.2) with real Wee-g sensor noise data and then attempts are made to independently identify the injected signal amongst the noise. An 10 minute-long example of Wee-g sensor noise data recorded in 2023 is shown in fig. 2.12a and its corresponding ASD plot is the one already presented in fig. 1.9, at the end of the previous chapter. As fig. 1.9 shows, the spectral density of this noise does not seem to have any overall upward or downward trend with increasing frequency, indicating that the noise is mostly random in nature (since random noise has a spectral density that is constant at all frequencies).

Figure 2.12b shows the same excerpt of noise after a submarine gravity profile has been added to it at the 5-minute point. The submarine profile added is shown separately in fig. 2.13a and describes the g_z due to a submarine travelling past a sensor at $5\,\mathrm{m\,s^{-1}}$ in a straight path for which $z = 30\,\mathrm{m}$ (see fig. 2.9a); making it $10\,\mathrm{m}$ beyond the estimated maximum detection range of the Wee-g of $\sim 20\,\mathrm{m}$. Note that the duration of the template shown in fig. 2.13a has been extended to match the duration of the noise data when it is added to it, as visible in fig. 2.12b . g_z in these extended parts of the added signal is simply assumed to be zero for convenience, rather than being calculated properly by choosing suitable start and end points of the submarine when generating the signal. This is unlikely to cause any significant errors in the rest of this work because at the time extents shown in fig. 2.13a (time$=0\,\mathrm{s}$ and $80\,\mathrm{s}$), g_z is only $\sim 5\,\mathrm{nGal}$, far below the noise level and close to zero on the scale of fig. 2.13a.

A zoomed in depiction of the noise before and after the signal is added to the noise is shown in fig. 2.13b which demonstrates how a signal of this size (with a peak g_z of $2.8\,\mathrm{\mu Gal}$) is quite hard to distinguish from the surrounding noise. Because of this, the injected signal would likely be difficult to identify if its position in the noisy data was unknown. However, if it is assumed that the shape of the signal being searched for (here, the submarine profile shown in fig. 2.13a) is known in advance, it becomes possible to more effectively search for that signal by looking for parts of the noisy data that correlate strongly with it. This process is known as matched filtering and is commonly used to extract known signals from random noise in the fields of digital communications, sonar, radar and astronomy [126–129].

Matched filtering is a signal processing technique that incrementally moves an expected signal template over a noisy data series and, at each step, quantifies how correlated the template is with the section of data that it currently overlies. Matched filtering is mathematically defined by finding the linear time-invariant (LTI) filter that maximises the signal-to-noise ratio (SNR)* of a noisy data series consisting of a known signal corrupted by additive stationary† stochastic noise

---

*The SNR is defined as the ratio between the signal power and the noise power in a measurement and is defined mathematically in eq. (2.23).

†For noise to be considered stationary, its characteristics (such as mean, variance and spectral distribution) must

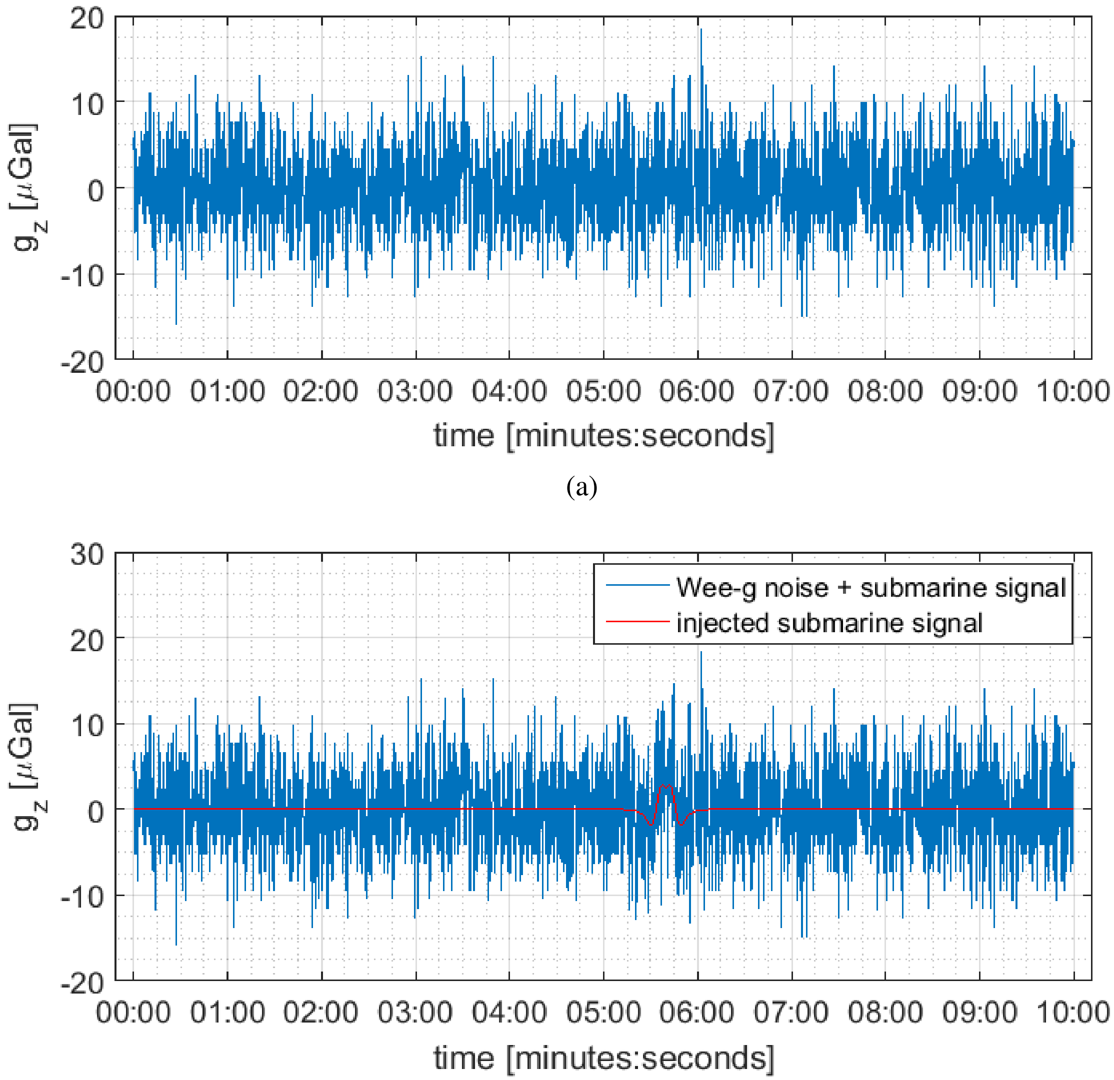

(a)

(b)

Figure 2.12: (a): Sensor noise recorded by a Wee-g gravimeter, obtained by decoupling the sensor output from gravitational and inertial effects, leaving a measure of the electronic noise floor of the device. (b): An artificial noisy submarine gravity signal, generated by adding a simulated submarine gravity signal, made using the method described in section 2.2 with $z = 30\,\mathrm{m}$, to the noise data shown in (a).

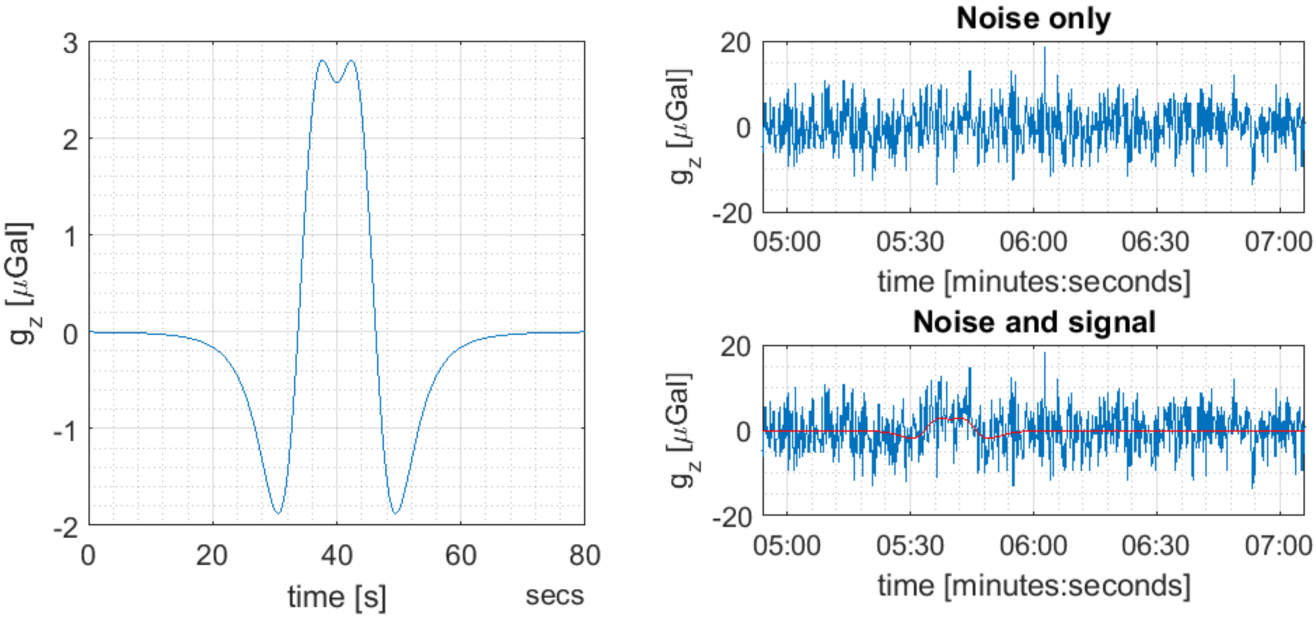

(a) (b)

Figure 2.13: (a): The submarine gravity signal used when making the artificial noisy signal shown in fig. 2.12b. The submarine signal was made using the method described in section 2.2 and considering a straight line trajectory for which $z = 30\,\mathrm{m}$ (see fig. 2.9a). (b): Close-up of the sensor noise and artificial signal plots in fig. 2.12 showing the small size of the gravity signal in comparison to the surrounding noise.

[130]. A full definition of the matched filter is given in many textbooks on signal processing [130,131] but will not be presented here for the sake of brevity. For a noisy signal $x(t)$ containing some known template signal $s(t)$, the matched filter output $y_{\mathrm{mf}}(t)$ is given by the convolution,

$$y_{\mathrm{mf}}(t) = h_{\mathrm{mf}}(t) * x(t) \ , \tag{2.21}$$

where $h_{\mathrm{mf}}(t)$ is the impulse response of the matched filter, which is defined as a time-reversed copy of the template signal,

$$h_{\mathrm{mf}}(t) = s(-t) \ . \tag{2.22}$$

Using eqs. (2.21) and (2.22), a matched filter was applied to both the noise-only data series shown in fig. 2.12 and the noisy signal shown in fig. 2.12b, using the submarine signal shown in fig. 2.13a as the template. The results of this are presented in fig. 2.14 and allow the matched filter's detection of the signal template amongst the noise to be examined in detail. The filter output in figs. 2.14a and 2.14b is seen to vary substantially with time as the degree of correlation between the template and the random noise it overlies changes, but there is a distinct additional signal around the 5:40 point in fig. 2.14b which coincides with the location of the peak of the submarine gravity signal within the data. This strongly implies the successful detection

---

not change over time.

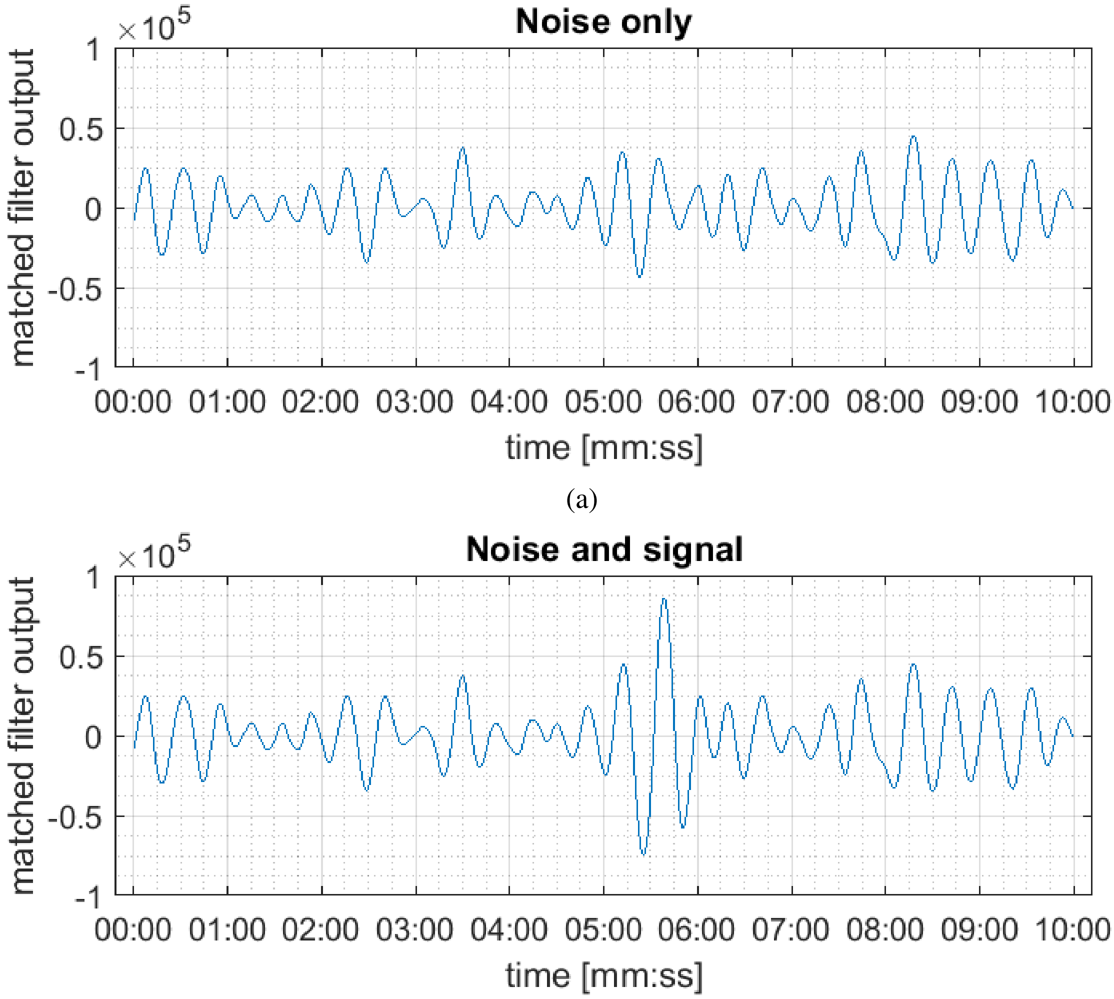

(a)

(b)

Figure 2.14: (a): Result of applying a matched filter to the 10 minute-long Wee-g sensor noise measurement shown in fig. 2.12a, while using the submarine signal shown in fig. 2.13a as the signal template. (b): Result of applying the same matched filter as in (a) to the noisy submarine signal measurement shown in fig. 2.12b. The noticeable peak at 5:40 in (b) coincides with the location of the injected signal.

of the submarine signal by the matched filter and the greater amplitude of this peak that its surroundings would make it detectable even if the noise-only data in fig. 2.14a was unknown (which would probably be the case in a real detection scenario).

The effectiveness of the matched filtering performed here can be quantified by considering the effect it has on the SNR of the data it is applied to, which is here defined as,

$$SNR = \frac{\left|y_{\mathrm{mf}}(t_{\mathrm{peak}})\right|^2}{\sigma^2}\,, \tag{2.23}$$

where $y_{\mathrm{mf}}(t_{\mathrm{peak}})$ is the peak amplitude of the filtered signal which occurs at time t_{peak} and, therefore, $\left|y_{\mathrm{mf}}(t_{\mathrm{peak}})\right|^2$ is the peak signal power at that moment. σ is the standard deviation of the filtered, 'noise only' data and σ^2 is the variance, which is equivalent to noise power when the noise is random and has a mean of zero (as it does here). Using eq. (2.23), the SNR of the unfiltered noisy signal in figs. 2.12b and 2.13b can be determined, taking $y_{\mathrm{mf}}(t_{\mathrm{peak}})$ as 2.8 μGal and $\sigma = 4.81$ μGal which gives an SNR of 0.34. For the filtered result, the peak signal is $y_{\mathrm{mf}}(t_{\mathrm{peak}}) = 8.62 \times 10^4$ and the noise standard deviation is $\sigma = 1.7 \times 10^4$, the SNR is 25.71, meaning that the matched filter has improved the SNR by a factor of ~ 76.

The output of a matched filter can be used to detect the presence of a template signal in a noisy dataset by choosing a suitable threshold that the filter output is only likely to exceed whether a real signal is present in the data. Finding a suitable level at which to set this threshold depends on the ambient level of noise in the filtered signal and how acceptable false positive detections are in the detection scenario considered. Exact threshold levels can be calculated mathematically [130] but this will not be looked into here due to time restraints.

The matched filter was also applied to a different artificial signal, shown in fig. 2.15a, which was made from a separate, 30 minute-long Wee-g sensor noise measurement, having the same submarine signal in fig. 2.13a added at the 15 minute point. This was done to test whether the matched filter could repeat the signal detection on a different noise sample and to see if the peak in the filter output due to a successful detection was consistently larger than the noise fluctuations in the filter output over a long period. A plot of this signal and the matched filtering result are shown in figs. 2.15a and 2.15b, respectively, and again demonstrate a substantial peak in the filter output corresponding with the location of the injected signal. For this case, the standard deviation of the 30 minute noise sample (before the signal was added) is 4.84 μGal and the peak amplitude of the injected signal is $y_{\mathrm{mf}}(t_{\mathrm{peak}}) = 2.8$ μGal, giving an initial, unfiltered SNR of 0.34. For the output of the matched filter, $\sigma = 1.79 \times 10^4$ and $s_{\mathrm{peak}} = 7.53 \times 10^4$, giving a post-filtering SNR of 17.7; an increase in SNR by a factor of 52.84 over the unfiltered data.

In both of the cases shown here, matched filtering substantially improves the SNR of simulated submarine gravity signals corrupted by Wee-g sensor noise data and allows a signal corresponding to a submarine travelling 30 m away to be detected; an improvement of 10 m on the estimated detection range with unfiltered data. This suggests that matched filtering would be an effective way to improve the detection range of Wee-g gravimeters when deployed underwater which would allow a larger area of sensor coverage to be provided by a given device. However, as mentioned at the end of section 2.3.1, it should be kept in mind that the simulations in this work rely on very basic assumptions about the density distribution of the submarine being detected (see fig. 2.1) and assume that the Wee-g could achieve the same sensitivity when deployed underwater in a waterproof enclosure. Because of these assumptions, the detection ranges predicted in this section should be treated as rough estimates only.

Future work could attempt to make more accurate estimates of the Wee-g's submarine detection range by making more accurate models of the density variations within a submarine to get more realistic estimates of the resulting gravitational field. Additionally, the density of submarines with different sizes and internal layouts could be modelled and matched filtering could

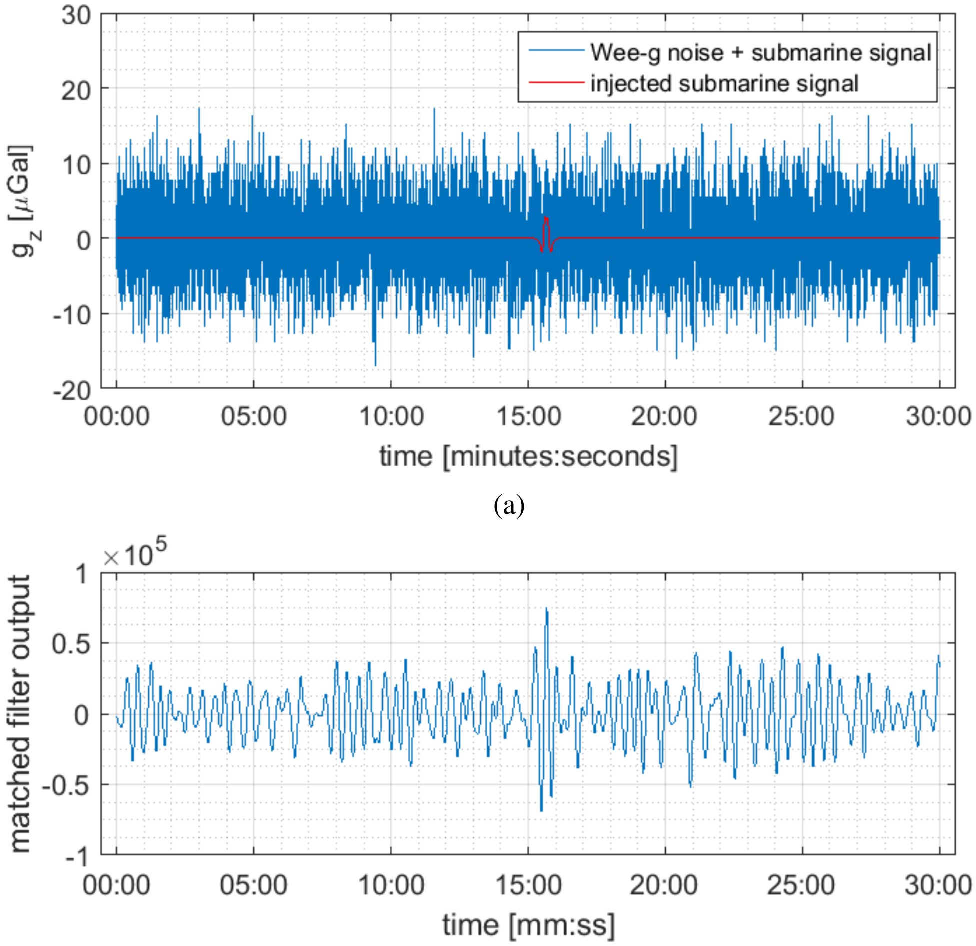

(a)

(b)

Figure 2.15: (a): A 30 minute-long sample of Wee-g sensor noise data with the submarine signal shown in fig. 2.13a added to it at the 15:00 point. (b): The result of applying a matched filter to the data shown in (a) while using the same signal in fig. 2.13a as the matched filter template. The significant peak in the filtered output coincides with the real location of the corrupted signal, indicating the matched filter has successfully detected it.

be used in an attempt to distinguish between detected signals originating from different density distributions, to identify the target of detection. Matched filtering is well-suited to this task and is commonly used for target classification in the fields of radar detection, sonar detection and gravitational wave astronomy [132–134]. Alternatively, machine learning methods have been developed that perform the same detection and characterisation tasks as matched filtering but are faster and more effective [135]. These techniques are likely also applicable to gravimetric submarine detection and could allow further improvement of the Wee-g's effective detection range.

2.4 Conclusion

Using gravity to detect submarines offers some unique benefits when compared to commonly used contemporary methods like sonar but will also likely have a comparatively limited range due to the inherent weakness of the gravitational force. This chapter details work done to simulate gravitational detection of submarines by single gravimeters and gravimeter arrays to investigate the size of such fields and estimate what detection range could be achieved using Wee-g MEMS gravimeters. Matched filtering is also investigated as a way of increasing this detection range by more efficiently searching for the expected signal in a noisy data set.

The model approximates the complicated density distribution of a submarine using a cylinder of similar proportions with a length-varying density chosen to resemble the linear density profile of a real submarine. The specific density profile used is not presented here for security reasons but an approximation of this profile is shown in fig. 2.1. A finite element analysis (FEA) is used to calculate gravitational field strength at a chosen point around the object by dividing it into many cylindrical polar volume elements and using a point mass approximation to find g due to every element individually. The accuracy of this method is tested against an analytic solution for gravity around a cylinder of uniform density and shown to be a good approximation, as long as enough elements are used in the FEA.

The gravitational field at a detector when the submarine model moves past in a straight line is simulated using the described FEA method in regular intervals as the submarine density model is moved past the chosen point along the desired path. These simulations are repeated for straight-line paths at varying distance from the detector and an estimate of the detection range of the Wee-g gravimeter is made by comparing the results to the $5\,\mu\text{Gal}/\sqrt{\text{Hz}}$ noise level of the device determined from sensor noise measurements (see fig. 2.12a). Assuming that the Wee-g would be capable of the same noise performance when deployed in a waterproof housing on the sea floor, its maximum detection range of the submarine model is estimated to be approximately 20 m by comparing the peak signal amplitude to the noise level.

Further modelling investigates the use of arrays of multiple Wee-g gravimeters used to detect a passing submarine to investigate the advantages of gravimeter arrays in comparison to single detectors. These models are based on the same FEA method but extended to simulate gravitational field at multiple detectors in an array as the submarine density model travels past. The first of these models consider 1D arrays consisting of 4 gravimeters arranged in a line as the submarine travels past either parallel or perpendicular to the array. These show that, in the parallel case, the submarine's speed and direction of travel can be inferred from phase delays in signals between detectors while, in the perpendicular case, the array can determine which side of the array the submarine is travelling on. Models are also made of submarine detection by a simple 2D gravimeter array, consisting of a square 11x11 grid of detectors and stills from surface plots of gravity at each detector are shown which allow a better visualisation of the gravitational field around the submarine. Use of 2D arrays could allow better localisation of submarines within range of the array but signal processing methods to do this are not investigated in this work.

Finally, matched filtering was investigated as a way to increase the predicted 20 m detection range of submarines by the Wee-g gravimeter, using foreknowledge of the shape of the gravity signal being searched for to better extract it from background noise. To do this, synthetic noisy submarine signals were generated by combining simulated gravity signals (from section 2.2) with real Wee-g sensor noise data and then applying matched filtering to recover the noise-corrupted signal. In the case of a simulated signal for a submarine travelling at a range of 30 m with speed $5\,\mathrm{m\,s^{-1}}$, corrupted with approximately $5\,\mu\mathrm{Gal}/\sqrt{\mathrm{Hz}}$ sensor noise, the matched filter was able to boost SNR enough that the signal (with a peak amplitude of 2.8 μGal) became clearly visible in the filter output. This was demonstrated on two different synthetic noisy signals, one 10 minutes long and the other 30 minutes long, both containing the same simulated 30 m submarine signal somewhere amongst the noise. In both cases the filtering increased SNR significantly: by a factor of ~ 76 in the 10 minute dataset and a factor of ~ 53 in the 30 minute dataset, with the submarine signal clearly identifiable by a large peak in filter output. From this, it is concluded that matched filtering increased the detection range of the Wee-g by 10 m in this case and would be worth considering for the real-life implementation of gravitational submarine detection in the future.

Chapter 3

Modelling gravitational terrain correction using high-resolution LiDAR elevation data

As mentioned in the introduction, there are many factors that determine the gravitational field strength at a point on the Earth's surface, such as the point's elevation and latitude as well as the surrounding topography and crust density. In order to use gravimeters to identify variations in crust density alone, it is necessary to calculate the size of the other effects and remove them from gravity survey data using the gravitational corrections described in section 1.3. Of these corrections, the gravitational effect of topography surrounding a measurement point, known as the terrain effect, is the most difficult and time-consuming to calculate. This section will outline why the terrain effect is important to consider and describe how it can be calculated relatively quickly using digital topographic data. This work aims to use particularly high-resolution LiDAR elevation data, available for the Campsie Fells (a range of hills north of Glasgow, Scotland), to find µGal accuracy terrain corrections.

3.1 Terrain correction overview

Broadly speaking, the terrain correction is an adjustment made to the Bouguer correction that replaces the infinite flat slab of terrain surrounding the measurement point (the Bouguer plate) with a more realistic consideration of topography. Any real-world deviation from the Bouguer plate, in the form of hills or valleys, around a gravitational measurement point will always act to reduce the vertical gravitational field strength, g. This is because hills act as an excess mass above the level of the measurement point and valleys act as a deficit of mass below, both of which reduce the downward pull of gravity when compared to the Bouguer plate assumption.

Ideally, the terrain correction would be found by integrating Newton's universal law of grav-

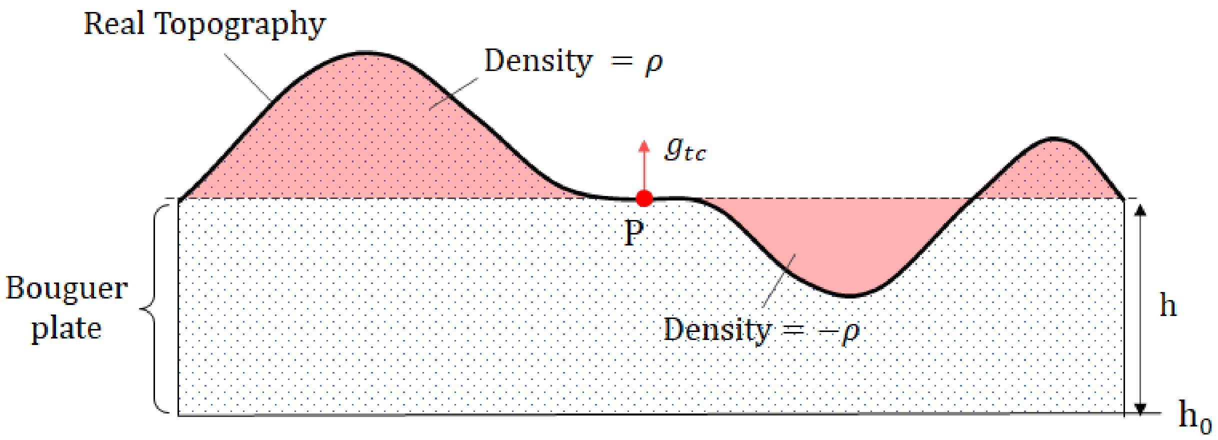

Figure 3.1: Diagram showing what causes gravitational terrain effects. Red-shaded areas are the deviations of the terrain from the hypothetical Bouguer plate and g_{tc} is the gravitational effect these deviations have, which is known as the terrain effect or terrain correction.

ity, eq. (1.3) over the volume of all surrounding hills and valleys, shown by the coloured areas in fig. 3.1. When doing this, all hills should be assumed to have the same density as the average rock density for the region and valleys should be treated as having the negative of this density to adjust the Bouguer correction appropriately. Usually, the average local rock density is not well known when performing gravity surveys and detecting variations in density is often the purpose of the survey itself. When a more accurate value is not known, it is commonly assumed that the average density of terrain is $\rho_t = 2670\,\mathrm{kg\,m^{-3}}$ [12, 58] and this assumption will be used throughout this work.

Underwater terrain, known as bathymetry, also has a similar effect on terrain correction as regular topography but must be treated slightly differently [58]. First, the regular topographic effect should be found, while treating any bodies of water as flat ground at the height of the water's surface. Then a separate bathymetric terrain correction can be calculated and added to the topographic value to find the combined terrain effect. The bathymetric terrain correction is found by integrating over the volume between the water surface and the bathymetry below while assigning this volume a density of $\rho = \rho_t - \rho_w$ where ρ_t is the average density of rock in the region and ρ_w is the average density of the water.

In reality, integrating Newton's law of gravity over the volume of surrounding hills and valleys to find terrain correction due to topography or bathymetry is not straightforward because the surfaces involved are usually complicated and difficult to describe mathematically. Instead, the terrain correction calculation can be approximated by replacing the real terrain features with simplified volumes, the gravitational fields of which are easier to calculate. The earliest method of doing this was developed by Hayford and Bowie [136] and improved on by Hammer [137]. This method divides the terrain surrounding the survey point into polar segments using a transparent template overlaid on the topographic map, as shown in fig. 3.2. The average elevation

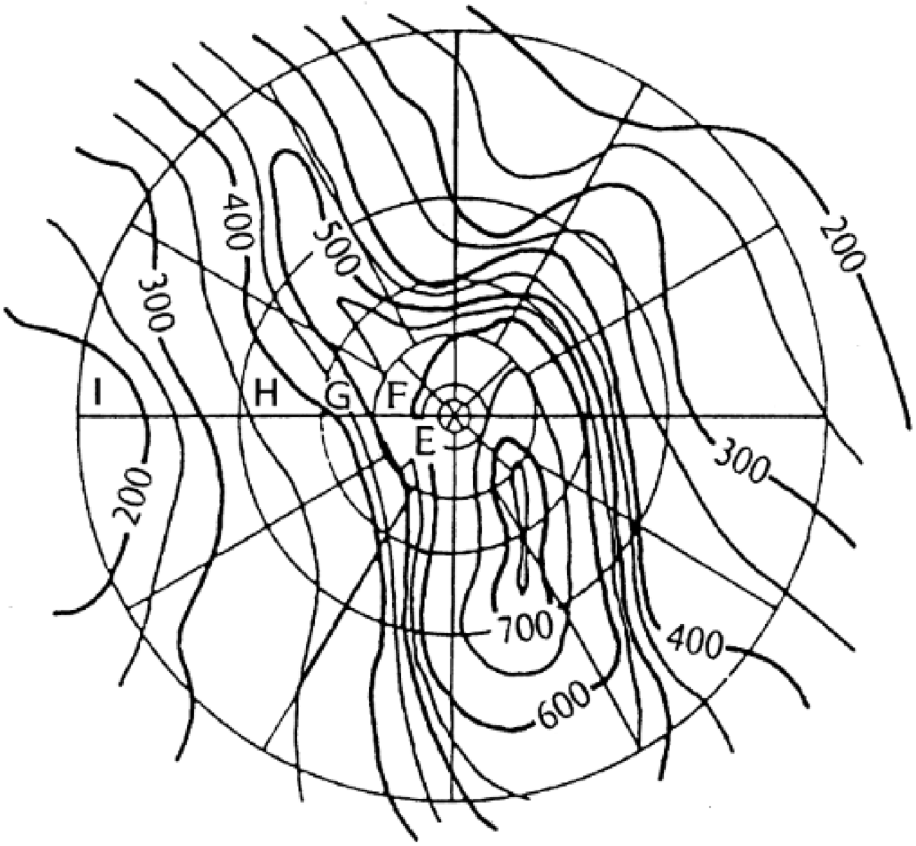

Figure 3.2: Diagram showing how local topography is divided into polar segments by overlaying a transparent template in the Hammer method of terrain correction (Picture taken from Seigel (1995) [12]).

of each segment is estimated by comparison with the topographic map or in situ at the measurement point and the gravitational effect of each segment is found using pre-calculated tables, derived from equations for the gravitational field strength at the centre of a hollow cylinder*. This technique has been widely used but is time-consuming and inconsistent due to the manual estimates that it requires and has a limited accuracy, which is worsened in areas of more severe topographic relief (when originally published, the method was quoted as having an accuracy of approximately 0.1 mGal) [137].

A faster method is to represent terrain using many vertical rectangular prisms (i.e. rectangular cuboids) of varying height and find g at the measurement point due to each prism using an analytical expression developed by Nagy for this purpose [138, 139]. This method needs to use a very large number of prisms to accurately represent terrain and so requires a large number of calculations to find the overall g_tc but is easily implemented using a computer. Other methods include vertical prisms with sloping tops or line-mass approximations of prisms as well as methods using Fourier analysis or representing terrain using parabolic surfaces [58, 62, 140–143].

It is common to use a combination of different methods when calculating terrain correction to speed up the process whilst maintaining accuracy. In particular, the Hammer method is often used to analyse terrain close to the measurement point and faster methods, like the rectangular prism approach, are used to analyse all other terrain quickly. In this work, terrain correction is calculated using only the rectangular prism method to simplify and speed up the process while using particularly high resolution terrain data and prism analysis for areas near the measurement point to maintain high accuracy. The following section will describe this method and how it was applied differently to terrain at different distances from the measurement point.

3.1.1 The rectangular prism method of calculating terrain correction

The rectangular prism method of terrain correction uses an array of vertically-oriented rectangular prisms (also known as ‘right rectangular prisms’, a type of cuboid) to form a representation of the topography around a survey point, as shown in fig. 3.3. The gravitational field at the survey point due to each prism is calculated using an analytic solution developed by Nagy [138, 139] which takes the form,

$$g_z(x,y,z) = G\rho \left[\left| \left| \left| x\ln(y+r) + y\ln(x+r) - z\tan^{-1}\frac{xy}{zr} \right|_{x_1}^{x_2} \right|_{y_1}^{y_2} \right|_{z_1}^{z_2} \right], \tag{3.1}$$

where g_z is the vertical gravitational field strength at the survey point due to the rectangular prism with boundaries described by x_1, x_2, y_1, y_2, and z_1, z_2, G is the universal gravitational constant ($G = 6.67\times10^{-11}\,\mathrm{m^3\,kg^{-1}\,s^{-2}}$), ρ is the density of the prism, x, y, z are the coordinates

---

[*] A hollow cylinder is used for this because individual segments have an inner and outer radius, as shown in hammer template figure and segments in any given ring form segments of a hollow cylinder. A full derivation is not provided here for the sake of brevity.

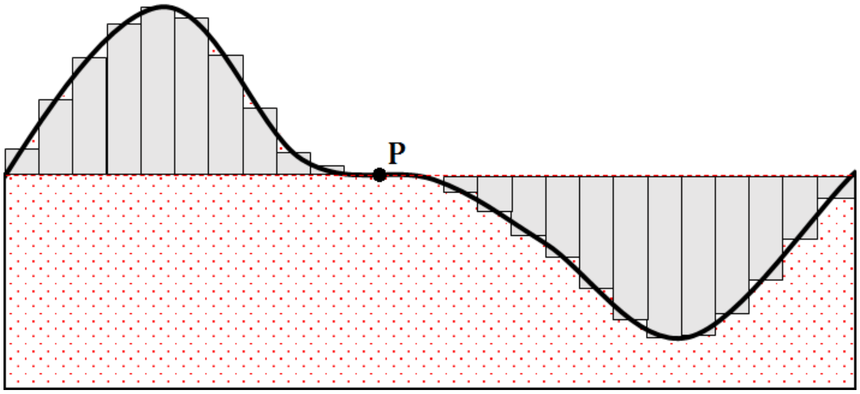

Figure 3.3: 2D diagram showing how rectangular prisms are used to represent hills and valleys around a gravity survey point, P, in order to find terrain correction with the prism method.

of the prism's interior and r, is the distance to a point (x,y,z) within the prism's interior, $r = \sqrt{x^2+y^2+z^2}$.

This expression finds an exact solution for g_z around a vertical rectangular prism and is derived by integrating Newton's universal law of gravitation over the volume of the prism and isolating the z-component of field strength. Solving for the stated boundary conditions, x_1, x_2, y_1, y_2, and z_1, z_2, this expression becomes a sum of 8 terms,

$$\begin{aligned} g_\mathrm{z} = {} & \delta g_\mathrm{z}(x_2,y_2,z_2) - \delta g_\mathrm{z}(x_1,y_2,z_2) + \delta g_\mathrm{z}(x_1,y_1,z_2) - \delta g_\mathrm{z}(x_2,y_1,z_2) \\ & + \delta g_\mathrm{z}(x_1,y_2,z_1) - \delta g_\mathrm{z}(x_2,y_2,z_1) + \delta g_\mathrm{z}(x_2,y_1,z_1) - \delta g_\mathrm{z}(x_1,y_1,z_1)\ , \end{aligned} \tag{3.2}$$

where g_z is the vertical component of gravitational field strength at the chosen point due to the rectangular prism and δg_z is as shown in eq. (3.1). A complete derivation of eq. (3.1) is presented by Nagy [139] and MacMillan [144] but is avoided here for the sake of brevity, as it is both lengthy and complicated. In some cases, it is possible for the arguments of the logarithms in the first and/or second terms of eq. (3.1) to be zero (for example when $x_1 = y_1 = z_1 = 0$), and in these cases those terms will be undefined, as a result of $\ln(0)$ being undefined. If any terms of eq. (3.1) are undefined during calculation, they should be set to zero because they have a zero-limit in this case, as detailed by Nagy [139]. When any of the terms in eq. (3.1) are undefined, they should be set to zero because, according to Nagy, at the locations where undefined terms arise (on the corners, edges and planes of the prism in question) they can be shown to have a zero-limit. The proof of this is mathematically complicated and will not be reproduced here for the sake of brevity.

The accuracy of the prism method is determined by how closely the prism representation matches the real terrain it represents, which depends on the horizontal size of the prisms used and the accuracy and resolution of the topographic data. This is because using prisms with a smaller horizontal size effectively increases the resolution of the prism representation of the topographic data and more accurate topographic data means a closer match to the real terrain.

A straightforward way of making such a prism representation is to use elevation data arranged in a format known as a Digital Elevation Model (DEM) which describes the topography of a region with a square 2D grid of elevation values. This format is particularly convenient because the regular 2D array of elevation values in the DEM can easily be used to choose the heights of prisms in a prism model of the same region. With this approach, the x-y size of prisms in the terrain model is determined by the horizontal resolution of the DEM, so a more accurate prism representation (i.e. one using smaller elements) can be made by using a higher-resolution DEM. The task then is to find or make DEMs that describe the surroundings of the location at which terrain correction is to be found to a high degree of accuracy.

This method of terrain correction is generally considered to be unsuitable for application to topography close to a survey point, within approximately 200 m to 1000 m. This is because, due to past limitations in available computing power and the resolution of topographic data, only low-resolution prism representations have been feasible, which will form a less accurate representation of the real terrain, especially nearby terrain. In the region close to a survey point, discrepancies between real topography and the prism representation can lead to large errors in calculated terrain correction, so the rectangular prism method is less accurate in these regions. As a result it has been mostly used for finding terrain correction due to more distant terrain, while closer regions are analysed using the slower and more labour-intensive Hammer method.

In this work, the rectangular prism method of terrain correction is used to analyse terrain across all distances from a measurement point (out to a standard outer limit, detailed in the next section), using high-resolution LiDAR data to make a high resolution prism representation of the nearby terrain to maintain accuracy. The following section describes how topographic maps were obtained to describe all areas of terrain around chosen survey points in this work.

3.1.2 Map generation

As mentioned in the previous section, the accuracy of terrain corrections found using the prism method is determined by the cross-sectional size of the prism elements which is itself determined by the horizontal resolution of the DEM used. Following this, the simplest approach to high accuracy terrain correction would be to use a single DEM with a very high resolution but this is problematic when considering a large area of terrain due to the large number of elements and computing load that would result. Specifically, handling large DEMs requires the use of equally large arrays and using this data to evaluate eq. (3.1) means a large number of these arrays must be created and stored in computer memory simultaneously, which can lead to crashes if there is not enough memory available.

A much less memory-intensive approach is to divide the calculation into different zones of terrain, determined by their distance from the computation point, and use lower resolution, less computationally demanding DEMs when analysing distant terrain. Because of the inverse-square relationship between gravitational field and distance, this will have little effect on the

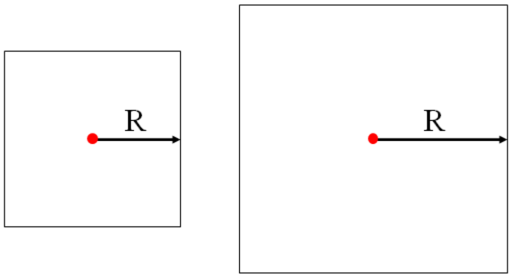

Figure 3.4: Outline of two differently-sized square maps showing how the variable R is used to describe their size.

accuracy of the overall terrain correction since each distant element only has a very small contribution to g_{tc}. Conversely, it is important that the highest resolution DEMs are used when analysing terrain immediately surrounding a survey point because terrain within the first few hundred meters can have a substantial impact on overall terrain correction.

In this work, the calculation of terrain correction is divided into three zones: an inner zone, middle zone and outer zone, and a lower map resolution is used for more distant zones. These are arranged as concentric square regions centred on the survey point and the zone size will be described by R, the distance along the x-axis (or y-axis) from the survey point to the map edge, as shown in fig. 3.4. Square maps were used because this is more convenient when using the prism model in which elements have a square base cross-section.

The position of the zone boundaries is determined by examining past work on terrain corrections in the literature and in some cases exaggerating these to ensure high accuracy. The details of what zone boundaries were chosen, what DEM resolution was used and the source of this height data are given separately for each zone in the following subsections.

Inner zone

Because of the large effect terrain in the inner zone can have, it is particularly important that accurate elevation data are used when finding terrain correction due to this region. For this work, airborne LiDAR elevation data was used that describes the elevation of the inner zone to either centimetre or millimetre accuracy (accuracy varies for different regions) with a horizontal resolution of 1m. Airborne LiDAR is a commonly used method of gathering high accuracy topographic data using laser ranging systems onboard light aircraft, helicopters or (more recently) drones [145] and the Campsie Fells dataset is available in DEM format online [146].

There is no single answer in the literature for what the extent of the inner zone should be. In most published gravity surveys, inner zone radius varies between 100 m and a few kilometres [141, 147–149], depending on the desired accuracy of the survey, the surrounding topography, and the experience or company policy of those performing it. Here, a larger radius of $R = 1\,\text{km}$ is used in order to avoid inner zone size limiting the accuracy of terrain correction and because this size of 1m resolution DEM could still be computed quickly. For each survey point in the

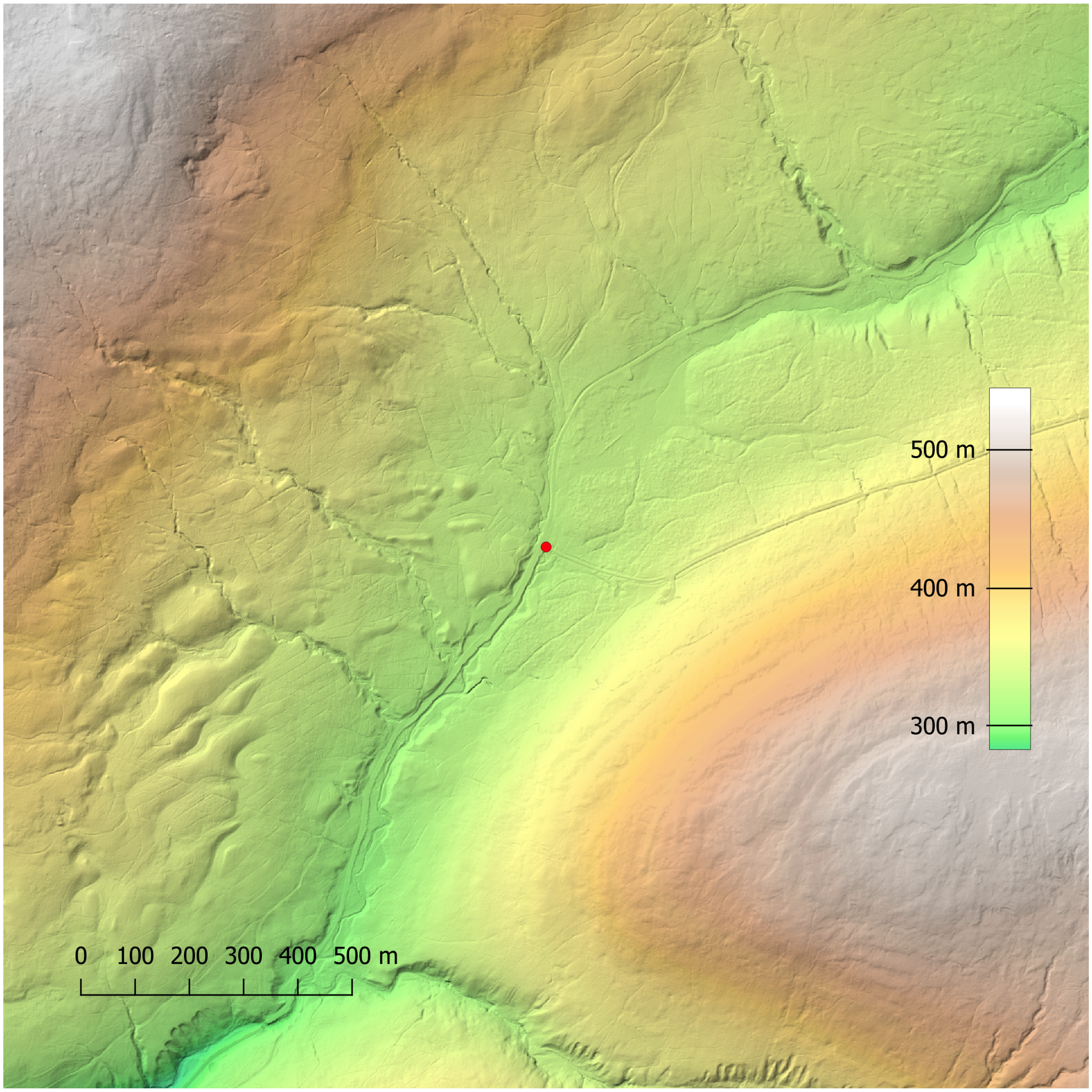

Figure 3.5: Example of a DEM used when describing inner zone topography using LiDAR data for the 2 km^2 around a measurement point (indicated by the red dot) in the Campsie Fells.

Campsies, a $2\,\mathrm{km}^2$ inner zone DEM was extracted from the overall LiDAR dataset and aligned so that the survey location was at its centre, at the shared vertex of the four centremost elements. An example of an inner zone DEM is shown in fig. 3.5 with the survey point marked at its centre.

It was found that the accuracy of the rectangular prism method of terrain correction is improved by ignoring the nearest 4 elements to the survey point during calculation, which effectively assumes the nearest 2 m^2 are totally flat, in the case of 1 m element resolution. This is covered in more detail later in section 3.3.2.

Middle zone

The middle zone concerns terrain beyond the inner zone up to a chosen limit and so lower resolution DEMs than for the inner zone can be used when calculating terrain correction without causing a significant loss of accuracy. The LiDAR data used for inner zone corrections could not simply be downsampled to make lower resolution DEMs for the middle zone because the available dataset does not describe a large enough area. Instead, topographic data for the middle zone were obtained in the form of Ordinance Survey contour maps, available online under an open government licence [150]. These contour maps have a horizontal resolution of 50m and contour intervals of 10m but are not available in DEM format, meaning they had to be converted before use in the prism terrain correction model.

The contour data is in a digital vector format called a "Shapefile" (.shp) which is specifically designed for describing geographical features using what is known as Geographical Information System (GIS) software. In this work, the open-source GIS software, QGIS version 2.18.14 [151] was used to transform these contour maps into DEMs using linear interpolation methods built in to the software. Figure 3.6 shows an example of contour data of the Campsie Fells and the resulting 50m resolution DEM made using QGIS. The DEMs made from the contour maps were chosen to have a 50m horizontal resolution and an extent of $R = 25\,\mathrm{km}$ giving them an area of $50\,\mathrm{km}^2$, centred on the survey point of interest. The 50m horizontal resolution was chosen because it matched the resolution of the contour maps from which the DEMs were made. Making a higher resolution of DEM (25m) from the same contour data was tested but ultimately led to a sub-microGal effect on terrain correction, so is unnecessary for this work. The central $2\,\mathrm{km}^2$ of the middle zone is ignored when finding terrain correction in this work because this area is already considered by the inner zone calculation and details on how this is done are given later in section 3.2.

Outer zone

The outer zone consists of terrain beyond the middle zone out to a chosen limit and, once again, even lower resolution DEMs can be used when calculating terrain correction without a significant loss in accuracy, due to the inverse-square behaviour of gravitational field with distance. By convention, an outer radius of 166.735 km is used when finding the terrain correction due

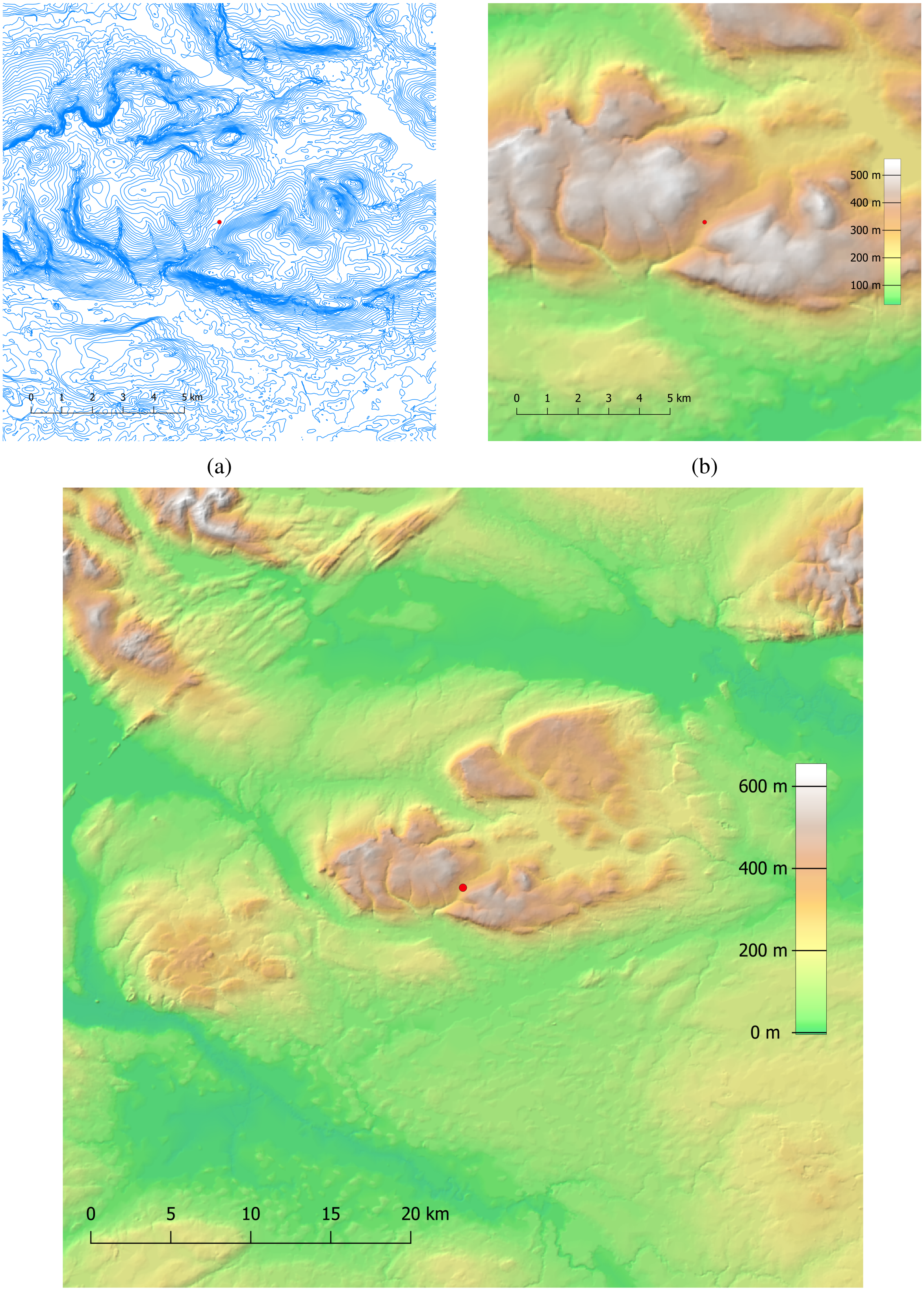

(a) (b)

(c)

Figure 3.6: (a) and (b): Example of OS contour data and a corresponding 50 m^2-resolution DEM made from it. The contour interval is 10m. (c): A full 50 km^2, DEM with a 50 m^2-resolution like those used to calculate terrain correction due to topography in the middle zone.

to distant topography [58, 152]. Terrain beyond this limit will only have a significant effect if it is extremely rugged or when there is a large elevation difference between different measurement points in a gravity survey [152]. In this work, there is not a great deal of terrain beyond 166.735 km (most of the Scottish highlands are within this limit) and the survey points considered have an elevation difference of approximately 200 m at most so this outer limit is considered suitable and used for all terrain corrections.

In the Campsies region, the 166.735 km outer zone contains large areas of ocean (the North sea and Irish sea) and so the terrain effect due to the bathymetry of these areas will likely have a significant effect and must be considered as well. To do this, publicly available DEMs were obtained that describe both the topography and bathymetry of the relevant area with a resolution of $15''$ (arcseconds; corresponding to an approximately $450\,\mathrm{m}^2$ horizontal resolution on the Earth's surface). This data, the GEBCO 2020 grid [153], is a combination of satellite radar data describing topography and bathymetry data obtained through various techniques and is downsampled to make $500\,\mathrm{m}^2$-resolution DEMs like the one shown in fig. 3.7 mapping the topography and bathymetry of the outer zone region.

3.2 MATLAB program to calculate terrain correction

A series of MATLAB programs have been written in order to use the prism method described in section 3.1.1 to calculate terrain correction from suitable inner, middle and outer zone DEM's describing the topography around a measurement point. For clarity, the program is divided into four separate MATLAB scripts, one of which handles all input data and calls the other three scripts as functions to calculate the terrain correction. MATLAB version R2015b was used when making these scripts and they are presented in appendix B. This section will describe how they work in detail and show some examples of their use on real-world terrain.

For map input the main program reads three square DEMs describing the inner, middle and outer zones that are described in in section 3.1.2, all of which must have the measurement point at their centre. As mentioned in the previous section, it is important that, where these maps overlap, the terrain correction is only calculated once using the highest-resolution data describing the region in question. For example, the centre $2\,\mathrm{km}^2$ of the middle zone is already described at a higher resolution by the inner zone, so the terrain correction due to this part of the middle zone DEM must be discarded. To do this, the programs can divide a DEM into many smaller subsections, which will be called quadrants, and then ignore those quadrants outside of the specified zone boundaries when calculating terrain correction. By carefully choosing the number of quadrants a DEM is divided into, areas already considered by higher-resolution DEMs can be ignored in larger, lower-resolution zones without additional DEM processing beforehand.

For example, by dividing a $340\,\mathrm{km}^2$ outer zone into a 68×68 grid of $5\,\mathrm{km}^2$ subsections, those forming the $50\,\mathrm{km}^2$ centre area can be removed to ignore the area already covered by

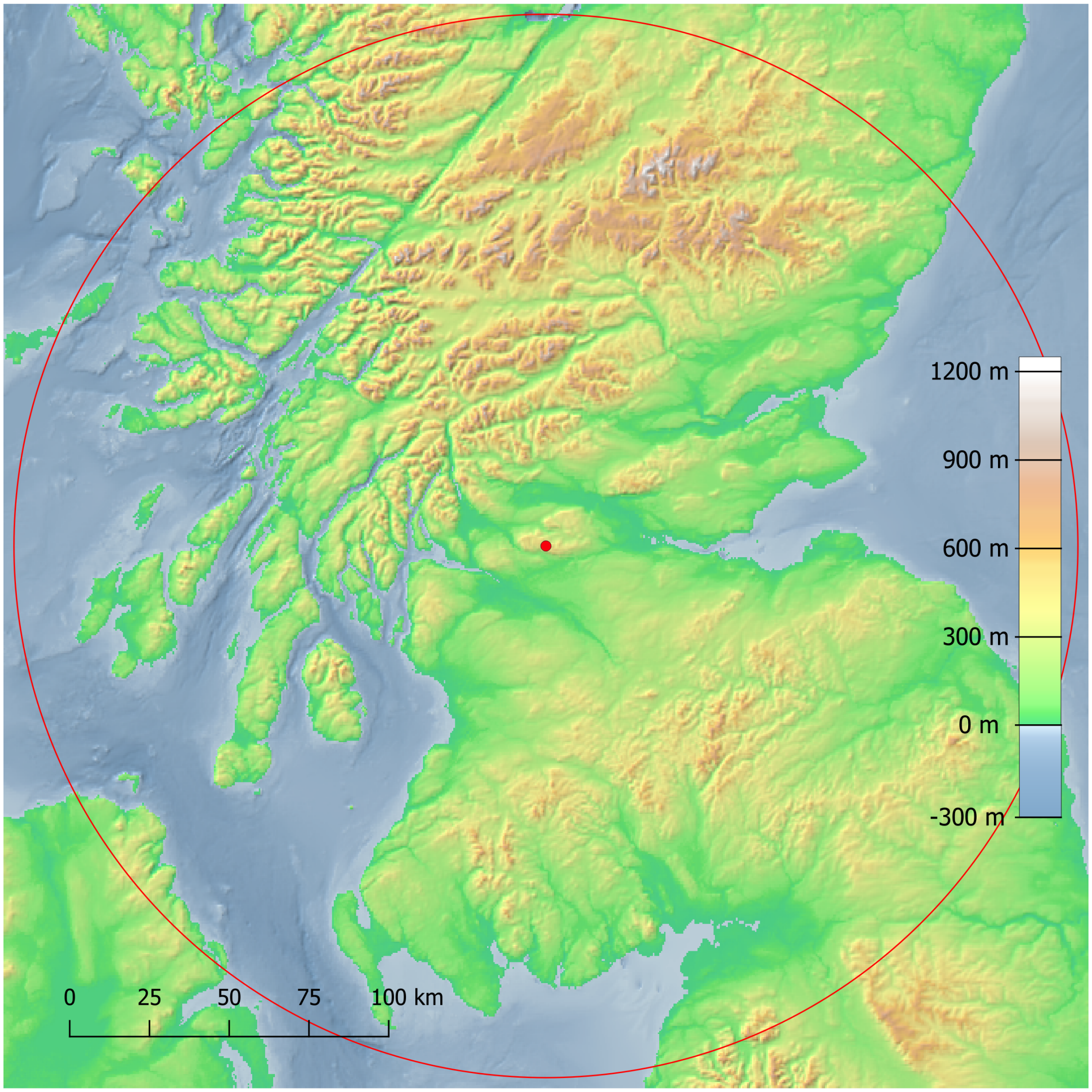

Figure 3.7: Example of a 500 m^2-resolution DEM used to describe outer zone topography and bathymetry around a survey point in the Campsie Fells, marked by the red dot, out to a distance of 166.735 km, shown by the red circle. The full map is 340 km^2 in size.

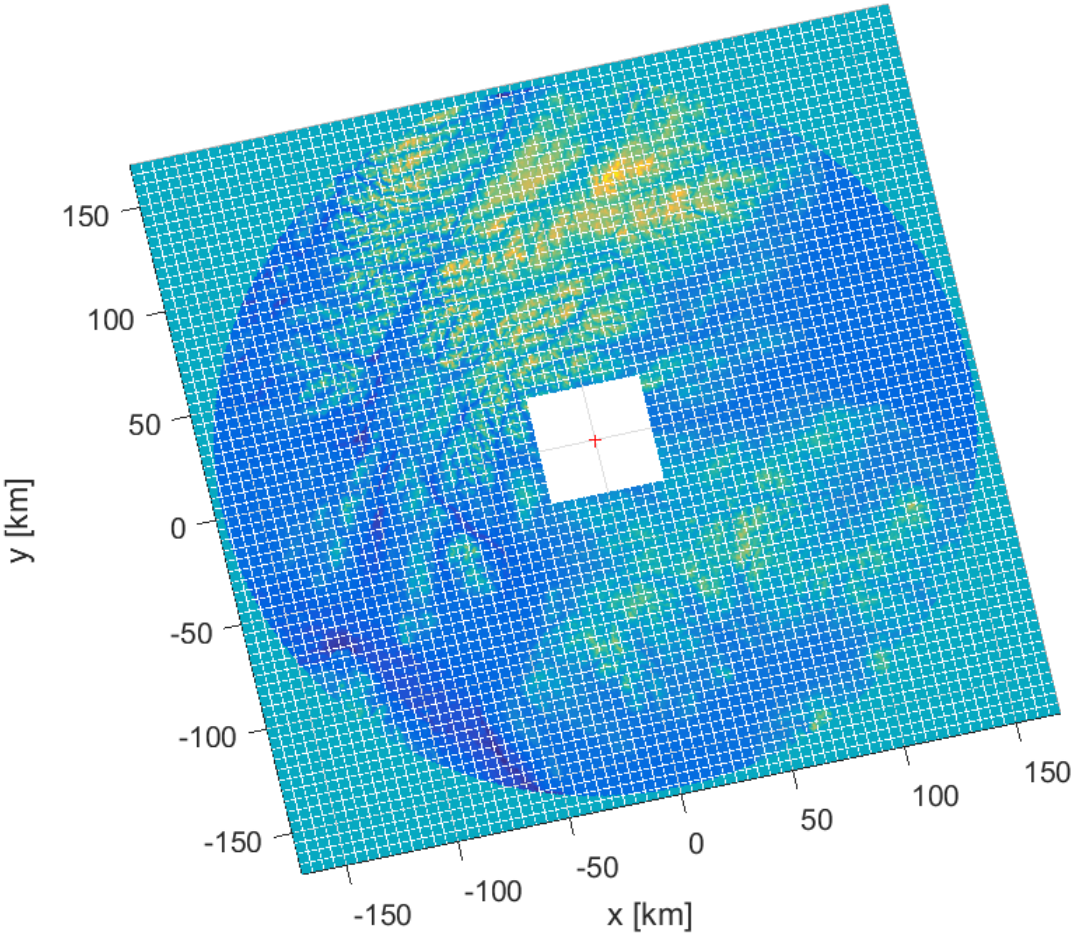

Figure 3.8: Example of an outer zone DEM divided into a 68×68 array of quadrants, resulting in each having a side length of 5 km, allowing the central 50 km^2 to be ignored easily. Elevation is set to zero (the same elevation as the survey point) beyond a radius of 166.735 km so that only terrain within a circular area is considered.

the middle zone, as shown in fig. 3.8. It should be emphasised that since it is only possible to ignore entire quadrants at once, the number of quadrants, div, must be chosen carefully so that areas to be removed are exactly covered by an integer number of quadrants. Dividing the DEMs into quadrants also has the benefit of reducing the computer memory required when running the program because smaller DEMs are handled at one time. This was found to avoid crashes and even increase the processing speed when analysing particularly large or high-resolution DEMs.

A radial limit of 166.735 km is applied to the outer DEM so that only terrain in a circular area of this radius is considered when finding terrain correction, as is convention. This is done by setting the elevation of every point on the DEM beyond $R = 166.735$ km to be equal to that of the measurement point, as shown in fig. 3.8, meaning regions beyond this boundary will have no impact on terrain correction.

3.2.1 Terrain correction program description

'terrain_correction.m' — the main program: The first MATLAB script acts as the primary program where all inputs are accepted and where the output — the calculated terrain correction — is delivered and is the only program manually run by the user. It requires the file path to the inner, middle and outer zone DEM files in 'GeoTIFF' (.tif) format, from which it automatically determines each map's horizontal resolution and makes 2D arrays containing the x-position, y-position and elevation of each DEM data point, relative to the map's centre. The program also requires the inner and outer limits, R_1 & R_2, of all three zones, where R is as shown in fig. 3.4, as well as a number, div, to specify how many quadrants each zone is to be divided into (where the result is $div \times div$ quadrants). For the zones described in section 3.1.2 the following input values are used: inner zone, $R_1 = 0\,\mathrm{m}$, $R_2 = 1\,\mathrm{km}$, $div = 20$; middle zone, $R_1 = 1\,\mathrm{km}$, $R_2 = 25\,\mathrm{km}$, $div = 50$; outer zone, $R_1 = 25\,\mathrm{km}$, $R_2 = 170\,\mathrm{km}$, $div = 68$. The terrain correction at the measurement point is calculated separately for each the inner, middle and outer zones using the 'zone_TC.m' function (described below) and the total terrain correction is found by summing the contributions of each zone.

'zone_TC.m' — first function: This function takes a DEM describing the inner, middle or outer zone, divides it into the specified number of quadrants, removes quadrants outside the given zone boundaries, and then calls other functions, described below, to use the Nagy prism method described in section 3.1.1 to calculate g_z at the origin due to each quadrant. The total terrain correction at the centre of the DEM in question is then calculated by summing the g_z contributions of all elements in all quadrants.

The 'zone_TC.m' function can also find the effect on terrain correction due to bathymetry (i.e. underwater topography) as well as normal topography and works on the assumption that all terrain at elevations below sea level is in fact underwater and the water density is $1030\,\mathrm{kg\,m^{-3}}$. This is done by first separating the input DEM into two new versions that describe topography (above-water elevation) and bathymetry (underwater elevation) separately and then calculating the contribution to g_z from each appropriately, using the approach described in section 3.1. The topography-only DEM is made by simply replacing all elevations below sea level with a flat surface at sea level height (an elevation of $0\,\mathrm{m}$) and, similarly, the bathymetry-only map has all areas above sea level replaced with a flat surface at sea level elevation. The terrain correction at the survey point due to each of these maps is then calculated separately using the 'prism_method_topography.m' function for the topography and the 'prism_method_topography.m' for bathymetry, which are described below. The total terrain correction is then the sum of the results from the topographic and bathymetric calculations.

The 'zone_TC.m' function can also be used to make plots of the topography and/or bathymetry maps before or after being divided into quadrants (like the ones shown in figs. 3.8, 3.9a and 3.9b), as well as plots showing the contributions to g_z from each element in the DEM (like those shown later in fig. 3.10).

‘prism_method_topography.m’ and ‘prism_method_bathymetry.m’ — the second functions: These functions use the Nagy prism method described in section 3.1.1 to calculate the gravitational terrain correction at the centre of a DEM describing topography (in the case of ‘prism_method_topography.m’) or bathymetry (in the case of ‘prism_method_bathymetry.m’) around a gravity survey point located at the origin. For input, both functions require the x,y-coordinates and elevations (relative to the survey point) of each point on the surface of the DEM, the horizontal resolution of the DEM (which is automatically determined from the DEM in the ‘terrain_correction.m’ program) and the average density of rock. The ‘prism_method_bathymetry.m’ function also requires the elevation above sea level of the survey point (also determined in ‘terrain_correction.m’) and the average density of water as inputs.

The topographic contribution to terrain correction is calculated by ‘prism_method_topography.m’ which defines rectangular prism elements as extending from the level of the survey point up or down to the topographic surface described by the DEM (as in fig. 3.3) and then uses eqs. (3.1) and (3.2) to find g_z due to each prism and sums the results. For the bathymetric contribution, ‘prism_method_bathymetry.m’ defines prisms as originating at sea level and extending down to the bathymetric surface described by the DEM and thus requires the elevation of the survey point as additional input so that sea level elevation can be determined. The density of prisms in the topographic case is simply the average density of rock but in the bathymetric case the density used must be the difference between the average density of rock and average density of water. These functions also both ignore the 4 prisms immediately surrounding the measurement point when finding terrain correction for the inner zone (thus assuming this area to be completely flat) as this was found to produce more accurate results, as discussed further in section 3.3 later.

With both of these functions, care is taken at every step of eq. (3.1) to set individual terms to zero if they are undefined, as instructed by Nagy [139] and discussed in section 3.1.1. Also, it was found that input elevation values must be stored using MATLAB’s ‘double’ data type instead of the ‘single’ data type, the latter of which only stores digits up to the 7th number after the decimal place during calculations. Use of the ‘single’ data type caused significant errors because very small variations between terms are important in eq. (3.1), particularly when $x \ll y$ or $y \ll x$. All programs in this work have been written to ensure that elevation values are handled using the ‘double’ data type, which stores digits up to the 15th number after the decimal place, to avoid errors.

3.2.2 Terrain correction examples

To demonstrate the terrain correction program’s performance, two locations in the Campsie Fells were chosen (shown in fig. 3.9) as hypothetical gravimeter survey points and the program was used to calculate terrain correction at both of them. The two survey points will be referred to as point A and point B and their locations and the surrounding topography are shown in fig. 3.9. Point A sits at latitude 55.981 013° and longitude −4.221 537° at an elevation of 71.13 m above sea level and point B is at latitude 55.993 601° and longitude −4.225 659° at 220.69 m above sea level (the point elevations have been determined from the LiDAR data describing the Campsie Fells). These two survey points were chosen because they have significantly different topography in their immediate surroundings, which helps demonstrate the models performance in different situations.

Sets of inner, middle and outer zone DEMs were made for both survey points (using the zones described in section 3.1.2) and the MATLAB program used these to calculate the terrain corrections to be 1.6235 mGal at point A and 2.8585 mGal at point B. The program was run on a PC with 8 GB of physical memory and a 3.2 GHz CPU and took approximately 9 s to read a set of 3 input DEMs and calculate the corresponding terrain correction value. The above results are comparable to published terrain correction values from surveys in similarly hilly surroundings [62, 147], which find terrain corrections to be between 1 mGal to 3 mGal, using established terrain correction methods (a combination of the Hammer method and rectangular prism or line-mass assumptions). This shows that the rectangular prism-only method described in section 3.1.1 is producing believable results, but a more in-depth investigation of its accuracy is undertaken in section 3.3.

The program is also able to make surface plots showing the g_z contribution of each element in a prism representation of terrain and such plots were made for the nearest $200\,\mathrm{m}^2$ around survey points A and B, shown in fig. 3.10. These help verify that the program is working as intended by demonstrating that nearby areas of large topographic relief have a larger effect on g_z at the survey point than more flat or distant areas, as expected when calculating terrain correction.

To investigate the program's handling of distant terrain in more detail, it was run repeatedly while gradually increasing the square radius, R (as defined in fig. 3.4), of terrain considered, making the plot of terrain correction against R shown in fig. 3.11. This plot shows how the specific topography at different distances contributes to the terrain correction at the survey point. For example, the topography in the surrounding 2 km ($R = 1\,\mathrm{km}$) of survey point B accounts for over half of the total terrain correction due to the steep surroundings while for point A this region only accounts for a small fraction of the total terrain correction. Conversely, the middle zone has a larger effect on terrain correction for point A as this is where the more rugged terrain of point B's inner zone is considered for point A.

For both survey points, terrain in the outer zone has a sub-0.1 mGal effect on terrain correction which is a good example of why terrain beyond 22 km often ignored in mGal-accuracy gravity surveys but is very significant in microgravity surveys.

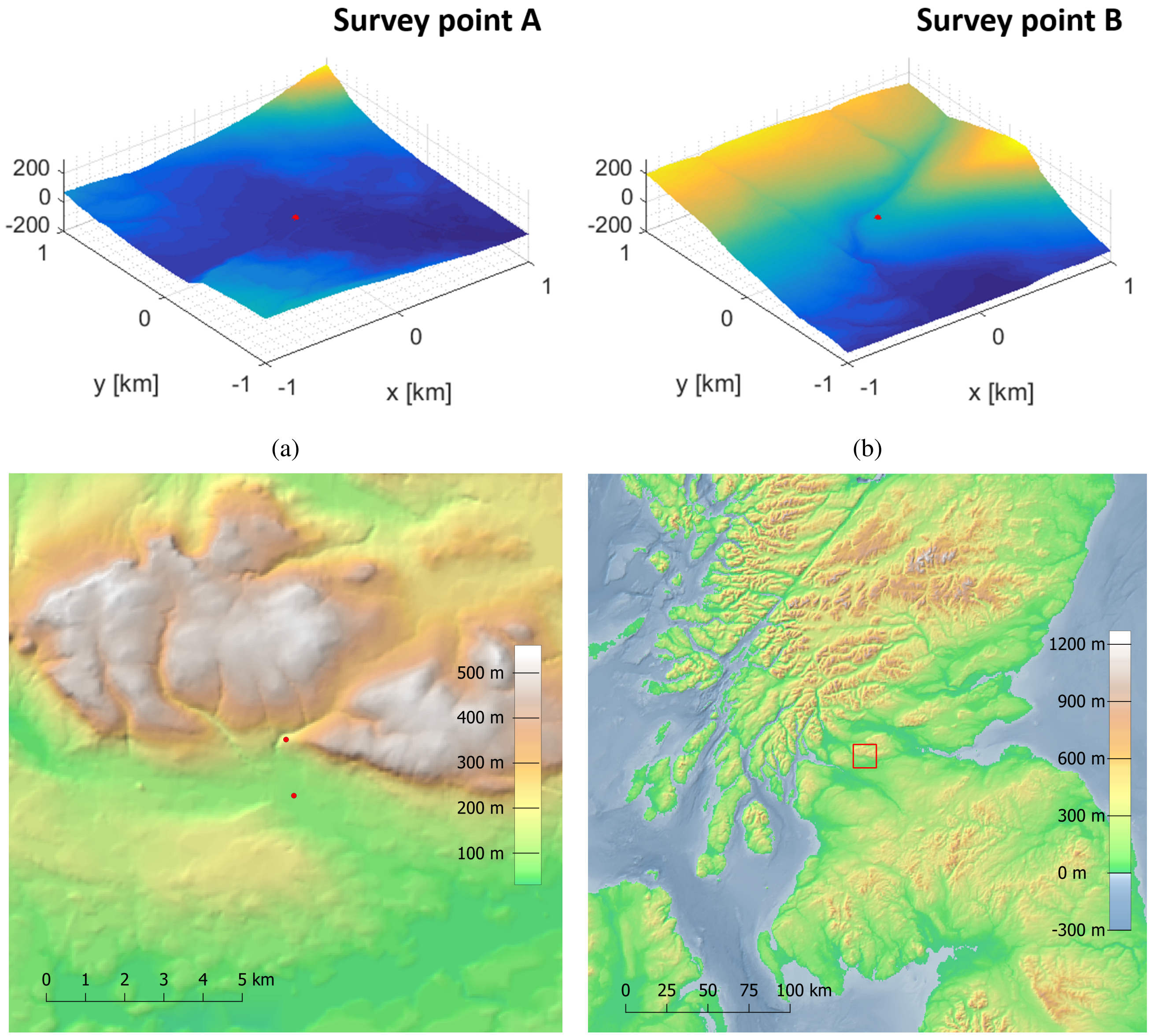

(a)

(b)

(c)

(d)

Figure 3.9: (a) & (b): 2 km^2 inner zone DEMs of the two survey points in the Campsie Fells used when testing the terrain correction program, plotted in MATLAB. (c): A roughly 13 km^2 map of the local region showing the position of the two survey points. (d): Large-scale, 340 km^2 map showing the location of the survey points in Scotland where the red box indicates the area shown in (c).

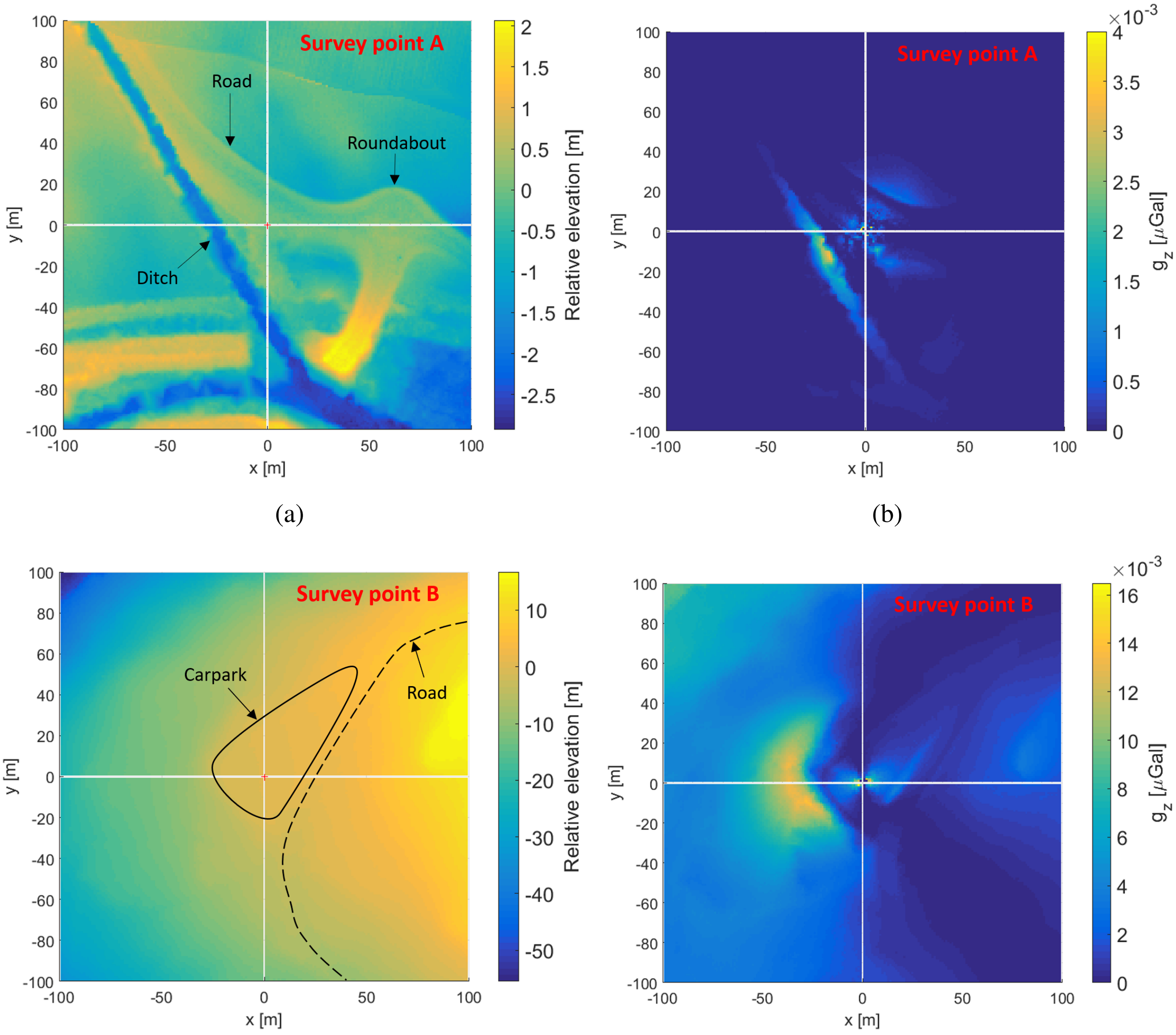

(a) (b)

(c) (d)

Figure 3.10: (a) & (c): Topographic maps showing the 200 m^2 area surrounding survey points A and B, respectively, with some features labelled. In both maps, the survey points are located at $(0,0,0)$. (b) & (d): Colour plots of the same areas showing the results of applying the prism method of terrain correction to the corresponding DEMs. The plots show the contribution to g_z (i.e. terrain correction) at the survey point due to each 1 m^2 prism element in the prism representation of the topography.

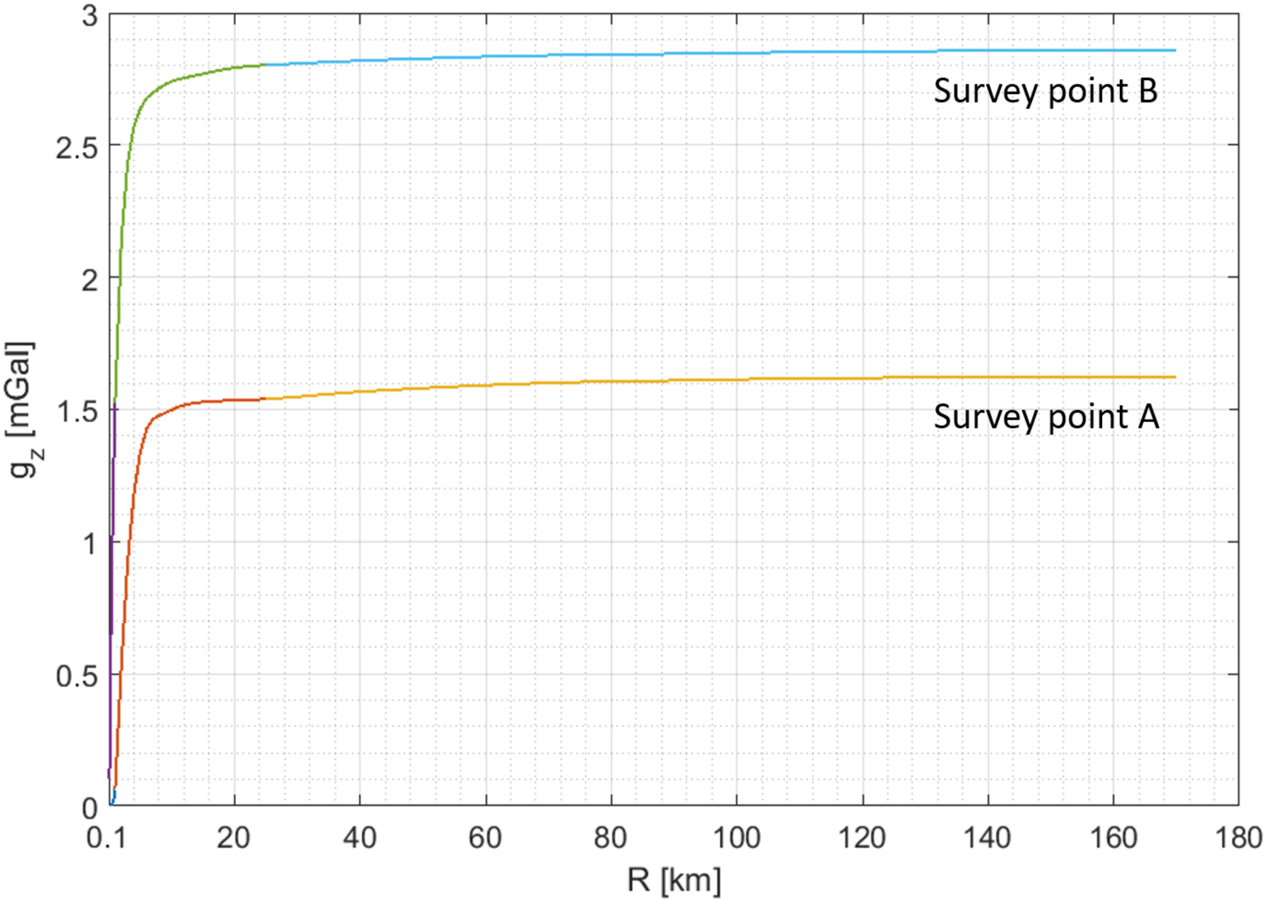

Figure 3.11: Graph showing how terrain correction at the two survey points shown in fig. 3.9 varies as the square radius *R* of topography considered by the terrain correction program is increased. The lines are each delineated into three colours to indicate the range of the inner zone (100 m to 1 km), middle zone (1 km to 25 km) and outer zone (25 km to 170 km) used in this work.

3.3 Investigating model accuracy

As discussed in section 3.1.1, the accuracy of the rectangular prism method of terrain correction is determined by the resolution and accuracy of the input elevation data it has to work with. Due to difficulty in gathering accurate and high-resolution elevation data, the rectangular prism method is generally considered unsuitable for calculating inner zone terrain corrections, where accurately representing the topography is particularly important. This work aims to use high-resolution LiDAR data and a similarly high-resolution rectangular prism analysis to try and maintain accuracy when using this prism method to find terrain corrections due to nearby terrain as well. This section covers the work done to determine whether the program is successful in this by testing its accuracy using simplified terrain geometries and corresponding analytical solutions for g_z (terrain correction) due to these bodies.

3.3.1 Comparison to the Hammer method

In section 3.2.2 the terrain correction program is applied to two locations in the Campsie Fells and shown to produce results that are believable in comparison to previously published terrain corrections calculated in similarly hilly terrain. This is a good indication that the program is working correctly but does not confirm this definitively as the published values did not use the exact same survey locations so the results in this work may only be similar by coincidence.

To test more rigorously if the rectangular prism method had been implemented correctly in the program, it was used to calculate the terrain correction due to a single annular segment, like the one shown in fig. 3.12a. This was done because such annular segments are used in the Hammer method of terrain correction and the terrain correction (g_z) due to these objects can be calculated easily using the analytic expression,

$$g_\mathrm{z} = \frac{G\rho\pi}{n}\left(\sqrt{R_1{}^2+h^2} - \sqrt{R_2{}^2+h^2} + (R_2 - R_1)\right) , \tag{3.3}$$

where G is the gravitational constant ($G = 6.67\times10^{-11}\,\mathrm{m^3\,kg^{-1}\,s^{-2}}$), ρ is the average density of rock in the region (assumed to be $2670\,\mathrm{kg\,m^{-3}}$), n is the number of angular segments that form a whole annulus, R_1 and R_2 are the inner and outer radii of the segment and h is the height of its top face, relative to the survey point [137]. If the rectangular prism method has been correctly implemented, there should be close agreement between it and the analytic solution in eq. (3.3) when both are used to calculate g_z due to the same object.

When carrying out this test, an annular segment was chosen for which $R_1 = 15\,\mathrm{m}$, $R_2 = 50\,\mathrm{m}$, $h = 10\,\mathrm{m}$ and $\rho = 2670\,\mathrm{kg\,m^{-3}}$. A rectangular prism representation of this segment was then made using prisms with a base size of $1\,\mathrm{m}^2$ and is shown in fig. 3.12b. Then the terrain correction due to this segment was calculated analytically using eq. (3.3) and then again by the MATLAB program using a prism representation of the segment described by a corresponding

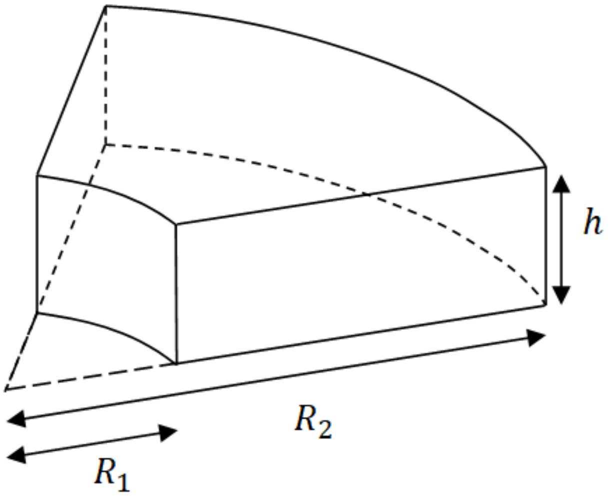

(a)

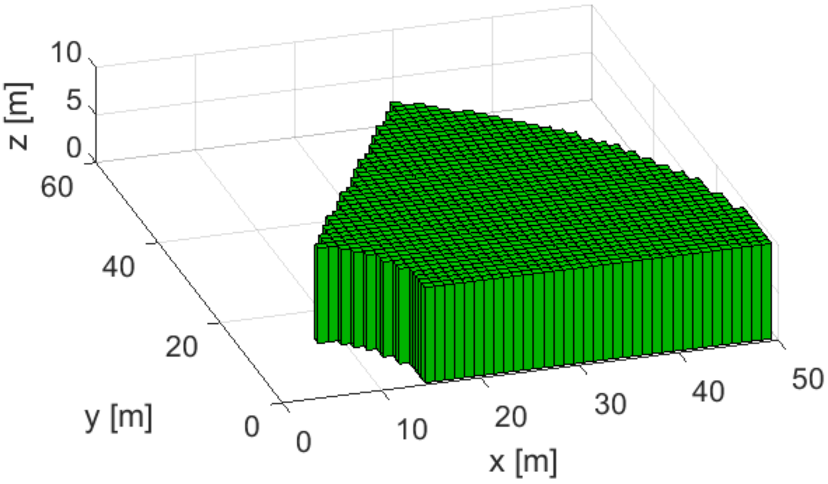

(b)

Figure 3.12: (a): Schematic of a single annular segment like those used in the Hammer method of terrain correction. (b): Diagram showing a prism representation of a Hammer segment used when testing the rectangular prism terrain correction program against the Hammer analytical solution.

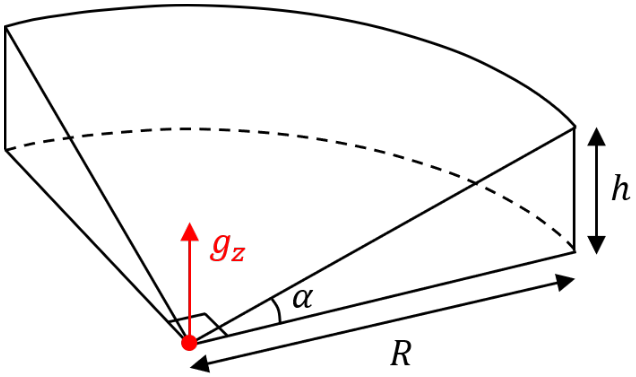

Figure 3.13: Schematic of a conically sloping quarter-wedge used to test how accurately the rectangular prism method can find the terrain correction, g_z due to nearby sloping surfaces. The analytic expression in eq. (3.4) calculates g_z at its thinnest point, shown in red.

DEM. The calculated g_z values were 38.00 µGal from the analytic solution and 37.07 µGal from the prism method, giving a sub-µGal discrepancy between the two methods of 0.93 µGal, probably arising from the imperfect prism representation of the curved surfaces of the segment. The close match between the analytical and prism calculations suggests that the rectangular prism method is implemented correctly in the MATLAB program and the 1 m resolution DEM achieves an accuracy of less than a few µGal.

3.3.2 Rectangular prism representation of sloped terrain

The representations of terrain made using the rectangular prism method are fundamentally limited in their ability to accurately represent sloping surfaces due to their flat-topped shape. As has been mentioned, the accuracy of these representations can be increased by using prisms with a smaller base size but there is a lower limit to the size of prisms that can be used, dictated by the available computing power and the horizontal resolution of available topographic data. Ideally, this work would investigate the use of sloping-topped vertical prisms which could be used to make more accurate representations of real topography using analytic solutions for g_z due to triangular, rectangular and n-sized vertical prisms with sloping tops that have been published in the literature [140, 149]. However, due to the time limitations, an investigation of the use of these methods for finding terrain correction is left to future work. Instead, a more detailed investigation is carried out into how effective the flat-topped rectangular prisms are when used to model a simple nearby sloping surface to test how accurate the method is when used to calculate inner zone terrain corrections using real topography.

The object chosen for this analysis is a conical quarter-slope, shown in fig. 3.13, for which the vertical component of gravitational field, g_z, at the thinnest point of the wedge is given by

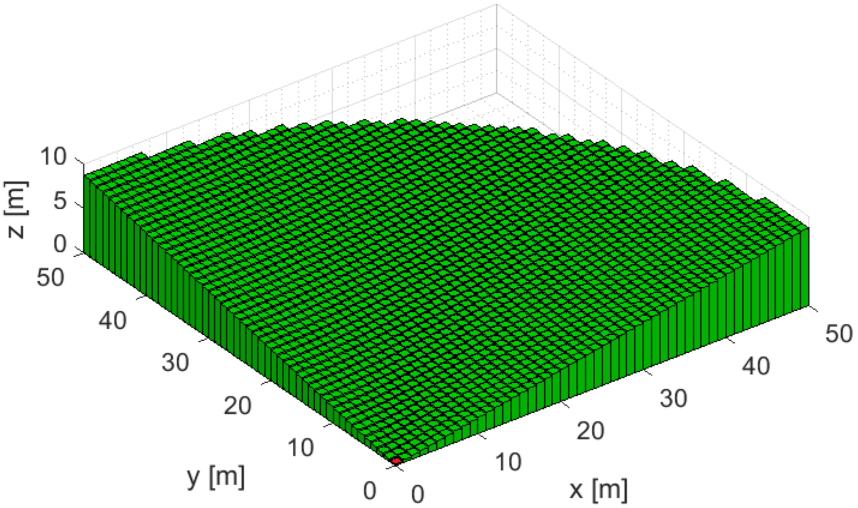

Figure 3.14: Example of a rectangular prism representation of a conical quarter-slope for which $R = 50\,\mathrm{m}$, $\alpha = 10^\circ$ and $h \approx 8.82\,\mathrm{m}$ using prisms with a base size of $1\,\mathrm{m}^2$. The prism closest to the origin is coloured red and discussed further in the text.

the analytical expression,

$$g_\mathrm{z} = \frac{\pi G \rho R}{2\sqrt{R^2+h^2}}\left(\sqrt{R^2+h^2}-R\right) , \tag{3.4}$$

where G is the gravitational constant, ρ is the density of the object and R and h are its radius and the height of its distant side, respectively [63]. Once again, a density of $\rho = 2670\,\mathrm{kg\,m^{-3}}$ is used for all calculations and $G = 6.67\times10^{-11}\,\mathrm{m^3\,kg^{-1}\,s^{-2}}$.

This particular object was chosen because its sloping face curves around the g_z calculation point such that there is a uniform slope towards the computation point in multiple directions which makes the shape harder to reproduce using flat-topped rectangular elements and helps determine the ‘worst-case’ accuracy of the prism method. Also, for this shape, g_z at the computation point is described by a relatively simple analytic solution and the object has a finite extent which makes it far easier to model with the finite prism representation. By calculating g_z using the rectangular prism method and comparing this to the analytic solution found using eq. (3.4), the accuracy of the prism method can be determined as the dimensions of the slope or size of the prism elements are changed. Figure 3.14 gives a visual example of a rectangular prism element representation of a conic slope made when calculating terrain correction using the prism method. To make this representation, the height of prisms was determined from the height of the sloping surface when at positions coincident with their x-y centres.

During this analysis, it was found that the prism element closest to the computation point, marked red in fig. 3.14, has a very large effect on calculated g_z (even when the prisms used are very small) and that ignoring this prism during the course of calculation actually improved the agreement between the prism and analytic methods. This is made clear in the following results and figures and is why the 'prism_method.m' program described in section 3.2 was made to ignore the four prisms adjacent to the measurement point when calculating inner zone terrain corrections.

Figure 3.15a plots the g_z calculated by the prism method and the analytic solution as the element size used in the former is varied for a slope where $\alpha = 5^\circ$ and $R = 40\,\mathrm{m}$. This shows that as the base size of elements used is decreased, the g_z value from the prism method always gets closer to the analytic solution, as is expected because a smaller element size leads to a more accurate, higher-resolution prism representation of the slope. The results also demonstrate that, for a given element size, including the nearest prism in the calculation leads to a large overestimate in g_z while ignoring it causes a much smaller underestimate, especially when larger element sizes are used. This is because the nearest element, like all flat-topped prisms, is an inaccurate representation of a sloping surface but, because it is adjacent to the computation point, it has a particularly damaging effect on the accuracy of the calculated g_z (due to the inverse-square relationship between gravitational field strength and distance) so excluding it improves accuracy. Figures 3.15b and 3.15c plot the percentage error (Δ) between the prism and analytic solutions as element size is changed and show that there is an approximately linear relationship between element size and the percentage error (i.e. when the element size is doubled, the percentage error increases by approximately a factor of 2). For a slope angle of 5°, radius of $40\,\mathrm{m}$, and element size of $1\,\mathrm{m}$ the modelling determines an error between the prism and analytic solutions of approximately $-0.1\,\mu\mathrm{Gal}$ if the nearest prism is ignored and roughly $1.5\,\mu\mathrm{Gal}$ if it is not (which corresponds to a percentage error, Δ, of approximately -2% and 37%, respectively).

Models were also made that used a fixed element size of $1\,\mathrm{m}$ and slope angle of 5° while varying the total radius of the slope to investigate the effect this has on the accuracy of g_z found by the prism method. The results of this modelling are shown in fig. 3.16 and figs. 3.16a and 3.16b again show that ignoring the prism closest to the origin significantly reduces the error in the prism method relative to the analytic solution. Figure 3.16a also shows that as slope radius is increased from $10\,\mathrm{m}$ to $200\,\mathrm{m}$, g_z values increase, as expected, but the size of the error between the analytic and prism methods, Δ_g does not vary much. This suggests that most of the error arises from prisms closest to the origin which explains why figs. 3.16b and 3.16c show the percentage error decreasing with increasing radius due to total g_z increasing while error remains relatively fixed (Numerically, the size of the error changes from $\Delta_g = 0.82\,\mu\mathrm{Gal}$ when $R = 10\,\mathrm{m}$ to $\Delta_g = 0.808\,\mu\mathrm{Gal}$ when $R = 200\,\mathrm{m}$).

Now that the error in g_z has been found to be relatively unaffected by the radius of the slope, the effect of varying the slope angle, α, will be investigated with a similar approach, using a fixed element size of $1\,\mathrm{m}^2$ and a slope radius of $40\,\mathrm{m}$. The results of these models are shown in fig. 3.17 for a range of slope angles from 1° to 30° in 1° increments. Figures 3.17c and 3.17d show that when the nearest prism element is ignored in the analysis, the error in

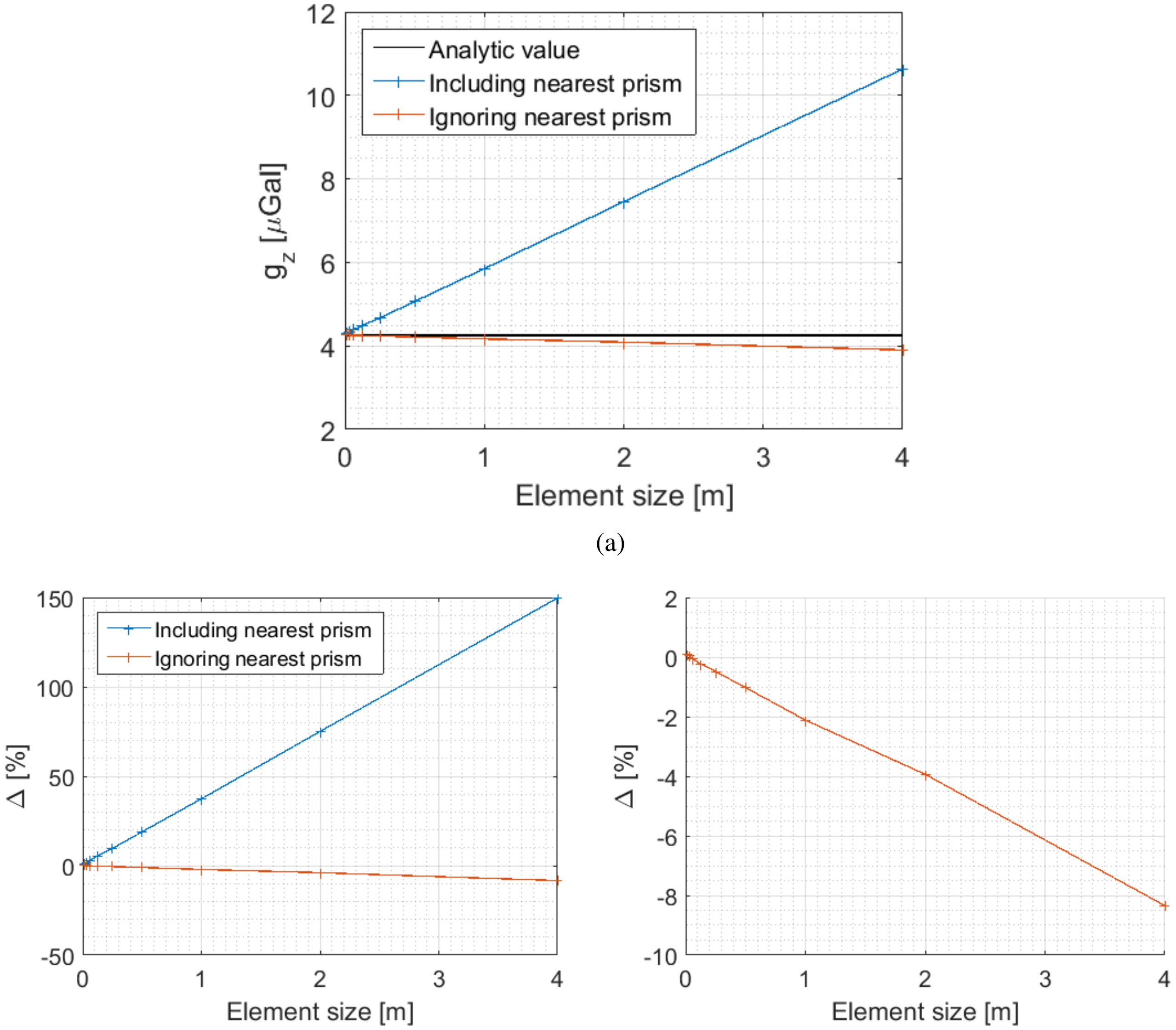

(a)

(b)

(c)

Figure 3.15: (a): Graph showing how varying element size affects g_z calculated using a rectangular prism method for a conic quarter-wedge for which $R = 40\,\text{m}$ and $\alpha = 5°$. (b): Graph of the percentage difference, Δ, between the analytic and the prism method g_z values shown in (a) plotted against element size. (c): Close up of the red line in (b).

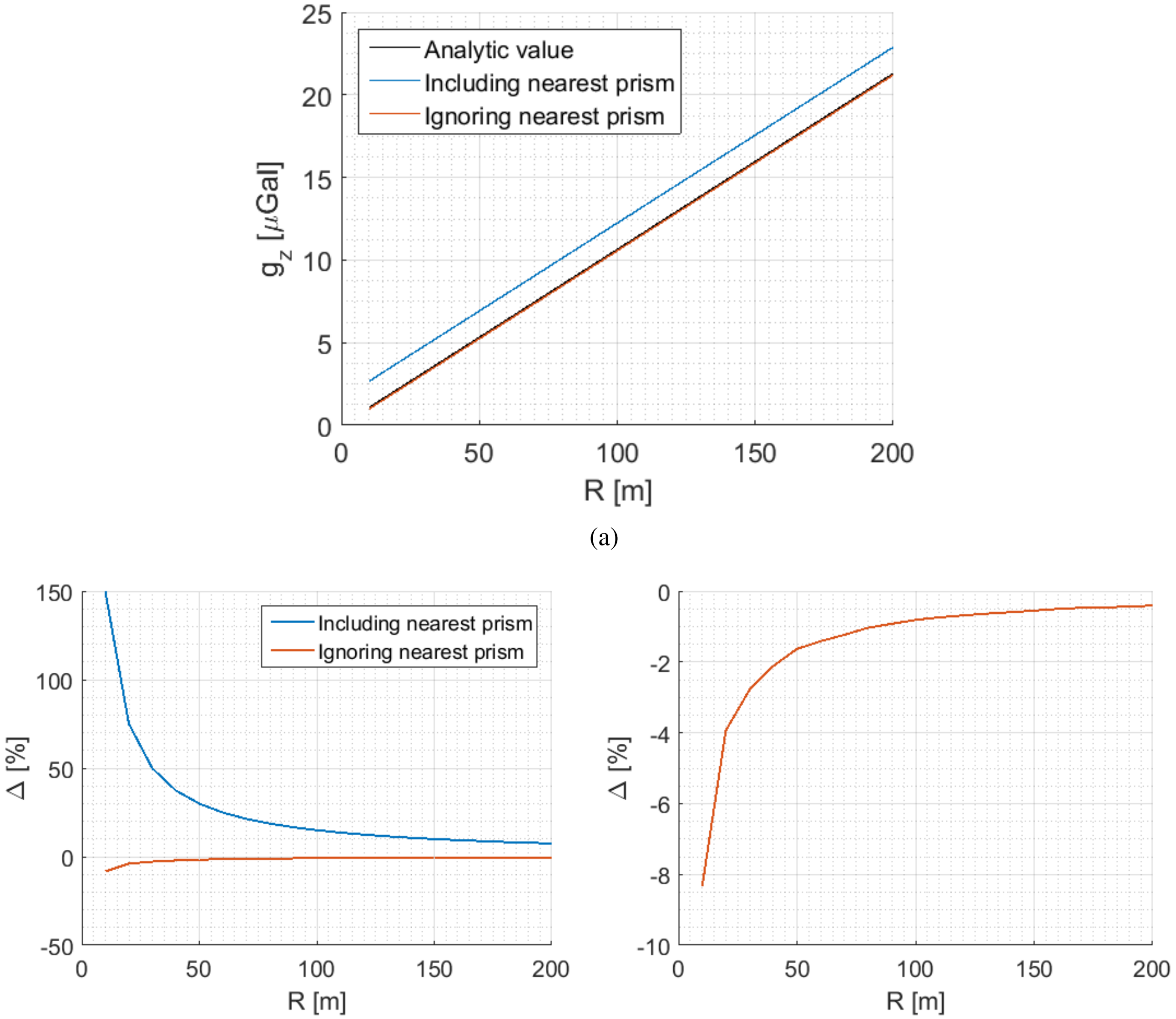

(a)

(b)

(c)

Figure 3.16: (a): Plot showing how varying the radius, R, of the conic slope affects the g_z calculated by the prism method and that found using the analytic solution for cases when the nearest prism is considered and ignored. (b): Plot of percentage difference between g_z found using the prism and analytic methods, Δ, when the innermost element is included or ignored in the prism method of finding g_z. (c): Close-up of the red line in (b).

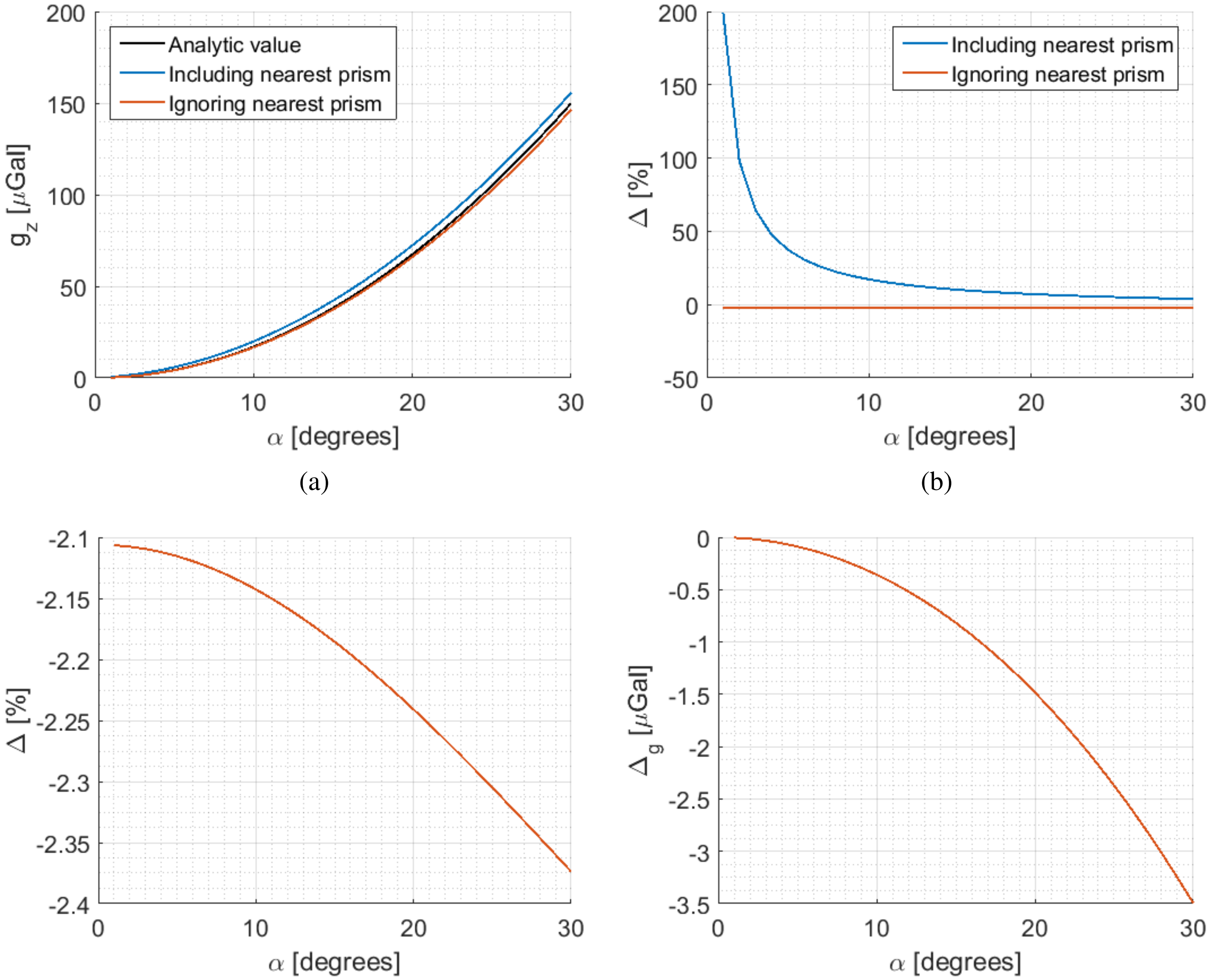

(a) (b)

(c) (d)

Figure 3.17: (a): Plot showing how varying the slope angle, α, the slope shown in fig. 3.13 affects the g_z calculated at it's thinnest point using both the prism method of terrain correction and the analytical solution given by eq. (3.4). The prism method result is given for cases when the prism nearest the computation point is both included and ignored during analysis. (b): Plot of percentage difference, Δ, between g_z found using the prism method and g_z as found by the analytic solution. (c): Plot of the red line in (b) only, in which the nearest prism is ignored when calculating g_z. (d): Plot of the difference between g_z found by the prism method when ignoring the nearest prism and g_z found by the analytic solution.

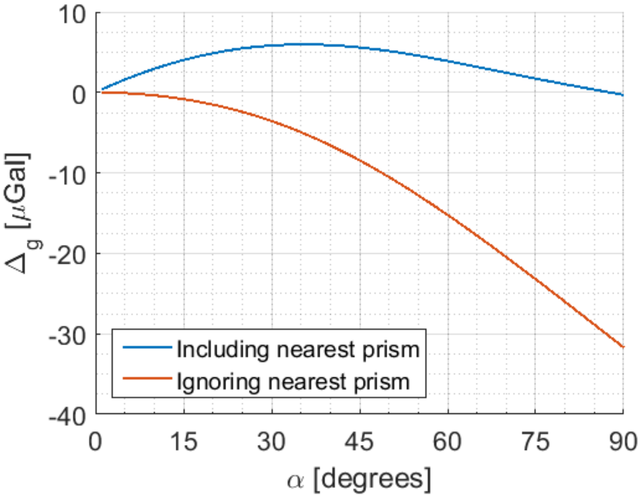

Figure 3.18: Plot showing how the difference, Δ_g, in µGal between g_z calculated analytically and with the prism method, varies with the slope angle of a conic quarter-slope, up to an angle of 90°. Results are shown for cases where the prism method ignores and includes the nearest prism during calculation.

the prism method gets larger as the slope gets steeper. Conversely, it is clear from figs. 3.17a and 3.17b that the opposite behaviour is observed if the nearest prism is not ignored, in which case the accuracy of the prism method improves as the slope angle increases. Figure 3.18 plots how the difference between analytic and prism solutions varies out to a slope angle of 90° and shows that including the nearest prism leads to a more accurate solution at angles greater than approximately 40°. However, it is standard practice when choosing gravitational survey points to avoid locations on a significant slope or excessively close to steep terrain in an attempt to reduce the total magnitude of terrain correction and the size of its associated errors. Because of this, real survey points will rarely be right next to steep terrain features and thus including the nearest prism will, in most real cases, be less accurate than ignoring it when calculating terrain corrections with the flat-topped prism method.

As mentioned before, the error in the prism method, Δ_g, gets larger as the slope angle, α, increases if the nearest prism is ignored, as shown in figs. 3.17c and 3.17d. Because the slope radius, R, has been shown to have a negligible effect on Δ_g and the element size is fixed at $1\,\mathrm{m}^2$ in this work, the predominant factor determining the accuracy of g_z as found by the prism method is α. Because of this, fig. 3.17d can be used to estimate the size of the error (Δ_g) when the prism method is applied to conic quarter-slopes of any radius when using this particular element size. For example, when $\alpha = 5°$, 10°, 20° or 30°, the resulting error is approximately $\Delta_g = 0.1\,\mu\mathrm{Gal}$, $0.4\,\mu\mathrm{Gal}$, $1.5\,\mu\mathrm{Gal}$ and $3.5\,\mu\mathrm{Gal}$, respectively.

Figure 3.17d could be used to estimate the maximum error in the flat-topped prism method when applied to nearby sloping terrain but the total g_z and related Δ_g would be even larger if a full, 360° conic slope were used instead of a quarter-slope, so this will be considered to find an upper estimate of the error. Due to the rotational symmetry of a conic quarter-slope, the g_z

and Δ_g due to a full 360° slope would simply be a factor of four larger than those for a quarter-slope of equivalent α. This means that the same relationship between α and Δ_g as in fig. 3.17d would be observed but with all y-axis values multiplied by four. A full 360° conic slope would result in α values of 5°, 10°, 20° or 30° causing an error in the flat-topped prism method of approximately $\Delta_g = 0.4\,\mu\text{Gal}$, $1.6\,\mu\text{Gal}$, $6\,\mu\text{Gal}$ and $14\,\mu\text{Gal}$, respectively. Since this sort of conical slope in which terrain slopes towards the computation point constantly in all directions will result in the largest g_z and Δ_g for any given slope angle, these results represent the upper limit for the estimated error of the flat-topped prism method of terrain correction.

3.4 Conclusion

High-quality terrain correction calculation is a vital part of collecting sub-mGal accuracy data from gravimetric surveys but contemporary methods of finding terrain correction (such as the Hammer method) are time-consuming and have limited accuracy, particularly when there is significant terrain relief in the first few hundred metres of a survey point. In this work the flat-topped prism method of terrain correction developed by Nagy is applied to terrain at all distances from a survey point out to the standard limit of 166.735 km using three different resolutions of prism analysis divided into an inner, middle and outer zone. This method of terrain correction has traditionally been considered insufficiently accurate to use when analysing inner zone terrain due to limitations in computing power and the lack of accurate, high-resolution topographic data meaning only a low-resolution analysis was possible. This work aims to use modern computing power and $1\,\text{m}^2$-resolution LiDAR elevation data to calculate high-accuracy terrain corrections for both nearby and distant terrain using the Nagy prism method to improve on the speed and accuracy of traditional methods.

The Nagy prism method of terrain correction models terrain around a survey point using an array of vertical, flat-topped rectangular prisms and uses an analytic solution for the vertical component of gravity (g_z) due to such prisms to calculate the terrain correction. Here, MATLAB programs have been written that apply this method to Digital Elevation Models (DEMs) describing topography around a survey point using a prism resolution dictated by the horizontal resolution of the supplied DEM elevation data. This means that DEMs with a higher resolution will be analysed using higher-resolution rectangular prisms (i.e. prisms with a smaller base size) which will lead to a more accurate representation of terrain and calculation of terrain correction. Because of the inverse-square relationship between gravitational field strength and distance, more distant terrain can be analysed using a lower prism resolution without sacrificing accuracy to speed up calculation. To take advantage of this, the terrain correction calculation is split into an analysis of 3 different DEMs describing inner, middle and outer zone terrain around a single survey point and a lower DEM resolution is used to describe more distant zones. The total terrain correction is then found by summing the contributions due to terrain in each zone, out to the chosen limit of 166.735 km from the survey point.

For an example, two survey points, A and B (shown in fig. 3.9), are chosen in the Campsie Fells, north of Glasgow, and the MATLAB programs are used to calculate terrain correction at each. When performing this analysis, the inner zone was defined as a square-shaped 2 km^2 area, centred on the survey point in question and its topography was described using extracts from 1 m^2-resolution LiDAR DEMs of the Campsies region, available from the Scottish Government [146]. The middle zone was a square-shaped 50 km^2 area centred on the survey point and its central 2 km^2 area, already being described by the inner zone, was ignored when finding terrain correction. Suitable 50 m^2-resolution middle zone DEMs were made from freely available 50 m^2-resolution Ordnance Survey contour data of the region [150]. The outer zone was a square 340 km^2 area centred on the survey point and its central 50 km^2 was also ignored as well as terrain beyond a radial distance of 166.735 km from the survey point at the centre. 500 m^2-resolution outer zone DEMs were extracted from the GEBCO grid dataset [153] which describes both topography and bathymetry far from the survey point. The MATLAB programs treat any ground elevation below sea level as being underwater and find terrain correction due to such areas appropriately.

The calculated terrain correction for each survey point was 1.6235 mGal at point A and 2.8585 mGal at point B; believable values for moderately hilly surroundings [62, 147]. On a PC with 8 GB of physical memory and a 3.2 GHz CPU, the program took approximately 9 s to calculate a single terrain correction value from a set of 3 input DEMs. Colour plots were made of the immediately surrounding topography for each survey point and compared to plots of the terrain correction contribution of every corresponding prism in the analysis which show the expected behaviour, where nearby and/or large features causing the largest terrain effects (see fig. 3.10). Similarly predictable behaviour is shown in fig. 3.11 which plots the calculated terrain correction as the outer radius used in the analysis is varied, which also demonstrates the large effect inner zone topography can have on overall terrain correction.

Despite producing believable results, further tests of the MATLAB model were carried out to ensure the Nagy prism method was implemented correctly in the programs written and to estimate their accuracy when used to calculate terrain corrections. For the first of these tests, the MATLAB programs were applied to a hypothetical terrain consisting of a single flat-topped polar segment (shown in fig. 3.12), equivalent to those used in the Hammer method of terrain correction, and the results from the MATLAB prism method were compared to an analytic solution. This showed a discrepancy of just under 1 μGal for a segment close to the computation point, likely caused by imperfect representation of curved faces of the segment by rectangular prism elements. The close agreement between the prism analysis and the analytic solution suggests that the programs written are working as intended and any remaining errors are inherent in the Nagy prism approach to modelling curved or sloping surfaces.

An estimate of the prism terrain correction method's accuracy when applied to inner zone terrain using a 1 m^2 resolution was found by considering simplified sloping topography and comparing the values found by the prism method with an analytic solution. The simplified topographies used for this assume terrain slopes towards the survey point consistently in all directions out to a fixed radius, forming conical slopes for which there is a relatively simple analytic solution for g_z [63]. These shapes were chosen because their combination of slope and radial curvature around the survey point makes them particularly hard to reproduce using flat-topped rectangular prisms which allows an upper estimate of the error in the prism method to be found (since terrain surrounding a real survey point is unlikely to be as challenging for the prism method).

By varying the radius and slope angle of the slope considered, it was found that most of the error in the prism method arises when analysing the nearest 10 metres or so, with the size of this error determined by the slope angle. Given this, a reasonable estimate of error can be found for a certain slope angle as long as the first few tens of metres of terrain are considered (here a radius of 40 m is used). A plot of error against slope angle was made (shown in fig. 3.17d) and used to conclude that the prism method has an error of less than 2 μGal when applied to inner zone terrain with a 10° slope in all directions towards the computation point. This result is used to conclude that for real gravitational survey points, where terrain is likely to be more favourable, the use of 1 m^2 resolution DEMs to find terrain correction as described in this chapter will contribute an additional error of less than 2 μGal to terrain correction calculations; while saving time and effort compared to older techniques.

Chapter 4

Field Surveys with a Scintrex CG-5 Gravimeter

During January of 2020 gravimetric surveys were carried out in and around Glasgow, Scotland using a Scintrex CG-5 relative gravimeter, borrowed from collaborators at INGV (Instituto Nazionale di Geofisica e Vulcanologia, National Institute of Geophysics and Volcanology) Catania, Italy. An outdoor survey was performed in the Campsie Fells, a range of hills 15 km north of Glasgow (in the same area that was considered in section 3.2.2) and another survey was carried out on the University of Glasgow campus in the cloisters of the Gilbert-Scott building (which are beneath part of the building but exposed to outdoor temperatures and winds). The aim of these surveys was to take gravity measurements using a contemporary, commercially-available gravimeter at outdoor locations in both rural and urban environments to use as a comparison when testing MEMS gravimeters in future. This chapter will first give an overview of the Scintrex CG-5 gravimeter and its capabilities and then describe the gravitational surveys carried out and their results.

4.1 The Scintrex CG-5 gravimeter

The Scintrex CG-5 Autograv is a commercially available relative gravimeter released in 2006 that uses a fused quartz spring-balance system to measure changes in local gravitational field strength and its relevant specifications are detailed below, according to the device's operating manual [154]. The CG-5 has a resolution of 1 μGal ($1 \times 10^{-8}\,\mathrm{m\,s^{-2}}$) and can detect changes in gravitational field strength over a range of more than 8 Gal ($0.08\,\mathrm{m\,s^{-2}}$). The device's susceptibility to tares (i.e. offsets in measurement resulting from experiencing external kinetic shocks) is such that tares are usually < 5 μGal for shocks up to 20 N. The device is tilt-sensitive and can be manually levelled using an adjustable tripod that comes with it and built-in tilt sensors that detect its angle off-vertical with an accuracy of ±0.5 arcseconds. Internal data processing software automatically applies gravitational corrections due to changes in tilt during measurement within a range of ±200 arcseconds but the best accuracy is achieved when tilt off vertical is less than ±10 arcseconds, which results in tilt-induced errors of $\sim 0.1\,\mu$Gal [57]. The stiffness of the quartz spring system is temperature-dependent, which can cause changes in proof mass position indistinguishable from gravity changes and so the system is temperature-controlled to within 0.5mK by an internal heating system. Any remaining temperature change of the spring system is monitored and a gravitational temperature correction is automatically applied to the detector's output readings to account for this.

Like all spring-based gravimeters, the CG-5 exhibits a long-term drift in measurements due to elastic relaxation of the spring and also because of ageing of the on-board temperature sensors. Under stable conditions, this drift is approximately linear and, when properly calibrated, the device applies a linear drift correction which reduces the rate of drift to approximately 0.02 mGal per day. Internal software can also provide an Earth tide correction as long as information about the approximate position on the Earth is provided. Finally, the internal software can perform a basic Hammer terrain correction using the method described in section 3.1 desired, though this feature is not used for any of the surveys in this work.

When taking a measurement, the CG-5 records 6 Hz raw data (i.e. 6 measurements per second) which is then averaged and saved as 1 Hz data (by default) for a specified observation time of up to 256 seconds. When complete, the standard deviation σ of all measurements in an observation is saved and can be used to calculate an error in the mean, $E(\mu)$, by assuming the background noise is normally distributed (i.e. Gaussian) and using the relationship

$$E(\mu) = \frac{\sigma}{\sqrt{N}}\,, \tag{4.1}$$

where N is the number of 1 Hz measurements taken during the observation [154]. This assumption is not particularly reliable because the noise in CG-5 measurements is unlikely to be truly normally distributed because of the device's aforementioned linear drift and non-Gaussian external noise sources, such as seismic noise.

4.2 Gravity Survey in the Campsie Fells

The Campsie Fells (or Campsies) are a range of hills in the central lowlands of Scotland, approximately 10 miles north of Glasgow. These hills were selected as the site of an outdoor gravimetry survey using the borrowed Scintrex CG-5 gravimeter because of their proximity to the University of Glasgow and the high-resolution LiDAR elevation data describing the topography of the region.

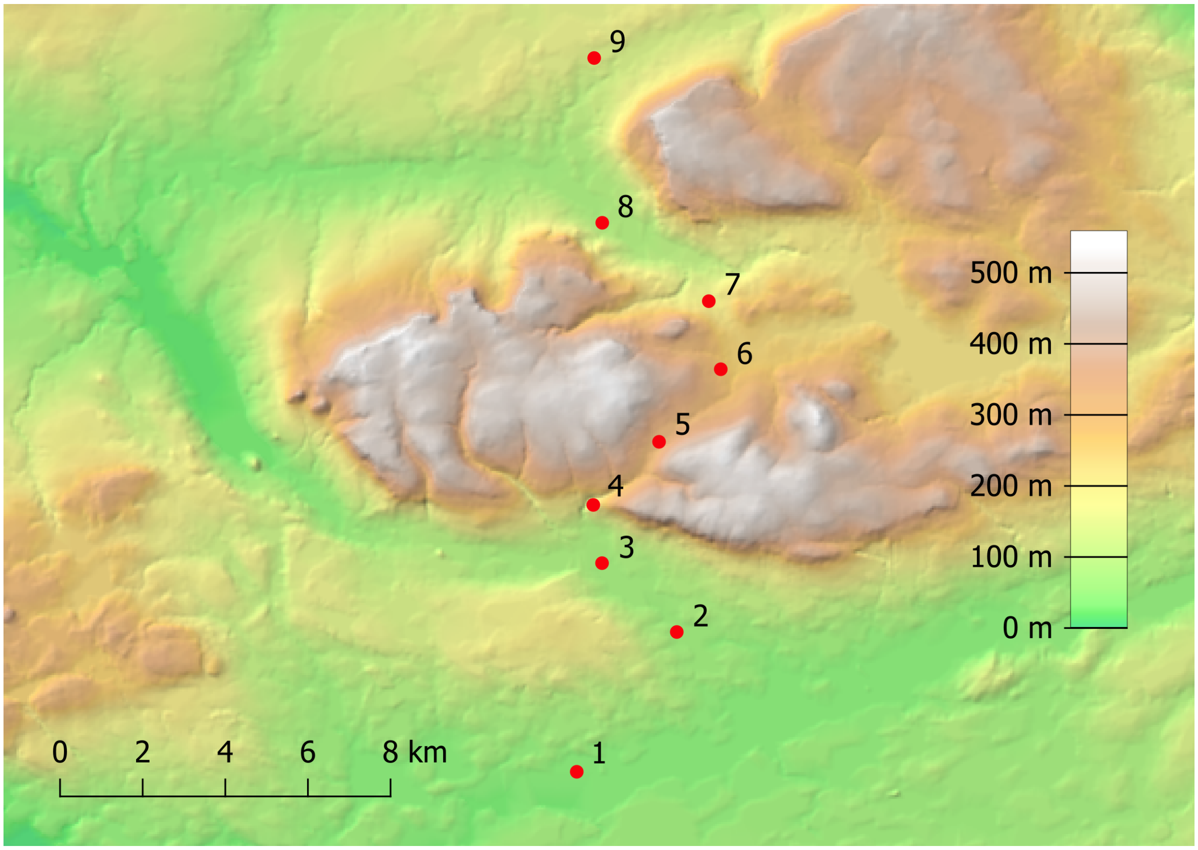

Figure 4.1: 50 m-resolution Digital Elevation Model (DEM) of the Campsie Fells showing the 9 survey points used in a gravimetry survey with the Scintrex CG-5. The contrast of the DEM represents elevation, with the lightest areas corresponding to 570 m above sea level and the darkest, 5 m.

4.2.1 Survey Locations

Before carrying out the survey, a total of 9 locations in the Campsies, pictured in fig. 4.1, were chosen to use as survey points, all lying along the B822 road travelling from the south to north of the hills. These survey points are all in lay-bys or car parks along the road to allow easy access by car and to provide a relatively smooth and flat surface immediately around the gravimeter to reduce errors in terrain correction. This also ensured that the $2\,\mathrm{km} \times 2\,\mathrm{km}$ area around each survey point (the inner zone) was covered by the available LiDAR elevation data to increase the accuracy when calculating terrain corrections later.

When performing the survey, the exact positioning of the gravimeter was decided in-situ to ensure that the first few metres around the detector were as flat as possible, in line with the assumptions made when calculating terrain correction discussed in section 3.1.1. After the survey location was decided, a GPS device was used to record its global coordinates but, due to a hardware failure, this data was later realised to be unusable. This realisation was after the CG-5 had been returned to its owner so a repeat of the survey using a working GPS was not an option. Instead, exact coordinates of the survey points were estimated by reference to aerial photography of the survey locations [155] and the 1 m-resolution LiDAR elevation data describing the nearby topography. Had the GPS worked as intended, elevation above sea level could have been determined with an uncertainty of $\sim 10\,\mathrm{mm}$.

While it would be possible to use aerial photography alone to estimate the coordinates of the survey locations, greater accuracy can be achieved by comparison with the LiDAR data, thanks to its high vertical accuracy (the LiDAR dataset available gives elevation values to centimetre accuracy or better). For example, fig. 4.2 shows an aerial photograph of the car park used as the location for survey point 4 alongside a LiDAR DEM describing the same area. The high vertical accuracy of the LiDAR data allows detailed features of the car park to be identified in the DEM so that the survey point can be located on both maps and the correct elevation above sea level can be extracted from the LIDAR map later. Errors will arise using this method due to the incorrect location of the measurement point on the aerial photos and any mistakes when positioning it on the DEM but it is estimated to be accurate to within 1 m to 3 m. This is not an ideal method of locating the measurement points used during the survey and some errors are expected, though the resulting estimates are likely accurate to within 1 m to 3 m of the real locations.

The elevation above sea level of survey locations was determined using the LiDAR data to the nearest centimetre or millimetre (depending on the vertical accuracy of the data at the point in question) and ranges from roughly 35 m above sea level at point 1 to 328 m at point 5. However, the aforementioned 1 m to 3 m uncertainty when determining the horizontal position of a measurement point could lead to a significant error in the point's elevation if its immediate surroundings are not flat (since the true location could be 1 m to 3 m further along a sloping surface). By looking at the LiDAR DEMs describing the inner zone around each measurement point, it was determined that this elevation error could be as large as $\pm 25\,\mathrm{cm}$ at the least flat

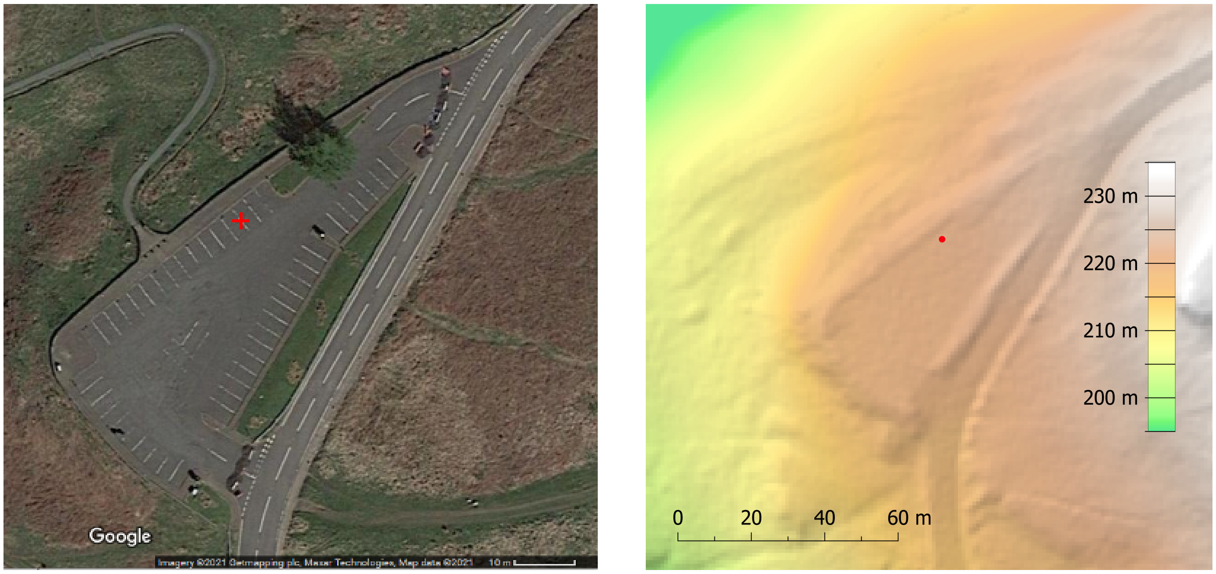

(a)

(b)

Figure 4.2: (a): Aerial photograph of the car park in the Campsie Fells used as point 4 in the Campsies gravimetry survey with the approximate position marked by the red cross (image from google [155]). (b): 1 m-resolution LiDAR DEM of the same area in which the shape and detailed features of the car park (such as the grassy areas) are visible in elevation differences.

measurement points, where the local ground gradient is $\approx 5^\circ$.

At a μGal level of accuracy, vertical gravitational field strength, g_z, varies quickly with elevation because of the combined impact of the free-air, Bouguer and curvature effects, as described in section 1.3.2. The steep vertical gradient of g_z means that an elevation uncertainty of ± 25 cm at a survey point will result in a noticeable g_z uncertainty of about ± 75 μGal (when assuming the average density of rock is $\rho = 2670\,\text{kg}$). Since the size of this error depends on how flat terrain is around a given survey point, separate estimates were made for each survey point, using the relevant LiDAR maps, and are given alongside the results of the survey (denoted as $E(\Delta g_z)$ in table 4.1 later). The size of this uncertainty varied from 15 μGal to 75 μGal at the measurement points used in the survey, making it much larger than the uncertainties associated with calculating the other gravitational corrections (listed in section 1.3.5). Because of this, $E_h(g_z)$ is treated as the dominant source of uncertainty, and uncertainties in the corrections are treated as negligible in comparison.

4.2.2 Survey Technique

When carrying out the gravity survey in the Campsie Fells, the CG-5 was transported by car, strapped to the back seat with a seatbelt. At each survey location, the measurement point was chosen and the CG-5 was positioned on it's tripod and levelled manually to within $10''$ (arcseconds) of vertical, according to its internal tilt sensors. It was then left untouched for 60 seconds to allow the internal spring system to settle and, after this, gravity measurements were recorded for 90 seconds before returning to the car and moving to the next location. As mentioned above, a GPS device was used to record the exact position of each survey point but, due to a technical fault in the GPS device, this data was unusable and position was estimated from satellite photography and LiDAR topography maps of the region instead.

The CG-5 was drift-calibrated before the survey to automatically adjust the measurements to account for linear drift and repeat readings were also taken at points 3 and 5 at the end of the survey to identify any residual drift. The only other time-dependent correction applied to the data was an Earth tide correction, calculated and applied by the CG-5 itself, which resulted in an approximately 25 μGal change over the duration of the survey (about 2.5 hours). The remaining gravitational corrections were calculated for each measurement point after the survey, using the expressions in section 1.3 for the free-air, Bouguer, latitude and curvature corrections. Terrain corrections were calculated using both the hammer method described in section 3.1 and the rectangular prism program described in section 3.1.1 to expand on comparison between the methods in that section. It should be noted that survey points 3 and 5 in this chapter are the same locations as survey points A and B used in section 3.1.1 to demonstrate the terrain correction program. Once all gravitational corrections were calculated, they were combined with the measured g_z as described in section 1.3.2 to find the Bouguer anomaly, a corrected value for Δg_z, which can be used to identify underlying variations in g_z caused by sub-surface density anomalies. As mentioned in the previous section, $E_h(g_\mathrm{z})$ is the g_z uncertainty caused by the uncertainty in determining the elevation of survey points and is assumed to be the dominant source of error, with other uncertainties treated as negligible.

4.2.3 Results

The results of the CG-5 measurements at the 9 survey locations in the Campsie Fells are presented in table 4.1, along with the various gravitational corrections calculated at each point and the elevation of the survey points, h. The estimated error in elevation of each survey point (arising from uncertainty in their horizontal location, as discussed in section 4.2.1) is also given as $E(h)$, and so is the error in Δg_z that this could cause, $E(\Delta g_\mathrm{z})$. For all Campsies measurements, the standard deviation, σ, during each 90 second observation was approximately 100 μGal or less so using eq. (4.1) gives an estimated error in the mean g_z of less than 12 μGal (ignoring any systematic errors in the measurement). Figure 4.3a plots the elevations, h, of the 9 survey points and fig. 4.3b plots the measured and corrected Δg_z values relative to the Δg_z values at point 1. Similar plots showing how the various gravitational corrections change between survey points are presented in figs. 4.4a and 4.4b, with the former showing larger-magnitude corrections (free-air, Bouguer and latitude effects) and the latter showing smaller corrections (terrain and curvature effects).

From fig. 4.4, it is apparent that a substantial part of the measured change in gravitational field strength, Δg_z, during the survey arises due to the combined free-air and Bouguer effects

Survey point	h [m]	$E(h)$ [m]	Δg_{z} [mGal]	$E_h(\Delta g_{\mathrm{z}})^*$ [mGal]	Δg_{fa} [mGal]	Δg_{B} [mGal]	Δg_{λ} [mGal]	Δg_{c} [mGal]	$\Delta g_{\mathrm{tc,h}}$ [mGal]	$\Delta g_{\mathrm{tc,p}}$ [mGal]	$\Delta g_{\mathrm{tot,p}}$ [mGal]
1	38.9825	0.05	0	0.015	0	0	0	0	0	0	0
2	59.0625	0.2	2.311	0.060	-7.431	2.695	2.614	0.035	0.602	0.582	3.817
3	71.13	0.15	0.991	0.045	-11.155	4.045	3.830	0.052	1.281	1.250	2.970
4	221.882	0.25	-28.457	0.075	-57.677	20.913	4.906	0.257	2.713	2.445	0.699
5	328.211	0.1	-44.750	0.030	-90.490	32.811	6.080	0.392	1.396	1.275	5.182
6	284.905	0.1	-27.210	0.030	-77.126	27.966	7.441	0.338	0.697	0.626	13.546
7	195.075	0.15	-12.145	0.045	-49.405	17.914	8.674	0.221	1.168	1.073	9.377
8	81.2325	0.1	0.726	0.030	-14.273	5.175	10.048	0.066	1.847	1.897	-2.188
9	144.6525	0.2	-12.475	0.060	-33.844	12.272	13.049	0.154	0.209	0.212	-4.317

Table 4.1: Results of the relative gravimetry survey in the Campsie Fells. Survey point 1 is chosen as the reference point for the survey and all measured gravity values and calculated corrections are presented as differences relative to those at this point. Here, h is the elevation above sea level of a survey point, $E(h)$ is the estimated error in h, Δg_{z} is the measured difference in g_{z} relative to that at survey point 1, $E_h(\Delta g_{\mathrm{z}})$ is the maximal error in Δg_{z} caused by $E(h)$, Δg_{fa} is the free-air correction, Δg_{B} is the Bouguer correction, Δg_{λ} is the latitude correction, Δg_{c} is the curvature correction, $\Delta g_{\mathrm{tc,h}}$ and $\Delta g_{\mathrm{tc,p}}$ are the terrain correction calculated using the Hammer and prism methods, respectively, and $\Delta g_{\mathrm{tot,p}}$ is the corrected g_{z} found by applying all corrections to the measured data shown in the Δg_{z} column (using only the prism method for terrain correction).

---

[*] This quantity, the error arising due to the uncertainty in survey point elevation, is generally far larger than other measurement errors are expected to be and, therefore, serves as a reasonable approximation for the overall error in the associated measurement.

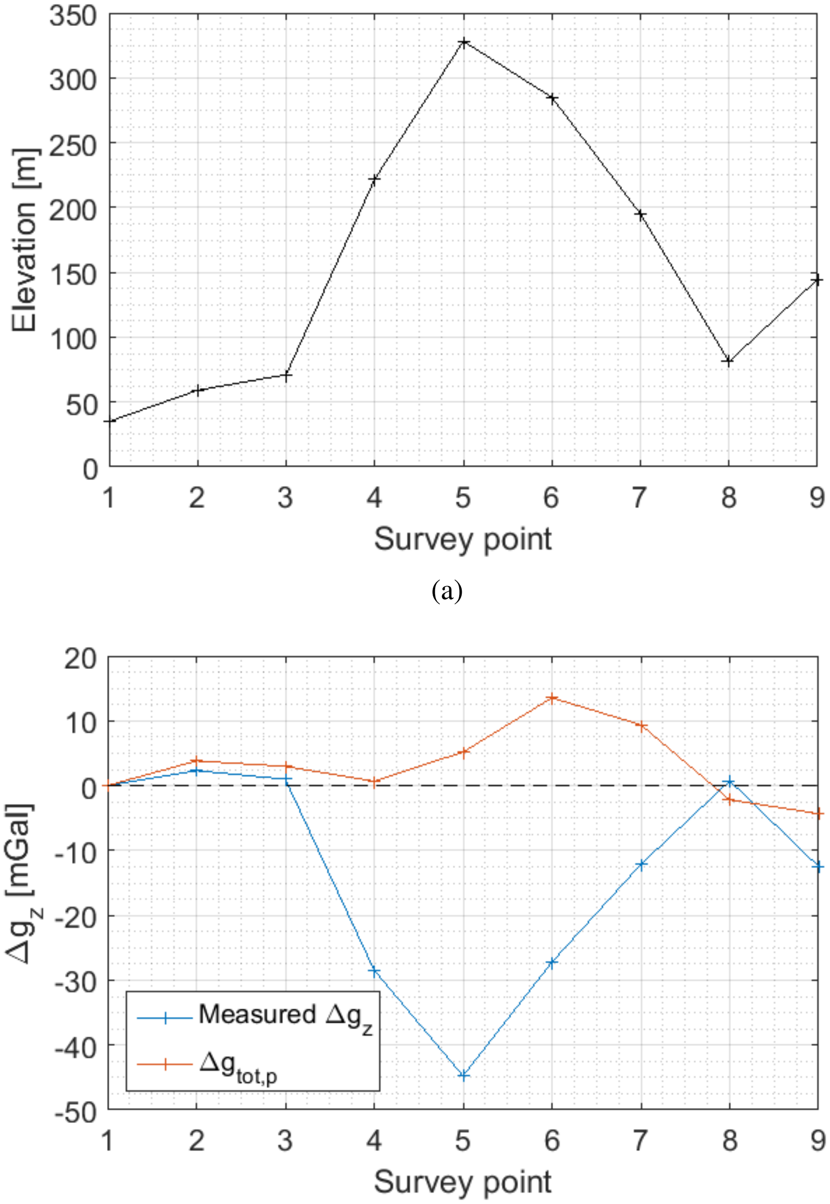

(a)

(b)

Figure 4.3: (a): Graph of elevation above sea level at the 9 survey points used in the Campsies survey. The error in these elevations is not visible on the scale used. (b): Graph of the change in gravity measured with the CG-5 gravimeter and the same data after applying the gravitational corrections described in section 1.3 using the prism method of terrain correction ($g_{\mathrm{tot,p}}$ in table 4.1). The majority of the difference between the measured and corrected Δg_{z} is caused by elevation-dependent effects. Uncertainties in plots (a) and (b) are too small to be visible on the scales used.

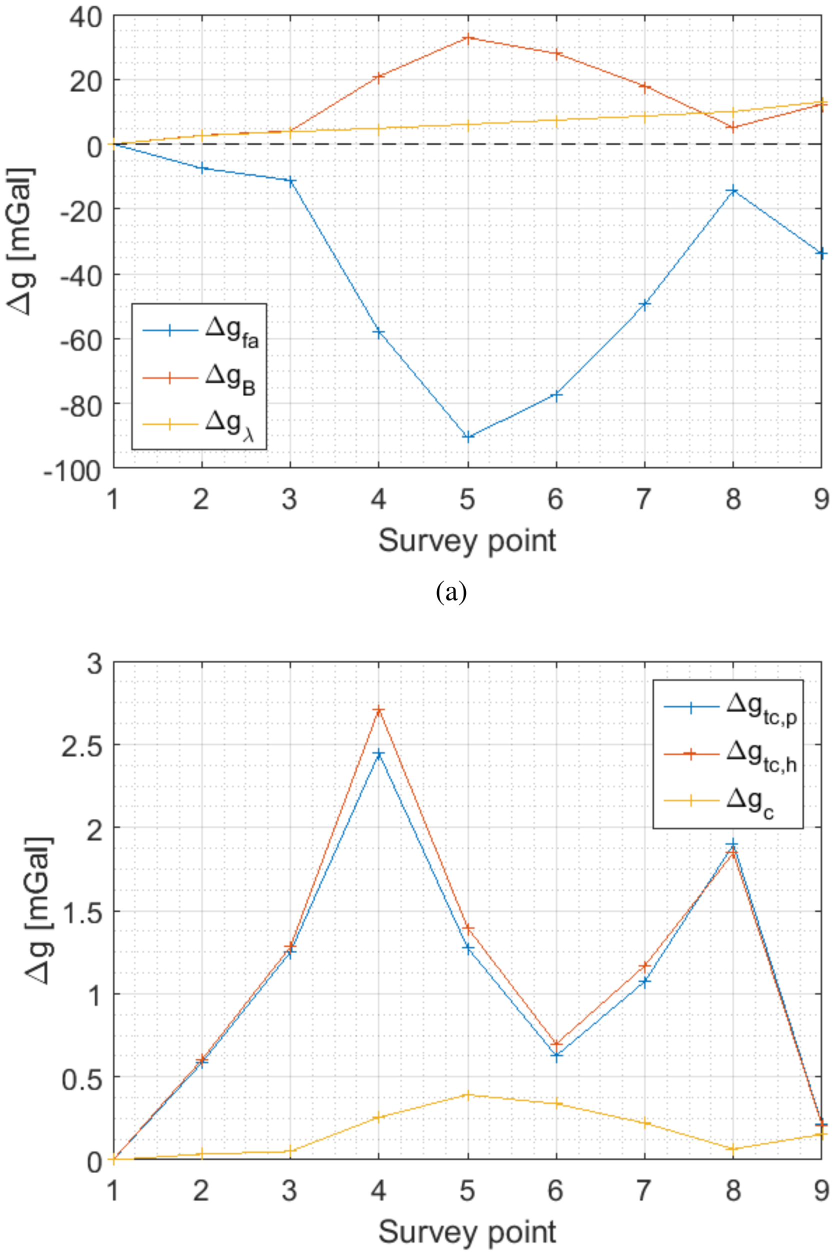

(a)

(b)

Figure 4.4: (a): Calculated change in the free-air correction, Δg_{fa}, Bouguer correction, Δg_{B}, and latitude correction, Δg_{λ}, relative to point 1 for the Campsies survey points. (b): Change in terrain correction calculated using the Hammer method, and the prism method, $\Delta g_{\mathrm{tc,h}}$ and $\Delta g_{\mathrm{tc,p}}$, and change in the curvature correction, Δg_{c}; all relative to point 1. Uncertainties in plots (a) and (b) are too small to be visible on the scales used.

caused by the different elevations of the survey points. The effect of latitude is smaller but still significant, causing a change of over 10 mGal between points 1 and 9 (where point 9 is roughly 17 km north of point 1). The curvature effect, shown in fig. 4.4b, is the smallest of all calculated corrections, due to elevation differences between points not being excessively large, but it is still significant in this survey at a sub-mGal level of accuracy.

As in section 3.3.1, the terrain corrections for the Campsies survey were calculated using both the Hammer and prism-based terrain correction programs described in sections 3.1 and 3.1.1 (note, points 3 and 4 in the Campsies survey are the same as points A and B shown in fig. 3.9). It should be noted that the digitised Hammer method using LiDAR data presented in the terrain chapter is being used for comparison here and that the traditional hammer method is likely to be much less accurate than this due to errors in topographic maps and manual estimation of inner zone elevations. The terrain corrections at each survey point, calculated using both methods, are plotted in fig. 4.4b and are shown to agree quite closely with one another, especially when the surrounding terrain is less rugged and terrain corrections are smaller. Point 8 is notably the only case where the prism method finds a larger value of terrain correction than the Hammer method but this is still thought to still reflect the inaccuracy of the latter method and to be a product of the specific topography surrounding this point (here, surroundings are particularly flat for the first few hundred metres before large hills begin, the gravitational effect of which is probably underestimated in places by the Hammer segment representation). When applying gravitational corrections to the measured Δg_z, terrain correction values calculated with the prism method are used because, as mentioned in section 3.3.1, the prism approach is a higher resolution analysis method and is more accurate, especially when in more rugged surroundings.

Analysing corrected data

In fig. 4.3b the corrected Δg_z at all measurement points is displayed as the red line, calculated by applying all gravitational corrections to the measured data, leaving only the underlying changes in gravity. As described in section 1.3, these remaining gravity anomalies will predominantly be caused by underground variations in density, so can be used to investigate the subterranean rock composition of the region. The most prominent feature in the corrected gravity profile is a peak in Δg_z between survey points 5 and 7, which suggests the presence of higher-density rock in the vicinity of these points. To try and explain this anomaly, a map of the bedrock geology of the Campsies was found to see if there are significant variations in surface rock composition correlated with the location of the anomaly. The map used here is the $1:625\,000$ scale Bedrock Geology UK North map available online [156] from the British Geological Survey (BGS) which is a downscaled version of $1:50\,000$ scale maps [157, 158] compiled from many outcrop samples, excavations and boreholes [159, 160]. The lower resolution $1:625\,000$ scale maps are used here as they are simpler and still provide sufficient information for a comparison between bedrock composition and the measured Δg_z variations in the Campsies survey. An

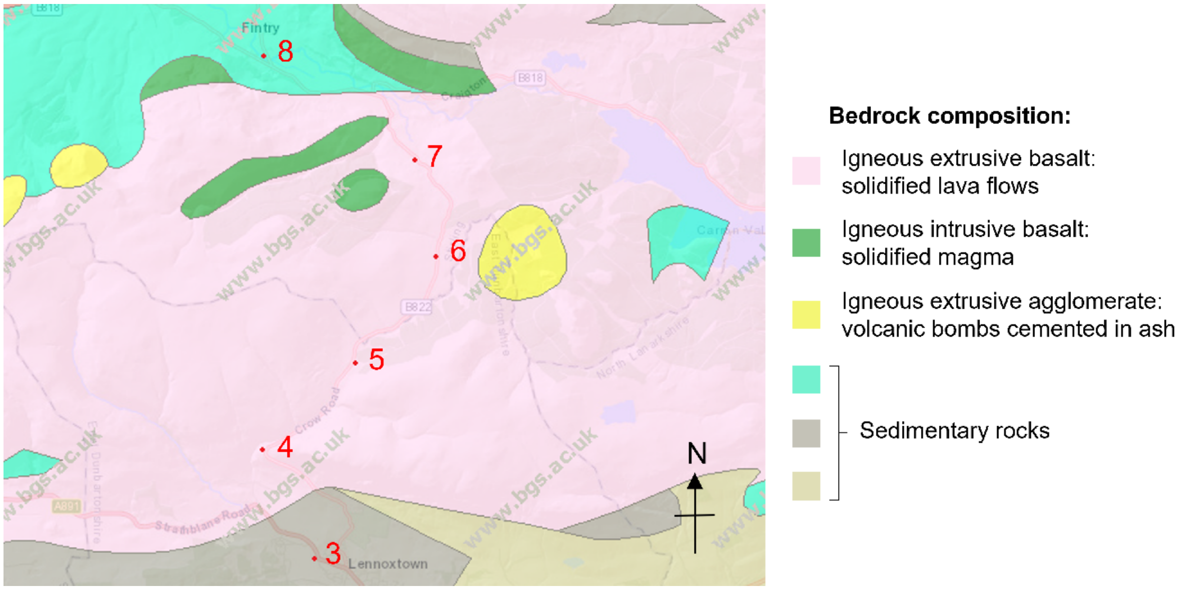

Figure 4.5: Geological bedrock composition map and key showing part of the Campsie Fells around CG-5 survey points 3 to 8 (labelled) [157].

excerpt from the 1 : 625 000 map showing the Campsie Fells is presented in fig. 4.5, with the position of nearby survey points marked, and shows that there are some variations around the location of the anomaly (points 5 to 7) but these are not particularly extensive.

In fig. 4.5, the pink-shaded areas describe regions where the surface layer of bedrock is made of igneous extrusive basalt. A rock is classified as igneous extrusive if it was formed from molten rock which solidified while above the Earth's surface, and the rock type (eg basalt) is determined by its specific mineral composition [161]. Yellow-shaded areas represent areas of agglomerate, another igneous extrusive rock but one formed of compacted volcanic ejecta consisting of rounded volcanic bombs cemented in a matrix of solidified volcanic ash [161]. Agglomerate is commonly found at, or near the site of, past volcanic craters. The dark green areas indicate igneous intrusive rock, formed from molten rock that solidified while beneath the Earth's surface; a slower cooling process that can lead to different physical properties (including density) in comparison to igneous extrusive rocks. The remaining areas indicate sedimentary rock which are formed of compacted particles of other rocks and/or organic materials, cemented together by pressure over time, and which tend to be less dense than igneous rocks [161, 162].

Comparing figure 4.5 with the corrected gz in fig. 4.3b shows that the large gravitational anomaly observed between survey points 5 to 7 does coincide with some variations in bedrock composition around points 6 and 7, but it is unclear whether these variations are the sole cause of the anomaly. The density of each bedrock type shown in fig. 4.5 is not known precisely and rocks of any given type (basalt, for example) can exhibit a wide range of densities, making it difficult to accurately model the gravitational effect of these areas of bedrock. Furthermore, the bedrock map only gives information about the upper surface of the bedrock layer so the structure of density variations deeper than this is not known, and may be a much more significant cause of the observed anomalies.

Further search of the literature found that an earlier gravitational survey of the entire Campsies region was carried out by W. R. Cotton, published in 1969 [163], in which particular attention was paid to the yellow area near point 6 in fig. 4.5, which Cotton names the Waterhead central volcanic complex. This survey was performed using three different relative gravimeters at various points: a Worden ‘Prospector’, which has an accuracy of 10 µGal; a Worden ‘Pioneer’, which has an accuracy of 15 µGal and a Frost gravimeter, which has an accuracy of 20 µGal [57, 163]. It is unclear which device was used when taking observations around the Waterhead area so the gravimeter accuracy for this survey is assumed to be at least that of the Frost gravimeter, 20 µGal. However, as will be discussed later, a significant amount of error is likely to have been introduced into Cotton’s survey during the correction process so the accuracy of his data is likely worse than that of the instruments used.

Cotton’s survey detected a large positive gravity anomaly centred near the Waterhead volcanic complex and a contour map of the measured Bouguer anomaly is presented in fig. 4.6, with nearby measurement points from the more recent CG-5 survey superimposed (survey point 9 is not visible in fig. 4.6, but still lies within the area covered by the full Bouguer anomaly map). Cotton attempted to determine the source of the large anomaly by modelling the gravitational effect of theorised, sub-surface, density variations in the shape of spheres, cylinders and flat-topped cones (frustums). From this, Cotton concluded the cause of the anomaly at Waterhead to be a 8 km × 6 km solidified magma chamber, roughly elliptical in shape (with its long axis oriented northwest-southeast) and extending from 500 m to 6 km below the surface.

A brief comparison will now be made between the results from Cotton’s gravitational survey in 1969 and those from the CG-5 survey, carried out approximately 50 years later. It is important to note that the Cotton survey and the CG-5 survey each use a different zero point for reference when giving relative change in gravitational field and, by coincidence, the zero reference of the older survey seems to match point 2 of the CG-5 survey. To assist comparison of the surveys, fig. 4.7 plots the corrected results from the CG-5 survey using point 2 as the zero reference alongside the g_z values from Cotton’s Bouguer anomaly map at the same locations, shown in fig. 4.6. The data from Cotton’s survey presented in fig. 4.7 was read from the contour map and so is only accurate to the nearest 0.5 mGal.

The old and more recent gravity surveys agree most closely at survey points 1 and 6 where Δg_z values are approximately 500 µGal less in the CG-5 survey than in Cotton’s survey. That both surveys agree relatively well at point 1 (the zero point originally used in the CG-5 survey) and point 6 (near where the peak gravity anomaly is observed in both surveys) is a good confirmation of the presence and approximate magnitude of the large gravity anomaly observed near point 6 in the CG-5 survey. The surveys also agree quite closely at point 9 (not shown in fig. 4.6) where the CG-5 survey observed a Δg_z of -8 µGal and Cotton’s survey measured approximately -7.5 µGal.

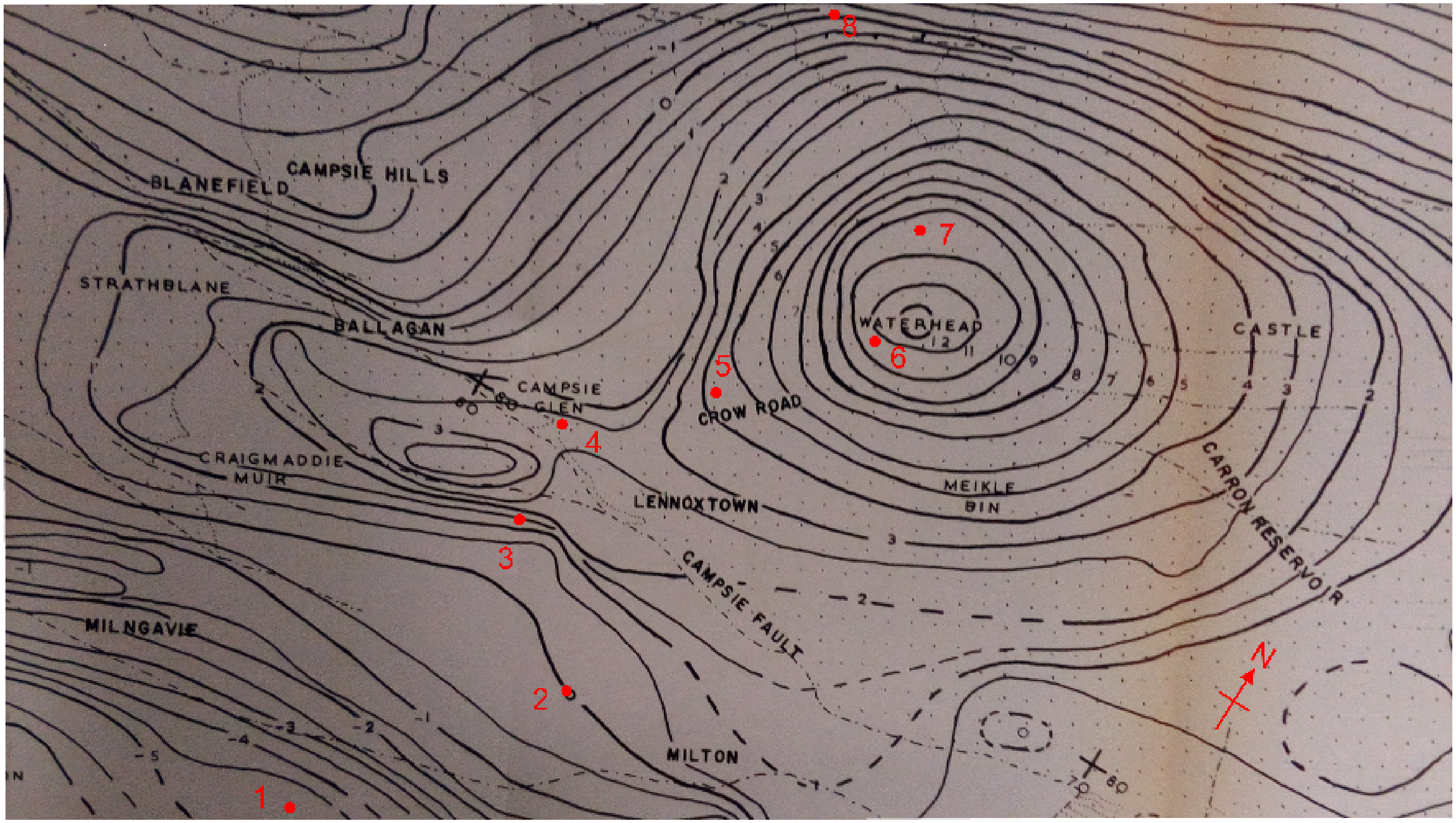

Figure 4.6: Contour map of Bouguer anomaly near the Waterhead volcanic complex compiled by Cotton [163] using 0.5 mGal contour intervals where the anomaly changes are gradual and 1 mGal intervals where they are steep. Survey points 18 used in the CG-5 survey detailed in this work are labelled on the map in red (survey point 9 is beyond the limits of this picture but still within the area covered by the full map [163]).

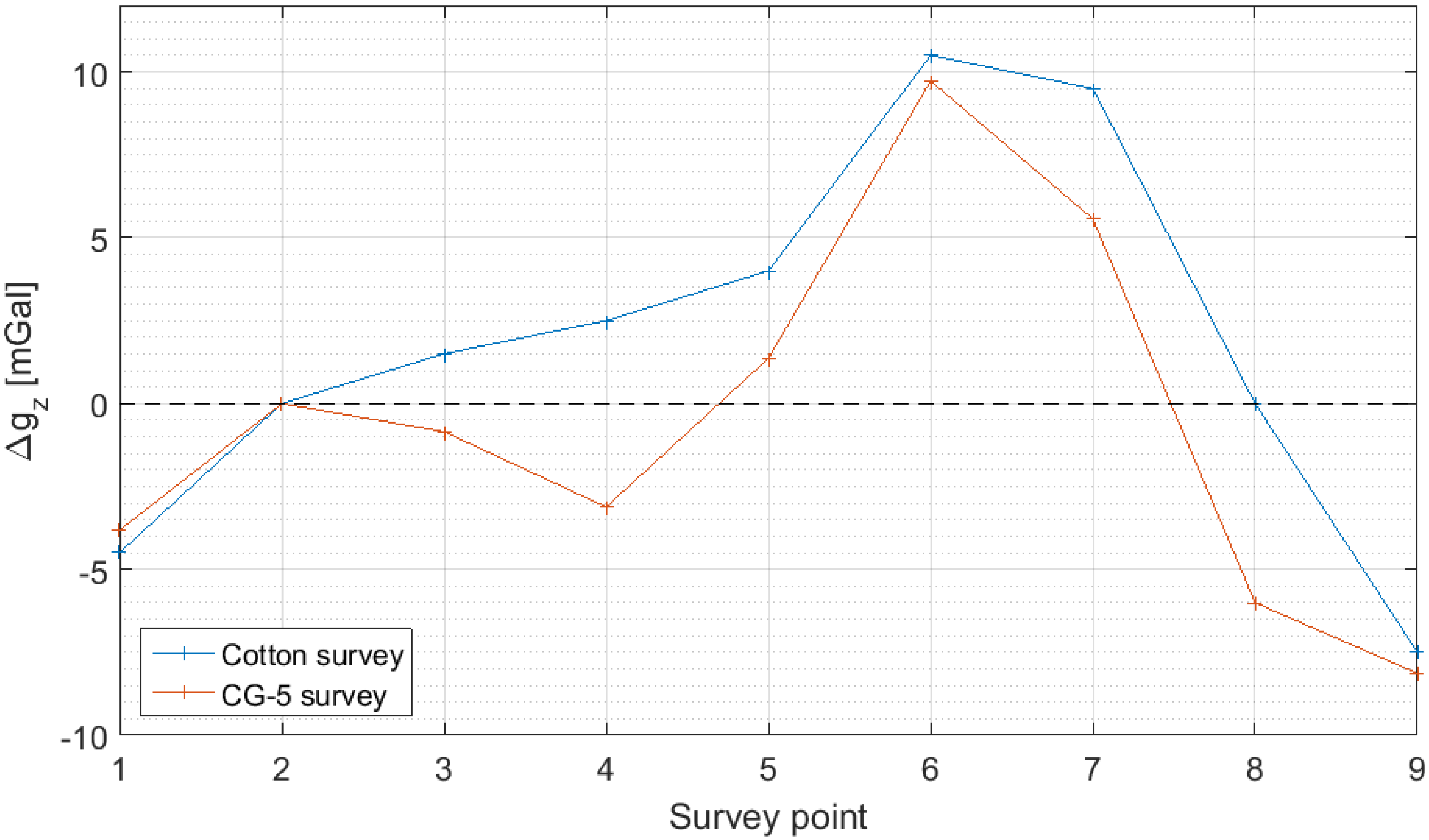

Figure 4.7: Graph of corrected Δg_z from the recent gravity survey in the Campsies adjusted so that Δg_z values are given relative to that a point 2 of the survey. Cotton survey datapoints is read to the nearest 0.5 mGal from the Bouguer anomaly map shown fig. 4.6.

There are larger disagreements between the surveys at all other measurement points and Δg_z values from the CG-5 survey are consistently less than those observed in Cotton's survey. The next closest agreement between the surveys is at point 3, where there is approximately a 1.5 mGal decrease in the newer survey and points 5 and 7 both show a decrease of about 3 mGal. The largest differences between the surveys are seen at points 4 and 8 where the decrease in Δg_z between the new and old survey is 5.5 mGal and 6 mGal, respectively.

These differences are all much larger than the expected error margins of the CG-5 survey as discussed in section 4.2.3 so point to either real changes in Bouguer anomaly in the region over the 50 years since Cotton's survey or errors in the execution of or corrections applied to either survey. The Campsie fells are not a particularly geologically active region so it seems very unlikely that such significant changes in Bouguer anomaly could have happened over the course of just 50 years so the accuracy of Cotton's survey will be scrutinised more closely.

It should be noted that the two largest points of disagreement between the surveys (points 4 and 8) are also the locations where terrain correction is the largest, as seen in fig. 4.4b, and that the surveys agree most closely where terrain correction is the smallest (at points 1, 6 and 9). This suggests that at least part of the disagreement between the surveys is due to inaccuracies in the terrain corrections calculated by Cotton, which is understandable given the method of correction he was using. Cotton used the traditional Hammer method of terrain correction described in section 3.1 which relies heavily on manual estimates of the topographic relief in the immediate surroundings of a survey point and finding average elevations from topographic maps, making it very susceptible to human error. The Hammer method is known to be especially inaccurate in areas of more rugged terrain because of the increased difficulty of accurately estimating distances and elevation changes, even when using surveying equipment, which can lead to errors of up to 3 mGal or more in hilly surroundings [152].

When the Hammer method was calculated in this work from the same elevation data as used in the prism method (producing the $\Delta g_{\mathrm{tc,h}}$ correction shown in table 4.1 and fig. 4.4b), the disagreement between the two methods was ~ 0.26 mGal at most. This is an indication of the inherent inaccuracy of the Hammer method when topography is well known, but the disagreement between Cotton's data and the CG-5 data is far larger than this, suggesting that the remainder of the discrepancy is, indeed, due to his errors when estimating topography. This supports the theory that the discrepancy of several mGal between Cotton's results and those of the CG-5 data is mostly due to errors in his estimates of the topography.

Cotton also only considered terrain out to a radius of roughly 22 km from the measurement point when finding terrain corrections instead of the 166.735 km limit used when correcting the CG-5 survey. This could have a noticeable effect on calculated terrain correction as, even though survey points are quite close together (so the distant terrain is generally similar), the difference in elevation between survey points can significantly affect the terrain correction at each one due to these same distant regions [58, 152]. An example of this is visible in fig. 3.11 which shows that, for survey points 3 and 4 in the Campsies, outer zone topography (25 km to 166.735 km from the survey point) has an effect of over 50 µGal on terrain correction.

Another part of the difference between the old and new surveys may be explained by the fact that Cotton did not consider the curvature correction when analysing his data. As shown by the Δg_c line in fig. 4.4b, this will lead to errors of up to 400 µGal at the measurement points of the CG-5 survey and will be even more significant at higher elevations. Also, the comparison between surveys has a limited accuracy as hand-drawn 0.5 mGal contour diagrams like the one shown in fig. 4.6 are used to read Bouguer anomaly values for Cotton's survey. Cotton does provide more accurate results tables for each survey point in his work [163] but the location of most points is not included and the remaining locations can only be approximated from maps of the same scale as the Bouguer anomaly contour maps.

Because of the aforementioned errors in Cotton's survey, the CG-5 survey is concluded to be a more accurate measure of Bouguer anomaly along the traverse from points 1 to 9 in fig. 4.1, though it consists of far fewer measurement points. This survey could serve as the basis for a re-surveying of the region or as a benchmark when testing future gravimeters, such as the Wee-g described in section 1.4.2.

4.3 Measurements in the cloisters of the Gilbert-Scott building at the University of Glasgow

As well as performing a gravity survey in the Campsie Fells, the borrowed Scintrex CG-5 was used to perform a localised survey of gravity in the cloisters (also called the undercroft) of the Gilbert-Scott building at the University of Glasgow. This location was chosen to complement the Campsies survey by setting a benchmark for gravity measurements in more built-up, urban areas and in buildings, against which the performance of future MEMS gravimeters can be compared.

The cloisters of the Gilbert-Scott building are a roughly 20 m × 30 m, flat, paved area of the ground floor of the building that are open to the outside on both sides but covered overhead by the rest of the building, above vaulted ceilings shown in fig. 4.8. This was a convenient space to perform a gravitational survey thanks to its large, flat floor and due to its proximity to the University of Glasgow physics department, where the CG-5 was being kept.

4.3.1 Survey technique

Gravity measurements were taken at 75 points in the cloisters, arranged in the 9×11 grid of positions shown in fig. 4.9 excepting grid nodes obstructed by columns (which are shown as the shaded areas in fig. 4.9). For reference, measurement points on the grid are split into lines and stations to indicate east-west and north-south position respectively, resulting in 9 lines and 11

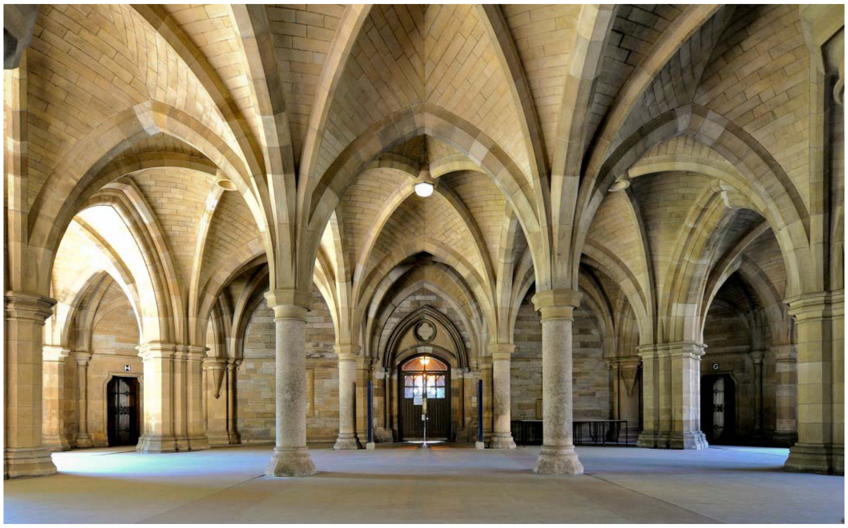

Figure 4.8: Photo looking south in the cloisters of the Gilbert-Scott building at the University of Glasgow Gilmorehill campus showing several columns and the vaulted ceilings (photo from University of Glasgow website [164]).

stations as labelled. The dimensions of the cloisters and positions of all measurement points were recorded after the survey using a tape measure to find the distance between the points and the surrounding walls and pillars. With this method, the position of the points is found to an estimated accuracy of $\pm 2\,\mathrm{cm}$

When taking measurements, the CG-5 was positioned as close as possible to the desired survey point by estimating it's location relative to the surrounding columns and walls. This was made easier by the survey points being in line with and/or equidistant from the surrounding columns and further assisted by the arrangement of paving slabs on the floor in some cases. An example of this is visible in fig. 4.10 in which the CG-5 is shown recording measurements in the cloisters at the line 4, station 2 location indicated in fig. 4.9.

Due to the large number of points, the survey was conducted over the course of several days and repeat measurements were used to account for any day-to-day variation in gravity (due to changes in atmospheric pressure and groundwater levels) and combine data from different days into a single dataset. At the start and end of each survey session, measurements were taken at the line 1, station 2 point and all other gravity values from that session are adjusted to be relative to this measurement. The measurement taken at the line 1, station 2 point at the end of each survey session was used to remove residual linear drift in the detector over the duration of the session.

The CG-5 was transported to the cloisters on foot (a 5-minute walk), set on its tripod and levelled, and left stationary for 5 minutes before beginning the survey to improve noise performance by allowing the spring system time to settle (as suggested by Seigel [12]). To reduce anthropogenic noise from passing pedestrians, all measurements were taken in the evenings after 6pm, when the building was less busy. In the case that a measurement was disturbed by

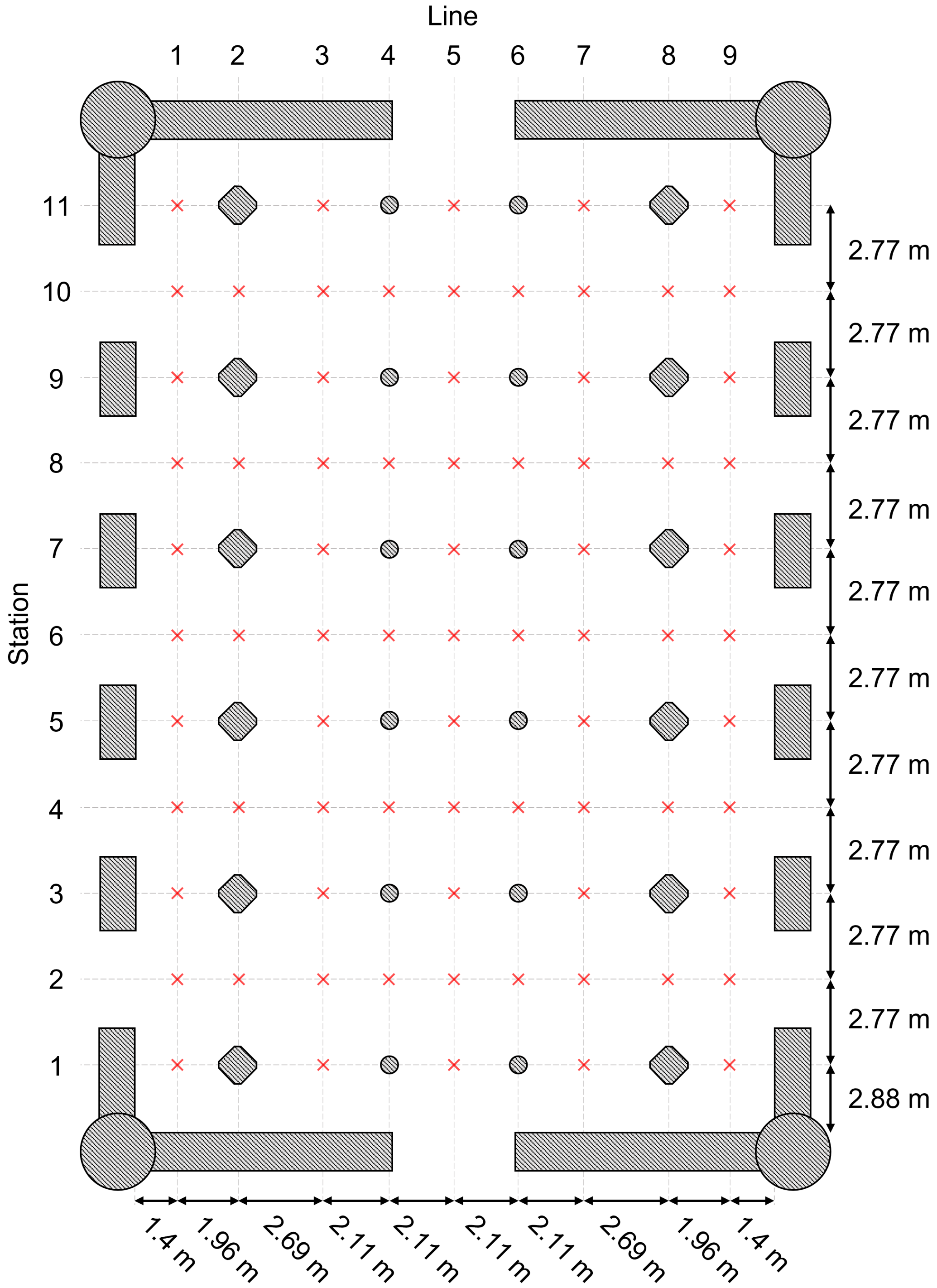

Figure 4.9: Schematic of the cloisters of the Gilbert-Scott building at the University of Glasgow where a gravity survey was performed (not to scale). The 75 measurement points used in the survey are labelled with red crosses.

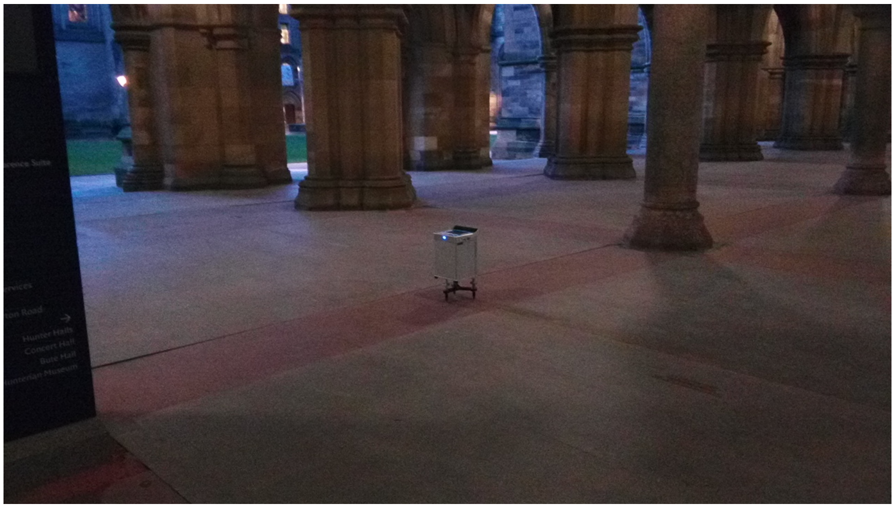

Figure 4.10: Photo of the CG-5 gravimeter taking data in the cloisters of the Gilbert-Scott building at the University of Glasgow. The detector is positioned at line 4, station 2 on the map in fig. 4.9.

someone walking past the device, the measurement was retaken. When moving between measurement points in the cloisters, the CG-5 was left to settle at the new position for 30 seconds before each measurement and then recorded data for 90 seconds. An integration time of between 120 to 150 seconds has been suggested in the literature to maximise the CG-5's sensitivity [165] but the shorter time of 90 seconds was used here to speed up collecting data, on account of the large number of survey points. After each measurement, the tilt of the device was checked and if it had moved past $\pm 10''$ of vertical while recording data, the measurement was repeated.

Most gravitational corrections described in section 1.3 and used in the Campsies survey were not applied to the cloisters data because of the small survey area and small elevation changes involved. This means there will be little variation in terrain or elevation corrections between survey points and any underlying effects are likely to show as a constant gradient in the data, so any localised gravity anomalies will still be observable. The only corrections applied were those performed internally by the CG-5 itself, namely Earth tide, tilt and temperature corrections.

4.3.2 Results

The results from the cloisters gravity survey are presented in fig. 4.11 as a 0.02 mGal-interval contour plot of Δg_z (relative to the line 1, station 2 point). This contour plot uses a spline interpolation to estimate Δg_z values in-between survey points and the location of columns in the measurement area are indicated by transparent grey shapes.

The data shows variations in Δg_z of more than $\pm 100\,\mu$Gal in the survey area over relatively short distances which suggests that the observed effects are caused by some combination of the surrounding building and underground density variations. Of these two effects, it is more likely that the latter are the main cause of the observed Δg_z features because the above-ground structure of the cloisters is quite symmetrical around the surveyed area and there is no obvious symmetry in the observed gravity data. No further attempt is made in this work to model the gravitational effect of the surrounding building due to time limitations and the complexity of the surrounding architecture.

To investigate the presence of underfloor density variations further, copies of the original building plans of the Gilbert-Scott building were obtained from the University of Glasgow library and relevant excerpts from these are reproduced in fig. 4.12. These plans show air ducts running beneath the floor of the cloisters that are approximately $2\,\mathrm{m} \times 2\,\mathrm{m}$ in profile, judging from the cross-section in fig. 4.12b. If accurate, this would mean that all survey points around the edges of the cloisters and through the centre (all points on lines 1, 5 and 9 and stations 1 and 11) lie above or very close to sizeable cavities that will reduce Δg_z at these points. Since the reference point for the survey (line 2 station 1) is itself above an air duct, points not above ducts ought to see a positive relative gravity anomaly, Δg_z, and those above air ducts should see the same or a similar Δg_z (assuming that the air ducts shown in fig. 4.12a are the dominant source of g_z variations). However, this behaviour is not seen consistently in the results shown in fig. 4.11. For example, Δg_z is larger in line 2 than line 1 for all stations, as expected but there is significant variation in Δg_z between different stations on the same lines (even when excluding interpolated data where columns are present) which are not explained by the layout of the planned air ducts. Similar behaviour is observed at line 5 where Δg_z is close to zero at some stations but not others and lines 8 and 9 even show the opposite behaviour expected, where g_z above an air duct is greater than that over solid ground in some places (station 10, lines 8 and 9, for example).

To more directly examine the effect of the underfloor air ducts shown in fig. 4.12, a simulation of the expected gravitational effect was made by representing the underfloor ducts with rectangular prisms of suitable size and density and using the Nagy prism method described in section 3.1.1 to calculate the resulting g_z. The dimensions of the air ducts were read from the to-scale building plans shown in fig. 4.12* and a model of the ducts was constructed, consisting of 5 rectangular prisms labelled A to E, arranged as shown in fig. 4.13a. Along their shorter side, prisms A,B,D and E each have an extent of 1.8 m and prism C has an extent of 1.37 m, while along their longer side, prisms A and E each have an extent of 19.94 m and prisms B,C and D have an extent of 29.26 m. In the vertical direction, the prism extents were approximated to a rectangular cross-section using fig. 4.12b as a reference (ignoring the non-flat upper and lower faces shown) and the upper and lower faces of all prisms were chosen to be at $-0.44\,\mathrm{m}$ and $-1.94\,\mathrm{m}$, respectively. The results of this simulation are presented in fig. 4.13b, showing how the calculated g_z varies in the same area surveyed during the CG-5 measurement, which is also indicated by the dotted red line in fig. 4.13a. Comparison between fig. 4.13b and fig. 4.11 shows little agreement between the simulated gravity field and the survey data, with the latter

---

[*] The full plans, too large to present in fig. 4.12, include scale bars, allowing the dimensions of the air ducts to be identified.

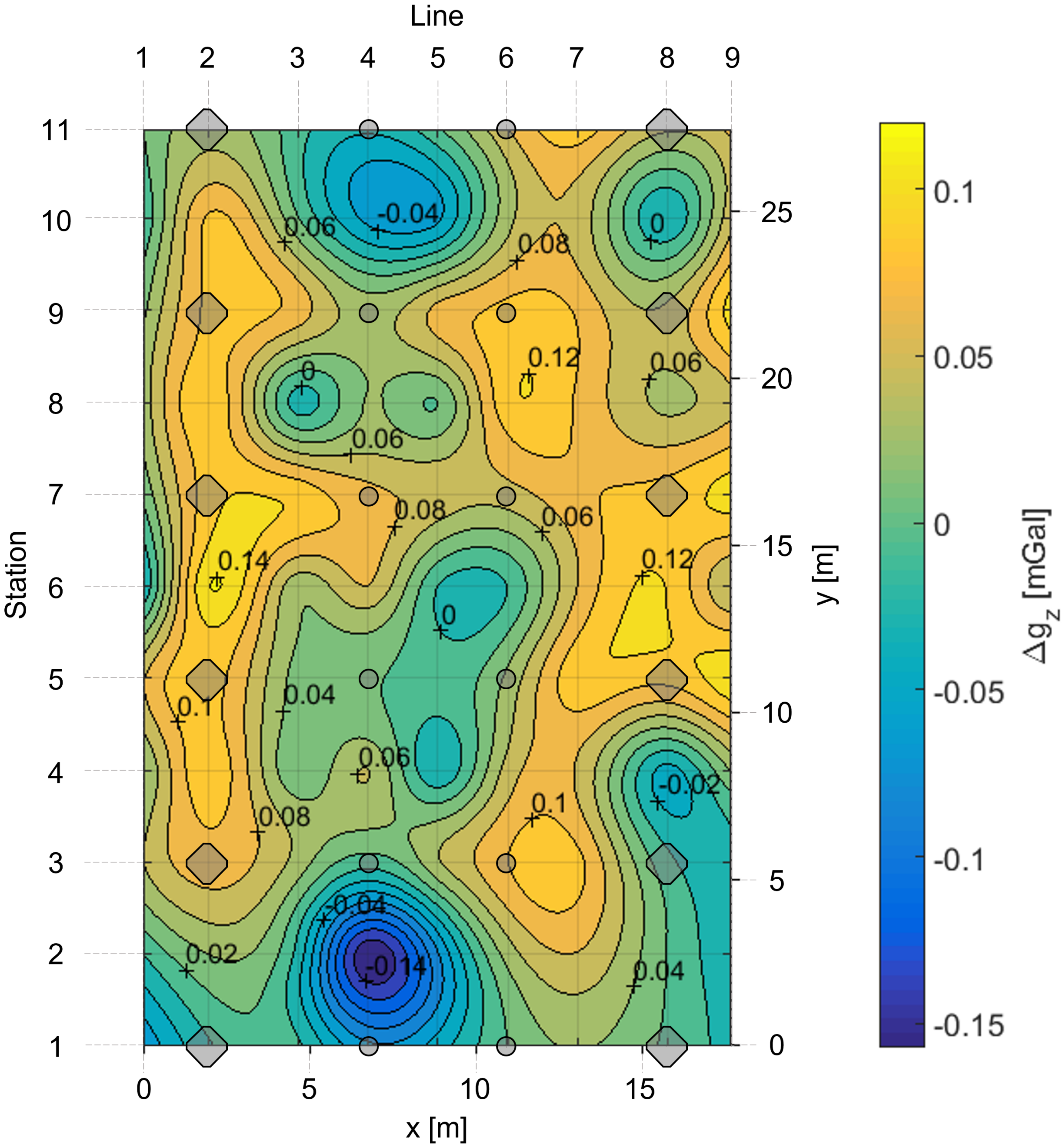

Figure 4.11: Contour plot of measured gravity anomaly in the cloisters of the Gilbert-Scott building at the University of Glasgow. Δg_z values are relative to that measured at the line 1, station 2 point and the contour interval is 0.02 mGal. Structural stone columns of the building in the measurement area are shown as transparent grey objects.

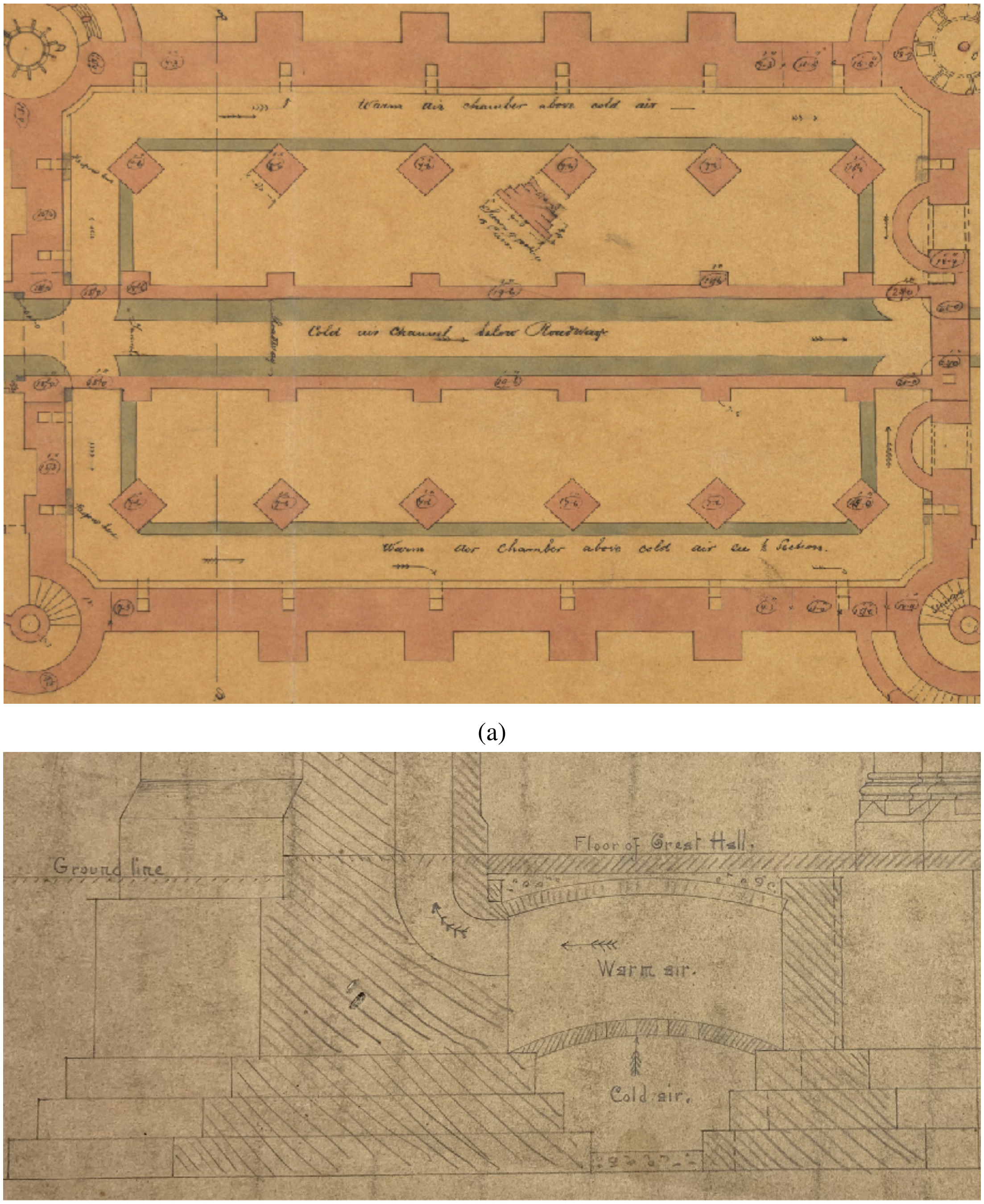

(a)

(b)

Figure 4.12: (a): Building plans of the cloisters of the Gilbert-Scott building at the University of Glasgow showing underfloor air ducts around the edge and through the centre of the floor as labelled. (b): Cross-section plan of the air duct running along one of the edges of the cloisters.

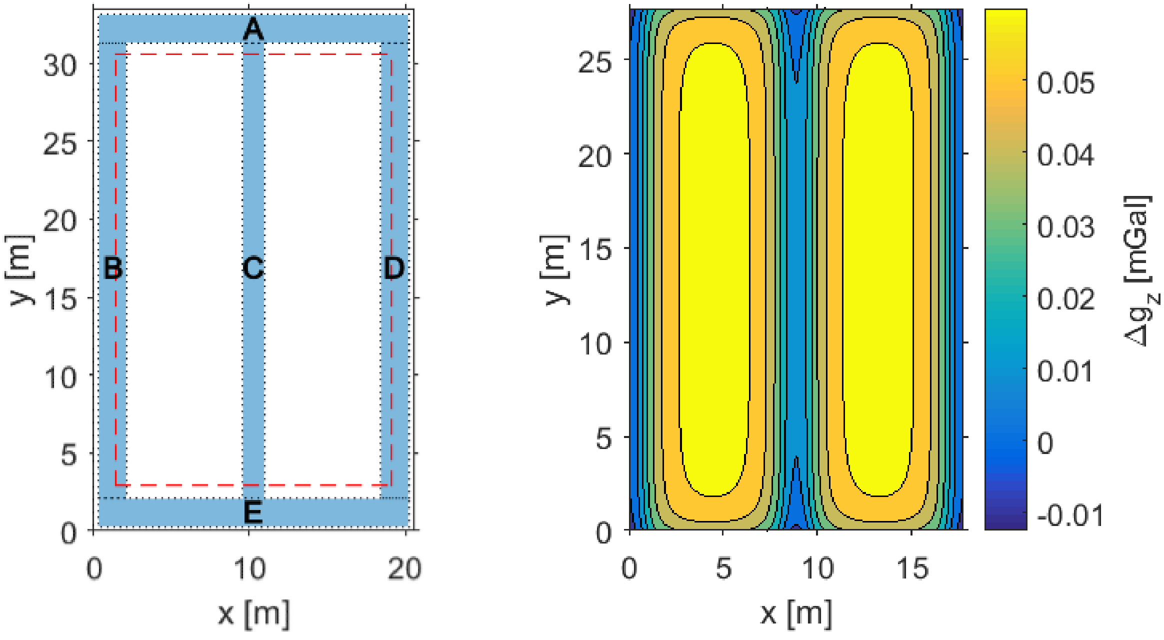

(a) (b)

Figure 4.13: (a): Cloisters layout with ducts, red rectangle shows extent of survey area (b): Simulated gz due to the ducts

showing g_z variations tens of μGal larger than the features in the simulated data with little spatial correlation.

Disagreements between the observed gravity anomalies and the simulated gravity field of the air ducts could be explained by inaccuracies in the plans themselves, which are over 140 years old and likely only describe the intention of what was to be made and are not a detailed, as-built description of the building. It is plausible that the ducts may have been partially filled in (with stone or other heavy material) during or after the original construction, which could explain why evidence of the ducts' presence is only seen in places in fig. 4.11. Also, there may be additional underground structures or density variations not described in the building plans that may have a significant effect, or the impact of the above-ground building structure could have a larger and less-symmetrical effect on gravity than originally thought. Finally, there may be errors in the measured gravity data, arising either internally in the detector or externally through vibrational noise or systematic errors that have distorted the results of the survey in places.

Systematic errors are known to occur occasionally when using spring-based gravimeters where the spring system does not return to the same level after being moved or struck, resulting in an offset or tare in the data [12]. The detector was not exposed to any large physical shocks during the cloisters measurements and no extreme tares are obvious from the repeat measurements carried out to quantify linear drift during the surveys. Despite this, it is possible that there are tares in the data that occurred when the detector was being repositioned and that these contributed to the unexpected results in fig. 4.11, when compared to the air duct plans.

Since carrying out the CG-5 survey, colleagues of the author have attempted to repeat measurement of the large anomaly in the cloisters while testing prototypes of the Wee-g MEMS gravimeter described in section 1.4.2. However, the cloisters were found to be too noisy of an environment to take accurate measurements in, thought to be because of ground motion from pedestrian traffic. The prototype sensor used for this had previously shown much better performance when in less busy indoor and other outdoor locations and the cloisters have since been discounted as a location for further gravimetric testing. It is still unclear whether the results of the CG-5 survey showed little evidence of the ducts due to unconsidered underground density variations or environmental noise in the cloisters.

4.4 Conclusion

A Gravitational survey was carried out along a roughly South-North traverse of the Campsie Fells (a range of hills 10 miles north of Glasgow, Scotland) using a Scintrex CG-5 gravimeter, the results of which are compared with a previous survey of the entire Campsie region performed by W. Cotton in 1969 [163]. The present survey consists of far fewer data points but uses a modern relative gravimeter (the CG-5) and a more accurate process of gravitational correction when analysing the results; including correction for the Earth's curvature and consideration of terrain corrections out to 166.735 km using the LiDAR/rectangular prism method described in chapter 3. The results of the CG-5 survey are directly compared to 0.5 mGal contour plots from the 1969 survey and show general agreement in describing a large gravity anomaly around a geological feature in the region referred to as the Waterhead volcanic complex by Cotton. There is some disagreement between the surveys on the exact magnitude and position of the anomaly which is attributed primarily to the less-accurate gravitational correction procedure used in the earlier survey. Specifically, Cotton used the Hammer method of terrain and relied on manual, in-situ, estimates of the topography immediately surrounding survey points which can lead to errors of 3 mGal or more when in moderately hilly surroundings, as in this case. Cotton also ignored curvature correction and only analysed terrain out to a distance of 22 km when finding terrain correction.

The accuracy of the CG-5 survey is limited to $\pm 75\,\mu\text{Gal}$ by uncertainty in the elevation of survey points arising because of a failure in the GPS equipment used during the survey, which could be rectified in future by repeating the survey using a working GPS system. Additional surveys are suggested to expand on the coverage of the single South-North traverse performed here to re-map the entirety of the Waterhead gravity anomaly using modern measurement and correction procedures. In Cotton's survey, gravitational modelling was used to infer the cause of the anomaly to be an $8\,\text{km} \times 6\,\text{km}$ solidified magma chamber extending from 500 m to 6 km below the surface and more accurate gravity data would allow this conclusion to be tested. Finally, repeat surveys in the near future will likely be performed with MEMS gravimeters developed at the University of Glasgow and the survey presented here can act as a benchmark to compare these devices against to test their performance.

A second gravity survey using the CG-5 was conducted in the cloisters of the Gilbert-Scott building at the University of Glasgow Gilmorehill campus to see if this would also be a suitable location for tests of future MEMS gravimeters. Gravity measurements were taken at a grid of 75 positions in the cloisters (where not obstructed by columns) and a 20 µGal-interval contour plot was made showing the results (see fig. 4.11). Because the survey took place in a confined and mostly flat area, most of the gravitational corrections described in section 1.3 are not applied to the collected data as they are likely to be insignificant in comparison to local changes in gravitational field (the only corrections applied were a tide correction and drift correction). Gravity anomalies with a range of 260 µGal were detected during the survey and background vibrational noise in the area was found to be fairly low when surveys were performed in the evenings (after 6pm).

To try and determine the cause of the observed gravity anomalies in the cloisters, plans of the Gilbert-Scott building were obtained (shown in fig. 4.12) which show that sizeable air ducts run underneath parts of the area surveyed. A basic simulation of the gravitational effect these ducts would cause was made by representing them as rectangular prisms and using the Nagy analytic solution presented in chapter 2. The results of this simulation (shown in fig. 4.13) show little correlation with the results of the CG-5 survey, which suggests either errors or noise in the gravity data collected or some inaccuracy or incompleteness of the plans obtained (which is plausible as they are over 140 years old). No consideration was given to the gravitational effect that the surrounding building's structure could have which could partly explain some of the observed anomalies and this is left to future work.

Since carrying out this survey, colleagues of the author have attempted further gravity measurements in the cloisters using prototype Wee-g devices but these have all found the area difficult to take accurate measurements in due to high environmental noise, thought to be due to ground motion from pedestrian traffic. Future measurements with Wee-g devices are planned to be carried out elsewhere.

Chapter 5

Conclusion

This work is broadly concerned with the modelling of gravitational fields that the currently in-development Wee-g MEMS gravimeter may be used to detect in future, in order to investigate the devices potential usefulness and/or to assist with the future data processing of results. The first chapter gives an introduction to gravity, gravimetry and the Wee-g MEMS gravimeter and the following chapters describe the modelling of gravitational fields of submarines, an improved method of calculating gravitational terrain corrections for terrestrial gravimetry, and a gravitational survey performed locally using a borrowed Scintrex CG-5 gravimeter. This chapter will give a brief summary of the work done in each of these 3 chapters as well as suggestions for future work on each.

5.1 Modelling submarine gravity

A finite element analysis (FEA) approach was used to simulate the gravitational field at a point or array of points as a submarine-approximating object moved past in a straight line to simulate submarine detection by single gravimeters or gravimeter arrays. The structure and density distribution of a real submarine is complicated so a simplified length-varying density was assigned to a cylinder of appropriate size (approximately 100 m long with a 10 m diameter) to make an approximation of a submarine. The linear density profile chosen for the cylinder was chosen such that the cylinder has a neutral buoyancy in seawater overall but is more dense halfway along its length and less dense either side of this, representing a heavy engine and air filled buoyancy tanks allowing it to maintain depth (detail of the density profile used is not given for security reasons at the request of QinetiQ, an industrial partner to this part of work). The FEA used to find the gravitational field due to the cylinder was programmed using MATLAB and divides the object into many cylindrical polar volume elements and calculates g due to each individual element using a point mass approximation, assuming all of an elements mass is located at its centre of mass. This method's accuracy was tested by applying it to a uniform-density cylinder and comparing the calculated gravitational field to an analytic solution for such an object (developed by Na *et al.* [117]) which show good agreement with each other, provided the cylinder is not too close to the computation point (where the analytic solution is not accurate) and sufficient elements are used in the FEA.

The MATLAB model was then used to calculate the gravitational field strength, g, at a single point or array of positions as the submarine-like density moved past to simulate the gravitational signal at a gravimeter or array trying to detect it. In these simulations, the submarine density moved in a straight-line path some distance above the detector/array and detectors were assumed to be sensitive in one direction only, parallel to the z-axis, like the Wee-g mems gravimeter. Simulations were repeated using submarine trajectories at varying distances above the detector/array and plots of g_z as a function of time at single detectors were made as well as animated surface plots showing g_z at all detectors in an array during the submarine's motion. These plots were used to estimate the maximum detection range of a similarly sized submarine by the Wee-g gravimeter to be approximately 20 m; determined by comparing the size of the peak g_z signal with the $5\,\mu\mathrm{Gal}/\sqrt{\mathrm{Hz}}$ noise floor of a Wee-g prototype, determined from measurements taken in 2023. This suggests that the Wee-g could be useful for the short-range detection of submarines in shallow waters around coasts or near ports and use of detector arrays could extend sensor coverage over a larger area.

Matched filtering was also investigated as a way to increase the predicted 20 m detection range of Wee-g gravimeter, through improved extraction of a submarine gravity signal from a noise-corrupted measurement. To do this, synthetic noisy submarine signals were generated by combining simulated submarine gravity signals with real Wee-g sensor noise data and then matched filtering was used to try and recover the injected signal. In the case of a simulated signal for a submarine travelling at a range of 30 m and speed $5\,\mathrm{m\,s^{-1}}$ corrupted with approximately $5\,\mu\mathrm{Gal}/\sqrt{\mathrm{Hz}}$ sensor noise, the matched filter was able to boost SNR enough that the signal (with a peak amplitude of 2.8 μGal) became clearly visible in the filter output. This was demonstrated on two different synthetic noisy signals, one 10 minutes long and the other 30 minutes long and in both cases the filtering increased SNR significantly and the 30 m-range submarine signal became clearly identifiable, indicating that the detection range had increased by 10 m.

The results of this work can be concluded as a preliminary validation that the Wee-g gravimeter could have applications in the short-range detection of submarines up to 30 m away. It should be kept in mind, however, that these results are predicated on the Wee-g being able to achieve comparable detector performance deployed underwater (In a watertight container) as on land, and on the assumptions about submarine density variations are sensible assumptions.

Future work

The biggest source of inaccuracy in the submarine gravity models presented in this work is likely to be due to the submarine density model used, which is only a very basic approximation of the density variations inside a real submarine. More accurate simulations could be developed that consider a cylindrical object with a more sophisticated linear density profile and/or with radial variations in density as well, to improve realism and better simulate gravitational field. Different density models could also be made that model the gravitational fields around submarines of different sizes and internal layouts to investigate how this affects detection range.

The modelling of sensor arrays demonstrated that they would allow additional information to be gathered about a detected submarine such as its speed, direction of travel and the azimuth to the submarine from the array but extracting this information from array data would require sophisticated data analysis methods. There may be some degree of crossover between the signal processing required for gravitational arrays and already existing methods (eg. for radar/sonar arrays) but there may be unique challenges associated with the nature of the gravitational field that could be addressed by further investigation. Future work could also investigate how gravimeter arrays should be designed for a given purpose, such as monitoring a river mouth or port entrance, and consider the specific signal processing that would be required for a given array layout.

The use of gravimeter arrays could also allow the overall sensitivity of the array to be increased past that of a single sensor by correlating measurements from different sensors in the array using machine learning methods similar to those developed for use in gravitational wave astronomy [135]. These methods can be used to extract a transient signal from background noise, providing that the shape of the signal is already known beforehand, improving the signal to noise ratio and potential detection range. Submarine gravity simulations like those made in this work could be used to make the large amounts of example data required to ‘train’ such machine learning algorithms and, if submarines with different density profiles are simulated, could potentially allow the identification of known types of submarine from their observed gravity profile.

5.2 Modelling gravitational terrain corrections using high-resolution LiDAR elevation data

Accurate gravitational terrain correction is the most complicated correction that must be applied to gravity survey data to extract useful information and traditional methods of calculating it are inaccurate and time-consuming. This work has demonstrated that by using high-resolution LiDAR elevation data, inner zone terrain corrections (i.e. analysis of terrain within the first kilometre or so of a measurement point) can be calculated in a matter of seconds and to a higher degree of accuracy than earlier methods (such as the Hammer method). This is achieved using MATLAB programs that apply the Nagy flat-topped prism method of terrain correction to terrain around a survey point out to the standard limit of 166.735 km in 3 stages, considering an inner, middle and outer zone of terrain, each using an appropriate resolution of analysis.

The terrain correction program is applied to 2 example locations in the Campsie Fells, north of Glasgow, where topography is described using digital elevation models (DEMs) with resolutions of $1\,\mathrm{m}^2$ for the inner zone (0 km to 1 km from the survey point), $50\,\mathrm{m}^2$ for the middle zone (1 km to 25 km from the survey point) and $500\,\mathrm{m}^2$ for the outer zone (25 km to 170 km from the survey point). The terrain corrections calculated for these two locations are 1.6235 mGal and 2.8585 mGal, believable values for moderately hilly surroundings, and were calculated in $\sim 9\,\mathrm{s}$ each on a PC with a 3.2 GHz processor and 8 GB of RAM.

The accuracy of the terrain correction program was tested by applying it to geometrically simple terrain surfaces and comparing its results to those found using suitable analytic solutions for the simple topography considered. This approach was used to confirm that the Nagy prism method used in the program was implemented correctly by applying it to a single 'Hammer segment', a flat-topped, cylindrical polar volume element of terrain of specified height, used in the traditional Hammer method of terrain correction. The terrain correction calculated by the MATLAB program was compared to the analytic solution for a Hammer segment and a close agreement was observed, suggesting that the Nagy prism method used in the program is working as intended.

Simple sloping topographies were also considered to test the program's accuracy when analysing inclined terrain very close to the survey point, since this is where the $1\,\mathrm{m}^2$ resolution Nagy flat-topped prism approach used in the program is least accurate. The topography used in these tests sloped towards the survey point uniformly in all directions out to a given radius, forming a conical depression (or hill, equivalently). This shape was chosen because it maximises the potential error arising when applying the prism method (because of the slope in all directions) and terrain correction can be calculated using a simple analytic expression for a conically sloping quarter-wedge. These tests found that the accuracy of the Nagy prism method was improved by ignoring the 4 prisms adjacent to the survey point in the prism representation and found that most of the remaining error is primarily determined by the slope angle. The relationship between error in the Nagy prism method and the slope angle used was calculated and plotted for a full conical slope of various angles and determined to be below than $2\,\mu\mathrm{Gal}$ when slope angle is $> 10°$. This is taken as a reasonable upper estimate of the accuracy of the MATLAB program when applied to inner zone terrain around real survey points, where terrain is unlikely to slope away in all directions at such a steep angle.

Future work

This work attempts to overcome the limited accuracy of the Nagy rectangular prism representation of terrain by using $1\,\mathrm{m}^2$ resolution elevation data and an equally high-resolution prism analysis but some inaccuracy still remains. The accuracy of the MATLAB program presented could be improved by simply increasing the resolution of the elevation data and analysis used but improvements could also be made by moving beyond the flat-topped rectangular prism model of topography used in the Nagy method. Analytic solutions for g_z due to rectangular, triangular and n-sided prisms with sloping tops have been published in the literature and could be used to more accurately represent surrounding topography and calculate terrain corrections in future programs. These analytic solutions are more complicated than that for regular, flat-topped, Nagy prisms so it may be more efficient to only use this sort of analysis when considering terrain extremely close to the survey point (perhaps defining a new ‘inner-inner’ zone).

5.3 Field surveys with a Scintrex CG-5 gravimeter

Two outdoor gravity surveys were performed using a Scintrex CG-5 relative gravimeter borrowed from collaborators at INGV Catania with the aim of establishing benchmark measurements that future MEMS gravimeters developed at the University of Glasgow can be tested against. The first of these surveys was performed in the Campsie Fells (hills north of Glasgow) and consists of 9 survey points along a road passing some of the most rugged terrain in the area along an approximately south-to-north traverse. The survey was carried out in a single day, transporting the CG-5 by car and the standard gravitational corrections described in section 1.3 were applied to the data afterwards to determine the change in Bouguer anomaly between measurement points. During this process, the terrain corrections were found using the high-resolution Nagy prism method described in section 3.1.1 with topographic information from the same sources as described in section 3.1.2.

After applying gravitational corrections, the Bouguer anomaly data observed in the CG-5 survey was compared to a Bouguer anomaly contour plot of the same region from a 1969 survey by W. Cotton to assess whether the results are believable. Both surveys show general agreement on the overall shape of the Bouguer anomaly across the 9 survey points used in the CG-5 survey and both identify a particularly large anomaly around a geological feature Cotton refers to as the Waterhead volcanic complex. There is a varying degree of disagreement between the two surveys, ranging from 0.5 mGal to 6 mGal which is attributed to the less accurate terrain correction method used in Cotton’s survey.

The accuracy of the CG-5 survey is limited by an uncertainty in the elevation of each survey point arising due to a failure in the GPS system used. Because of this, the exact position of the gravimeter at each survey point had to be estimated from aerial photographs of the survey locations [155] and the corresponding elevation of these points was found from the LiDAR DEMs used when finding terrain correction. This process resulted in an estimated uncertainty in survey point elevation of up to ±25 cm (depending on the steepness of surrounding terrain), which causes a potential error in Bouguer anomaly of up to ±75 μGal when applying elevation-dependent gravitational corrections.

The second gravitational survey was carried out on the University of Glasgow campus, in the cloisters of the Gilbert-Scott building; a roughly 25 m × 35 m paved flat area on the ground floor, open to the outdoors on two sides while still being mostly sheltered from wind and rain by the rest of the building. Measurements were taken with the CG-5 at a grid of 75 survey points (shown in fig. 4.9) over the course of 3 days, using repeat measurements of the same positions to tie together surveys from separate days. Most gravitational corrections described in section 1.3 were not applied to the results of this survey because of the flat nature and small size of the survey area (only a tide correction and drift correction were applied to the results).

The results of the survey are displayed in a coloured contour plot fig. 4.11 and show variations in gravity greater than $\pm 120\,\mu\text{Gal}$ in places which were thought to be caused by a combination of underground density variations and the gravitational effects of the surrounding building's structure. Plans of the building were obtained that show a series of air ducts beneath the floor of the cloisters but only sporadic correlation is apparent between the underfloor layout and the observed gravitational field, suggesting either errors in the survey or inaccuracies in the plans (which are over 140 years old). A model of the gravitational field expected to be caused by the ducts was made and showed little correlation with the survey results which gravitational field variations with a larger amplitude than the predicted duct signals. From this it is concluded that the detection of the ducts was not successful, due either to environmental noise during the survey or inaccuracies in the building plans.

Future work

Additional gravity surveys in the Campsie Fells could be performed to test the accuracy of the findings of the survey carried out in this work and to more comprehensively map the large anomaly observed in the region by Cotton's survey. Such measurements would be a good way to demonstrate the practical in-the-field capabilities of future Wee-g MEMS devices or other portable gravimeters. Further mapping of the large gravity anomaly associated with the Waterhead volcanic complex seen by Cotton could also allow a more accurate determination of the characteristics of this geological feature.

Further gravity surveys in the cloisters of the Gilbert-Scott building at the University of Glasgow could be attempted to investigate whether the results of the original survey are dominated by environmental noise (as they appear to be) or not. Also, future work could look at modelling the gravitational effect of the building above and around the cloisters survey area to determine the impact that this had on the measurement.

Appendix A

Programs to simulate gravity of a passing submarine

This appendix contains copies of the MATLAB scripts described in section 2.2.3 to simulate the gravitational field of a submarine passing a single gravimeter or gravimeter array.

‘single_detector_g_field.m’

```
% - This calculates g and its components at a gravimeter as a ...
    submarine-like cylinder moves past.
%   The cylinder has a length-varying density described by ...
    'density_plot.xls'.
%   The function "cylinder_elements.m" finds the centre of mass of ...
    cylindrical polar elements describing the cylinder when at its ...
    starting location and the function "cylinder_g.m" moves these along ...
    the specified trajectory while calculating g and its components at ...
    the origin.

%% defining inputs and outputs
% ===Inputs===

G = 6.67e-11; % gravitational constant

%% details of the cylindrical density and the 4 trajectories
% cylinder specifications
l = 100; % cylinder length in metres
R = 5; % cross-sectional radius
Th = pi/2; % angle between central axis of cylinder and z-axis
Ph = 0; % angle in x-y plane between central axis of cylinder and +ve x-axis

```

```
% starting point of cylinder's centre
x0 = -200;
y0 = 0;
z0 = 20;

% details of the cylinder's motion
di = 400; % distance moved in x-direction
ni = 400; % number of steps in the movement
s = di/ni; % step size
t = s/5; % time taken for each step assuming the submarine has a speed ...
    of 5 m/s

%% describing locations of cylinder elements for a vertical cylinder ...
    centred at (x0,y0,z0)
nr = 30; % number of radial elements
nt = 30; % number of angular elements
nl = 100; % number of length elements

% ===Outputs===
% vectors describing how gravity varies at the origin during the motion:
% gxtot - x-component of gravitational field
% gytot - y-component of gravitational field
% gztot - z-component of gravitational field
% gtot -- magnitude of total gravitational field


%% making cylinder
% finding locations of cylinder elements for a cylinder centred at the ...
    origin with the specified location and orientation:
[x,y,z,v,P] = cylinder_elements(l,R,Th,Ph,x0,y0,z0,nr,nt,nl); % see ...
    'cylinder_elements.m'


%% moving the cylinder and calculating gravity at the origin at each step

% function that finds g at the (i,j,k) detector when the cylindrical ...
    density moves past:
[gtot,gxtot,gytot,gztot] = cylinder_g(ni,s,x,y,z,v,P); % see 'cylinder_g.m'

% converting g values to microGal
g = gtot * 100e6;
gx = gxtot * 100e6;
gy = gytot * 100e6;
gz = gztot * 100e6;
```

‘multiple_detector_g_field.m’

```
% - This model calculates g at a gravimeter array when a cylinder with ...
    linear density distribution 'P' moves past.
%   The gravimeter array is a cubic arrangement of equidistant detectors ...
    collectively centred on the origin.
%   This script uses "cylinder_elements.m" to generate the ...
    submarine-like density and "cylinder_g.m" to move the cylinder and ...
    find the resulting g.

%% defining inputs and outputs
% ===Inputs===
G = 6.67e-11; % gravitational constant

%% describing the array of detectors
a = 8; % separation of detectors
nx = 10; % number of detectors in x-direction
ny = 10; % number of detectors in y-direction
nz = 1; % number of detectors in z-direction

% coordinates of detectors
ax = (-(nx-1)*a/2):a:((nx-1)*a/2);
ay = (-(ny-1)*a/2):a:((ny-1)*a/2);
az = (-(nz-1)*a/2):a:((nz-1)*a/2);

%% details of the cylindrical density and its trajectory
l = 100; % length in metres
R = 5; % cross-sectional radius
Th = pi/2; % angle between central axis of cylinder and z-axis
Ph = 0; % azimuth of central axis of cylinder relative to +ve x-axis

% starting point of cylinder's centre
x0 = -200;
y0 = 10;
z0 = 10;

% details of the cylinder's motion
di = 400; % distance moved in x-direction
ni = 400; % number of steps in the movement - Note changing this affects ...
    how the x-axis is labelled, best results at 400
s = di/ni; % step size
t = s/5; % time taken for each step assuming the submarine has a speed ...
    of 5 m/s

%% describing locations of cylinder elements for a vertical cylinder ...
```

```
    centred at (x0,y0,z0)
nr = 30; % number of radial elements
nt = 30; % number of angular elements
nl = 100; % number of length elements

% ===Outputs===
% cell arrays containing vectors of gravitational field for each ...
    detector in the array:
% gx - x-component of gravitational field
% gy - y-component of gravitational field
% gz - z-component of gravitational field
% g -- magnitude of total gravitational field


%% making cylinder
% finding locations of cylinder elements for a cylinder centred at the ...
    origin and alligned with the z-axis:
[x,y,z,v,P] = cylinder_elements(l,R,Th,Ph,x0,y0,z0,nr,nt,nl); % see ...
    'cylinder_elements.m'



%% loops to move the cylinder and calculate the components of g at each ...
    step at each detector
% cell arrays to store g,gx,gy,gz values at each detector location
g = cell(ny,nx,nz);
gx = cell(ny,nx,nz);
gy = cell(ny,nx,nz);
gz = cell(ny,nx,nz);

% loops that iterate over each detector and find g and its components at ...
    that point.
for k = 1:nz
for j = 1:ny
for i = 1:nx
% shifting the cylinder's starting point to account for the ith,jth,kth ...
    detector's offset from the centre
x2 = x - ax(i);
y2 = y - ay(j);
z2 = z + az(k);

% function that finds g at the (i,j,k) detector when the cylindrical ...
    density moves past:
[gtot,gxtot,gytot,gztot,rho] = cylinder_g(ni,s,x2,y2,z2,v,P); % see ...
    'cylinder_g.m'

```

```
% finding g values in microGal
gtot = gtot * 100e6;
gxtot = gxtot * 100e6;
gytot = gytot * 100e6;
gztot = gztot * 100e6;

% storing the g values of each detector in cell arrays.
g{j,i,k} = gtot; % total magnitude of g
gx{j,i,k} = gxtot; % x-component
gy{j,i,k} = gytot; % y-component
gz{j,i,k} = gztot; % z-component
end
end
end
```

‘cylinder_elements.m’

```
% Function that finds the cartesian coordinates of cylindrical polar ...
    volume elements of a cylinder of specified size
% Cylinder is centred at x0,y0,z0. Number of elements used and the ...
    orientation of the cylinder are also specified

function [x,y,z,v,P] = ...
    cylinder_elements(length,radius,elevation,azimuth,x0,y0,z0,nr,nt,nl)
%% input and output documentation:
% ---Inputs---
% length       =  Length of the cylinder
% radius       =  Radius of the cylinder
% elevation    =  angle between the cylinder's axis and the z-axis
% azimuth      =  angle in the x-y plane between the cylinder's axis and ...
    the x-axis
% x0,y0,z0     =  x,y,z coordinates of the cylinder's starting position ...
    (defined from the cylinder's centre)
% nr,nt,nl  =  number of radial, angular and length elements used to ...
    describe the cylinder
%
% ---Outputs---
% x,y,z = coordinates of the centres of mass of all cylindrical polar ...
    elements used to describe the cylinder
% v = volumes of all elements used to describe the cylinder
% P = densities of all elements used to describe the cylinder (derived ...
    from mass_plot.xls)

```

```

%% describing locations of cylinder elements for a cylinder centred at ...
    the origin and alligned with the z-axis:
dr = radius / nr; % size of radial elements
dt = (2*pi) / nt; % size of angular elements
dl = length / nl; % size of length elements

r1 = 0:dr:radius-dr; % range of inner radii of elements
r2 = dr:dr:radius; % range of outer radii of elements
rcom = (4*(r2.^3 - r1.^3)*sin(dt/2)) ./ (3*dt*(r2.^2 - r1.^2)); % range ...
    of radial distances to the centre of mass of elements

th = 0:dt:(2*pi)-dt; % range of angular position of elements
l = (-length/2 + (dl/2)):dl:(length/2 - (dl/2)); % range of element ...
    positions along the length of the cylinder

[Rcom,Th,L] = meshgrid(rcom,th,l); % resizing rbcom,tb and lb vectors to ...
    be 3D arrays of equal size

% elevation = elevation + (pi/2); % this makes the cylinder axis ...
    alligned with the x-y plane when Thb = 0, else it is alligned with ...
    the z-axis

%% rotating and translating element coordinates to shift the cylinder to ...
    its actual location
Ry = [cos(elevation),0,sin(elevation) ; 0,1,0 ; ...
    -1*sin(elevation),0,cos(elevation)]; % rotation matrix to rotate ...
    coords about y-axis to give correct elevation angle
Rz = [cos(azimuth),-1*sin(azimuth),0 ; sin(azimuth),cos(azimuth),0 ; ...
    0,0,1]; % rotation matrix to rotate coords about z-axis to give coor

R1 = meshgrid(r1,th,l);
R2 = meshgrid(r2,th,l);

% preallocating variables to speed up loop
X = zeros(nt,nr,nl);
Y = zeros(nt,nr,nl);
Z = zeros(nt,nr,nl);
x = zeros(nt,nr,nl);
y = zeros(nt,nr,nl);
z = zeros(nt,nr,nl);
v = zeros(nt,nr,nl);

% loop which carries out the translation and rotations for each cylinder ...
    element
for i = 1:nt
```

```
for j = 1:nr
for k = 1:nl
[d,e,f] = pol2cart(Th(i,j,k),Rcom(i,j,k),L(i,j,k));

% describing x,y,z coords of ith,jth,kth element
X(i,j,k) = d;
Y(i,j,k) = e;
Z(i,j,k) = f;

% describing the volume of ith,jth,kth element
v(i,j,k) = (R2(i,j,k)^2 - R1(i,j,k)^2) * (dt/2) * dl;

% rotating about the y-axis to the correct elevation, Thb
o = Ry * [X(i,j,k) ; Y(i,j,k) ; Z(i,j,k)];
x(i,j,k) = o(1);
y(i,j,k) = o(2);
z(i,j,k) = o(3);

% rotating about the z-axis to the correct azimuth, Phb
q = Rz * [x(i,j,k) ; y(i,j,k) ; z(i,j,k)];
x(i,j,k) = q(1);
y(i,j,k) = q(2);
z(i,j,k) = q(3);

% translating the coordinates to the centre the cylinder on the desired ...
    location
x(i,j,k) = x(i,j,k) + x0;
y(i,j,k) = y(i,j,k) + y0;
z(i,j,k) = z(i,j,k) + z0;
end
end
end

%% Describing the density of elements
% reading a linear density model of the cylinder from an excel file
a = xlsread('density_plot.xls','Sheet1');
p = a(:,2); % density of each length section of the cylinder

% making an array of size (nr,nt,nl) describing the density of all elements
[d,e,P] = meshgrid(rcom,th,p); % d and e are unused variables

% calculating the volume of each element
v = (R2.^2 - R1.^2) * (dt/2) * dl; % matrix of element volumes, required ...
    to find g
end
```

‘cylinder_g.m’

```
% - Function that finds g at the origin due to a cylinder split into ...
    cylindrical polar elements as it moves past the origin

function [gtot,gxtot,gytot,gztot] = cylinder_g(ni,s,x,y,z,v,P)
%% input and output documentation:
% inputs:
% ni    - number of steps in the cylinder's movement
% s     - step size of cylinder movement
% x,y,z - initial coordinates of the centres of mass of the cylinder ...
    elements
% v     - array containing the volume of each element
% P     - array containing the density of each element

% outputs:
% gtot  - magnitude of g at the origin
% gxtot - x-component of g at the origin
% gytot - y-component of g at the origin
% gztot - z-component of g at the origin

%% preparing some important variables
G = 6.67e-11; % gravitational constant

% preallocating variables to speed up loop later on
gtot = zeros(1,ni);
gxtot = zeros(1,ni);
gytot = zeros(1,ni);
gztot = zeros(1,ni);


%% loop to find total g and its components over time
t = 1; % counter to use in loop
while t ≤ ni
x = x + s; % x coords of elements at the current time

[ph,th,r] = cart2sph(x,y,z); % polar coordinates of all cylinder ...
    elements at the current step

%% finding total g at centre due to all elements
% g and its components due to individual elements
g = (G*v.*(P)) ./ (r.^2); % using size, density and radial distance ...
    arrays to find g contributions
gx = g .* cos(th) .* cos(ph);  % x-component of each g contribution
gy = g .* cos(th) .* sin(ph);  % y-component of each g contribution
```

```
gz = g .* sin(th);               % z-component of each g contribution

% total g components
gxtot(t) = -1*sum(sum(sum(gx)));
gytot(t) = -1*sum(sum(sum(gy)));
gztot(t) = -1*sum(sum(sum(gz)));

% total g (magnitude)
gtot(t) = sqrt(gxtot(t)^2 + gytot(t)^2 + gztot(t)^2);

t = t + 1;
end
```

Appendix B

Programs to calculate terrain correction

This appendix contains copies of the MATLAB programs described in section 3.2 to calculate gravitational terrain corrections using Digital Elevation Models of topography and bathymetry.

‘terrain_correction.m’

```
% Program to calculate terrain correction from 3 DEMs describing ...
   topography (and optionally bathymetry) around a gravitational survey ...
   point
%% defining inputs and outputs
% ===Inputs===
% density -- average density of rock in kg/m^-3
% path_s --- filepath to the inner zone DEM in .tif format
% path_m --- filepath to the middle zone DEM in .tif format
% path_l --- filepath to the outer zone DEM in .tif format
% div_s ---- number of quadrants to divide inner zone DEM into during ...
   analysis
% div_m ---- number of quadrants to divide middle zone DEM into during ...
   analysis
% div_l ---- number of quadrants to divide outer zone DEM into during ...
   analysis
% inlim_s -- inner limit of the inner zone map in metres (usually zero)
% inlim_m -- inner limit of the middle zone map in metres
% inlim_l -- inner limit of the outer zone map in metres
% outlim_s - outer limit of the inner zone map in metres
% outlim_m - outer limit of the middle zone map in metres
% outlim_l - outer limit of the outer zone map in metres

% ===Outputs===
% tc_s ----- inner zone terrain correction
% tc_m ----- middle zone terrain correction
```

```
% tc_l ----- outer zone terrain correction
% tc ------- total terrain correction

density = 2670; % rock density to use in calculations

% - directory of DEMs -
path_s = '-file directory here-';
path_m = '-file directory here-';
path_l = '-file directory here-';

% number of divisions to split the maps into during the analysis
div_s = 20;
div_m = 50;
div_l = 68;

% inner and outer limits to use for the maps
inlim_s = 0;
outlim_s = 1000;

inlim_m = 1000;
outlim_m = 25000;

inlim_l = 25000;
outlim_l = 170000;


%% reading map data from .tif files
% === inner zone map ===
info_s = geotiffinfo(path_s); % getting details of the map (for finding ...
    x,y coords)
[topo_s,stats_s] = geotiffread(path_s); % reading the .tif file into a ...
    matrix
topo_s(topo_s < 0) = 0;
e_s = stats_s.CellExtentInWorldX;

% x-y coordinates of map data points
[x_s,y_s] = pixcenters(info_s);
[x_s,y_s] = meshgrid(x_s,y_s);

% extracting map center coordinates
px_s = stats_s.XWorldLimits(1) + (stats_s.RasterExtentInWorldX/2);
py_s = stats_s.YWorldLimits(1) + (stats_s.RasterExtentInWorldY/2);
p0 = [px_s,py_s]; % x-y coords of computation point (using british ...
    national grid coordinates)
p0(3) = interp2(x_s,y_s,flipud(topo_s),p0(1),p0(2)); % interpolating to ...
    find elevation at p0
```

```

x_s = x_s - p0(1);
y_s = y_s - p0(2);
topo_s = topo_s - p0(3);

% === middle zone map ===
info_m = geotiffinfo(path_m); % getting details of the map (for finding ...
    x,y coords)
[topo_m,stats_l] = geotiffread(path_m); % reading the .tif file into a ...
    matrix
topo_m(topo_m < 0) = 0;
e_m = stats_l.CellExtentInWorldX;

% x-y coordinates of map data points
[x_m,y_m] = pixcenters(info_m);
[x_m,y_m] = meshgrid(x_m,y_m);

% shifting coords so the center is at (0,0,0)
x_m = x_m - p0(1);
y_m = y_m - p0(2);
topo_m = topo_m - p0(3);

% === outer zone map ===
info_l = geotiffinfo(path_l); % getting details of the map (for finding ...
    x,y coords)
[topo_l,stats_l] = geotiffread(path_l); % reading the .tif file into a ...
    matrix
topo_l(topo_l < 0) = 0;
e_l = stats_l.CellExtentInWorldX;

% x-y coordinates of map data points
[x_l,y_l] = pixcenters(info_l);
[x_l,y_l] = meshgrid(x_l,y_l);

% shifting coords so the center is at (0,0,0)
x_l = x_l - p0(1);
y_l = y_l - p0(2);
topo_l = topo_l - p0(3); %

%% Terrain correction due to small map
tc_s = zone_TC(x_s,y_s,topo_s,p0(3),e_s,div_s,inlim_s,outlim_s,density);


%% Terrain correction due to medium map
tc_m = zone_TC(x_m,y_m,topo_m,p0(3),e_m,div_m,inlim_m,outlim_m,density);

```

```
%% Terrain correction due to large map
tc_l = zone_TC(x_l,y_l,topo_l,p0(3),e_l,div_l,inlim_l,outlim_l,density);


%% total terrain correction
tc = tc_s + tc_m + tc_l;
```

‘zone_TC.m’

```
% Splits a DEM into quadrants and finds total gz at (0,0) using ...
    rectangular prism approximation
% (DEM analysed one quadrant at a time to decrease memory load).
% Includes bathymetry by assuming everything below sea level to be ...
    underwater (pw = 1000kg^m-3).
function [gz] = zone_TC(X,Y,topo,h,element,div,inlimit,outlimit,density)
%% defining inputs and output
% ===inputs===
% X,Y ------ coordinates of prism centres
% topo ----- topographic map of the region (describes the height of prisms)
% h -------- elevation of survey point (used when considering bathymetry)
% element -- x-y side length of prisms
% div ------ parameter that decides how many cells to split the DEM into ...
    (div x div array)
% inlimit -- x and y extent within which cells are ignored
% outlimit - x and y extent beyond which cells are ignored
% density -- density of rock
wdensity = 1030; % density of water in kg/m^3, used when considering ...
    bathymetry

% ===output===
% gz ------- vertical component of gravitational field at (0,0)


%% splitting map into quadrants
s = size(topo);

% div decides the number of regions to divide the map into (to give num ...
    x num regions)
siz = s(1)/div; % number of regions in each direction

N = siz*ones(1,div); % # of regions in x direction
M = siz*ones(1,div); % # of regions in y direction
```

```

Quadrants = mat2cell(topo,M,N); % cell array made of the divided ...
    quadrants of the topography
xx = mat2cell(X,M,N); % corresponding cell array with x-coords of ...
    divided quadrants
yy = mat2cell(Y,M,N); % corresponding cell array with y-coords of ...
    divided quadrants
Nr = length(N) * length(M); % total number of regions (used for plotting)


%% Identifying distant quadrants and ignoring too-distant quadrants ...
    (according to specified inner and outer limits for this zone)
q = size(xx); % finding number of quadrants in the cell arrays

% finding the closest element to (0,0) in each cell, these are used when ...
    checking limits
for i = 1:q(1)
for j = 1:q(2)
xnear(j,i) = min(min(abs(xx{j,i})));
ynear(j,i) = min(min(abs(yy{j,i})));
end
end

% --defining limits as logical arrays--
cellsize = element*siz; % side length of each region
% outer limit
ox = (xnear ≥ -outlimit + cellsize/2) .* (xnear ≤ outlimit - ...
    cellsize/2); % x limits
oy = (ynear ≥ -outlimit + cellsize/2) .* (ynear ≤ outlimit - ...
    cellsize/2); % y limits
OL = ox .* oy; % logical matrix showing cells within the outer limits

% inner limit
ix = (xnear < -inlimit + cellsize/2) + (xnear > inlimit - cellsize/2);
iy = (ynear < -inlimit + cellsize/2) + (ynear > inlimit - cellsize/2);
IL = ix + iy; % summing the two logical matrices to combine them, the ...
    next line changes any 2's back to boolean 1's
a = find(IL ≠ 0); IL(a) = 1; % logical matrix showing cells beyond the ...
    inner limits

% combining the two to give one logical array showing which cells are ...
    within the limits
lims = OL.*IL;

[xout,yout] = find(lims == 1); % coords of cells outside the limits

```

```

%% making separate topography and bathymetry maps
for i = 1:div
for j = 1:div
qu = Quadrants{i,j}; % ith map quadrant
above = qu ≥ -h;
below = qu <  -h;

qu_a = qu;
qu_b = qu;

qu_a(below) = -h;
qu_b(above) = -h;

land{i,j} = qu_a;
water{i,j} = qu_b;
end
end


%% terrain correction due to topography and bathymetry (calculated ...
    separately)
% for the case when no quadrants are within the given boundaries:
if sum(size(xout)) ≤1
gz = 0;

% for all other cases:
else
% finding terrain correction due to each valid quadrant
Gz_land = cell(size(land)); % empty cell arrays to hold gz values of ...
    each element in a quadrant
Gz_water = cell(size(water));

% - considering topography -
% applying prism_method.m function to each quadrant sequentially
for I = 1:length(xout) % looping over the number of quadrants
xI = xx{xout(I),yout(I)}; % x data for current quadrant
yI = yy{xout(I),yout(I)}; % y data for current quadrant
Land = land{xout(I),yout(I)}; % elevation data for current quadrant

% gz of each element for current quadrant (using h = 0 in prism_method.m ...
    so it applies to topohraphy)
gzI_land = prism_method_topography(xI,yI,Land,element,density);
Gz_land{xout(I),yout(I)} = gzI_land;
end

```

```
% summing all quadrants to find total gz due to topography
for k = 1:sum(sum(lims == 1))
a = Gz_land{yout(k),xout(k)};
Gzo_land(k) = sum(sum(a));
end

% - considering bathymetry -
% applying prism_method.m function to each quadrant sequentially
for I = 1:length(xout) % looping over the number of quadrants
xI = xx{xout(I),yout(I)}; % x data for current quadrant
yI = yy{xout(I),yout(I)}; % y data for current quadrant
Water = water{xout(I),yout(I)}; % elevation data for current quadrant

% gz of each element for current quadrant (using h = h in prism_method.m ...
    so it applies to bathymetry)
gzI_water = prism_method_bathymetry(xI,yI,Water,element,density,wdensity,h);
Gz_water{xout(I),yout(I)} = gzI_water;
end

% summing all quadrants to find total gz due to bathymetry
for k = 1:sum(sum(lims == 1))
a = Gz_water{yout(k),xout(k)};
Gzo_water(k) = sum(sum(a));
end

% total gz
gz = sum(sum(Gzo_land))+ sum(sum(Gzo_water));
end
```

‘prism_method_topography.m’

```
%% function that finds the terrain correction at (0,0) due to the input ...
    topography using the Nagy rectangular prism method
function [gz] = prism_method_topography(x,y,land,e,p)
%% defining inputs and outputs
% ===Input===
% x,y -- coordinates of prism centres
% land - topographic map of the region
% e ---- x-y side length of prisms
% p ---- density of prisms
%
% ===Output===
% gz --- vertical component of gravitational field at origin [mGal]
```

```


%% Finding the boundaries of the prisms
x1 = x - e/2; x2 = x + e/2;
y1 = y - e/2; y2 = y + e/2;
z1 = zeros(size(land)); z2 = (land);

% This line ensures that z1 has NaN's in the same places as in z2, which ...
    leads to the edge
% elements of the imported topographic map (which are NaN due to the ...
    interpolation) being ignored
z1(isnan(z2)) = NaN;


%% treating the 4 elements immediately surrounding the centre as flat; ...
    setting their height = 0 (so z2-z1 = 0)
R = sqrt(x.^2 + y.^2); % radial distance from the centre of all points
z2(R < 2*e) = 0; % elements within a distance of 2*elementsize have no ...
    effect
% (^ since elements are square, this acts on inner 4 elements only)


%% Finding g at the origin
% This replaces any individual terms that are undefined (i.e. NaN or ...
    Inf) with zero.
% gz is the final answer, it is found from 8 terms: gz1, gz2, ... , gz8.
% Each term itself has 3 sub-terms: gz1a, gz1b and gz1c.
% Each sub-term is evaluated on separate lines and replaced with zero if ...
    it is NaN or Inf.

G = 6.67e-11; % gravitational constant

% function that finds radius
r = @(x,y,z) (sqrt(x.^2 + y.^2 + z.^2));

%% finding the 8 terms
% finding gz1 (x2,y2,z2)
gz1a = (-1*G*p) .* (x2.*log(y2 + r(x2,y2,z2)));
gz1a(isnan(gz1a)) = 0;
gz1a(isinf(gz1a)) = 0;

gz1b = (-1*G*p) .* (y2.*log(x2 + r(x2,y2,z2)));
gz1b(isnan(gz1b)) = 0;
gz1b(isinf(gz1b)) = 0;

gz1c = (-1*G*p) .* ((z2.*atan((x2.*y2) ./ (z2.*r(x2,y2,z2)))));
```

```
gz1c(isnan(gz1c)) = 0;
gz1c(isinf(gz1c)) = 0;

gz1 = gz1a + gz1b - gz1c;


% finding gz2 (x1,y2,z2)
gz2a = (-1*G*p) .* (x1.*log(y2 + r(x1,y2,z2)));
gz2a(isnan(gz2a)) = 0;
gz2a(isinf(gz2a)) = 0;

gz2b = (-1*G*p) .* (y2.*log(x1 + r(x1,y2,z2)));
gz2b(isnan(gz2b)) = 0;
gz2b(isinf(gz2b)) = 0;

gz2c = (-1*G*p) .* ((z2.*atan((x1.*y2) ./ (z2.*r(x1,y2,z2)))));
gz2c(isnan(gz2c)) = 0;
gz2c(isinf(gz2c)) = 0;

gz2 = gz2a + gz2b - gz2c;


% finding gz3 (x1,y1,z2)
gz3a = (-1*G*p) .* (x1.*log(y1 + r(x1,y1,z2)));
gz3a(isnan(gz3a)) = 0;
gz3a(isinf(gz3a)) = 0;

gz3b = (-1*G*p) .* (y1.*log(x1 + r(x1,y1,z2)));
gz3b(isnan(gz3b)) = 0;
gz3b(isinf(gz3b)) = 0;

gz3c = (-1*G*p) .* ((z2.*atan((x1.*y1) ./ (z2.*r(x1,y1,z2)))));
gz3c(isnan(gz3c)) = 0;
gz3c(isinf(gz3c)) = 0;

gz3 = gz3a + gz3b - gz3c;


% finding gz4 (x2,y1,z2)
gz4a = (-1*G*p) .* (x2.*log(y1 + r(x2,y1,z2)));
gz4a(isnan(gz4a)) = 0;
gz4a(isinf(gz4a)) = 0;

gz4b = (-1*G*p) .* (y1.*log(x2 + r(x2,y1,z2)));
gz4b(isnan(gz4b)) = 0;
gz4b(isinf(gz4b)) = 0;
```

```

gz4c = (-1*G*p) .* ((z2.*atan((x2.*y1) ./ (z2.*r(x2,y1,z2)))));
gz4c(isnan(gz4c)) = 0;
gz4c(isinf(gz4c)) = 0;

gz4 = gz4a + gz4b - gz4c;


% finding gz5 (x2,y2,z1)
gz5a = (-1*G*p) .* (x2.*log(y2 + r(x2,y2,z1)));
gz5a(isnan(gz5a)) = 0;
gz5a(isinf(gz5a)) = 0;

gz5b = (-1*G*p) .* (y2.*log(x2 + r(x2,y2,z1)));
gz5b(isnan(gz5b)) = 0;
gz5b(isinf(gz5b)) = 0;

gz5c = (-1*G*p) .* ((z1.*atan((x2.*y2) ./ (z1.*r(x2,y2,z1)))));
gz5c(isnan(gz5c)) = 0;
gz5c(isinf(gz5c)) = 0;

gz5 = gz5a + gz5b - gz5c;


% finding gz6 (x1,y2,z1)
gz6a = (-1*G*p) .* (x1.*log(y2 + r(x1,y2,z1)));
gz6a(isnan(gz6a)) = 0;
gz6a(isinf(gz6a)) = 0;

gz6b = (-1*G*p) .* (y2.*log(x1 + r(x1,y2,z1)));
gz6b(isnan(gz6b)) = 0;
gz6b(isinf(gz6b)) = 0;

gz6c = (-1*G*p) .* ((z1.*atan((x1.*y2) ./ (z1.*r(x1,y2,z1)))));
gz6c(isnan(gz6c)) = 0;
gz6c(isinf(gz6c)) = 0;

gz6 = gz6a + gz6b - gz6c;


% finding gz7 (x1,y1,z1)
gz7a = (-1*G*p) .* (x1.*log(y1 + r(x1,y1,z1)));
gz7a(isnan(gz7a)) = 0;
gz7a(isinf(gz7a)) = 0;

gz7b = (-1*G*p) .* (y1.*log(x1 + r(x1,y1,z1)));
```

```
gz7b(isnan(gz7b)) = 0;
gz7b(isinf(gz7b)) = 0;

gz7c = (-1*G*p) .* ((z1.*atan((x1.*y1) ./ (z1.*r(x1,y1,z1)))));
gz7c(isnan(gz7c)) = 0;
gz7c(isinf(gz7c)) = 0;

gz7 = gz7a + gz7b - gz7c;


% finding gz8 (x2,y1,z1)
gz8a = (-1*G*p) .* (x2.*log(y1 + r(x2,y1,z1)));
gz8a(isnan(gz8a)) = 0;
gz8a(isinf(gz8a)) = 0;

gz8b = (-1*G*p) .* (y1.*log(x2 + r(x2,y1,z1)));
gz8b(isnan(gz8b)) = 0;
gz8b(isinf(gz8b)) = 0;

gz8c = (-1*G*p) .* ((z1.*atan((x2.*y1) ./ (z1.*r(x2,y1,z1)))));
gz8c(isnan(gz8c)) = 0;
gz8c(isinf(gz8c)) = 0;

gz8 = gz8a + gz8b - gz8c;


%% resulting gz
gz = gz1 - gz2 + gz3 - gz4 - gz5 + gz6 - gz7 + gz8;
```

'prism_method_bathymetry.m'

```
%% function that finds the terrain correction at (0,0) due to input ...
    bathymetry using an FEA method with rectangular prism elements of ...
    uniform size

function [gz] = prism_method_bathymetry(x,y,water,e,p_r,p_w,h)
%% defining inputs and outputs
% ===Input===
% x,y -- coordinates of prism centres
% water - bathymetric map of the region
% e ---- x-y side length of prisms
% p_r -- density of rock
% p_w -- density of water
```

```
% h ---- elevation difference between sea level and computation point (0,0)
%
% ===Output===
% gz = vertical component of gravitational field at origin [mGal]

%% Density to use for prisms
p = p_r - p_w;

%% Finding the boundaries of the prisms
x1 = x - e/2; x2 = x + e/2;
y1 = y - e/2; y2 = y + e/2;
z1 = zeros(size(water))-h; z2 = (water);

% This line ensures that z1 has NaN's in the same places as in z2, which ...
    leads to the edge
% elements of the imported topographic map (which are NaN due to the ...
    interpolation) being ignored
z1(isnan(z2)) = NaN;


%% treating the 4 elements immediately surrounding the centre as flat; ...
    setting their height = -h (so z2-z1 = 0)
R = sqrt(x.^2 + y.^2); % radial distance from the centre of all points
z2(R < 2*e) = -h; % elements within a distance of 2*elementsize have no ...
    effect
% (^ since elements are square, this acts on inner 4 elements only)


%% Finding g at the origin
% This replaces any individual terms that are undefined (i.e. NaN or ...
    Inf) with zero.
% gz is the final answer, it is found from 8 terms: gz1, gz2, ... , gz8.
% Each term itself has 3 sub-terms: gz1a, gz1b and gz1c.
% Each sub-term is evaluated on separate lines and replaced with zero if ...
    it is NaN or Inf.

G = 6.67e-11; % gravitational constant

% function that finds radius
r = @(x,y,z) (sqrt(x.^2 + y.^2 + z.^2));

%% finding the 8 terms
% finding gz1 (x2,y2,z2)
gz1a = (-1*G*p) .* (x2.*log(y2 + r(x2,y2,z2)));
gz1a(isnan(gz1a)) = 0;
gz1a(isinf(gz1a)) = 0;
```

```

gz1b = (-1*G*p) .* (y2.*log(x2 + r(x2,y2,z2)));
gz1b(isnan(gz1b)) = 0;
gz1b(isinf(gz1b)) = 0;

gz1c = (-1*G*p) .* ((z2.*atan((x2.*y2) ./ (z2.*r(x2,y2,z2)))));
gz1c(isnan(gz1c)) = 0;
gz1c(isinf(gz1c)) = 0;

gz1 = gz1a + gz1b - gz1c;


% finding gz2 (x1,y2,z2)
gz2a = (-1*G*p) .* (x1.*log(y2 + r(x1,y2,z2)));
gz2a(isnan(gz2a)) = 0;
gz2a(isinf(gz2a)) = 0;

gz2b = (-1*G*p) .* (y2.*log(x1 + r(x1,y2,z2)));
gz2b(isnan(gz2b)) = 0;
gz2b(isinf(gz2b)) = 0;

gz2c = (-1*G*p) .* ((z2.*atan((x1.*y2) ./ (z2.*r(x1,y2,z2)))));
gz2c(isnan(gz2c)) = 0;
gz2c(isinf(gz2c)) = 0;

gz2 = gz2a + gz2b - gz2c;


% finding gz3 (x1,y1,z2)
gz3a = (-1*G*p) .* (x1.*log(y1 + r(x1,y1,z2)));
gz3a(isnan(gz3a)) = 0;
gz3a(isinf(gz3a)) = 0;

gz3b = (-1*G*p) .* (y1.*log(x1 + r(x1,y1,z2)));
gz3b(isnan(gz3b)) = 0;
gz3b(isinf(gz3b)) = 0;

gz3c = (-1*G*p) .* ((z2.*atan((x1.*y1) ./ (z2.*r(x1,y1,z2)))));
gz3c(isnan(gz3c)) = 0;
gz3c(isinf(gz3c)) = 0;

gz3 = gz3a + gz3b - gz3c;


% finding gz4 (x2,y1,z2)
gz4a = (-1*G*p) .* (x2.*log(y1 + r(x2,y1,z2)));
```

```
gz4a(isnan(gz4a)) = 0;
gz4a(isinf(gz4a)) = 0;

gz4b = (-1*G*p) .* (y1.*log(x2 + r(x2,y1,z2)));
gz4b(isnan(gz4b)) = 0;
gz4b(isinf(gz4b)) = 0;

gz4c = (-1*G*p) .* ((z2.*atan((x2.*y1) ./ (z2.*r(x2,y1,z2)))));
gz4c(isnan(gz4c)) = 0;
gz4c(isinf(gz4c)) = 0;

gz4 = gz4a + gz4b - gz4c;


% finding gz5 (x2,y2,z1)
gz5a = (-1*G*p) .* (x2.*log(y2 + r(x2,y2,z1)));
gz5a(isnan(gz5a)) = 0;
gz5a(isinf(gz5a)) = 0;

gz5b = (-1*G*p) .* (y2.*log(x2 + r(x2,y2,z1)));
gz5b(isnan(gz5b)) = 0;
gz5b(isinf(gz5b)) = 0;

gz5c = (-1*G*p) .* ((z1.*atan((x2.*y2) ./ (z1.*r(x2,y2,z1)))));
gz5c(isnan(gz5c)) = 0;
gz5c(isinf(gz5c)) = 0;

gz5 = gz5a + gz5b - gz5c;


% finding gz6 (x1,y2,z1)
gz6a = (-1*G*p) .* (x1.*log(y2 + r(x1,y2,z1)));
gz6a(isnan(gz6a)) = 0;
gz6a(isinf(gz6a)) = 0;

gz6b = (-1*G*p) .* (y2.*log(x1 + r(x1,y2,z1)));
gz6b(isnan(gz6b)) = 0;
gz6b(isinf(gz6b)) = 0;

gz6c = (-1*G*p) .* ((z1.*atan((x1.*y2) ./ (z1.*r(x1,y2,z1)))));
gz6c(isnan(gz6c)) = 0;
gz6c(isinf(gz6c)) = 0;

gz6 = gz6a + gz6b - gz6c;
```

```
% finding gz7 (x1,y1,z1)
gz7a = (-1*G*p) .* (x1.*log(y1 + r(x1,y1,z1)));
gz7a(isnan(gz7a)) = 0;
gz7a(isinf(gz7a)) = 0;

gz7b = (-1*G*p) .* (y1.*log(x1 + r(x1,y1,z1)));
gz7b(isnan(gz7b)) = 0;
gz7b(isinf(gz7b)) = 0;

gz7c = (-1*G*p) .* ((z1.*atan((x1.*y1) ./ (z1.*r(x1,y1,z1)))));
gz7c(isnan(gz7c)) = 0;
gz7c(isinf(gz7c)) = 0;

gz7 = gz7a + gz7b - gz7c;


% finding gz8 (x2,y1,z1)
gz8a = (-1*G*p) .* (x2.*log(y1 + r(x2,y1,z1)));
gz8a(isnan(gz8a)) = 0;
gz8a(isinf(gz8a)) = 0;

gz8b = (-1*G*p) .* (y1.*log(x2 + r(x2,y1,z1)));
gz8b(isnan(gz8b)) = 0;
gz8b(isinf(gz8b)) = 0;

gz8c = (-1*G*p) .* ((z1.*atan((x2.*y1) ./ (z1.*r(x2,y1,z1)))));
gz8c(isnan(gz8c)) = 0;
gz8c(isinf(gz8c)) = 0;

gz8 = gz8a + gz8b - gz8c;


%% resulting gz
gz = gz1 - gz2 + gz3 - gz4 - gz5 + gz6 - gz7 + gz8;
```

Bibliography

[1] O. Pedersen. *Early Physics and Astronomy: A Historical Introduction*. Early Physics and Astronomy: A Historical Introduction. Cambridge University Press, 1993.

[2] Issac Newton. *The Principia: mathematical principles of natural philosophy*. Univ of California Press, 1999.

[3] A. Einstein. *Die Grundlage der allgemeinen Relativitätstheorie*. Annalen der Physik und Chemie. J.A. Barth, 1916.

[4] Tilman Sauer. Albert einstein's 1916 review article on general relativity, 2004.

[5] C.W. Misner, K.S. Thorne, and J.A. Wheeler. *Gravitation*. Number pt. 3 in Gravitation. W. H. Freeman, 1973.

[6] J Ries, S Bettadpur, R Eanes, Z Kang, U Ko, C McCullough, P Nagel, N Pie, S Poole, T Richter, H Save, and B Tapley. The Development and Evaluation of the Global Gravity Model GGM05, 2016. Center for Space Research, The University of Texas at Austin.

[7] K. Ford, P. Keating, and M. D. Thomas. Overview of Geophysical Signatures Associated with Canadian Ore Deposits. Technical Report 5, Geological Association of Canada, Mineral Deposits Division, St. John's, NL, 2007.

[8] Lisa A Morgan. Geophysical Characteristics of Volcanogenic Massive Sulfide Deposits Volcanogenic Massive Sulfide Occurrence Model. *U.S. Geological Survey Scientific Investigations Report 2010–5070 –C*, (January 2012):113–131, 2012.

[9] Adel Shirazy, Aref Shirazi, Hamed Nazerian, Keyvan Khayer, and Ardeshir Hezarkhani. Geophysical Study: Estimation of Deposit Depth Using Gravimetric Data and Euler Method (Jalalabad Iron Mine, Kerman Province of IRAN). *Open Journal of Geology*, 11(08):340–355, 2021.

[10] Tomáš Havlík. Phase Equilibrium of Copper Iron Sulphides. In *Hydrometallurgy*, pages 29–59. Elsevier, 2008.

[11] M.D. Thomas, J.A. Walker, P. Keating, R. Shives, F. Kiss, and W.D. Goodfellow. Geophysical atlas of massive sulphide signatures. Technical report, Geological Survey of Canada Open File 3887, 105 p, 2000.

[12] H. O. Seigel, I. Brcic, and P. Mistry. A guide to high precision land gravity surveys. *Scintrex Limited*, 222, 1995.

[13] V. Oliveira, J. Matos, M. Bengala, N. Silva, P. Sousa, and L. Torres. Geology and geophysics as successful tools in the discovery of the Lagoa Salgada Orebody (Sado Tertiary Basin - Iberian Pyrite Belt), Grândola, Portugal. *Mineralium Deposita*, 33(1-2):170–187, dec 1997.

[14] Fernando Carlos Lopes, Alcides José Pereira, and Vasco Manuel Mantas. Mapping of salt structures and related fault lineaments based on remote-sensing and gravimetric data: The case of the Monte Real salt wall (onshore west-central Portugal). *AAPG Bulletin*, 96(4):615–634, apr 2012.

[15] Alexander J. O. Jenkins, Derbew Messfin, and Wooil Moon. Gravity modelling of salt domes and pinnacle reefs. *Journal of the Canadian Society of Exploration Geophysicists*, 19(1):51–56, 1983.

[16] Mark E. Ander and David A. Chapin. Borehole gravimetry: A review. In *SEG Technical Program Expanded Abstracts 1997*, pages 531–534. Society of Exploration Geophysicists, jan 1997.

[17] J.V. Popta, J.M.T. Heywood, S.J. Adams, and D.R. Bostock. Use of Borehole Gravimetry for Reservoir Characterisation and Fluid Saturation Monitoring. In *All Days*. SPE, oct 1990.

[18] Alfred Kleusberg, Derrick Peyton, and David Wells. Airborne gravimetry and the Global Positioning System. In *Record - IEEE PLANS, Position Location and Navigation Symposium*, pages 273–278. IEEE, 1990.

[19] A. Wooldridge. Review of modern airborne gravity focusing on results from GT-1a surveys. *First Break*, 28(5), may 2010.

[20] Biao Lu, Franz Barthelmes, Svetozar Petrovic, Christoph Förste, Frank Flechtner, Zhicai Luo, Kaifei He, and Min Li. Airborne Gravimetry of GEOHALO Mission: Data Processing and Gravity Field Modeling. *Journal of Geophysical Research: Solid Earth*, 122(12):10,586–10,604, dec 2017.

[21] James S. Famiglietti. Remote sensing of terrestrial water storage, soil moisture and surface waters. In *The State of the Planet: Frontiers and Challenges in Geophysics*, volume 150, pages 197–207. 2004.

[22] Guillaume Ramillien, J. S. Famiglietti, and J. Wahr. Detection of continental hydrology and glaciology Signals from GRACE: A review. *Surveys in Geophysics*, 29(4-5):361–374, oct 2008.

[23] Liangjing Zhang, Henryk Dobslaw, Tobias Stacke, Andreas Güntner, Robert Dill, and Maik Thomas. Validation of terrestrial water storage variations as simulated by different global numerical models with GRACE satellite observations. *Hydrology and Earth System Sciences*, 21(2):821–837, feb 2017.

[24] B. Wouters, J. A. Bonin, D. P. Chambers, R. E.M. Riva, I. Sasgen, and J. Wahr. GRACE, time-varying gravity, Earth system dynamics and climate change. *Reports on Progress in Physics*, 77(11):116801, nov 2014.

[25] NASA-JPL. GRACE Mission Overview. `https://www.nasa.gov/mission_pages/Grace/overview/index.html`, 2002.

[26] Shin Chan Han, C. K. Shum, Christopher Jekeli, and Doug Alsdorf. Improved estimation of terrestrial water storage changes from GRACE. *Geophysical Research Letters*, 32(7):1–5, apr 2005.

[27] Xiaogong Hu, Jianli Chen, Yonghong Zhou, Cheng Huang, and Xinhao Liao. Seasonal water storage change of the Yangtze River basin detected by Grace. *Science in China, Series D: Earth Sciences*, 49(5):483–491, may 2006.

[28] B. R. Scanlon, Z. Zhang, A. Rateb, A. Sun, D. Wiese, H. Save, H. Beaudoing, M. H. Lo, H. Müller-Schmied, P. Döll, R. van Beek, S. Swenson, D. Lawrence, M. Croteau, and R. C. Reedy. Tracking Seasonal Fluctuations in Land Water Storage Using Global Models and GRACE Satellites. *Geophysical Research Letters*, 46(10):5254–5264, may 2019.

[29] Marc J. Leblanc, Paul Tregoning, Guillaume Ramillien, Sarah O. Tweed, and Adam Fakes. Basin-scale, integrated observations of the early 21st century multiyear drought in Southeast Australia. *Water Resources Research*, 45(4), apr 2009.

[30] Ole B. Andersen, Sonia I. Seneviratne, Jacques Hinderer, and Pedro Viterbo. GRACE-derived terrestrial water storage depletion associated with the 2003 European heat wave. *Geophysical Research Letters*, 32(18):1–4, sep 2005.

[31] J. L. Chen, C. R. Wilson, B. D. Tapley, Z. L. Yang, and G. Y. Niu. 2005 drought event in the Amazon River basin as measured by GRACE and estimated by climate models. *Journal of Geophysical Research: Solid Earth*, 114(5), may 2009.

[32] Soumendra N. Bhanja, Abhijit Mukherjee, Matthew Rodell, Yoshihide Wada, Siddhartha Chattopadhyay, Isabella Velicogna, Kishore Pangaluru, and James S. Famiglietti. Groundwater rejuvenation in parts of India influenced by water-policy change implementation. *Scientific Reports*, 7(1):7453, dec 2017.

[33] Scott B. Luthcke, Anthony A. Arendt, David D. Rowlands, John J. McCarthy, and Christopher F. Larsen. Recent glacier mass changes in the Gulf of Alaska region from GRACE mascon solutions. *Journal of Glaciology*, 54(188):767–777, sep 2008.

[34] Thomas Jacob, John Wahr, W. Tad Pfeffer, and Sean Swenson. Recent contributions of glaciers and ice caps to sea level rise. *Nature*, 482(7386):514–518, feb 2012.

[35] Bert Wouters, Alex S. Gardner, and Geir Moholdt. Global glacier mass loss during the GRACE satellite mission (2002-2016). *Frontiers in Earth Science*, 7, may 2019.

[36] H. Rymer and G. C. Brown. Gravity fields and the interpretation of volcanic structures: Geological discrimination and temporal evolution. *Journal of Volcanology and Geothermal Research*, 27(3-4):229–254, mar 1986.

[37] J. Kauahikaua, T. Hildenbrand, and M. Webring. Deep magmatic structures of Hawaiian volcanoes, imaged by three-dimensional gravity models. *Geology*, 28(10):883–886, 2000.

[38] José Fernández, Antonio Pepe, Michael P. Poland, and Freysteinn Sigmundsson. Volcano Geodesy: Recent developments and future challenges. *Journal of Volcanology and Geothermal Research*, 344:1–12, sep 2017.

[39] Daniele Carbone, Luciano Zuccarello, Gilberto Saccorotti, and Filippo Greco. Analysis of simultaneous gravity and tremor anomalies observed during the 2002-2003 Etna eruption. *Earth and Planetary Science Letters*, 245(3-4):616–629, may 2006.

[40] Hazel Rymer, John B. Murray, Geoff C. Brown, Fabrizio Ferrucci, and William J. McGuire. Mechanisms of magma eruption and emplacement at Mt Etna between 1989 and 1992. *Nature*, 361(6411):439–441, feb 1993.

[41] Maurizio Battaglia, Joachim Gottsmann, Daniele Carbone, and José Fernández. 4D volcano gravimetry. *Geophysics*, 73(6):WA3–WA18, nov 2008.

[42] P. Jousset, S. Dwipa, F. Beauducel, T. Duquesnoy, and M. Diament. Temporal gravity at Merapi during the 1993-1995 crisis: An insight into the dynamical behaviour of volcanoes. *Journal of Volcanology and Geothermal Research*, 100(1-4):289–320, jul 2000.

[43] D. Carbone, G. Budetta, and F. Greco. Bulk processes some months before the start of the 2001 Mt. Etna eruption, highlighted through microgravity studies. *Journal of Geophysical Research*, 108, 2003.

[44] Shin-Chan Han, C. K. Shum, Michael Bevis, Chen Ji, and Chung-Yen Kuo. Crustal Dilatation Observed by GRACE After the 2004 Sumatra-Andaman Earthquake. *Science*, 313(5787):658–662, aug 2006.

[45] Shin Chan Han, Jeanne Sauber, and Scott Luthcke. Regional gravity decrease after the 2010 Maule (Chile) earthquake indicates large-scale mass redistribution. *Geophysical Research Letters*, 37(23), dec 2010.

[46] Yusaku Tanaka and Kosuke Heki. Long- and short-term postseismic gravity changes of megathrust earthquakes from satellite gravimetry. *Geophysical Research Letters*, 41(15):5451–5456, aug 2014.

[47] Lei Wang, C. K. Shum, and Christopher Jekeli. Gravitational gradient changes following the 2004 December 26 Sumatra-Andaman Earthquake inferred from GRACE. *Geophysical Journal International*, pages no–no, oct 2012.

[48] Shin Chan Han, Jeanne Sauber, and Riccardo Riva. Contribution of satellite gravimetry to understanding seismic source processes of the 2011 Tohoku-Oki earthquake. *Geophysical Research Letters*, 38(24), dec 2011.

[49] Farzam Fatolazadeh, Mehdi Raoofian Naeeni, Behzad Voosoghi, and Armin Rahimi. Estimation of fault parameters using GRACE observations and analytical model: Case study: The 2010 Chile earthquake. *Journal of Geodynamics*, 108:26–39, jul 2017.

[50] Jaroslava Pánisová and Roman PaŠteka. The use of microgravity technique in archaeology: A case study from the St. Nicolas church in Pukanec, Slovakia. *Contributions to Geophysics and Geodesy*, 39(3):237–254, jan 2009.

[51] Jorge Padín, Angel Martín, and Ana Belén Anquela. Archaeological microgravimetric prospection inside don church (Valencia, Spain). *Journal of Archaeological Science*, 39(2):547–554, feb 2012.

[52] R. Pašteka, P. Zahorec, J. Papčo, J. Mrlina, H.-J. Götze, and S. Schmidt. The discovery of the "muons-chamber" in the Great pyramid; could high-precision microgravimetry also map the chamber? *Journal of Archaeological Science: Reports*, 43:103464, jun 2022.

[53] Anestis J Romaides, James C Battis, Roger W Sands, Alan Zorn, Donald O Benson, and Daniel J DiFrancesco. A comparison of gravimetric techniques for measuring subsurface void signals. *Journal of Physics D: Applied Physics*, 34(3):433–443, feb 2001.

[54] A. A. Arzi. Microgravimetry for Engineering Applications. *Geophysical Prospecting*, 23(3):408–425, sep 1975.

[55] Damien Closson, Najib Abou Karaki, Musa Jad Hussein, Hassan Al-Fugha, André Ozer, and Abdullah Mubarak. Subsidence et effondrements le long du littoral jordanien de la mer Morte : Apports de la gravimétrie et de l'interférométrie radar différentielle. *Comptes Rendus - Geoscience*, 335(12):869–879, oct 2003.

[56] H. Moritz. Geodetic Reference System 1980. *Journal of Geodesy*, 74(1):128–133, mar 2000.

[57] W Torge. *Gravimetry*. Walter de Gruyter, 1989.

[58] D. A. G. Nowell. Gravity terrain corrections - an overview. *Journal of Applied Geophysics*, 42(2):117–134, 1999.

[59] E.C. Bullard. Gravity measurements in East Africa. *Philosophical Transactions of the Royal Society of London. Series A, Mathematical and Physical Sciences*, 235(757):445–531, aug 1936.

[60] T. R. LaFehr. An exact solution for the gravity curvature (Bullard B) correction. *Geophysics*, 56(8):1179–1184, 1991.

[61] X. Q. Ma and D. R. Watts. Terrain correction program for regional gravity surveys. *Computers and Geosciences*, 20(6):961–972, 1994.

[62] Horng-Yuan Yen, Yih-Hsiung Yeh, and Chao-Huei Chen. Gravity Terrain Corrections of Taiwan. *Terrestrial, Atmospheric and Oceanic Sciences*, 5(1):001, 1994.

[63] J. Fullea, M. Fernàndez, and H. Zeyen. FA2BOUG-A FORTRAN 90 code to compute Bouguer gravity anomalies from gridded free-air anomalies: Application to the Atlantic-Mediterranean transition zone. *Computers and Geosciences*, 34(12):1665–1681, 2008.

[64] Yoshiaki Tamura. Analysis of Earth Tides Data. In *The Practice of Time Series Analysis*, pages 327–339. Springer New York, New York, NY, 1999.

[65] A. Prasad, R. P. Middlemiss, K. Anastasiou, S. G. Bramsiepe, A. Noack, D. J. Paul, K. Toland, P. R. Utting, and G. D. Hammond. A Nineteen Day Earth Tide Measurement with a MEMS Gravimeter. sep 2021.

[66] Michel Van Camp and Paul Vauterin. Tsoft: graphical and interactive software for the analysis of time series and Earth tides. *Computers and Geosciences*, 31(5):631–640, jun 2005.

[67] Gerhard Jentzsch. Earth tides and ocean tidal loading. In *Tidal Phenomena*, pages 145–171. Springer-Verlag, Berlin/Heidelberg, 2005.

[68] P. J. Clarke and N. T. Penna. Ocean Tide Loading and Relative GNSS in the British Isles. *Survey Review*, 42(317):212–228, jul 2010.

[69] A. Lambert, S. D. Pagiatakis, A. P. Billyard, and H. Dragert. Improved ocean tide loading corrections for gravity and displacement: Canada and northern United States. *Journal of Geophysical Research: Solid Earth*, 103(B12):30231–30244, dec 1998.

[70] J. B. Merriam. Atmospheric pressure and gravity. *Geophysical Journal International*, 109(3):488–500, jun 1992.

[71] David A. Chapin. The theory of the Bouguer gravity anomaly: A tutorial. *The Leading Edge*, 15(5):361–363, may 1996.

[72] T M Niebauer, G S Sasagawa, J E Faller, R Hilt, and F Klopping. A new generation of absolute gravimeters. *Metrologia*, 32(3):159–180, jan 1995.

[73] T. Niebauer. Gravimetric Methods – Absolute and Relative Gravity Meter: Instruments Concepts and Implementation. In *Treatise on Geophysics*, pages 37–57. Elsevier, 2015.

[74] Mark Kasevich and Steven Chu. Atomic interferometry using stimulated Raman transitions. *Physical Review Letters*, 67(2):181–184, jul 1991.

[75] A. Peters, K. Y. Chung, and S. Chu. High-precision gravity measurements using atom interferometry. *Metrologia*, 38(1):25–61, feb 2001.

[76] J. Le Gouët, T. E. Mehlstäubler, J. Kim, S. Merlet, A. Clairon, A. Landragin, and F. Pereira Dos Santos. Limits to the sensitivity of a low noise compact atomic gravimeter. *Applied Physics B: Lasers and Optics*, 92(2):133–144, aug 2008.

[77] Lucien LaCoste. The zero-length spring gravity meter. *The Leading Edge*, 7(7):20–21, jul 1988.

[78] John M. Goodkind. The superconducting gravimeter. *Review of Scientific Instruments*, 70(11):4131–4152, nov 1999.

[79] Scintrex. CG-6 Autograv brochure, 2017.

[80] Micro-g LaCoste. FG5-X brocure. Technical report.

[81] R. P. Middlemiss, A. Samarelli, D. J. Paul, J. Hough, S. Rowan, and G. D. Hammond. Measurement of the Earth tides with a MEMS gravimeter. *Nature*, 531(7596):614–617, 2016.

[82] Robert Bogue. Recent developments in MEMS sensors: A review of applications, markets and technologies. *Sensor Review*, 33(4):300–304, sep 2013.

[83] Heinz-Hermann Essen, Frank Krüger, Torsten Dahm, and Ingo Grevemeyer. On the generation of secondary microseisms observed in northern and central Europe. *Journal of Geophysical Research: Solid Earth*, 108(B10), oct 2003.

[84] Simone Lepore and Marek Grad. Analysis of the primary and secondary microseisms in the wavefield of the ambient noise recorded in northern Poland. *Acta Geophysica*, 66(5):915–929, oct 2018.

[85] A. Prasad, S. G. Bramsiepc, R. P. Middlemiss, J. Hough, S. Rowan, G. D. Hammond, and D. J. Paul. A Portable MEMS Gravimeter for the Detection of the Earth Tides. *Proceedings of IEEE Sensors*, 2018-Octob(July):28–31, 2018.

[86] D. Carbone, L. Antoni-Micollier, G. Hammond, E. de Zeeuw - van Dalfsen, E. Rivalta, C. Bonadonna, A. Messina, J. Lautier-Gaud, K. Toland, M. Koymans, K. Anastasiou, S. Bramsiepe, F. Cannavò, D. Contrafatto, C. Frischknecht, F. Greco, G. Marocco, R. Middlemiss, V. Ménoret, A. Noack, L. Passarelli, D. Paul, A. Prasad, G. Siligato, and P. Vermeulen. The NEWTON-g Gravity Imager: Toward New Paradigms for Terrain Gravimetry. *Frontiers in Earth Science*, 8, oct 2020.

[87] John Heidemann, Milica Stojanovic, and Michele Zorzi. Underwater sensor networks: applications, advances and challenges. *Philosophical Transactions of the Royal Society A: Mathematical, Physical and Engineering Sciences*, 370(1958):158–175, jan 2012.

[88] Janine Guinan, Colin Brown, Margaret F.J. Dolan, and Anthony J Grehan. Ecological niche modelling of the distribution of cold-water coral habitat using underwater remote sensing data. *Ecological Informatics*, 4(2):83–92, may 2009.

[89] H M Manik. Acoustic Characterization of Fish and Seabed Using Underwater Acoustic Technology in Seribu Island Indonesia. *Journal of Marine Science: Research and Development*, 5(1):1–9, 2014.

[90] Philippe Blondel. *The Handbook of Sidescan Sonar*. Springer Berlin Heidelberg, Berlin, Heidelberg, 2009.

[91] Christian De Moustier and Haruyoshi Matsumoto. Seafloor acoustic remote sensing with multibeam echo-sounders and bathymetric sidescan sonar systems. *Marine Geophysical Researches*, 15(1):27–42, 1993.

[92] W I Stewart, Dezhang Chu, Sandipa Malik, S Lerner, and Hanumant Singh. Quantitative seafloor characterization using a bathymetric sidescan sonar. *IEEE Journal of Oceanic Engineering*, 19(4):599–610, 1994.

[93] R J J Dost and C M M Mannaerts. Generation of lake bathymetry using sonar, satellite imagery and GIS. In *Proceedings of the 2008 ESRI international user conference: GIS, Geography in action. San Diego, Florida*, 2008.

[94] Hassen Yesuf, Tena Alamirew, Assefa M. Melesse, and Mohammed Asse. Bathymetric Mapping for Lake Hardibo in Northeast Ethiopia Using Sonar. *International Journal of Water Sciences*, page 1, 2012.

[95] A C Keller. Submarine Detection by Sonar. *Transactions of the American Institute of Electrical Engineers*, 66(1):1217–1230, jan 1947.

[96] X. Lurton. *An Introduction to Underwater Acoustics: Principles and Applications*. Geophysical Sciences Series. Springer, 2002.

[97] R. T. Kessel and R. D. Hollett. Underwater intruder detection sonar for harbour protection: State of the art review and implications. 2006.

[98] L. P. Boivin, W. F. Davidson, R. S. Storey, D. Sinclair, and E. D. Earle. Determination of the attenuation coefficients of visible and ultraviolet radiation in heavy water. *Applied Optics*, 25(6):877, mar 1986.

[99] Anclré Morel and Louis Prieur. Analysis of variations in ocean color. *Limnology and Oceanography*, 22(4):709–722, jul 1977.

[100] Hendrik Buiteveld, J. H. M. Hakvoort, and M. Donze. Optical properties of pure water. pages 174–183, oct 1994.

[101] N. Jerlov. Beam attenuation. In *Marine Optics*, chapter 3, pages 47–66. Elsevier, 2, reprint edition, 1976.

[102] JTO Kirk. Attenuation of light in natural waters. *Marine and Freshwater Research*, 28(4):497, 1977.

[103] D.M. Kocak and B. Ouyang. Underwater imaging: photographic, digital and video techniques. In *Subsea Optics and Imaging*, chapter 11, pages 275–297. Elsevier, 2013.

[104] ZhongPing Lee, Alan Weidemann, John Kindle, Robert Arnone, Kendall L. Carder, and Curtiss Davis. Euphotic zone depth: Its derivation and implication to ocean-color remote sensing. *Journal of Geophysical Research*, 112(C3):C03009, mar 2007.

[105] P. Lunkenheimer, S. Emmert, R. Gulich, M. Köhler, M. Wolf, M. Schwab, and A. Loidl. Electromagnetic-radiation absorption by water. *Physical Review E*, 96(6):062607, dec 2017.

[106] R J Urick. *Principles of Underwater Sound*. Peninsula Publishing, 1983.

[107] Finn B. Jensen. Propagation and Signal Modeling. In *Handbook of Signal Processing in Acoustics*, pages 1669–1693. Springer New York, New York, NY, 2008.

[108] J. L. Stewart and E. C. Westerfield. Actlve Sonar Detection. 1953.

[109] Edmund J. Sullivan. Active Sonar. In *Handbook of Signal Processing in Acoustics*, pages 1737–1755. Springer New York, New York, NY, 2008.

[110] Brian H. Maranda. Passive Sonar. In *Handbook of Signal Processing in Acoustics*, pages 1757–1781. Springer New York, New York, NY, 2008.

[111] E J Nelson. Passive and active sonar prosecution of diesel submarines by nuclear submarines, 2008.

[112] F. J. Millero and F. Huang. The density of seawater as a function of salinity (5 to 70 g/kg) and temperature (273.15 to 363.15 K). *Ocean Science*, 5(2):91–100, may 2009.

[113] Trevor J. McDougall, David R. Jackett, Daniel G. Wright, and Rainer Feistel. Accurate and Computationally Efficient Algorithms for Potential Temperature and Density of Seawater. *Journal of Atmospheric and Oceanic Technology*, 20(5):730–741, may 2003.

[114] E.C. Bullard and R. I. B. Cooper. The determination of the masses necessary to produce a given gravitational field. *Proceedings of the Royal Society of London. Series A. Mathematical and Physical Sciences*, 194(1038):332–347, sep 1948.

[115] Yongen Cai and Chi-yuen Wang. Fast finite-element calculation of gravity anomaly in complex geological regions. *Geophysical Journal International*, 162(3):696–708, sep 2005.

[116] Toshio Fukushima. Precise and Fast Computation of the Gravitational Field of a General Finite Body and Its Application to the Gravitational Study of Asteroid Eros. *The Astronomical Journal*, 154(4):145, sep 2017.

[117] Sung Ho Na, Hyoungrea Rim, Young Hong Shin, Mutaek Lim, and Yeong Sue Park. Calculation of gravity due to a vertical cylinder using a spherical harmonic series and numerical integration. *Exploration Geophysics*, 46(4):381–386, 2015.

[118] I. S. Gradshteyn and I. M. Ryzhik. Special Functions. In Daniel Zwillinger, Victor Moll, I S Gradshteyn, and I M Ryzhik, editors, *Table of Integrals, Series, and Products (Eighth Edition)*, chapter 8, pages 867–1013. Academic Press, Boston, eighth edition, 2015.

[119] Edward Dawson. *An investigation into the effects of submergence depth, speed and hull length-to-diameter ratio on the near surface operation of conventional submarines*. PhD thesis, University of Tasmania, 2014.

[120] S Haykin, J H Justice, N L Owsley, J L Yen, and A C Kak. Array signal processing. 1985.

[121] H Krim and M Viberg. Two decades of array signal processing research: the parametric approach. *IEEE Signal Processing Magazine*, 13(4):67–94, jul 1996.

[122] L. Bjorno. Developments in sonar and array technologies. In *2011 IEEE Symposium on Underwater Technology and Workshop on Scientific Use of Submarine Cables and Related Technologies*, pages 1–11. IEEE, apr 2011.

[123] David K Barton. Modern radar system analysis. *Norwood*, 1988.

[124] Sebastian Rost. Array seismology: Methods and applications. *Reviews of Geophysics*, 40(3):1008, 2002.

[125] G.H. Rieke. Infrared Detector Arrays for Astronomy. *Annual Review of Astronomy and Astrophysics*, 45(1):77–115, sep 2007.

[126] Zhishan Zhao, Anbang Zhao, Juan Hui, Baochun Hou, Reza Sotudeh, and Fang Niu. A Frequency-Domain Adaptive Matched Filter for Active Sonar Detection. *Sensors*, 17(7):1565, jul 2017.

[127] J.R. Roman, M. Rangaswamy, D.W. Davis, Qingwen Zhang, B. Himed, and J.H. Michels. Parametric adaptive matched filter for airborne radar applications. *IEEE Transactions on Aerospace and Electronic Systems*, 36(2):677–692, apr 2000.

[128] Roberto Vio and Paola Andreani. Everything you always wanted to know about matched filters (but were afraid to ask), 2021.

[129] Samantha A Usman, Alexander H Nitz, Ian W Harry, Christopher M Biwer, Duncan A Brown, Miriam Cabero, Collin D Capano, Tito Dal Canton, Thomas Dent, Stephen Fairhurst, Marcel S Kehl, Drew Keppel, Badri Krishnan, Amber Lenon, Andrew Lundgren, Alex B Nielsen, Larne P Pekowsky, Harald P Pfeiffer, Peter R Saulson, Matthew West, and Joshua L Willis. The PyCBC search for gravitational waves from compact binary coalescence. *Classical and Quantum Gravity*, 33(21):215004, nov 2016.

[130] A.V. Oppenheim and G.C. Verghese. *Signals, Systems and Inference*, chapter 14. Pearson Education, 2015.

[131] Steven W. Smith. *The Scientist and Engineer's Guide to Digital Signal Processing*, chapter 7. California Technical Publishing, USA, 1997.

[132] Leslie M. Novak, Gregory J. Owirka, and Christine M. Netishen. Radar target identification using spatial matched filters. *Pattern Recognition*, 27(4):607–617, apr 1994.

[133] H. Akbarally and L. Kleeman. A sonar sensor for accurate 3D target localisation and classification. In *Proceedings of 1995 IEEE International Conference on Robotics and Automation*, volume 3, pages 3003–3008. IEEE.

[134] Benjamin J. Owen and B. S. Sathyaprakash. Matched filtering of gravitational waves from inspiraling compact binaries: Computational cost and template placement. *Phys. Rev. D*, 60:022002, Jun 1999.

[135] Hunter Gabbard, Michael Williams, Fergus Hayes, and Chris Messenger. Matching Matched Filtering with Deep Networks for Gravitational-Wave Astronomy. *Physical Review Letters*, 120(14):141103, apr 2018.

[136] John Fillmore Hayford and William Bowie. *Geodesy: the effect of topography and isostatic compensation upon the intensity of gravity*, volume 4. US Government Printing Office, 1912.

[137] Sigmund Hammer. Terrain Corrections for Gravimeter Stations, 1939.

[138] Dezso Nagy. The prism method for terrain corrections using digital computers. *Pure and Applied Geophysics PAGEOPH*, 63(1):31–39, 1966.

[139] D. Nagy, G. Papp, and J. Benedek. The gravitational potential and its derivatives for the prism. *Journal of Geodesy*, 74(7-8):552–560, 2000.

[140] D. A. Smith. The gravitational attraction of any polygonally shaped vertical prism with inclined top and bottom faces. *Journal of Geodesy*, 74(5):414–420, 2000.

[141] Mariano Loddo and Domenico Schiavone. Bouguer Correction for a Spherical Earth: Application to the Etna Data. In *Quaderni di Geofisica*, number November, pages 45–50, 2004.

[142] Y. C. Li and M. G. Sideris. Improved Gravimetric Terrain Corrections. *Geophysical Journal International*, 119(3):740–752, 1994.

[143] Michael G. Sideris. A Fast Fourier Transform method for computing terrain corrections. *Manuscripta Geodaetica*, 10(March):66–73, 1985.

[144] W D MacMillan. *The Theory of the Potential*. McGraw-Hill Book Company, Inc, New York, NY, 1930.

[145] Bharat Lohani and Suddhasheel Ghosh. Airborne LiDAR Technology: A Review of Data Collection and Processing Systems. *Proceedings of the National Academy of Sciences India Section A - Physical Sciences*, 87(4):567–579, 2017.

[146] Scottish Government and Joint Nature Conservation Committee. LiDAR for Scotland phases 1 to 4 DTM. `https://remotesensingdata.gov.scot`, 2022.

[147] Paramesh Banerjee. Gravity measurements and terrain corrections using a digital terrain model in the NW Himalaya. *Computers and Geosciences*, 24(10):1009–1020, 1998.

[148] J. Panisova, R. Pašteka, J. Papčo, and M. Fraštia. The calculation of building corrections in microgravity surveys using close range photogrammetry. *Near Surface Geophysics*, 10(5):391–399, 2012.

[149] A. C.R. Ketelaar. A system for computer-calculation of the terrain correction in gravity surveying. *Geoexploration*, 14(1):57–65, 1976.

[150] Ordnance Survey. OS Terrain® 50: UK topographic contour data, howpublished = `"https://osdatahub.os.uk/downloads/open/Terrain50"`, year = 2022.

[151] QGIS development team. QGIS website. `https://www.qgis.org/en/site/`, 2022.

[152] T. R. Lafehr. Standardization in gravity reduction. *Geophysics*, 56(8):1170–1178, aug 1991.

[153] GEBCO. 2020 GEBCO Grid. `https://www.gebco.net/data_and_products/gridded_bathymetry_data/`, 2020.

[154] Scintrex. *CG-5 Autograv Operation Manual*. Scintrex.

[155] Google. Google Maps. `https://www.maps.google.com`, 2022.

[156] British Geological Survey. Geology of Britain Viewer. `http://mapapps.bgs.ac.uk/geologyofbritain/home.html`, 2016.

[157] British Geological Survey. BGS 1:50 000 series, Sheet 31W (Scotland), Airdrie, Solid Geology.

[158] I. H. Forsyth, I. H. S. Hall, and A. A. McMillan. *Geology of the Airdrie District*. H.M. Stationery Office, 1996.

[159] P Stone. *Bedrock Geology UK North*. British Geological Survey, Keyworth, Nottingham, 2008.

[160] Alan Smith. A new edition of the bedrock geology map of the United Kingdom. *Journal of Maps*, 5(1):232–252, jan 2009.

[161] Jürgen H Schön. Chapter 1 - Rocks—Their Classification and General Properties. In Jürgen H Schön, editor, *Physical Properties of Rocks*, volume 65 of *Developments in Petroleum Science*, pages 1–19. Elsevier, 2015.

[162] Jürgen H Schön. Chapter 4 - Density. In Jürgen H Schön, editor, *Physical Properties of Rocks*, volume 65 of *Developments in Petroleum Science*, pages 109–118. Elsevier, 2015.

[163] William Rodney Cotton. *A Geophysical Survey of the Campsie and Kilpatrick Hills*. PhD thesis, University of Glasgow, 1969.

[164] University of Glasgow. University of Glasgow, Explore webpage. `https://www.gla.ac.uk/explore/visit/attractions/tour/cloisters/`, 2022.

[165] Daniel Boddice, Phillip Atkins, Anthony Rodgers, Nicole Metje, Yuriy Goncharenko, and David Chapman. A novel approach to reduce environmental noise in microgravity measurements using a Scintrex CG5. *Journal of Applied Geophysics*, 152:221–235, 2018.